ČESKÉ VYSOKÉ UČENÍ TECHNICKÉ V PRAZE

Fakulta stavební

Katedra mechaniky

Parameters identification of advanced constitutive models of soils

DISERTAČNÍ PRÁCE

Ing. Tomáš Kadlíček

Doktorský studijní program: Stavební inženýrství

Studijní obor: Fyzikální a materiálové inženýrství

Školitel: Prof. Ing. Michal Šejnoha, Ph.D., DSc.
Ing. Tomáš Janda, Ph.D.

Praha, 2019

ČESKÉ VYSOKÉ UČENÍ TECHNICKÉ V PRAZE
Fakulta stavební
Thákurova 7, 166 29 Praha 6

PROHLÁŠENÍ

Jméno doktoranda: Ing. Tomáš Kadlíček

Název disertační práce: Parameters identification of
advanced constitutive models of soils

Prohlašuji, že jsem uvedenou disertační práci vypracoval/a samostatně pod vedením školitele Prof. Ing. Michala Šejnohy, Ph.D., DSc..
Použitou literaturu a další materiály uvádím v seznamu použité literatury.

Disertační práce vznikla v souvislosti s řešením projektu: TA04031603

V Praze dne ....
podpis

Contents

List of Figures

List of Tables

Acknowledgements

Foremost, I would like to express my graditude to my supervisor Prof. Michal Sejnoha for his patience, motivation and leadership during my Ph.D study and I am particularly grateful for his guidence and mentoring during writing of this thesis. I am also deeply grateful to my supervisor Dr. Tomas Janda for his thorough advices during my Ph.D study.

My gratitude also belongs to the doc. David Masin for the counseling and encouraging discussions he provided me with during the development of my work.

Last but not the least, I would like to thank to my family for the limitless support and solace I was provided during my life and studies.

Abstrakt

Tato práce se zabývá kalibračními metodami pro tři pokročilé materiálové modely, jmenovitě elastoplastický Cam-Clay, Von Wolffersdoffovův hypoplastický model pro hrubozrnné zeminy a Mašínův hypoplastický model pro jemnozrnné zeminy s náležitými konstitutivními rovnicemi a kalibračními postupy pro materiálové parametry. Následně je provedena sensitivní analýza materiálových parametrů, jejíž výsledky jsou zohledněny při vývoji kalibračního programu ExCalibre. Tento program určuje materiálové parametry na základě zkoušek stlačitelnosti a triaxiálních zkoušek. Následně je provedena korelace mezi materiálovými parametry a materiálovými charakteristikami zemin. Práce je zakončena příkladem implementace Von Wolffersdoffova hypoplastického modelu do programu GEO5 MKP.

Abstract

This thesis is dedicated to the development of calibration methods for three advanced constitutive models of soils, namely elastoplastic Cam-Clay model, Von Wolffersdoff's hypoplastic model to coarse grained soils and Masin's hypoplastic model for fine grained soils. Corresponding constitutive equations and recommended calibration methods for their parameters identification are thoroughly described. Following the results of a sensitivity analysis which was performed on the models parameters, a development of a calibration software ExCalibre is described. The calibration software determines the models parameters on the basis of compression and triaxial laboratory experiments. Subsequently, the correlation analysis is performed for hypoplastic models to establish the link between the models parameters and soil properties. The thesis is concluded with an implementation of the hypoplastic sand model into the GEO5 FEM software.

Introduction

Even though the geotechnical engineering has experienced a significant development in the field of a constitutive modelling and numerous new approaches, such as hypoplasticity or bounding surface plasticity have been pursued, these advanced theories are still less common in engineering practise and their use is mostly limited to the academic studies. This state is probably caused by the lack of either knowledge regarding the theory of advanced soil models or tools necessary for the prompt and reliable calibration of the models parameters. Therefore, the complexity of the calibration is often beyond capabilities of a common engineer. This thesis, therefore, aims at facilitating operations related to the calibration of advanced soil models and thus narrow the gap between the academic and engineering community. In order to meet this goal, the thesis is concerned with three objectives.

The first objective is to develop an easily accessible calibration software for the advanced constitutive models, which requires a minimum of external user's intervention with clearly interpretable results. To this purpuse, a calibration software ExCalibre was developed at the Czech Technical University with the cooperation of Charless University and Geotechnica plc. The constitutive models selected for the calibration are elastoplastic Modified Cam-Clay model, Wolffersdorff's hypoplastic sand model and Masin's hypoplastic clay model. A theory regarding the selected constitutive models is thoroughly described in the first chapter. Recommended and proposed calibration methods are described in the second chapter and the third chapter is dedicated to the methods solving nonlinear equations and methods integrating differential equations. The ExCali-

bre software operates as a free to use online application which in exchange for a service gather the calibration input data. Establishing the calibration procedures was preceded by the sensitivity analysis which indicated an impact of each parameter individually on the models predictions. Following the sensitivity analysis, the calibration procedures were developed and thoroughly tested. The testing was performed on a library of laboratory experiments provided by Charless University and Geotechnika plc. consisting of coarse grained soils from nine locations and fine grained soils from seventeen locations. A development of software ExCalibre is described in the fourth chapter.

The second objective is to find correlations between the soils characteristics and hypoplastic models parameters. This correlations should later serve as a tool for a prompt estimation of the parameters values. The calibration of the models parameters was performed by the software ExCalibre. An assessment and evaluation of the correlations in the fifth chapter was achieved by emloying linear and nonlinear regression. It was revealed that strong correlations can be found in case of the hypoplastic clay model while the correlations were less significant in case of the hypoplastic sand model. All the observed correlations can be found in the Appendix A and Appendix B.

The third objective was to implement the hypoplastic sand model to GEO5 FEM software and thus supplementing a constitutive soil models library. The implementation and its testing against the Triax software is described in the sixth chapter. Triax is a single element software developed for various constitutive models simulating laboratory experiments.

The future works related to the topic of this thesis might be dedicated to the extension of the constitutive models calibrated by the ExCalibre software. The intergranular enhancement of the hypoplastic models could be of the particular interest. Furthermore, the observed correlations can be later improved once additional laboratory input data are gathered through the ExCalibre software.

1. Constitutive models

Constitutive models together with the finite element method softwares form an inherent tool in the nowadays engineering calculations. Due to a rapid development in the Information Technology, engineers are provided with higher computational power and more sophisticated numerical models that can be employed. However, the use of the advanced soil models in the practise is still rare and more simple elasto-plastic models such as Mohr-Coulomb are often preffered. Even though these simple models can well predict a stress failure, their predicted stress strain response does not agree with a state and history dependent behaviour of soils. It is worth noting, however, that the prediction capabilities of these models can be improved with further extensions or enhancements.

Extensions of the basic soil models

- Strain hardening/softening - Enables expansion of the yield surface with respect to the evolution of the plastic strain.
- Additional stiffness - Adds additional stiffness for unloading or links the stiffness evolution with depth.
- Cut off models - Adds addtitional yield surface to reduce accessible tensile stresses.
- Cap models - Adds addtional yiled surface along the hydrostatic axis to avoid excessive stresses.

More advantageous can be the use of advanced soil models that can well predict both soil failure and nonlinear stress strain behaviour as well as strain hardening and softening. The state of advanced soil models is usually presented in the common space of a deviatoric stress q, mean stresses p and void ratio e in $q \times p \times e$ space, while all admissible states are covered by the so called

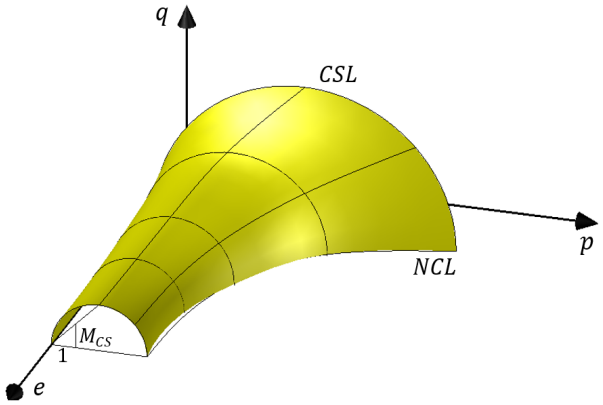

Figure 1.1: State Boundary Surface

State Boundary Surface (SBS) as shown in Fig. 1.1. The following advanced soil models are addressed in the thesis:

Advanced soil models

- Modified Cam-Clay model [2]
- Masin's hypoplastic clay model [3]
- Von Wolffersdoff's hypoplastic sand model [4]

Further sections are concerned with the basic features of both basic and advanced soil models. The basic models are represented by the Mohr-Coulomb model as it well represents usually employed models in FEM softwares and the advanced soil models are represented by the Cam-Clay model and hypoplastic sand and hypoplastic clay models. The following tensorial multiplications are used in this chapter:

- $\mathbf{A} \cdot \mathbf{B} = A_{ij}B_{jk} = C_{ik}$
- $\mathbf{A} : \mathbf{B} = A_{ij}B_{ij} = c$
- $\mathbf{A} \otimes \mathbf{B} = A_{ij}B_{kl} = C_{ijkl}$
- $||\mathbf{A}|| = \sqrt{A_{ij}A_{ij}}$

1.1 Elastoplastic models

This section is dedicated to the elastoplastic theory and it is further divided into three parts. The first part aims to outline the general elastoplastic theory, relations and mathematical formulations. The second part is focused on the Mohr-Coulomb model for it represents one of the stepping stones in geotechnical numerical modelling and it is up to day one of the most often employed constitutive model. The third part is concerned with the Modified Cam-Clay model. This model successfully incorporates the stiffness dependency on a density represented by a void ratio e and belongs to the group of so called Critical State Soil Models.

1.1.1 General definitions

The father of plasticity is often regarded Henri Tresca who observed by thorough testing a relation between the yielding and maximal shear stress [5]. The Tresca failure criterion forms an infinite hexagonal prism in the principal stress space called the yield surface. This prism is symmetric along the so called hydrostatic axis which can be characterized by the condition of an equilibrium of the principal stresses $\sigma_1 = \sigma_2 = \sigma_3$. According to this condition, one can reach an infinite mean stress p without failure while exhibiting the elastic strain ε_{el} . However, if any of the principal stresses increases independently of the others, the stress state will eventually reach the yield surface and the plastic strain ε_{pl} will be produced. The exact position of the stress state in the principal stress space with respect to the yield surface is described by the loading function $F(\boldsymbol{\sigma}, \boldsymbol{\kappa})$, where $\boldsymbol{\sigma}$ represents the Cauchy second order stress tensor and $\boldsymbol{\kappa}$ vector of the state hardening parameters. The yield surface is in the pripcipal stress space defined by the condition $F(\boldsymbol{\sigma}, \boldsymbol{\kappa}) = 0$.

Described behaviour demonstrates the main feature of the elastoplastic model that is decomposition of the total strain ε_{tot}into the elastic ε_{el} and plastic ε_{pl} components. The elastoplastic material exhibits plastic yielding if both conditions in Eq. (1.1.1) are fulfilled, i.e. the stress state occurs on the yield surface

while a further loading is conducted

$$F(\boldsymbol{\sigma}, \boldsymbol{\kappa}) = 0, \qquad \left(\frac{\partial F}{\partial \boldsymbol{\sigma}}\right) : \mathrm{d}\boldsymbol{\sigma} > 0. \tag{1.1.1}$$

The pure elastic strain emerges in one of the scenarios defined by Eqns. (1.1.2)–(1.1.4):

- The stress state occurs on the yield surface with subsequent unloading

$$F(\boldsymbol{\sigma}, \boldsymbol{\kappa}) = 0, \qquad \left(\frac{\partial F}{\partial \boldsymbol{\sigma}}\right) : \mathrm{d}\boldsymbol{\sigma} < 0. \tag{1.1.2}$$

- The stress state occurs on the yield surface with subsequent neutral loading

$$F(\boldsymbol{\sigma}, \boldsymbol{\kappa}) = 0, \qquad \left(\frac{\partial F}{\partial \boldsymbol{\sigma}}\right) : \mathrm{d}\boldsymbol{\sigma} = 0. \tag{1.1.3}$$

- The stress state occurs inside the yield surface upon loading

$$F(\boldsymbol{\sigma}, \boldsymbol{\kappa}) < 0. \tag{1.1.4}$$

The stress state cannot occur outside of the yield surface and thus, the condition presented by Eq. (1.1.5) is not admissible

$$F(\boldsymbol{\sigma}, \boldsymbol{\kappa}) > 0. \tag{1.1.5}$$

In order to assure that the stress state remains on the yield surface during loading, the total differential of the first condition in Eq. (1.1.1) called the *consistency condition* becomes zero, see Eq. (1.1.6)

$$\mathrm{d}F = \left(\frac{\partial F}{\partial \boldsymbol{\sigma}}\right) : \mathrm{d}\boldsymbol{\sigma} + \left(\frac{\partial F}{\partial \boldsymbol{\kappa}}\right) \cdot \mathrm{d}\boldsymbol{\kappa} = 0. \tag{1.1.6}$$

The determination of direction of the plastic strain increment $d\varepsilon_{pl}$ according to the principal strains requires to involve the hypothesis of the so called *flow rule*, which postulates that the direction of the plastic date occurs perpendicular to the so called *plastic potential surface* G. Similarly to the yield surface F, the plastic potential surface is defined in the principal stress space by $G = G(\boldsymbol{\sigma}, \boldsymbol{\kappa})$. The case when Eq. (1.1.7) is applied is called the *associated plasticity*, otherwise is called the *non-associated plasticity*. In general, Eq. (1.1.7) is not in agreement with the behaviour of soil

$$F(\boldsymbol{\sigma}, \boldsymbol{\kappa}) = G(\boldsymbol{\sigma}, \boldsymbol{\kappa}). \tag{1.1.7}$$

The increment of the plastic strain is then evaluated by Eq. (1.1.8), where $d\lambda$ is a scalar variable called *plastic multiplier*. It is clear that $d\lambda = 0$ in the case of elastic response and the condition $\lambda > 0$ generates plastic strain

$$d\varepsilon_{pl} = d\lambda \frac{\partial G}{\partial \boldsymbol{\sigma}}. \tag{1.1.8}$$

The increment of the total strain $d\varepsilon_{tot}$is defined as a sum of the elastic $d\varepsilon_{el}$ and plastic $d\varepsilon_{pl}$ strain increments, see Eq. (1.1.9). When deriving the increment of the elastic strain $d\varepsilon_{el}$ from Eq. (1.1.9) and subsequently substituting into the constitution relation for the elastic material one can obtain relation for the elasto-plastic material in Eq. (1.1.10), where $\mathbf{D}_{el}$ represents the elastic stiffness matrix

$$d\varepsilon_{tot} = d\varepsilon_{el} + d\varepsilon_{pl}, \tag{1.1.9}$$

$$d\boldsymbol{\sigma} = \mathbf{D}_{el} : (d\varepsilon_{tot} - d\varepsilon_{pl}) = \mathbf{D}_{el} : \left(d\varepsilon_{tot} - h(F) d\lambda \frac{\partial G}{\partial \boldsymbol{\sigma}} \right), \tag{1.1.10}$$

, where

$$h[F] = \begin{cases} 0, & F < 0, \\ 1, & F \geq 0. \end{cases} \tag{1.1.11}$$

The function $h(F)$ is so called heaviside function representing a typical switch function of the elastoplastic models. It is worth noting that once the condition $F \leq 0$ is broken for a new stress increment, the loading condition is changed from elastic to plastic and the intersection between the direction of loading and yield surface has to be found in order to correctly initiate the plastic loading.

The magnitude of the plastic multiplier $\mathrm{d}\lambda$ can be derived from the *consistency condition* Eq. (1.1.6) when rearranged to the so called *Melan's form*, see Eq. (1.1.12),

$$\mathrm{d}F = \left(\frac{\partial F}{\partial \boldsymbol{\sigma}}\right) : \mathrm{d}\boldsymbol{\sigma} + H\mathrm{d}\lambda \tag{1.1.12}$$

with

$$H = -\left(\frac{\partial F}{\partial \boldsymbol{\kappa}}\right) \cdot \frac{\partial \kappa}{\partial \lambda}, \tag{1.1.13}$$

where H represents the *modulus of plastic hardening*.

When substituting the expression of $\mathrm{d}\boldsymbol{\sigma}$ from Eq. (1.1.10) to the consistency condition Eq. (1.1.6), the formulation of $\mathrm{d}\lambda$ yields Eq. (1.1.14). Further substitution into Eq. (1.1.10) for $\mathrm{d}\lambda$ from Eq. (1.1.14) produces Eq. (1.1.15)

$$\mathrm{d}\lambda = \frac{\left(\frac{\partial F}{\partial \boldsymbol{\sigma}}\right) : \mathbf{D}_{el} : \mathrm{d}\boldsymbol{\varepsilon}_{tot}}{H + \left(\frac{\partial F}{\partial \boldsymbol{\sigma}}\right) : \mathbf{D}_{el} : \left(\frac{\partial G}{\partial \boldsymbol{\sigma}}\right)}, \tag{1.1.14}$$

$$\mathrm{d}\boldsymbol{\sigma} = \left(\mathbf{D}_{el} - \frac{\left(\mathbf{D}_{el} : \frac{\partial G}{\partial \boldsymbol{\sigma}}\right) \otimes \left(\frac{\partial F}{\partial \boldsymbol{\sigma}} : \mathbf{D}_{el}\right)}{H + \left(\frac{\partial F}{\partial \boldsymbol{\sigma}}\right) : \mathbf{D}_{el} : \left(\frac{\partial G}{\partial \boldsymbol{\sigma}}\right)}\right) : \mathrm{d}\boldsymbol{\varepsilon}_{tot} = \tag{1.1.15}$$

$$= \mathbf{D}_{elpl} : \mathrm{d}\boldsymbol{\varepsilon}_{tot}, \tag{1.1.16}$$

, where $\mathbf{D}_{elpl}$ represents so called elastoplastic tangent stiffness matrix [6].

From the abovementioned stress-strain relations, it is clear that the direction of the plastic flow is independent of the stress direction and the direction of the plastic flow is defined solely by the plastic potential surface. Furthermore, the plastic flow can be further divided into a deviatoric and volumetric plastic strain. In the case of simple elastoplastic models such as Mohr-Coulomb or Drucker-Prager, the non-associated plasticity can be employed in the way that the resulting plastic strain represents actual soil state, i.e., positive volumetric strain for loose sand and negative volumetric strain for overconsolidated sand while sheared under drained conditions. Hereinafter, the Mohr-Coulomb and Cam-Clay model will be discussed. The Mohr-Coulomb model is still probably the most common elastoplastic model in a general engineering practice and the Cam-Clay model can be seen as the the stepping stone in the attempt to reliably simulate soil's behaviour and it is often incorporated in the FEM software model libraries.

1.1.2 Mohr-Coulomb model

The Morh-Coulomb model connects Mohr's circle with Coulomb's failure criterion. The typical feature of this model is a characterization of a soil state with respect to the current stress state only. Neither density of the specimen nor history of a loading are considered. Model's yield surface $F(\sigma_1, \sigma_2, \sigma_3) = 0$ is defined with the aid of the principal stresses by

$$F(\sigma_1, \sigma_2) = \frac{1}{2}(\sigma_1 - \sigma_2) + \frac{1}{2}(\sigma_1 + \sigma_2)\sin\varphi - c\cos\varphi = 0 \tag{1.1.17}$$

for one side of an infinite hexagonal pyramid opened along the hydrostatic axis, see Fig. 1.2. The plastic potential surface $G(\sigma_1, \sigma_2, \sigma_3) = 0$ can be defined by

$$G(\sigma_1, \sigma_2) = \frac{1}{2}(\sigma_1 - \sigma_2) + \frac{1}{2}(\sigma_1 + \sigma_2)\sin\psi = 0. \tag{1.1.18}$$

Equtions for the other sides of the yield surface can be derived by the permuatation of the stress indexes [6]. The Mohr-Coulomb model requires the following parameters:

- E - Young's modulus
- ν - Poisson's ratio
- c - Cohesion
- φ - Angle of internal friction
- ψ - Angle of dilatancy

It is worth noting that these parameters are rather state variables than soil's parameters as they are valid only for a certain range of stresses. Consequently, the same soil occurring in different states should be defined by different sets of parameters. Even though the resulting stress/strain relation of the Mohr Coulomb model is not accurate it still well manages to address the stress failure criterion of the soil specimen [6].

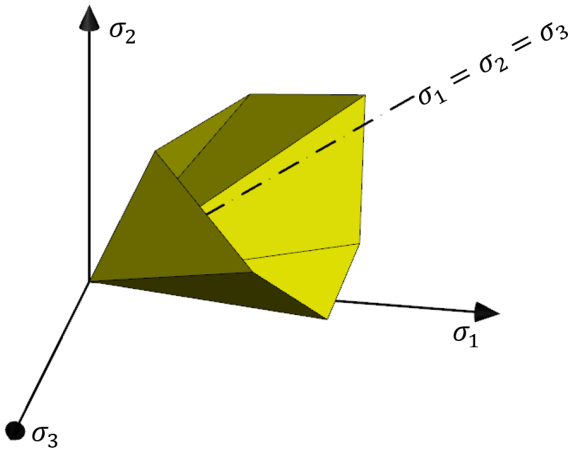

Figure 1.2: Mohr-Coulomb failure surface in the principal stress space

Though the parameter ψ is recommended to be derived from internal friction angle φ as $\psi = \varphi$ - 30, the parameter ψ can be set in a specific way to simulate three different conditions:

- $\psi = 0$ - No volumetric strain is produced during plastic yielding
- $\psi > 0$ - Soil exhibits a dilation during plastic yielding, the soil is relatively dense
- $\psi < 0$ - Soil exhibits a contraction during plastic yielding, the soil is relatively loose

In the case of single element test softwares which represent a convenient tool to show a constitutive models' behaviour and capabilities, the calculation of stress and strain increment is often changed from the principal stress space σ_1, σ_2, and σ_3 to the space of invariant stresses p and q which is not, however, possible in the case of the Mohr-Coulomb model since the yield surface has sharp edges and therefore more then one side of the yield surface pyramid is affected during a triaxial compression/extension. In addition, further equations in this section are expressed in the principal stresses and strains which enables to rewrite the Cauchy second order stress tensor as a vector.

For the sake of clarity the calculation of a stress/strain increment is shown hereinafter. As it was pointed out in Eqns. (1.1.1)–(1.1.4) a typical feature of the elasto-plastic models is a switch function which determines whether the state is on or inside of the yield surface and the stress/strain increment is calculated accordingly.

Given the fact that the specimen is experiencing a strain driven loading and the condition Eq. (1.1.4) or Eq. (1.1.2) is fulfilled, the stress state occurs inside the yield surface and the stress increment is defined by

$$\mathrm{d}\boldsymbol{\sigma} = \mathbf{D}_{el} \cdot \mathrm{d}\boldsymbol{\varepsilon}_{tot}, \tag{1.1.19}$$

where

$$\mathrm{d}\boldsymbol{\sigma}^T = \mathrm{d}\boldsymbol{\sigma}^T(\mathrm{d}\sigma_1, \mathrm{d}\sigma_2, \mathrm{d}\sigma_3), \tag{1.1.20}$$

$$\mathrm{d}\boldsymbol{\varepsilon}_{tot}^T = \mathrm{d}\boldsymbol{\varepsilon}_{tot}^T(\mathrm{d}\varepsilon_{tot,1}, \mathrm{d}\varepsilon_{tot,2}, \mathrm{d}\varepsilon_{tot,3}) \tag{1.1.21}$$

and

$$\mathbf{D}_{el} = \begin{bmatrix} \dfrac{E(1-\nu)}{(1+\nu)(1-2\nu)} & \nu & \nu \\ \nu & \dfrac{E(1-\nu)}{(1+\nu)(1-2\nu)} & \nu \\ \nu & \nu & \dfrac{E(1-\nu)}{(1+\nu)(1-2\nu)} \end{bmatrix}.$$

However, if the condition Eq. (1.1.1) is to be fulfilled, the stress increment is calculated by Eq. (1.1.15) with corresponding partial derivations defined by

$$\frac{\mathrm{d}F}{\mathrm{d}\sigma} = \frac{1}{2}(1 + \sin\varphi, -1 + \sin\varphi, 0)^T \tag{1.1.22}$$

and

$$\frac{\mathrm{d}G}{\mathrm{d}\sigma} = \frac{1}{2}(1 + \sin\psi, -1 + \sin\psi, 0)^T \tag{1.1.23}$$

If no hardening parameter $\boldsymbol{\kappa}$ is defined, the hardening modulus $H = 0$ and the plastic pultiplier $\mathrm{d}\lambda$ from Eq. (1.1.10) and Eq. (1.1.14) takes a form of

$$\mathrm{d}\lambda = \left(\frac{(1+\sin\varphi)E_D d\varepsilon_1 + (-1+\sin\varphi)E_D d\varepsilon_2}{(1+\sin\varphi)E_D(1+\sin\psi) + (-1+\sin\varphi)E_D(-1+\sin\psi)} \right), \quad (1.1.24)$$

where

$$E_D = \frac{E(1-\nu)}{(1+\nu)(1-2\nu)} \quad (1.1.25)$$

The stress increment defined by Eq. (1.1.10) can be for the Mohr-Coulomb model expressed in the matrix notation by

$$\begin{pmatrix} \mathrm{d}\sigma_1 \\ \mathrm{d}\sigma_2 \\ \mathrm{d}\sigma_3 \end{pmatrix} = \begin{bmatrix} E_D & \nu & \nu \\ \nu & E_D & \nu \\ \nu & \nu & E_D \end{bmatrix} \left[\begin{pmatrix} \mathrm{d}\varepsilon_{tot,1} \\ \mathrm{d}\varepsilon_{tot,2} \\ \mathrm{d}\varepsilon_{tot,3} \end{pmatrix} - h(F)\frac{1}{2}\mathrm{d}\lambda \begin{pmatrix} 1+\sin\varphi \\ -1+\sin\varphi \\ 0 \end{pmatrix} \right]. \quad (1.1.26)$$

1.1.3 Modified Cam-Clay model

A significant step forward in the constitutive modelling of soil's behaviour was the Original CamClay model [7]. This model successfully incorporated an influence of a void ratio e and divides material properties to state variables and material parameters. Cam-Clay belongs to the group of the so Critical State Soil models and thus the model predicts a failure once the critical state is reached and no other volumetric strain increment is generated. A shortcoming of this model was the shape of the yield surface which was created by a curve of a natural logarithm. This shape consequently led to a nonzero increment of the plastic deviatoric strain $d\varepsilon_{pl}^{v}$ during loading along the isotropic normal compression line (INCL). Later work on the Modified Cam Clay (MCC) model replaced logarithmic shaped yield surface by the elliptic one [2]. The Cam-Clay model is defined by the following parameters.

- λ - Slope of the NCL line in the $\ln p \times e$ space
- e_0 - Void ratio at $p = 1$kPa on the INCL line in the $\ln p \times e$ space
- κ - Slope of the swelling line in the $\ln p \times e$ space
- ν - Poisson's ratio
- M_{cs} - Slope of the critical state line (CSL) in the deviatoric plane

The ellipsoidal yield surface in the principal stress space, see Fig. 1.3a, is defined by Eq. (1.1.27), where p_c represents the overconsolidation pressure

$$F(p, q, p_c) = \frac{q^2}{M_{cs}^2} + p^2 - p_c p = 0. \tag{1.1.27}$$

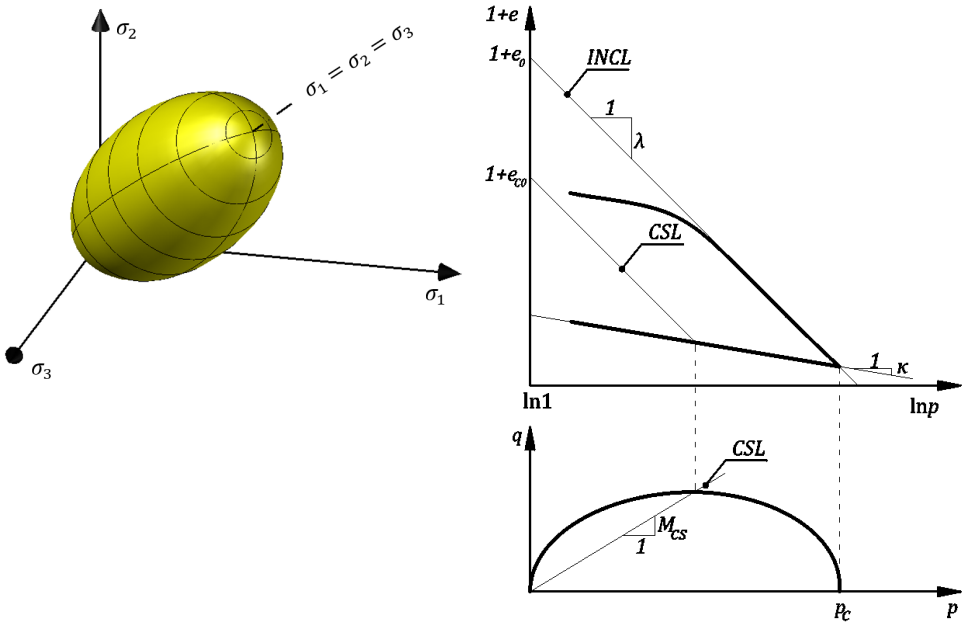

(a) MCC failure surface in the principal stress space

(b) MCC failure surface in the meridian stress space

Figure 1.3: MCC failure surface

The typical feature of the Cam-Clay model is the *isotropic hardening/softenning rule*, see Eq. (1.1.28), which defines the relation between the overconsolidation pressure p_c and volumetric plastic strain ε_{pl}^{v} and thus controls the expansion of the elliptical yield surface

$$\dot{p}_c = \frac{p_c(1+e)\dot{\varepsilon}_{pl,v}}{\lambda - \kappa}. \tag{1.1.28}$$

Due to the shape of the yield surface, the distance between the initial critical void ratio and isotropic void ratio can be calculated by Eq. (1.1.29), where e_{c0} represents the critical state void ratio at $p = 1\text{kPa}$

$$e_{c0} = e_0 - \lambda \ln 2. \tag{1.1.29}$$

The relations for the bulk modulus K and shear stiffness modulus G are defined by

$$K = \frac{p(1+e)}{\kappa} \tag{1.1.30}$$

and

$$G = \frac{3(1-2\nu)}{2(1+\nu)}K \tag{1.1.31}$$

Furthermore the model exhibits the elastic strain increment $\mathrm{d}\varepsilon^{v}_{el}$ during unloading or loading inside the yield surface, see Eq. (1.1.32), and the plastic volumetric strain strain $\mathrm{d}\varepsilon^{v}_{pl}$ during expansion of the yield surface, see Eq. (1.1.33).

$$\dot{p} = \frac{p\dot{\varepsilon}_{el,v}(1+e)}{\kappa}, \tag{1.1.32}$$

$$\dot{p} = \frac{p\dot{\varepsilon}_{tot,v}(1+e)}{\lambda}. \tag{1.1.33}$$

The stress/strain increment predicted by the Modified Cam-Clay model for the elastic loading/unloading is defined by

$$\mathrm{d}\boldsymbol{\sigma} = \mathbf{D}_{el} \cdot \mathrm{d}\boldsymbol{\varepsilon}_{tot} \tag{1.1.34}$$

with

$$\mathrm{d}\boldsymbol{\sigma}^{T} = (\mathrm{d}p, \mathrm{d}q), \tag{1.1.35}$$

$$\mathrm{d}\boldsymbol{\varepsilon}^{T}_{tot} = (\mathrm{d}\varepsilon_{tot,p}, \mathrm{d}\varepsilon_{tot,q}) \tag{1.1.36}$$

and

$$\mathbf{D}_{el} = \begin{bmatrix} K & 0 \\ 0 & 3G \end{bmatrix} \tag{1.1.37}$$

where the elastic matric $\mathbf{D}_{el}$ is defined with the aid of the moduli K and G.

In the case of plastic loading the stress increment is defined by Eq. (1.1.10) while the partial derivatives of the elastoplastic stiffness matrix Eq. (1.1.15) are expressed below

$$\frac{\mathrm{d}F}{\mathrm{d}p} = 2p - p_c, \tag{1.1.38}$$

$$\frac{\mathrm{d}F}{\mathrm{d}q} = \frac{2q}{3M_{cs}^2}, \tag{1.1.39}$$

$$H = \frac{F}{\mathrm{d}\boldsymbol{\kappa}}\frac{\mathrm{d}\boldsymbol{\kappa}}{\mathrm{d}\lambda} = -(2p - p_c)\frac{p_c p}{\lambda - \kappa}. \tag{1.1.40}$$

The resulting plastic multiplier $\mathrm{d}\lambda$ and increment of plastictic strains are expressed by

$$\mathrm{d}\lambda = \left(\frac{(2p - p_c)K\, d\varepsilon_{tot,p} + \dfrac{2q}{3M_{cs}^2} d\varepsilon_{tot,q}}{(2p - p_c)\dfrac{-p_c p}{\lambda - \kappa} + (2p - p_c)^2 K + \left(\dfrac{2q}{3M_{cs}^2}\right)^2 3G} \right) \tag{1.1.41}$$

and

$$\mathrm{d}\boldsymbol{\varepsilon}_{pl} = \mathrm{d}\lambda \frac{\mathrm{d}F}{\mathrm{d}\boldsymbol{\sigma}}. \tag{1.1.42}$$

Substituting G for F in Eq. (1.1.42) when comparing to Eq. (1.1.8) implies associative flow rule.

The increment of the overconsolidation pressure p_c from Eq. (1.1.28) is integrated and expressed by

$$\mathrm{d}p_c = \exp\left(\frac{-d\varepsilon_{pl,v}}{(\lambda - \kappa)}\right). \tag{1.1.43}$$

The stress increment Eq. (1.1.10) of the Modified Cam-Clay model can defined with the aid of Eqns. (1.1.34)–(1.1.42) in the terms of matrix notation by

$$\begin{pmatrix} \mathrm{d}p \\ \mathrm{d}q \end{pmatrix} = \begin{bmatrix} K & 0 \\ 0 & 3G \end{bmatrix} \left[\begin{pmatrix} \mathrm{d}\varepsilon_{tot,p} \\ \mathrm{d}\varepsilon_{tot,q} \end{pmatrix} - h(F)\mathrm{d}\lambda \begin{pmatrix} 2p - p_c \\ 2q/3M_{cs}^2 \end{pmatrix} \right]. \tag{1.1.44}$$

Even though the model provides a nonlinear relation between the stress and strain, it still exhibits a recoverable elastic strain at large deformations, which is in contradiction with observed soil behaviour and thus is not suitable for cyclic loadings. Furthermore, the Modified Cam-Clay model tends to overestimate the peak friction angle φ_p during shearing on the dry side and the shape of the yield surface in the meridian space also does not well correspond with the observation and overestimates the stress failure in the triaxial extension. These shortcomings might lead to unsafe designs. The Cam-Clay model serves as the baseline for many different later works and modifications of the Critical State Soil models, such as [8].

1.2 Hypoplastic models

The following chapters are dedicated to the theory of hypoplasticity. The section *General definitions* covers in short a development of the hypoplasticity from the very beginning to the comprehensive Von Wilffersdorff's and Masin hypoplastic models. The second and third section concentrates on the particular examples of the hypoplastic models for sands and clays which calibrations are required from calibration program.

1.2.1 General definitions

The initial studies and development of the hypoplastic equations put forth by Kolymbas in [9] are reviewed first. The Bauer and Gudehus hypoplastic model, which incorporated dependency on the void ratio and stress level is discussed next and finally the Von Wolffersdorff's hypoplastic sand model and Masin's hypoplastic clay model is introduced.

Initial studies

The hypoplasticity emerges in the 70s as an alternative approach to the elastoplastic constitutive modelling of granular materials behaviour such as coarse grained soils. Unlike the theory of elastoplasticity, which in general employs the yield surface to simulate failure and divides the total strain to the elastic and plastic, the hypoplasticity does not involve yield surface to simulate failure and the failure is a consequence of reaching the critical state.

Analogous to the elastoplasticity, the hypoplasticity in the literature distinguishes between two surfaces:

- Limit surface - Can be also referred to as a failure surface or yield surface. This surface is defined in the stress space by the condition of vanishing both stress rate $\dot{\sigma} = 0$ and volumetric strain rate.

- Boundary surface - Also can be referred to as state boundary surface, asymptotic state boundary surface, swept-out memory surface. These ti-

tles, however, does not always represent the same thing. The state boundary surface covers all admissible states, the asymptotic state boundary surface and swept-out memory surface represents all asymptotic states, e.i., states that are reached after a sufficient amount of loading in the same strain rate direction. One of these state is also the critical state.

As the soil is in general subjected to the large deformation and, the difference between the original undeformed and the final deformed state is distinguishable. The theory of infinitesimal small strain theory is thus insufficient and finite strain theory is needed. Kolymbas[9] used Jauman objective stress rate tensor $\mathring{\boldsymbol{\sigma}}$ defined by

$$\mathring{\boldsymbol{\sigma}} = \boldsymbol{\sigma} + \boldsymbol{\sigma} \cdot \mathbf{W} - \mathbf{W} \cdot \boldsymbol{\sigma}, \tag{1.2.1}$$

where $\boldsymbol{\sigma}$ and $\mathbf{W}$ is the Cauchy stress rate tensor and the spin rate tensor, respectively. In order to fulfill the objectivity condition, the objective stress rate tensor $\mathring{\boldsymbol{\sigma}}$ has to comply with

$$\mathring{\boldsymbol{\sigma}}' = \mathbf{Q} \cdot \mathring{\boldsymbol{\sigma}} \cdot \mathbf{Q}^T, \tag{1.2.2}$$

where $\mathbf{Q}$ represents the rotation matrix.

Kolymbas [9] expressed the Jauman tensor as a symmetric tensor-value function $\mathbf{H}$ of a strain rate $\mathbf{D}$ and Cauchy tensor $\boldsymbol{\sigma}$ as

$$\mathring{\boldsymbol{\sigma}} = \mathbf{H}(\boldsymbol{\sigma}, \mathbf{D}). \tag{1.2.3}$$

In order to fulfil the requirement of the objectivity, the function $\mathbf{H}$ has to fulfil the condition

$$\mathbf{Q} \cdot \mathbf{H}(\boldsymbol{\sigma}, \mathbf{D}) \cdot \mathbf{Q}^T = \mathbf{H}(\mathbf{Q} \cdot \boldsymbol{\sigma} \cdot \mathbf{Q}^T, \mathbf{Q} \cdot \mathbf{D} \cdot \mathbf{Q}^T), \tag{1.2.4}$$

which implies the independence of coordination system.

The tensor-value function $\mathbf{H}$ of two symmetric tensors can be decomposed as Eq. (1.2.5) shows, where ϕ_i are isotropic scalar functions, which form a function basis composed of ten invariants. These functions multiply the so called generators. For the function of two isotropic symmetric tensors there are nine generators ($\mathbf{I}$,$\boldsymbol{\sigma}$,$\mathbf{D}$,$\boldsymbol{\sigma}^2$,$\mathbf{D}^2$,$\boldsymbol{\sigma}\cdot\mathbf{D}+\mathbf{D}\cdot\boldsymbol{\sigma}$,$\boldsymbol{\sigma}^2\cdot\mathbf{D}+\mathbf{D}\cdot\boldsymbol{\sigma}^2$,$\boldsymbol{\sigma}\cdot\mathbf{D}^2+\mathbf{D}\cdot^2\boldsymbol{\sigma}$,$\boldsymbol{\sigma}^2\cdot\mathbf{D}^2+\mathbf{D}^2\cdot\boldsymbol{\sigma}^2$), see [9] [10] [11].

$$\begin{aligned}\mathbf{H}(\boldsymbol{\sigma},\mathbf{D}) = {} & \phi_0\mathbf{I} + \phi_1\boldsymbol{\sigma} + \phi_2\mathbf{D} + \phi_3\boldsymbol{\sigma}^2 + \phi_4\mathbf{D}^2 + \\ & \phi_5(\boldsymbol{\sigma}\cdot\mathbf{D} + \mathbf{D}\cdot\boldsymbol{\sigma}) + \phi_6(\boldsymbol{\sigma}^2\cdot\mathbf{D} + \mathbf{D}\cdot\boldsymbol{\sigma}^2) + \\ & \phi_7(\boldsymbol{\sigma}\cdot\mathbf{D}^2 + \mathbf{D}^2\cdot\boldsymbol{\sigma}) + \phi_8(\boldsymbol{\sigma}^2\cdot\mathbf{D}^2 + \mathbf{D}^2\cdot\boldsymbol{\sigma}^2)\end{aligned} \tag{1.2.5}$$

$$\begin{aligned}\phi_i = {} & \phi_i(\mathrm{tr}\boldsymbol{\sigma}, \mathrm{tr}\boldsymbol{\sigma}^2, \mathrm{tr}\boldsymbol{\sigma}^3, \mathrm{tr}\mathbf{D}, \mathrm{tr}\mathbf{D}^2, \mathrm{tr}\mathbf{D}^3, \\ & \mathrm{tr}(\boldsymbol{\sigma}\cdot\mathbf{D}), \mathrm{tr}(\boldsymbol{\sigma}^2\cdot\mathbf{D}), \mathrm{tr}(\boldsymbol{\sigma}\cdot\mathbf{D}^2), \mathrm{tr}(\boldsymbol{\sigma}^2\cdot\mathbf{D}^2))\end{aligned} \tag{1.2.6}$$

When permutating the invariants in the isotropic scalar functions ϕ_i one can create a great number of the tensor-value functions $\mathbf{H}$. In addition, the mathematical software was used in order to find the most suitable form of the function $\mathbf{H}$. The selection of an appropriate function was subjected to the study of:

- Shape of response envelopes
- Proportional strain paths
- Drained triaxial test, oedometric test and simple shear test
- Limit surface

The functions which provided an unacceptable prediction of a soil behaviour were rejected. After some modification the most suitable equation was received in the form of: [11] [12]

$$\mathring{\boldsymbol{\sigma}} = \mathbf{H}(\boldsymbol{\sigma}, \mathbf{D}) = C_1 \mathbf{D} \mathrm{tr}\boldsymbol{\sigma} + C_2 \frac{\boldsymbol{\sigma} \mathrm{tr}(\boldsymbol{\sigma} \cdot \mathbf{D})}{\mathrm{tr}\boldsymbol{\sigma}} + \left(C_3 \frac{\boldsymbol{\sigma} \cdot \boldsymbol{\sigma}}{\mathrm{tr}\boldsymbol{\sigma}} + C_4 \frac{\boldsymbol{\sigma}^* \cdot \boldsymbol{\sigma}^*}{\mathrm{tr}\boldsymbol{\sigma}} \right) ||\mathbf{D}||, \tag{1.2.7}$$

where

$$\boldsymbol{\sigma}^* = \boldsymbol{\sigma} - \frac{1}{3} \mathrm{tr}\boldsymbol{\sigma} \mathbf{1}, \tag{1.2.8}$$

$$\mathbf{1} = \delta_{ij}. \tag{1.2.9}$$

Coefficients C_i represent material constants and $\boldsymbol{\sigma}^*$ the deviatoric stress tensor where $\mathbf{1}$ is the identity matrix and δ_{ij} Kronecker delta. Such an equation can be further simplified to

$$\mathring{\boldsymbol{\sigma}} = \mathbf{L}(\boldsymbol{\sigma}, \mathbf{D}) + \mathbf{N}(\boldsymbol{\sigma}, \mathbf{D}) = \mathbf{L}(\boldsymbol{\sigma}) : \mathbf{D} + \mathbf{N}(\boldsymbol{\sigma}) ||\mathbf{D}|| \tag{1.2.10}$$

with respect to $\mathbf{D}$, where $\mathbf{L}$ and $\mathbf{N}$ represent linear fourth and nonlinear second order tensor, respectively. The effect of the tensors can be presented in such way that when omitting the tensor $\mathbf{N}$ from Eq. (1.2.10) the response envelope would have an elliptic shape with the original stress placed into the centre of the ellipse and therefore, provides a hypoelastic response. Incorporating the tensor $\mathbf{N}$ into Eq. (1.2.10) moves and rotates the response envelope out of the original stress state. Tensor $\mathbf{D}$ can be separated from both tensors when defined in the principal stress and strain space, as further evolution of Eq. (1.2.10) shows. The basic hypoplastic equation is thus obtained, which is in the nature nonlinear and produce two different stiffnesses for the loading and unloading conditions. Notice that the tensor function Eq. (1.2.10) contains only one state variable, which is the tensor stress $\boldsymbol{\sigma}$ [12].

Bauer's and Gudehus' hypoplastic model

The next step in the development of the hypoplastic models was an explicit formulation of the critical state and incorporating the void ratio e as a state

variable. The critical state can be characterized by vanishing of stress rate and volumetric strain rate under continuous stretching, see Eq. (1.2.11).

$$\mathring{\boldsymbol{\sigma}} = \mathbf{L}(\boldsymbol{\sigma}) : \mathbf{D} + \mathbf{N}(\boldsymbol{\sigma})||\mathbf{D}|| = 0. \tag{1.2.11}$$

In [13] the failure surface f of the hypoplastic model was found by following analysis. Since the hypoplastic model is strain rate independent the strain tensor $\mathbf{D}$ can be expressed as a unit tensor with property

$$\mathbf{D}^T : \mathbf{D} = 1 \tag{1.2.12}$$

applied. When deriving strain tensor $\mathbf{D}$ from Eq. (1.2.11) the analogue of the elastoplastic *flow rule* at the critical state is formed by

$$\frac{\mathbf{D}}{||\mathbf{D}||} = \overrightarrow{\mathbf{D}} = \mathbf{D} = -\mathbf{L}^{-1} : \mathbf{N}, \tag{1.2.13}$$

where $\overrightarrow{\mathbf{D}}$ represents the direction of strain rate. At this poing, the direction of the plastic flow was not determined in advance unlike in the case of elastoplastic models such as the Mohr-Coulomb, Cam-Clay etc. [13]. Similar approach of deriving both the failure surface and flow rule was adopted later by Wolffersdoff [14] and Niemunis [15].

The failure surface f is expressed by Eq. (1.2.14) when substituting Eq. (1.2.13) to Eq. (1.2.12) as

$$f(\boldsymbol{\sigma}) = \mathbf{N}^T : (\mathbf{L}^{-1})^T : \mathbf{L}^{-1} : \mathbf{N} - 1 = 0 \tag{1.2.14}$$

Since the $\boldsymbol{\sigma}$ and $\mathbf{D}$ are related at the failure surface f by Eq. (1.2.13), they are coaxial, which is not, however, in a general case satisfied [13].

Incorporating the dependency of the model on the void ratio was the next logical step, since the behaviour of soils is significantly influenced by the stress state and void ratio relation. The observations of triaxial tests suggest [13]:

- The dilatancy and the peak friction angle decrease with an increasing confining pressure for the identical initial void ratio.
- The dilatancy and the peak friction angle decrease with an increasing initial void ratio for the identical confining pressure.
- When the dense specimen is subjected to the low confining pressure, the stress strain curve exhibits a peak followed with softening, which later stabilizes on a certain level of stress while the deformation continue. Such a state is referred to as critical state and is characterized by the critical void ratio and critical friction angle.
- A dense specimen under a high confining pressure and loose specimen under a low confining pressure do not show the peak followed by softening and exhibits a similar behaviour.

According to the aforesaid propositions, the hypoplastic constitutive equation should be written in the term of [13]

$$\mathring{\boldsymbol{\sigma}} = \mathbf{H}(\boldsymbol{\sigma}, \mathbf{D}, e), \tag{1.2.15}$$

with the void ratio rate defined by

$$\dot{e} = (1 + e)\mathrm{tr}\mathbf{D}. \tag{1.2.16}$$

Bauer [16] and Gudehus [17] put forward the form of hypoplastic as

$$\mathring{\boldsymbol{\sigma}} = f_b(e, \boldsymbol{\sigma}) f_e(e)[\mathbf{L}(\hat{\boldsymbol{\sigma}}) : \mathbf{D} + f_d(e)\mathbf{N}(\hat{\boldsymbol{\sigma}})||\mathbf{D}||], \tag{1.2.17}$$

which significantly improved the hypoplastic sand model by implementing the effect of the void ratio and stress level via scalar functions of barotropy (f_b), and pyknotropy (f_e, f_d). Equation (1.2.17) is thus a modification of the original hypoplatic equation (1.2.10). The tensor $\hat{\boldsymbol{\sigma}}$ denotes the so called granular stress ratio tensor. The precise form of the scalar functions and tensors is revealed in subsequent sections.

Von Wolffersdoff's hypoplastic model

Although significantly improved, the model overestimated the critical state for directions other then the one corresponding to the triaxial test. The model also did not have an explicitly defined failure surface, which, according to the conducted studies, shaped as a three-sided cone with the vertex situated in the origin of the principal stress space resembling the Matsuoka-Nakai failure surface [14, 17]. According to the predefined abovementioned shape, Wolffersdorff modified the tensors **L** and **N** of Eq. (1.2.17) in order to respect the Drucker-Prager and Matsuoka-Nakai failure surface [14], the resulting failure surface in principal stress space is illustrated in Fig. 1.4.

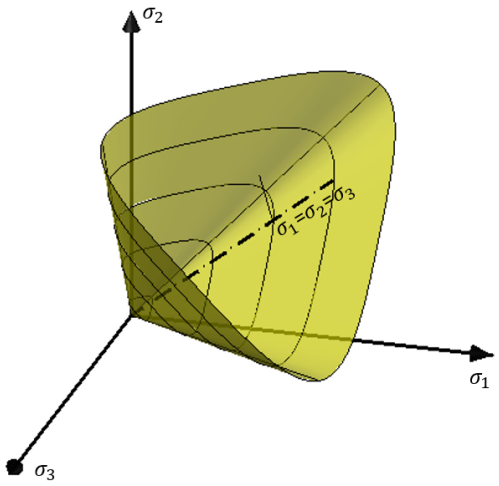

Figure 1.4: Hypoplastic sand failure surface in the principal stress space

In spite of explicitly incorporating the failure surface, the hypoplastic model is still not applicable to simulate a cyclic loading, for it exhibits too low initial stiffness. Such a drawback is eliminated when using enhancement of small strain stiffness model introduced in [18], which reliably simulates now number of cyclic loadings and significantly increases the initial stiffness.

Generalized hypoplasticity

Even though the initial studies were conducted by the trial and error optimization, the eventual hypoplastic equation took a form Eq. (1.2.10). In [12] it was

shown that for the critical state the stress increment holds $\mathring{\boldsymbol{\sigma}} = 0$ and the strain direction at the critical state is derived as

$$\overrightarrow{\mathbf{D}} = -\mathbf{L}^{-1} : \mathbf{N}, \tag{1.2.18}$$

which can be seen as the counterpart of the elastoplastic flow rule Eq. (1.1.8) [15].

Furthermore, with additional modification an expression for the failure surface f can be obtained when normalizing both sides of Eq. (1.2.18). Thus the direction of the strain rate $\overrightarrow{\mathbf{D}}$ is excluded from Eq. (1.2.19) and the relation for the failure surface f is expressed solely in terms of stresses as

$$f = ||\mathbf{L}^{-1} : \mathbf{N}|| - 1 = 0, \tag{1.2.19}$$

which can be seen as an counter part of the elastoplastic yield surface Eq. (1.1.1).

In [15] and [19] it was stated that the tensors $\mathbf{L}$ and $\mathbf{N}$ are interconnected and a change in one tensor might inconveniently change other features of the model such as a hypoplastic flow rule or shape of the yield surface etc. Therefore, Niemunis in [15] introduced tensorial function $\mathbf{B}$ as

$$\mathbf{B} = \mathbf{L}^{-1} : \mathbf{N} \tag{1.2.20}$$

and direction of flow $\mathbf{m}$

$$\mathbf{m} = \overrightarrow{\mathbf{B}}. \tag{1.2.21}$$

at the critical state ($\mathring{\boldsymbol{\sigma}} = 0$, $\mathrm{tr}(\mathbf{D}) = 0$). From Eq. (1.2.19), respective Eq. (1.2.22), the inequality -1$<f<$0 is satisfied and $f =$ -1 is applied for isotropic compression and $f = 0$ for the critical state. The function f thus can be expressed as

$$f = ||\mathbf{B}|| - 1 = 0. \tag{1.2.22}$$

The degree of nonlinearity Y was introduced as a convenient function replacing f, see Eq. (1.2.23). The function Y, respectively f, has to be carefully selected as it controls a nonlinear behaviour between the limits -1$<f<$0

$$Y = f + 1. \tag{1.2.23}$$

The $generalized$ form of the hypoplastic equation (1.2.10) then takes the form of

$$\mathring{\boldsymbol{\sigma}} = \mathbf{L} : (\mathbf{D} - Y\mathbf{m}||\mathbf{D}||) \tag{1.2.24}$$

Rearrangement of Eq. (1.2.10) allows to define separately the forth order tensor $\mathbf{L}$, which represents a tangent stiffness of the hypoelastic constitutive model, hypoplastic flow rule $\mathbf{m}$ and shape of the failure surface f. Similar approach was earlier undertaken by Von Wolffersdoff in [14] while Niemunis in [18] came to the more general form, which was later adopted by Masin in [19].

1.2.2 Von Wolffersdorff's hypoplastic sand model

The Wolffersdorff's hypoplastic model is nowadays widely used in the academic field and is referred to as the hypoplastic model for sand or hypoplastic model for coarse grained soils. Based on the Bauers's and Gudehus's model, Wolffersdorff improved the hypoplastic equation for the predefined failure surface, the hypoplastic model for sand can be expressed in the basic form of Eq. (1.2.17).

$$\mathring{\boldsymbol{\sigma}} = f_b(e,\boldsymbol{\sigma}) f_e(e)[\mathbf{L}(\hat{\boldsymbol{\sigma}}) : \mathbf{D} + f_d(e)\mathbf{N}(\hat{\boldsymbol{\sigma}})||\mathbf{D}||]$$

The forth order tensor $\mathbf{L}$ and the second order tenor $\mathbf{N}$ are expressed in the form respecting the Drucker-Prager and Matsuoka-Nakai failure surfaces as

$$\mathbf{L} = \frac{1}{\hat{\boldsymbol{\sigma}} : \hat{\boldsymbol{\sigma}}} \left(F^2\mathbf{I} + a^2\hat{\boldsymbol{\sigma}} \otimes \hat{\boldsymbol{\sigma}}\right) \tag{1.2.25}$$

and

$$\mathbf{N} = \frac{aF}{\hat{\boldsymbol{\sigma}} : \hat{\boldsymbol{\sigma}}}(\hat{\boldsymbol{\sigma}} + \hat{\boldsymbol{\sigma}}^*), \tag{1.2.26}$$

where

$$\mathbf{I} = \mathbf{I}_{ijkl} = \delta_{ik}\delta_{jl} \tag{1.2.27}$$

represents the forth order identity matrix. Scalar functions a and F are expressed by

$$a = \frac{\sqrt{3}(3 - \sin\varphi_c)}{2\sqrt{2}\sin\varphi_c} \tag{1.2.28}$$

and

$$F = \sqrt{\frac{1}{8}\tan^2\psi + \frac{2 - \tan^2\psi}{2 + \sqrt{2}\tan\psi\cos 3\vartheta}} - \frac{1}{2\sqrt{2}}\tan\psi, \tag{1.2.29}$$

with invariants

$$\tan\psi = \sqrt{3}||\hat{\boldsymbol{\sigma}}^*|| \tag{1.2.30}$$

and

$$\cos 3\vartheta = -\sqrt{6}\frac{\mathrm{tr}\left(\hat{\boldsymbol{\sigma}}^* \cdot \hat{\boldsymbol{\sigma}}^* \cdot \hat{\boldsymbol{\sigma}}^*\right)}{\left(\hat{\boldsymbol{\sigma}}^* : \hat{\boldsymbol{\sigma}}^*\right)^{\frac{3}{2}}}. \tag{1.2.31}$$

Stress tensors $\hat{\boldsymbol{\sigma}}$ and $\hat{\boldsymbol{\sigma}}^*$ represents the stress ratio and the deviatoric part of the stress ratio respectively

$$\hat{\boldsymbol{\sigma}} = \frac{\boldsymbol{\sigma}}{\mathrm{tr}\boldsymbol{\sigma}}, \tag{1.2.32}$$

$$\hat{\boldsymbol{\sigma}}^* = \hat{\boldsymbol{\sigma}} - \frac{1}{3}\mathbf{1}. \tag{1.2.33}$$

Von Wolffersdorff's hypoplastic model employs eight parameteres φ_c, h_s, n, e_{d0}, e_{c0}, e_{i0}, α and β which are discussed together with the calibration procedures later in Chapter 2.

- h_s - Granular hardness
- n - Parameter controling the curvature of the compression line
- e_{i0} - Limiting void ratio of the isotropic compression line
- e_{c0} - Limiting void ratio of the critical compression line
- e_{d0} - Limiting void ratio of the highestdensity compression line
- φ_c - Critical state friction angle
- α - Exponent controlling peak friction angle
- β - Exponet controling model's stiffness

Hereinafter, the scalar functions f_d, f_e and f_b are described in detail as they incorporate the influence of the stress level and density into the hypoplastic model.

Pyknotropy

Bauer [17] introduced scalar functions f_b,f_e and f_d in order to cover the very basic characteristics of soil mechanics that is the pressure and density dependency. Dependency of the density is characterized by functions f_e and f_d as follows:

$$f_d = r_e^{\alpha} \tag{1.2.34}$$

with

$$r_e = \frac{e - e_d}{e_c - e_d} \tag{1.2.35}$$

and

$$f_e = \left(\frac{e_c}{e}\right)^{\beta}, \tag{1.2.36}$$

where e_c represents a void ratio at the critical state, e_d void ratio of the maximal density and e the current state of the void ratio. It is said that 1-r_e corresponds to the density index I_d. It can be simply deduced that when the void ratio e corresponds to the void ratio of the maximal density e_d in Eq. (1.2.34), then the function $f_d = 0$ and Eq. (1.2.17) is reduced to the hypoelastic form. When the initial void ratio increases, the peak friction angle and the dilatancy decreases, the function f_d thus controls a relative height of the peak in the stress/strain curve under the triaxial loading (peak friction angle). The parameter α usually falls within the range $0.1<\alpha<0.3$. The function f_e increases the stiffness (increase the size of a response envelope) with increasing density and thus the position of the peak in the stress/strain curve. The parameter β falls within the range $1<\beta<1.1$ [17] [16].

Barotropy

The pressure dependency of the void ratio can be according to [16] defined for the proportional isotropic compression in the $p \times e$ space by

$$e_i = e_{i0} \exp\left[-\left(\frac{3p}{h_s}\right)^{n}\right]. \tag{1.2.37}$$

It was stated that this relation well correlates with the evaluation of numerous tests and well matches various granular materials for wide range of stresses [16]. This equation can be seen as a counterpart to the expression for the proportional isotropic compression of the Cam-Clay model Eq. (1.1.33) in the $\ln p \times e$ space. However, the initial void ratio e_{i0} corresponds with the mean pressure $p = 0$. When differentiating Eq. (1.2.37) with respect to time, one obtains

$$3\dot{p}_s = \frac{\dot{e}_i}{e_{i0}} \frac{h_s}{n} \left(\frac{3p_s}{h_s} \right)^{1-n}. \tag{1.2.38}$$

The parameter e_{i0} here represents the maximal void ratio, which corresponds to the arrangement of particles in the gravitation free space. The parameter h_s stands for the granular hardness and the exponent n controls the curvature of the void ratio evolution curve, p represents the mean stress. It is postulated that the limiting void ratios of the critical state e_c and the maximal density e_d decrease with the mean pressure in the same manner as the isotropic void ratio e_i by

$$\frac{e_c}{e_i} = \frac{e_{c0}}{e_{i0}} \tag{1.2.39}$$

and

$$\frac{e_d}{e_i} = \frac{e_{d0}}{e_{i0}}. \tag{1.2.40}$$

Therefore, analogous equations to Eq. (1.2.37) were adopted for the evolution of the critical state void ration e_c

$$e_c = e_{c0} \exp \left[- \left(\frac{3p}{h_s} \right)^n \right] \tag{1.2.41}$$

and void ratio at the maximal density e_d as

$$e_d = e_{d0} \exp \left[- \left(\frac{3p}{h_s} \right)^n \right]. \tag{1.2.42}$$

All three limiting curves are depicted in Fig. 1.5. Any state above e_i or beneath e_d curve is not admissible. Figure 1.6 depicts the presumed hypoplastic sand model's state boundary surface in the principal stress space. It is worth noting the limitation of the state boundary surface in between both isotropic NCL and line of maximal density.

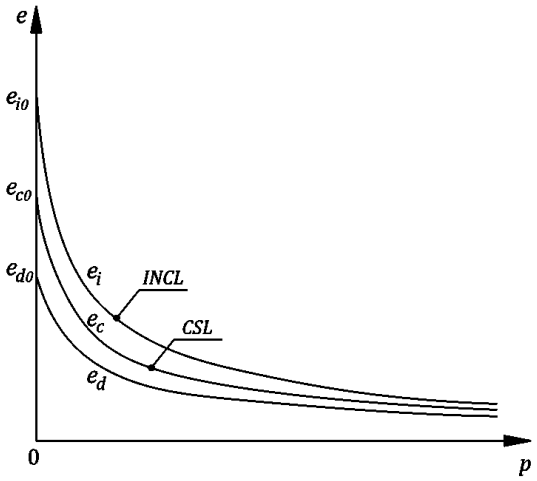

Figure 1.5: Limiting void ration curves in p × e

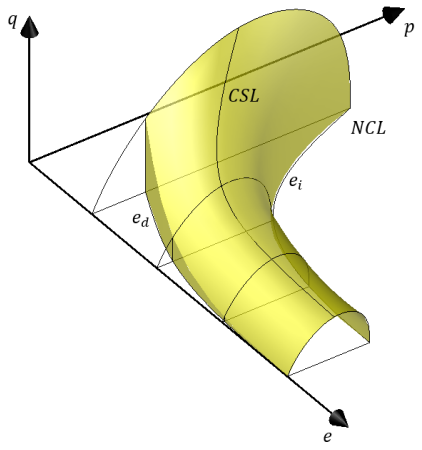

Figure 1.6: Hypoplastic sand SBS

The form of the scalar function f_b can be derived from the Eq. (1.2.17) while considering the proportional isotropic compression. When substituting the Eqns. (1.2.25)–(1.2.30) and Eq. (1.2.37), one can obtain

$$f_b = \frac{h_s}{n h_i} \left(\frac{e_{i0}}{e_{c0}} \right)^{\beta} \frac{1 + e_i}{e_i} \left(\frac{-3p}{h_s} \right)^{1-n}, \tag{1.2.43}$$

with scalar function h_i defined by

$$h_i = \left[3 + a^2 - \sqrt{3} a \left(\frac{e_{i0} - e_{d0}}{e_{c0} - e_{d0}} \right)^{\alpha} \right]. \tag{1.2.44}$$

1.2.3 Masin's hypoplastic clay model

Despite the fact that the Von Wolffersdorff hypoplastic model well characterizes coarse grained soils such as sands, it was discussed in [20] and later mentioned in [11] and [19] that Von Wolffersdorff's hypoplastic model does not well simulate the behaviour of clays. Given the fact that the shape of the response envelope is influenced by the single parameter φ_c, it exhibits extremely slender shape of response envelope for low critical friction angles which are characteristic for clays. The shear stiffness is therefore underestimated. Herle and Gudehus in [20] put forth an enhancement which included two additional constants c_1 and c_2 and one additional parameter r adjusting the tensor $\mathbf{L}$. This parameter controls the bulk and shear stiffness ratio at isotropic state, which is according to research almost equal to 1 [20]. This model improved the prediction capability of the hypoplastic model for soils with low friction angle. However, there were observed several shortcomings and the model required further improvements. [19]

- The model defines nonzero minimal void ratio e_{d0}, which is not in agreement with the characteristics of fine grained soils, where e_{d0} equal to zero is admissible [19].
- It is not possible to explicitly determine the slope of the swelling line while subjected to unloading. The slope of swelling line is modified by both index parameters α and β, where fitting the parameters to swelling line is performed on the basis of parametric study [19].
- In the case of clay, it is possible to write the stress/void ratio relation for proportional loading in terms of logarithmic expression. Such an expression was already adopted by elastoplastic CamClay model, which is sufficiently accurate and can be defined by two parameters. The swelling line can be then defined by a single parameter [19].

Different approach was taken by Masin [19] who developed a hypoplastic model for clay based on theory of the generalized hypoplasticity proposed by Niemunis [15]. He introduced parameters λ^*,κ^*,N,φ_c and ν which are in the

physical meaning closely related to the parameters of the model Cam-Clay. The model, however, had a several drawbacks such as an unrealistic shape of the boundary surface for high ratios of parameter's combinations κ^*/λ^*, an incorrect development of shear stiffness during shearing and a problematic definition of the tensor $\mathbf{L}$, which made it uneasy for a future development or enhancement by a small strain stiffness model [3]. Masin later redefined his original model [19] in [3] with the aid of the studies [21, 22, 23] where was defined so called *Asymptotic State Boundary Surface* (ASBS). Asymptotic State Boundary Surface covers all states, characteristic for soil behaviour [24] called asymptotic states which are ultimately reached after sufficient stretching, see Fig. 1.7a. In this thesis, Masin's version of the hypoplastic model for clays [3] is considered with those following parameters:

- λ^* - Slope of the NCL line in the $\ln p \times \ln(1+e)$ space
- N - Position the NCL line in the $\ln p \times \ln(1+e)$ space
- κ^* - Slope of the swelling line in the $\ln p \times \ln(1+e)$ space
- ν - Poisson's ratio
- φ_c - Critical state friction angle

The meaning of parameters λ^*, κ^*, N and φ_c are ilustrated in Fig. 1.7b for the compression test as well as in the meridian space. The original basic hypoplastic Eq. (1.2.17) and later generalized form Eq. (1.2.24) can be rewritten to

$$\mathring{\boldsymbol{\sigma}} = f_s \mathbf{L} : \mathbf{D} - \frac{f_d}{f_d^A} \mathbf{A} : \mathbf{d} ||\mathbf{D}||, \tag{1.2.45}$$

while tensors $\mathbf{N}$ and $\mathbf{L}$ takes the form of Eq. (1.2.46) and Eq. (1.2.47), respectively

$$\mathbf{N} = -\frac{\mathbf{A} : \mathbf{d}}{f_s f_d^A}, \tag{1.2.46}$$

$$\mathbf{L} = \mathbf{I} + \frac{\nu}{1-2\nu} \mathbf{1} \otimes \mathbf{1}. \tag{1.2.47}$$

The forth order tensor $\mathbf{A}$ emerges from the condition $\mathring{\boldsymbol{\sigma}} = 0$ applied in Eq. (1.2.17) while scalar function f_d^A represents the value of pyknoropy f_d on ASBS. The tensor $\mathbf{D}^{\mathrm{A}}$ is an asymptotic strain related to the current stress state

$$\mathbf{A} = f_s \mathbf{L} + \frac{\boldsymbol{\sigma}}{\lambda^*} \otimes \mathbf{1}. \tag{1.2.48}$$

The proposed shape of the ASBS respects the Matsuoka-Nakai failure criterion in the deviatoric plane and fulfils the equality of the mobilized friction angle φ_m and the critical state friction angle $\varphi_c = \varphi_m$ for $p_e/p = 2$, where p_e represents the Hvorslev equivalent pressure. Since the critical state occurs at $p_e/p = 2$, CSL in $\ln p \times \ln(e+1)$ space is similarly to MCC model defined by $\Gamma = N - \lambda^* \ln 2$.

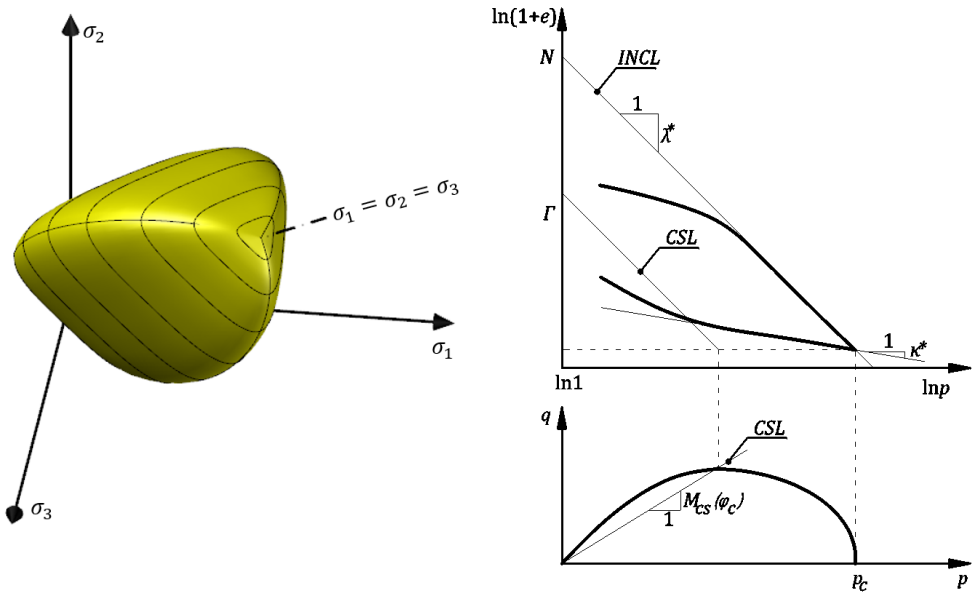

(a) HC ASBS surface in the principal stress space

(b) HC model parameters in the meridian stress space

Figure 1.7: HC failure surface

The failure function f is expressed by

$$f = F_m + \left(\frac{p}{p_e}\right)^{\omega} - 1 = 0, \tag{1.2.49}$$

where F_m is the Matsuoka-Nakai factor expressed in the terms of stress invariants I_1, I_2 and I_3 defined by

$$F_m = \frac{9I_3 + I_1 I_2}{I_3 + I_1 I_2}, \qquad I_1 = \mathrm{tr}\boldsymbol{\sigma}, \tag{1.2.50}$$
$$I_2 = \frac{1}{2}\left[\boldsymbol{\sigma} : \boldsymbol{\sigma} - {I_1}^2\right],$$
$$I_3 = \det\boldsymbol{\sigma}.$$

The second term in Eq. (1.2.49) assures the value of the mobilised friction angle $\varphi_m = 0$ for $p/p_e = 1$, $\varphi_m = \varphi_c$ for $p/p_e = 2$ and $\varphi_m = 90^\circ$ for $p/p_e = \infty$. The exponent ω from Eq. (1.2.50) is expressed by

$$\omega = -\frac{\ln(\cos^2\varphi_c)}{\ln 2} + a(F_m - \sin^2\varphi_c). \tag{1.2.51}$$

The second term in Eq. (1.2.51) influences the shape of ASBS in meridian space for other stress states which can be modified through the shape factor a and consequently influencing the peak friction angle. For $a = 0.3$ the shape of ASBS in the meridian plane resemble the Cam-Clay model on the wet side of the failure surface.

The asymptotic strain direction $\mathbf{d}$ is defined by

$$\mathbf{d} = \frac{\mathbf{D}^{\mathrm{A}}}{||\mathbf{D}^{\mathrm{A}}||}, \tag{1.2.52}$$

where $\mathbf{D}^{\mathrm{A}}$ represents the mutual dependency of strain and stress directions and can be seen as a hypoplastic flow rule

$$\mathbf{D}^{\mathrm{A}} = -\hat{\boldsymbol{\sigma}}^* + \mathbf{1}\left[\frac{2}{3} - \frac{\cos 3\theta + 1}{4}F_m^{1/4}\right]\frac{F_m^{\xi} - \sin^{\xi}\varphi_c}{1 - \sin^{\xi}\varphi_c}. \tag{1.2.53}$$

Among the most important features are the predictions of the critical state when the mobilised friction angle $\varphi_m = \varphi_c$, for the isotropic compression $\varphi_m = 0$. To predict the K_0 state the Jaky formula $K_0 = 1$ - $\sin\varphi_c$ should be fulfilled. Limits of the mobilised friction angle are $\varphi_m = 90^\circ$, which is rather a theoretical limitation.

The values of the exponent ξ

$$\xi = 1.7 + 3.9 \sin^2 \varphi_c, \tag{1.2.54}$$

was found as a result of optimalization seaking the best fit with the Jaky formula [11].

Pyknotropy

The pyknotropy factor f_d controls a nonlinear part of the hypoplastic equation and consequently soil's stiffness dependency on the relation of the mean stress p and Hvorlev stress p_e in the form of

$$f_d = \left(\frac{2p}{p_e}\right)^{\alpha}, \tag{1.2.55}$$

where

$$\alpha = 2 \tag{1.2.56}$$

The pyknotropy factor f_d for the state occuring on the ASBS designated as f_d^A is defined by

$$f_d^A = 2^{\alpha}(1 - F_m)^{\alpha/\omega} \tag{1.2.57}$$

and arises from the combinations of the Eqns. (1.2.49)–(1.2.55).

Barotropy

Masin's model employs a pressure dependency of the void ratio similar to the Cam-Clay model, see Eq. (1.1.33), which well correlates with the clay's behaviour. Pressure/void ratio dependency takes the form of

$$p_e = \exp\left[\frac{N - \ln(1 + e)}{\lambda^*}\right] \tag{1.2.58}$$

and in the rate form of

$$\dot{p} = -\frac{p_e}{\lambda^*}\left(\frac{\dot{e}}{1+e}\right), \tag{1.2.59}$$

and

$$\mathrm{tr}\mathbf{D} = \varepsilon_v = \frac{\dot{e}}{1+e}. \tag{1.2.60}$$

The barotropy factor is derived from Eq. (1.2.45) while considering unloading from the isotropic state. The equation (1.2.45) then takes a form

$$\dot{p} = -f_s\left(\frac{1}{3}+\frac{\nu}{1-2\nu}\right)\frac{\dot{e}}{1+e} - f_s\left(\frac{1}{3}+\frac{\nu}{1-2\nu}+\frac{p}{\lambda^*}\right)\frac{\dot{e}}{1+e}, \tag{1.2.61}$$

while $\dot{\epsilon}_v = \dot{e}/(1+e)$. Furthermore, considering Eq. (1.2.59) the barotropy takes a form of

$$f_s = \frac{2p}{2}\left(\frac{1}{\lambda^*}+\frac{1}{\kappa^*}\right)\frac{1-\nu}{1+\nu} \tag{1.2.62}$$

Three advanced constitutive models, namely elastoplastic Modified Cam-Clay, hypoplastic sand model and hypoplastic clay model, were described in detail in the preceding sections. Even though the models are based on two distinct theories the more generalized approach developed by Niemunis in [15] gives an opportunity to develop hypoplastic models in the way resebling elastoplastic constitutive models such as failure/yield surface plastic/hypoplastic flow rule etc.

A significant advantage of the hypoplastic models is a lack of the switch function, which not only divides total strains ε_{tot} into the elastic ε_{el} and plastic ε_{pl} parts but also requires to satisfy a consistency condition Eq. (1.1.6) once the plastic strain is generated. The hypoplastic models on the other hand does not distingush between the elastic and plastic strains.

2. Parameteres and calibration procedures

Hereinafter, the calibration mechanisms for hypoplastic sand and hypoplastic clay model will be described. The Modified Cam-Clay model calibration is merged with the calibration of hypoplastic clay model since both models' parameters are closely related.

2.0.1 Von Wolffersdoff's hypoplastic model for sand

Von Wolffernsdorff's hypoplastic model for sand defines eight parameters φ_c, h_s, n, e_{d0}, e_{c0}, e_{i0}, α and β, which can be divided into two groups according to a laboratory test that has to be conducted in order to obtain the desired values. The first group of parameters, namely φ_c, α and β, can be preferably determined from the results of a drained triaxial test. The second group of parameters h_s, n, e_{d0}, e_{c0} and e_{i0} can be obtained from either oedometric or isotropic compression test. The parameters governing CSL, namely h_s, n and e_{c0} can also be determined from the set of undrained triaxial test [11, 1].

Critical state friction angle φ_c

The critical state friction angle φ_c influences the hypoplastic model through Eqns. (1.2.26)–(1.2.28). The critical state occurs when the stress rate and the volumetric stress rate vanish. The critical state friction angle φ_c can be directly calculated from the results of a triaxial shear test displayed in the invariant space $s' \times t'$, where stresses s' and t' are the effective stresses defined in terms of the effective principal stresses as

$$s' = (\sigma'_1 + \sigma'_3)/2 \tag{2.0.1}$$

and

$$t' = (\sigma'_1 - \sigma'_3)/2 \tag{2.0.2}$$

To gain reliable results three triaxial shear tests are usually performed to evaluate φ_c. In the case of sand soils it is preferred to perform drained triaxial test as it is promptly executed because of highly porous structure of sands. Parameter φ_c can be estimated using the least square method as

$$t' = a \times s' \tag{2.0.3}$$

with the slope of the critical state line a

$$a = \frac{\sum_{i=1}^{n} s'_i t'_i}{\sum_{i=1}^{n} s'^2_i}. \tag{2.0.4}$$

Stresses s'_i and t'_i in Eq. (2.0.4) represent the critical state reached for the i-th triaxial test. Evaluation of the critical state friction angle is straightforward with the aid of

$$\varphi_c = \arcsin(a), \tag{2.0.5}$$

see also Fig. 2.1, where are depicted three undrained triaxial tests and slope a of CSL in $t' \times s'$ space.

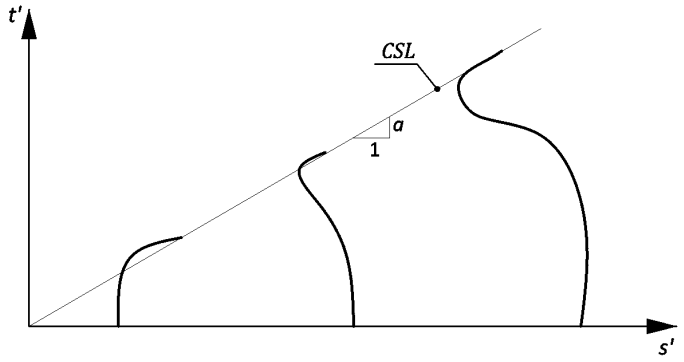

Figure 2.1: Undrained triaxial tests in $s' \times t'$

Although φ_c can be determined by Eq. (2.0.5) when conducting the triaxial test, it is possible to estimate φ_c as an angle of repose φ_{rep} as was presented in [1]. The idea is that the soil reaches a quasi-critical state owing to the steady flow of grain rolling downhill. The angle of repose is measured from the base of a heap made by lifting of a funnel filled with a coarse soil. The funnel should be lifted slowly and continuously so that no dynamic waves are inflicted upon the heap. The measured angle of repose is also influenced by a roughness of a base beneath the heap. The base should be rough to restrict sliding of grains on the base.

This method is suitable particularly for dry granular soils with grains sizes smaller than 0.1mm. If the volume of these grains is beneath 20%, they do not have a significant effect on the measurement and thus can be sieved out. With an increasing percentage of fine grains, the influence of cohesive forces caused by air humidity generates an unrealistically high φ_c. Executing of the triaxial shear test then becomes inevitable. It is, however, possible that the deformation localize into a shear band in which an actual stress does not correspond to the measured stress. In order to minimalize the effect of localization, the specimen should be in the loosest possible state and the frictionless platens in the triaxial test should be used [11, 16].

Parameters h_s and n

The granular hardness h_s and the exponent n can be found in Eqns. (1.2.37)–(1.2.43) and thus imply increasing bulk modulus with the mean pressure p. To determinate parameters h_s and n either oedometric or isotropic compression test results can be used while considering K_0 to be a constant for a proportional loading along NCL. Since the specimen for the eodometric test should be in the loosest possible state, similarly to the assumption of the critical state that arise during the formation of heap mentioned previously, we can consider the specimen to be in the critical state. Then the Jaky formula $K_0 = 1\text{-}\sin\varphi_c$ is sufficiently justified and one can write

$$p = \frac{\sigma_a + 2K_0\sigma_a}{3}. \tag{2.0.6}$$

Equation (2.0.6) can be written in the logarithmic expression as

$$\ln \sigma_a = \ln\left(\frac{3p}{1+2K_0}\right) = \ln\left(\frac{3}{1+2K_0}\right) + \ln p. \tag{2.0.7}$$

The compression index C_c denotes the tangent of an oedometric curve in $\ln \sigma_a \times e$ space, see Fig. 2.2a,

$$C_c = \frac{\Delta e}{\Delta \ln \sigma_a}. \tag{2.0.8}$$

According to Eq. (2.0.7), the compression index C_c can be expressed in the therm of mean stress p as

$$C_c = \frac{\Delta e}{\Delta \ln p}. \tag{2.0.9}$$

The oedometric test might be more appreciated as it is simple to execute and allows for reaching higher pressure values. The specimen should be prepared in a very loose state. It should be either dry or fully saturated in order to suppress cohesive or chemical forces which might influence the progression of proportional loading curve. The calibration of the parameters h_s and n is not recommended to perform by means of regression analysis or at least not initially, as both parameters influence the very same compression curve and thus one can obtain more combinations of h_s and n to define the same curve. Consequently, it is recommended to evaluate these parameters such as to reflect their physical meaning. The granular hardness h_s can be directly obtained when differentiating Eq. (1.2.37) with respect to time as

$$e = -ne\left(\frac{3p}{h_s}\right)^n \left(\frac{3p}{h_s}\right)^{-1} \left(\frac{3p}{h_s}\right) = -\frac{ne}{p}\left(\frac{3p}{h_s}\right)^n p \tag{2.0.10}$$

and with the aid of Eq. (2.0.9) as

$$h_s = 3p_3 \left(\frac{ne_3}{C_{c,3}} \right)^{\frac{1}{n}}. \tag{2.0.11}$$

The most suitable way si to obtain the parameter h_s from the central part of the compression line and thus capture the overall slope of the compression line, see Fig. 2.2a, where the recommended state is designated with subscript 3 [11, 16].

The exponent n can be obtained when considering two different states on the proportional loading curve with unique values of the mean pressure p and void ratio e as

$$n = \left(\frac{h_s}{3p_1} \right)^n \frac{C_{c,1}}{e_1} = \left(\frac{h_s}{3p_2} \right)^n \frac{C_{c,2}}{e_2} \tag{2.0.12}$$

then

$$n = \frac{\ln \left(\dfrac{e_1 C_{c,2}}{e_2 C_{c,1}} \right)}{\ln \left(\dfrac{p_2}{p_1} \right)}. \tag{2.0.13}$$

It is preferable to choose states on the far extremes of the compression curve labelled with subscripts 1 and 2 in Fig. 2.2a [11, 16].

$$n = \frac{\ln \left(\dfrac{e_1 C_{c,2}}{e_2 C_{c,1}} \right)}{\ln \left(\dfrac{p_2}{p_1} \right)} \tag{2.0.14}$$

Fig. 2.2b and Fig. 2.2c show the effect of parameters h_s and n. The granular hardness h_s controls the overall slope of the proportional compression curves, whereas the exponent n affects its curvature. It is worth pointing out that even though Eq. (1.2.37) is valid for wide range of stresses it is less reliable for mean stresses $p \cong 0$ and $p \to \infty$. The parameters h_s and n derived by aforesaid procedure are accurate only for non-crushing values of pressure as h_s and n change with the change of granulometric properties and non-zero initial stress values [11, 16, 1].

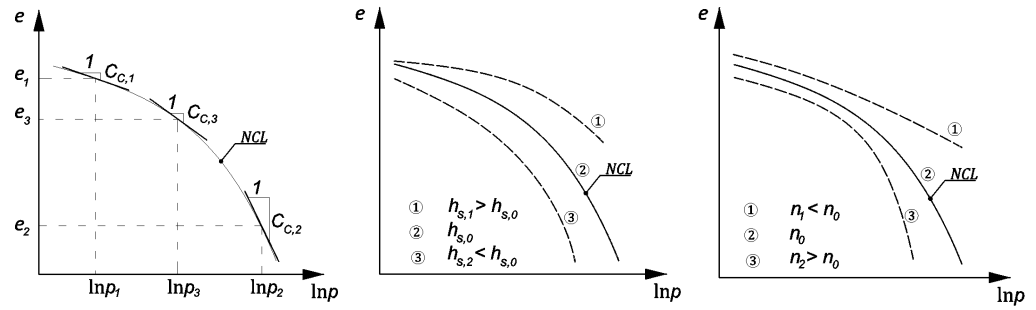

(a) Compression index (b) effect of h_s (c) effect of n

Figure 2.2: Parameters h_s and n

Initial critical void ratio e_{c0}

An evolution of the critical void ratio e_c with the mean pressure p is defined by Eq. (1.2.41), where e_{c0} refers to the critical void ratio at $p = 0$. Given that the parameters h_s and n are already known, e_{c0} can be obtained from the oedometric or isotropic compression test. It has been experimentally confirmed that e_{c0} closely corresponds to the e_{max} and equality $e_{max} \approx e_{c0}$ is admissible. The test to determine e_{max} is conducted by pouring a sand to the mold so that the sand is in the naturally loose state. Since the specimen for the oedometric test should be prepared in the loose state, that means

$$e_0 \approx e_{max}, \tag{2.0.15}$$

it is possible to consider the initial void ratio e_0 at the beginning of the compression as the critical void ratio e_{c0} at the zero pressure.

If the compression curves are not a reliable source of information, e_{c0} can be obtained from the triaxial undrained test as the critical state is eventually reached for the particular mean stress p and the corresponding critical void ratio e_c. When substituting these values to Eq. (1.2.41) the evaluation of e_{c0} is straightforward, see Fig. 2.3. Obtaining the parameters of CSL from the drained triaxial test is not possible since since the void ratio in the shear band, where the critical state occurs, does not correlate with the void ratio of the whole specimen [11, 1].

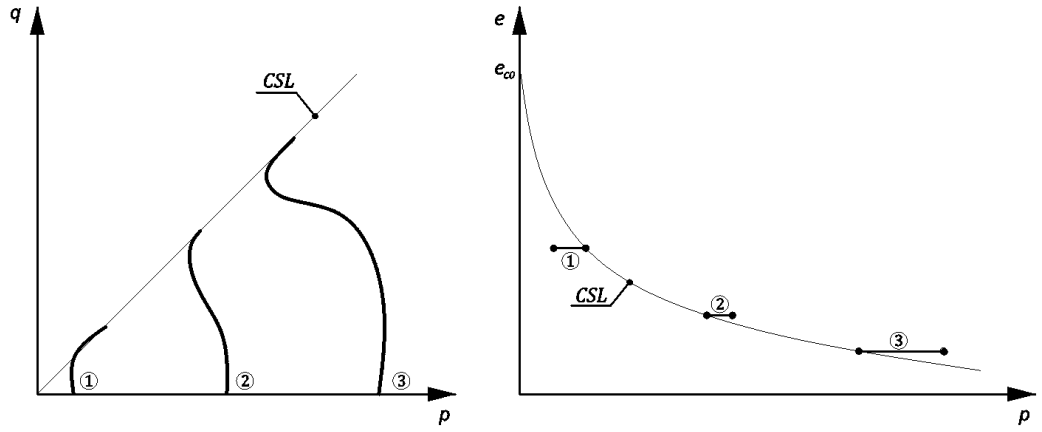

Figure 2.3: Calibration of e_{c0} from undrained triaxial tests

Initial isotropic void ratio e_{i0}

An evolution of the isotropic void ratio e_i with the mean pressure p is defined by Eq. (1.2.37). The parameter e_{i0} is more a fictitious value as it is represented by an array of identical spherical in the gravity free space. Although such a state is experimentally unfeasible, it can be postulated that [11, 1]

$$e_{i0} = 1.2 e_{max}. \tag{2.0.16}$$

Void ratio at the maximal density e_{d0}

The parameter e_{d0} represents a void ratio of maximal density in the gravity free space. Its evolution is given by Eq. (1.2.42). The best densification can be reached by cyclic shearing with a small amplitude and constant vertical pressure. One thus gets the maximal density void ratio e_d for a given mean pressure p, see Fig. 2.4. Thereafter e_{d0} is obtained by substituting reached void ratio e_d to Eq. (1.2.42). Based on experimental studies the parameter can be estimated as [11, 1]

$$e_{d0} = 0.5 e_{c0}. \tag{2.0.17}$$

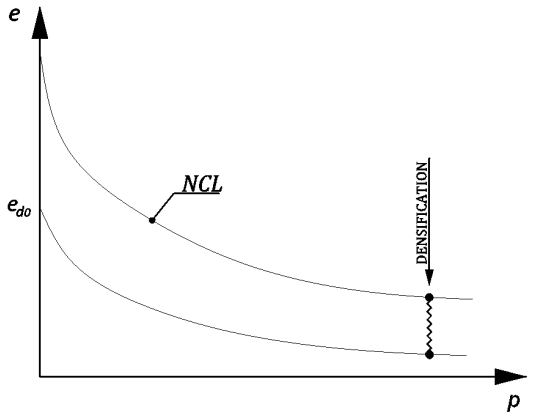

Figure 2.4: Evaluation of e_{d0}

Exponents α and β

Although explicit procedures to obtain both exponents can be found in [1], it seems to be advantageous to obtain these parameters by means of a parametric study providing all other parameters are already evaluated. The exponent α appears in Eq. (1.2.34).

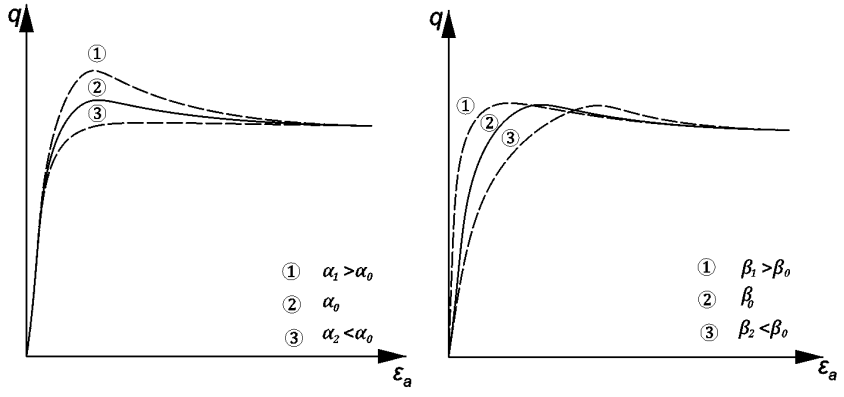

(a) The effect of parameter α

(b) The effect of parameter β

Figure 2.5: Parameters α and β

It influences the nonlinear part of the hypoplastic model for the current density and controls the value of the peak friction angle φ_p. The parameter β in Eq. (1.2.36) influences the overall stiffness for the current density and consequently the position of the peak of the triaxial stress/strain curve. Effects of both α and β for the drained triaxial test are demonstrated in Fig. 2.5.

The effect of parameter α under undrained triaxial conditions is demonstrated in Fig. 2.6. Similarly to the drained conditions the increasing parameter α promote more dilatative behaviour, see Fig. 2.6a. This behaviour can be also expressed by the evolution of the mobilized friction angle φ_{mob} or its conterpart $\eta = q/p$ from the meridian plane, see η plotted with axial strain ε_a in Fig. 2.6b.

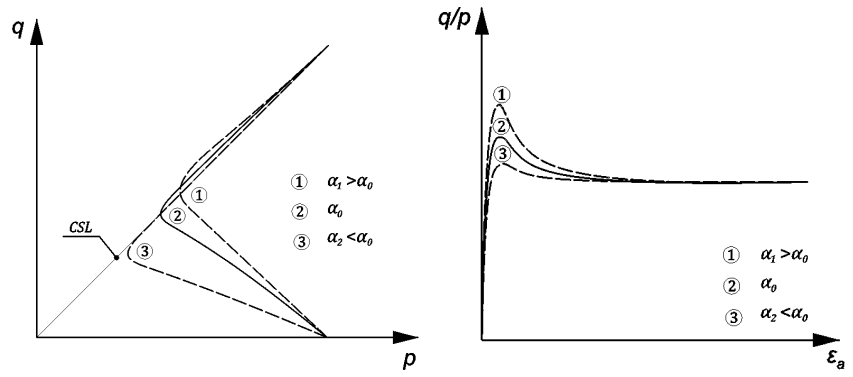

(a) Effect of α in $p \times q$

(b) Effect of α on M_{mob}

Figure 2.6: Effect of the parameter α under undrained triaxial conditions

2.0.2 Masin's hypoplastic model for clays and Modified Cam-Clay model

Modified Cam-Clay model is defined by five parameters, namely λ, κ, e_0, ν and M_{cs} and its yield surface creates an ellipsoid in the principal stress space along the hydrostatic axis.

The hypoplastic clay model is defined by five parameters, which properties are almost identical to those needed in the formulation of the elastoplastic Cam-Clay model. The hypoplastic model's ASBS resembles the yield surface of the Cam-Clay model the deviatoric plane and requires the following five parameters λ^*, κ^*, N, ν and φ_c.

This section the most notably concentrated on the calibration of the hypoplastic clay model while a calibration differences are mention in case of MCC model. All parameters can be calibrated on the basis of basic laboratory tests, namely the triaxial shear test and the isotropic compression or oedometric test.

Critical state friction angle φ_c and slope M_{cs}

The critical state friction angle φ_c can be directly calculated from the results of triaxial shear test displayed in the $s' \times t'$ space. A similar procedure as used for the calibration of φ_c for hypoplastic sand model can be adopted. It is preferable to conduct the triaxial test on the reconstituted soil specimens since the critical state can be easier observed. The reconstituted sample has a consistency at the liquid limit w_L and is made from the original sample. It is not admissible to use estimation $\varphi_c \approx \varphi_{rep}$.

Modified Cam-Clay model defines the slope of critical state line M_{cs}, see Fig. 1.3b, in the deviatoric plane instead of critical state friction angle φ_c. The parameter M_{cs} can be calculated for the triaxial compression according to

$$M_{cs} = \frac{6 \sin \varphi_c}{3 - \sin \varphi_c} \tag{2.0.18}$$

Parameters λ^* and κ^*

These parameters are defined in the $\ln(e+1) \times \ln p$ space, see Fig. 2.7. Both

parameters can possibly be determined from oedometric or isotropic compression test without any other modification. In the case of overconsolidated soils, it is more convenient to perform the tests on the reconstituted soil samples. As Fig. 2.7 illustrates for an undisturbed specimen, it might not be possible to determine correct λ^* due to the limitations of the laboratory devices. In Fig. 2.7 are depicted differences in the final values of the NCL slope λ_r^* for reconstituted and λ_u^* for the undisturbed specimen. The former one has shattered structure but its slope of the correct NCL remains the same. Futhermore, an incorrect value of parameter $\lambda^* = \lambda_u^*$ also predicts an incorect value of $N = N_u$.

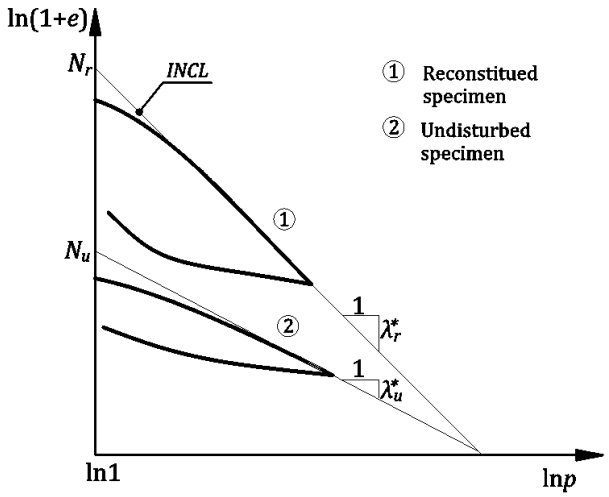

Figure 2.7: Parameter λ^* and different sample conditions

The parameter κ^* should be preferably calibrated form the results of undisturbed soil samples in order to capture the soil structure behaviour, since it also controls a nonlinear behaviour inside the state boundary surface. Both parameters can be directly evaluated from the laboratory test when converting $\varepsilon_v \times p$ or $\varepsilon_a \times \sigma_a$ to $\ln(e+1) \times \ln p$ space. The void ratio e_i at the loading step i is calculated as

$$e_i = (1 + e_0) \exp(\varepsilon_{v,i}) - 1. \tag{2.0.19}$$

Parameters λ^* and κ^* can be subsequently evaluated by

$$\lambda^* = \frac{\ln(1+e_{max-1}) - \ln(1+e_{max})}{\ln p_{max} - \ln p_{max-1}} \tag{2.0.20}$$

and

$$\kappa^* = \frac{\ln(1+e_{max+1}) - \ln(1+e_{max})}{\ln p_{max} - \ln p_{max+1}}, \tag{2.0.21}$$

where the subscript index *max* refers to the step with the maximal stress level. Subscripts $max-1$ and $max+1$ then refer to the previous and subsequent loading step respectively. These calculations are shown in Fig. 2.8 for both parameters λ^* and κ^*.

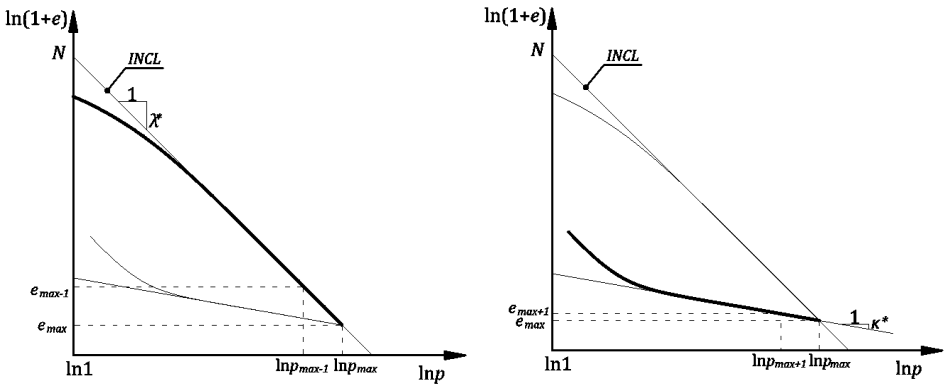

(a) Determinition of the parameter λ^* (b) Determinition of the parameter κ^*

Figure 2.8: Determinition of the parameters λ^* and κ^*

The exact procedure is used for the determinition of parameters λ and κ of MCC while $\ln p \times e$ space has to be considered for the calibration.

Parameter *N*

The parameter *N*, similarly to e_{i0} in hypoplastic sand model, controls the position of NCL in the $\ln(e+1) \times \ln p$ space and corresponds to the void ratio at the mean stress p=1 kPa. It is depicted in Fig.2.9a together with parameters λ^* and κ^*. The parameter *N* can be directly calibrated from the isotropic compression test when passing isotropic NCL with the slope of λ^* through the maximal stress of loading step according to

$$N_{iso} = \ln(e_{max} + 1) + \lambda^* \ln p_{max}. \tag{2.0.22}$$

The parameter is marked as N_{iso} in Fig. 2.9a. However, when the oedometric test is used for the calibration, the loading path is parallel to the isotropic compression path and the obtained parameter N_{edo} is shifted beneath the isotropic compression line. The value of N_{edo} has to be then adjusted by ΔN. This adjustment can by performed by running the simulation of oedometric test with already calibrated parameters, including N_{edo} and plot the results of the simulation against the data of the oedometric laboratory experiment. The vertical difference ΔN between both curves implies the correct position of NCL, see Fig. 2.9a. The calculation of N with respect to the oedometric test is defined by

$$N_{edo} = \ln(e_{max} + 1) + \lambda^* \ln \sigma_{a,max} \tag{2.0.23}$$

and

$$N_{iso} = \Delta N + N_{edo} \tag{2.0.24}$$

Furthermore, the value of parameter N can be different for the reconstituted and undisturbed soil sample due to the soil structure. In case of cemented soils it is recommended to use the model for meta-stable structure [25] and calibrate the final value of N based on the results derived from a reconstituted soil sample (N_r) and additionaly take into account the cementing by sensitivity variable s, see Fig 2.9b. This model, however, is not considered in this thesis.

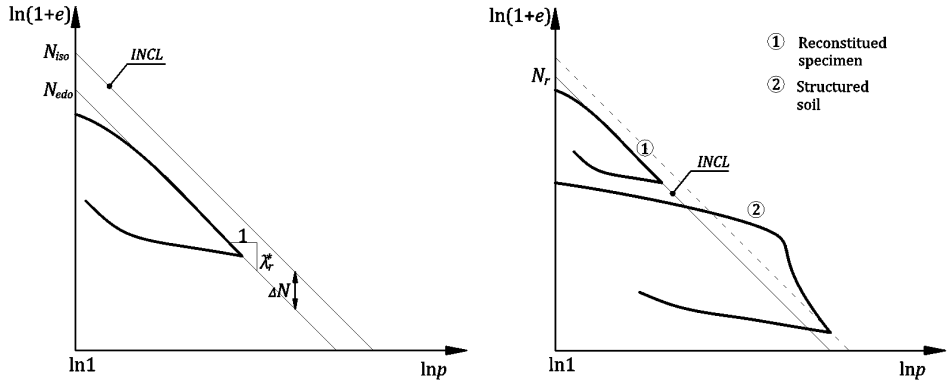

(a) The effect of the laboratory test on N

(b) The effect of the soil structure on N

Figure 2.9: Parameter N under different conditions

For the minor structure effects, it is thus preferable to calibrate N from the undisturbed soil sample and consequently properly capture compression test. Desctibed procedure can be used for the determinition of parameter e_0 controling the position of INCL of the MCC model. The space ln $p \times e$ has to be once again considered for the calibration.

Parameter ν

The parameter ν controls the ratio of the bulk modulus K_i and shear stiffness modulus G_i at the isotropic state.

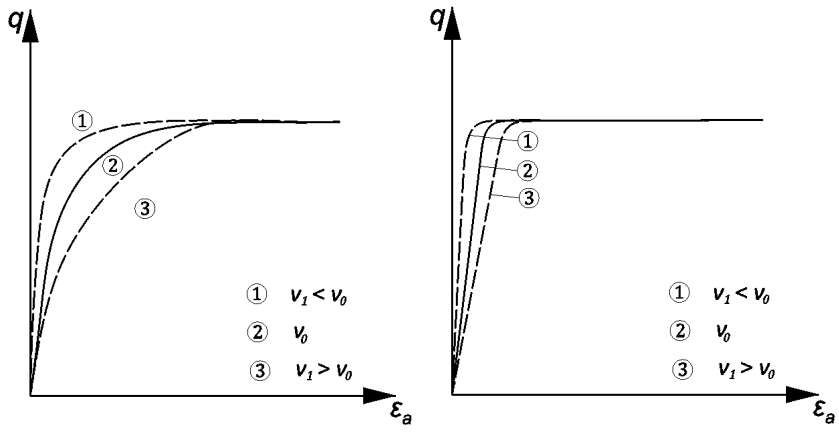

(a) The effect of ν on hypoplastic model

(b) The effect of ν on MCC model

Figure 2.10: The effect of ν under undrained triaxial conditions

The most convenient way of its determination is to employ the parametric study of triaxial shear test in the $q \times \varepsilon_a$ plane as seen in Fig. 2.10a for different values of ν.

Since the parameter ν controls nonlinearity of the hypoplastic model, its value should be prefferably calibrated using an undisturbed soil sample, which is more relevant to the current state of soil. The parameter ν in MCC model controls the relation of elastic shear modulus G and bulk modulus K, therefor, it should be preferably calibrated on the elastic part of the shear test, see Fig. 2.11a. The effect of the parameter ν under drained conditions is shown in Fig. 2.11b.

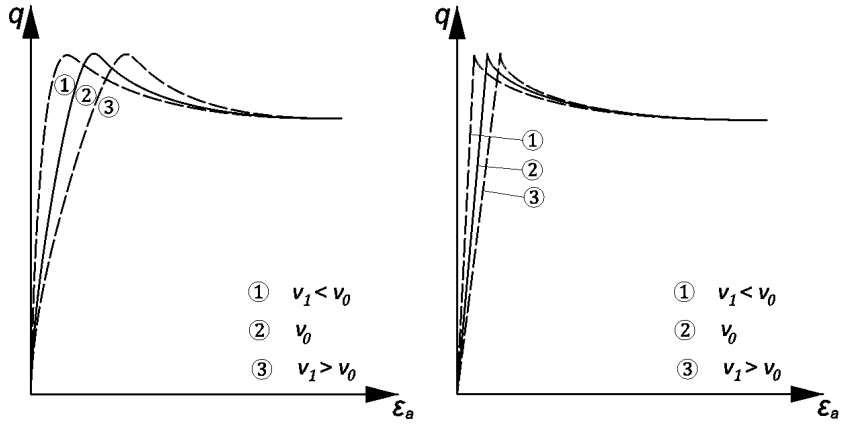

(a) The effect of ν on hypoplastic model (b) The effect of ν on MCC model

Figure 2.11: The effect of ν under drained triaxial conditions

An inseparable part of the calibration is the determination of the initial void ratio e so that the critical state is reached at the same value of a deviatoric stress for both the simulation and laboratory experiment, see Fig. 2.12 for the effect of the initial void ratio under the undrained triaxial conditions.
In case of the drained triaxial test the determinition of the initial void ratio aims match the the peach friction angle φ_c of both simulataion and experiment results,see Fig 2.13 for the effect of the initial void ratio under the drained triaxial conditions.

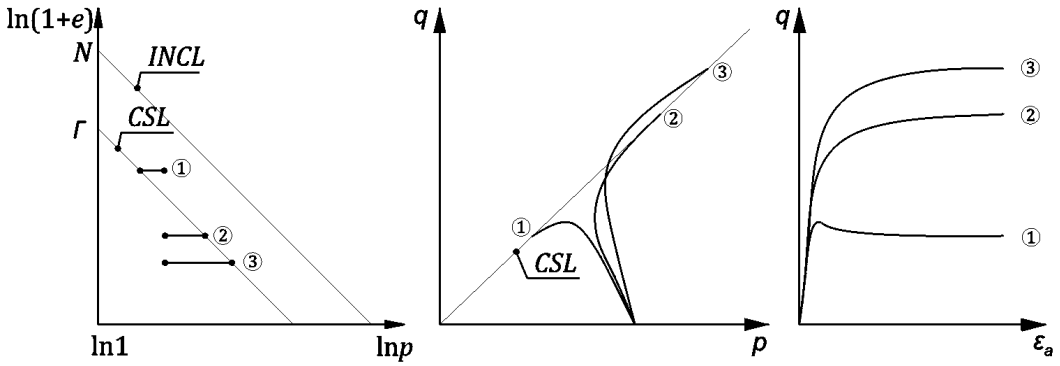

Figure 2.12: The effect of the initial void ratio under undrained triaxial conditions

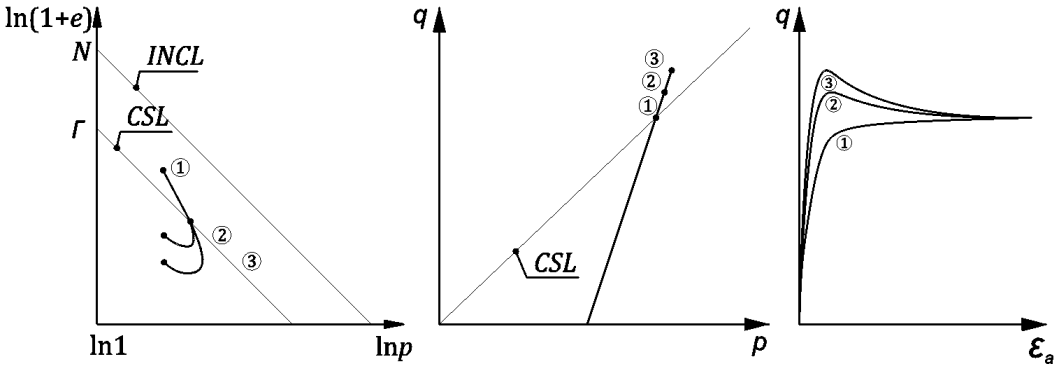

Figure 2.13: The effect of the initial void ratio under drained triaxial conditions

.

3. Solution strategies

The key aspect in the analysis of advanced soil models is to properly integrate constitutive equation

$$\dot{\boldsymbol{\sigma}} = \mathbf{D}_t(\boldsymbol{\sigma}, \boldsymbol{\kappa}) : \dot{\boldsymbol{\varepsilon}} \tag{3.0.1}$$

and find the best estimation of the tangent stiffness matrix $\mathbf{D}_t$ and consequently a stress increment $\Delta\boldsymbol{\sigma}$ corresponding to a given strain increment $\Delta\boldsymbol{\varepsilon}$ as

$$\int_t^{t+\Delta t} \frac{\Delta\boldsymbol{\sigma}}{\Delta t}\mathrm{d}t = \int_t^{t+\Delta t} \mathbf{D}_t(\boldsymbol{\sigma}, \boldsymbol{\kappa}) : \frac{\Delta\boldsymbol{\varepsilon}}{\Delta t}\mathrm{d}t. \tag{3.0.2}$$

Equation (3.0.1) represents the form of the stress-strain law to be integrated over the time intervat Δt as suggested by Eq. (3.0.2) to yield

$$\boldsymbol{\sigma}_{n+1} = \boldsymbol{\sigma}_n + \Delta\boldsymbol{\sigma}, \tag{3.0.3}$$

where

$$\boldsymbol{\sigma}(t = 0) = \boldsymbol{\sigma}_n \tag{3.0.4}$$

and

$$\boldsymbol{\sigma}(t = 1) = \boldsymbol{\sigma}_{n+1}. \tag{3.0.5}$$

Given a specific form of $\mathrm{d}\boldsymbol{\sigma}$ we distinguish between the explicit,

$$\boldsymbol{\sigma}_{n+1} = \boldsymbol{\sigma}_n + \mathbf{D}_t(\boldsymbol{\sigma}_\mathbf{n}, \boldsymbol{\kappa}_\mathbf{n}) : \Delta\boldsymbol{\varepsilon}, \tag{3.0.6}$$

and implicit,

$$\boldsymbol{\sigma}_{n+1} = \boldsymbol{\sigma}_n + \mathbf{D}_t(\boldsymbol{\sigma}_{\mathbf{n+1}}, \boldsymbol{\kappa}_{\mathbf{n+1}}) : \Delta\boldsymbol{\varepsilon}, \tag{3.0.7}$$

integration scheme [26]. As suggested by Eqns. (3.0.4)–(3.0.5) the pseudotime t lies with in the interval $t \in < 0, 1 >$.

Example of the explicit methods are the forward Euler method and the forward Runge-Kutta method in various modifications. The accuracy of both methods is heavily influenced by the size step as the error at the end of the each step is added to the total error. Consequently, the substepping is often used to reduce this effect.

Implicit methods are represented by the backward Euler method and the backward Runge-Kutta methods. Since $\boldsymbol{\sigma}_{n+1}$ in Eq. (3.0.7) is not known in advance, the solution requires root finding iteration procedure such as the Newton method at each step. Even though the implicit methods are more computation demanding, they are valued for their high calculation stability [27]. An example of a widely used implicit Euler's method is the Closest Point Projection Method (CPPM) in solving the elastoplastic constitutive equation with performing the so called elastic predictor and plastic corrector steps [28].

Subsequent sections will focus on Newton method, the adaptive forward Euler method and the Runge-Kutta-Fehlberg method. Newton's method is probably one of the most distinguished optimization method and its application can be found in many engineering softwares. This method is also used in the calibration software ExCalibre for the optimization. The Runge-Kutta-Fehlberg45 method is used in the Fine's GEO5 FEM software in the integration of the hypoplastic differential equation and the Euler method represents a stepping stone in the evaluation of the differential equations.

3.0.1 Newton's method

Apart from the use of the Newton-Raphson method in the pursue of the function's root $f(x) = 0$ of at least once differentiable function, Newton's optimization method can be used in optimization procedure while searching for the stacionary

points $f'(x) = 0$ for at least twice differentiable function. This procedure can be used in a process of a minimization of the objective function value $f(x)$ while at the same time finding the best solution x.

The Newton's method uses the second order approximation of $f(x)$ in each step and requires at least twice differentiable function defined as

$$x_{n+1} = x_n - \gamma \frac{f'(x_n)}{f''(x_n)} \tag{3.0.8}$$

in the case of one variable and

$$\mathbf{x}_{n+1} = \mathbf{x}_n - \gamma \mathbf{H}(f(\mathbf{x}_n))^{-1} \cdot \bigtriangledown f(\mathbf{x}_n) \tag{3.0.9}$$

in the case of multi-variable space, where

$$\mathbf{H}(f(\mathbf{x}_n)) = \begin{pmatrix} \frac{\partial^2 f}{\partial x_1^2} & \cdots & \frac{\partial^2 f}{\partial x_1 x_n} \\ \vdots & \ddots & \vdots \\ \frac{\partial^2 f}{\partial x_n x_1} & \cdots & \frac{\partial^2 f}{\partial x_n^2} \end{pmatrix} \tag{3.0.10}$$

represents a positive semi-definite hessian matrix containing second order partial derivatives and

$$\bigtriangledown f(\mathbf{x}_n)^T = \left(\frac{\partial f}{\partial x_1}, \cdots, \frac{\partial f}{\partial x_n} \right) \tag{3.0.11}$$

is the gradient $\bigtriangledown f(\mathbf{x_n})$ contains first order partial derivatives. A scalar γ might be used in order to keep a next step in reasonable bounds and belong to l-limits $0 < \gamma \leq 1$.

A weakness of the Newton's method (as well as other gradient based methods) is its dependency on the initial estimation x_0 since the function $f(x)$ can define several local extremes while the object of interest is the global minimal one. Attention thus has to be paid as the best selection of the first estimation or, in the case of high uncertainty, the optimization can be conducted from sevelal

initial approximations. Moreover, this comes to extreme attention in the case of higher number of variables where also statistic sampling methods are exploited in order to choose a representative combination of a given variable space.

Since the Newton's optimization uses the second order approximation at each step and converges towards the closest stationary point the method can converge to either maximum or minimum, see Fig. (3.0.8). In the case when minimization is in the interest a control of the gradient should be employed and thus force a convergence towards the minimum value of the objective function $f(x)$ [27].

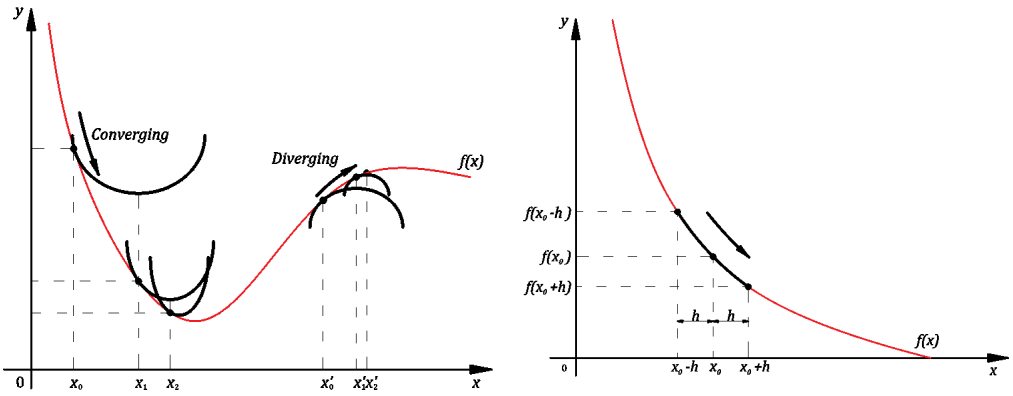

(a) Newton's 2nd order approximation

(b) Finite difference method

Figure 3.1: Newton's method approximation

Newton's method in this thesis is used to minimize an error function representing a deviation between a given laboratory experiment and a corresponding numerical simulation. During the optimization the best solution $f'(x) = 0$ for the relevant material parameter or state variable is found. If the explicit expression of the error function is absent, the function derivatives have to be obtained by means of the finite difference method. The first and second derivatives are then expressed as shown in Fig. 3.1b by

$$\frac{\mathrm{d}f(x)}{\mathrm{d}x} = \frac{f(x+h) - f(x-h)}{2h} \tag{3.0.12}$$

$$\frac{\mathrm{d}^2 f(x)}{\mathrm{d}x^2} = \frac{f(x+h) - 2f(x) + f(x-h)}{h^2} \tag{3.0.13}$$

for one variable and by

$$\frac{\mathrm{d}f(x)}{\mathrm{d}x} = \frac{f(x+h) - f(x-h)}{2h} \tag{3.0.14}$$

$$\frac{\mathrm{d}^2 f(x)}{\mathrm{d}x^2} = \frac{f(x+h) - 2f(x) + f(x-h)}{h^2} \tag{3.0.15}$$

$$\frac{\partial f(x_1, x_2)}{\partial x_1} = \frac{f(x_1 + h_1, x_2) - f(x_1 - h_1, x_2)}{2h_1} \tag{3.0.16}$$

$$\frac{\partial f(x_1, x_2)}{\partial x_2} = \frac{f(x_1, x_2 + h_2) - f(x_1, x_2 - h_2)}{2h_2} \tag{3.0.17}$$

$$\frac{\partial^2 f(x_1, x_2)}{\partial x_1^2} = \frac{f(x_1 + h_1, x_2) - 2f(x_1, x_2) + f(x_1 - h_1, x_2)}{h_1^2} \tag{3.0.18}$$

$$\frac{\partial^2 f(x_1, x_2)}{\partial x_2^2} = \frac{f(x_1, x_2 + h_2) - 2f(x_1, x_2) + f(x_1, x_2 - h_2)}{h_2^2} \tag{3.0.19}$$

$$\frac{\partial^2 f(x_1, x_2)}{\partial x_1 x_2} = \left(\frac{f(x_1 + h_1, x_2 + h_2) - f(x_1 + h_1, x_2 - h_2) -}{1} \right.$$

$$\left. \frac{-f(x_1 - h_1, x_2 + h_2) + f(x_1 - h_1, x_2 - h_2)}{1} \right) \frac{1}{4h_1 h_2} \tag{3.0.20}$$

for two variables. The size of the step h has a significant impact on the final solution and convergence of the Newton's method.

3.0.2 Explicit Euler's method

The Euler method is a simple technique to solve a differential equation once the initial conditions are known. The first order Euler method is defined by

$$\mathrm{d}\boldsymbol{\sigma} = \mathbf{D}_n(\boldsymbol{\sigma}_n, \boldsymbol{\kappa}_n)\mathrm{d}\varepsilon \tag{3.0.21}$$

$$\tag{3.0.22}$$

and

$$\boldsymbol{\sigma}_{n+1} = \boldsymbol{\sigma}_n + \mathrm{d}\boldsymbol{\sigma}, \tag{3.0.23}$$

which means that the local truncation error is proportional to the square of the step size. This method is heavily size step dependent as the error at the end of each step is accumulated. Therefore, to keep the eventual error small the size step has to be kept small.

Slone in [29] put forth an adaptive solution of the modified Euler method by subdividing of the loading step into smaller substeps. The modified Euler method calculates an *average* tangent stiffness operator **D'**. Consequently, the method is of the second order (local truncation error is proportional to the cube of the step size) defined by

$$\mathbf{D}'_n = \frac{1}{2}\left[\mathbf{D}_n(\boldsymbol{\sigma}_n, \boldsymbol{\kappa}_n) + \mathbf{D}_{n+1}(\boldsymbol{\sigma}_{n+1}, \boldsymbol{\kappa})_{n+1}\right], \tag{3.0.24}$$

while

$$\mathrm{d}\boldsymbol{\sigma} = \mathbf{D}'_n\mathrm{d}\varepsilon_k \tag{3.0.25}$$

and

$$\mathrm{d}\varepsilon_k = q\mathrm{d}\varepsilon, \tag{3.0.26}$$

see Fig. 3.2b. The most importat aspect is the adaptive reduction of the step size with respect to the truncation error $\mathbf{E}$ defined as

$$\mathbf{E}^{\sigma}_{k+1} = \frac{1}{2}[-\mathrm{d}\boldsymbol{\sigma}_n + \mathrm{d}\boldsymbol{\sigma}_{n+1}] \tag{3.0.27}$$

by the factor

$$q = 0.8\left(\frac{TOL^{\sigma}}{R^{\sigma}_{k+1}}\right)^{1/2}, \tag{3.0.28}$$

where

$$R^{\sigma}_{k+1} = \frac{||\mathbf{E}^{\sigma}_{k+1}||}{||\boldsymbol{\sigma}_{k+1}||} \leq TOL^{\sigma}. \tag{3.0.29}$$

TOL^{σ} in Eq. (3.0.29) represents the assumed tolerance usually defined in the limits of $10^{-2} - 10^{-5}$ [29].

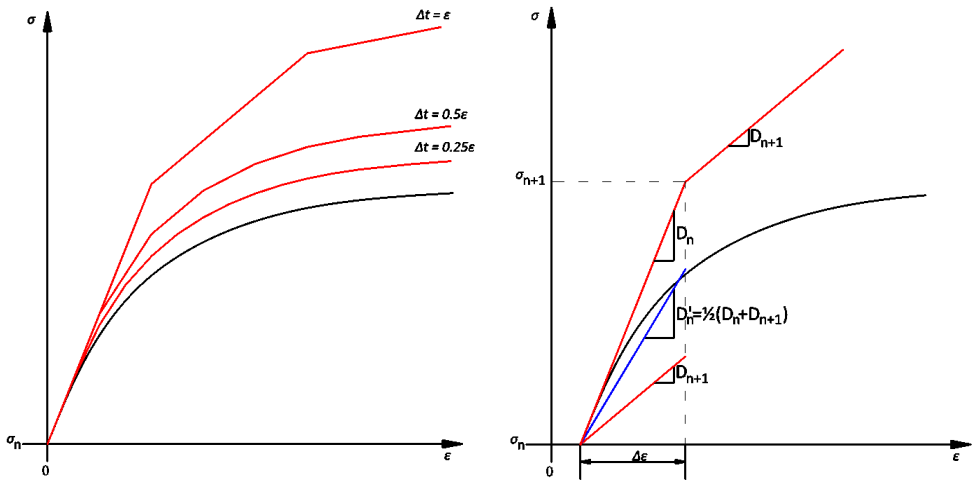

(a) Second order Euler approximation

(b) Finite difference method

Figure 3.2: Second order Euler approximation

In case of elastoplastic models, should be introduced

$$\boldsymbol{\kappa}_{\mathbf{n+1}} = \boldsymbol{\kappa}_{\mathbf{n}} + g(\boldsymbol{\sigma}_{\mathbf{n+1}}, \boldsymbol{\kappa}_{\mathbf{n}})\mathrm{d}t_k, \tag{3.0.30}$$

where

$$\mathrm{d}t_k = q\mathrm{d}t \tag{3.0.31}$$

to account for potential hardening. This also calls for the introduction of the error on the hardenning parameters according to

$$\mathbf{E}^{\kappa}_{k+1} = \frac{1}{2}[-\mathrm{d}\boldsymbol{\kappa}_{\mathbf{n}} + \mathrm{d}\boldsymbol{\kappa}_{\mathbf{n+1}}] \tag{3.0.32}$$

Then the factor q can be expressed as

$$q = \max\left[0.8\left(\frac{TOL^{\sigma}}{R^{\sigma}_{k+1}}\right)^{1/2}, 0.8\left(\frac{TOL^{\kappa}}{R^{\kappa}_{k+1}}\right)^{1/2}\right], \tag{3.0.33}$$

where

$$R^{\kappa}_{k+1} = \frac{||\mathbf{E}^{\kappa}_{k+1}||}{||\boldsymbol{\kappa}_{k+1}||} \leq TOL^{\kappa}. \tag{3.0.34}$$

The factor q should be limited within $0.1 \leq q \leq 0.5$.

In the initial works regarding the implementation of the hypoplastic model explicit Euler's first order method was used [30]. Even though the method does not provide the same accuracy as the backward Euler method, it is often applied and appreciated for its simplicity and calculation speed. Furthermore, it is often difficult to obtain a partial derivatives in the case of complicated constitutive models for the Newton's iterative method [28]. The forward Euler method is used as a solution method for the integration of the hypoplastic and Cam-Clay equations in single element simulations of the Excalibre calibration software.

3.0.3 Runge-Kutta method

The explicit Runge-Kutta-Felhberg RKF45 method is implemented in the GEO5 FEM software for the Masin's hypoplastic clay model and the same method is used for the Wolffersdorff's hypoplastic model. Similarly to the Euler's method it is an explicit method with a simple implementation. This method requires six tangent stiffness operator $\mathbf{D_{n+\theta}}$ in each step, more specifically initial state ($\theta = 0$), the final state ($\theta = 1$) and the four midpoints fulfilling $0 < \theta < 1$ according to Eqns. (3.0.35)–(3.0.40). When compared to Euler's method, the method is more demanding with respect to the computational power. On the other hand, it is well compensated with high accuracy and calculation stability.

$$\Delta\boldsymbol{\sigma_1} = \mathbf{D_n}(\boldsymbol{\sigma_n}, \boldsymbol{\kappa_n})\Delta\boldsymbol{\varepsilon} \tag{3.0.35}$$

$$\Delta\boldsymbol{\sigma_2} = \mathbf{D_{n+1/4}}(\boldsymbol{\sigma_n} + \frac{1}{4}\Delta\boldsymbol{\sigma_1}, \boldsymbol{\kappa_{n+1/4}})\Delta\boldsymbol{\varepsilon} \tag{3.0.36}$$

$$\Delta\boldsymbol{\sigma_3} = \mathbf{D_{n+3/8}}(\boldsymbol{\sigma_n} + \frac{3}{32}\Delta\boldsymbol{\sigma_1} + \frac{9}{32}\Delta\boldsymbol{\sigma_2}, \boldsymbol{\kappa_{n+3/8}})\Delta\boldsymbol{\varepsilon} \tag{3.0.37}$$

$$\Delta\boldsymbol{\sigma_4} = \mathbf{D_{n+12/13}}(\boldsymbol{\sigma_n} + \frac{1932}{2197}\Delta\boldsymbol{\sigma_1} - \frac{7200}{2197}\Delta\boldsymbol{\sigma_2} + \tag{3.0.38}$$
$$+ \frac{7296}{2197}\Delta\boldsymbol{\sigma_3}, \boldsymbol{\kappa_{n+12/13}})\Delta\boldsymbol{\varepsilon}$$

$$\Delta\boldsymbol{\sigma_5} = \mathbf{D_{n+1}}(\boldsymbol{\sigma_n} + \frac{439}{216}\Delta\boldsymbol{\sigma_1} - 8\Delta\boldsymbol{\sigma_2} + \frac{3680}{513}\Delta\boldsymbol{\sigma_3} - \tag{3.0.39}$$
$$- \frac{845}{4104}\Delta\boldsymbol{\sigma_4}, \boldsymbol{\kappa_{n+1}})\Delta\boldsymbol{\varepsilon}$$

$$\Delta\boldsymbol{\sigma_6} = \mathbf{D_{n+1/2}}(\boldsymbol{\sigma_n} - \frac{8}{27}\Delta\boldsymbol{\sigma_1} + 2\Delta\boldsymbol{\sigma_2} - \frac{3544}{2565}\Delta\boldsymbol{\sigma_3} + \tag{3.0.40}$$
$$+ \frac{1859}{4104}\Delta\boldsymbol{\sigma_4} - \frac{11}{40}\Delta\boldsymbol{\sigma_5}, \boldsymbol{\kappa_{n+1/2}})\Delta\boldsymbol{\varepsilon}$$

The RKF45 method executes two approximations defined by

$$\boldsymbol{\sigma}^{\mathbf{1}}_{\mathbf{n+1}} = \boldsymbol{\sigma}_{\mathbf{n}} + \frac{25}{216}\boldsymbol{\sigma}_{\mathbf{1}} + \frac{1408}{2565}\boldsymbol{\sigma}_{\mathbf{3}} + \frac{2197}{4101}\boldsymbol{\sigma}_{\mathbf{4}} - \frac{1}{5}\boldsymbol{\sigma}_{\mathbf{5}} \tag{3.0.41}$$

and

$$\boldsymbol{\sigma}^{\mathbf{2}}_{\mathbf{n+1}} = \boldsymbol{\sigma}_{\mathbf{n}} + \frac{16}{135}\boldsymbol{\sigma}_{\mathbf{1}} + \frac{6656}{12825}\boldsymbol{\sigma}_{\mathbf{3}} + \frac{28561}{56430}\boldsymbol{\sigma}_{\mathbf{4}} - \frac{9}{50}\boldsymbol{\sigma}_{\mathbf{5}} + \frac{2}{55}\boldsymbol{\sigma}_{\mathbf{6}} \tag{3.0.42}$$

as approximations of the forth and second order, respectively.

The adaptive evalulation of the step size at the end of each step is defined by

$$h = sh, \tag{3.0.43}$$

where

$$s = \left(\frac{TOL\ h}{2||\boldsymbol{\sigma}^{\mathbf{2}}_{\mathbf{n+1}} - \boldsymbol{\sigma}^{\mathbf{1}}_{\mathbf{n+1}}||} \right)^{0.25}. \tag{3.0.44}$$

The consequence of Eq. (3.0.44) is an increase of the step size if the two approximations are considered close or the step size is decreased if the values are not regarded as close. TOL in Eq. (3.0.44) represents a user defined error control tollerance.

Improving the optimization method is an ongoing process and various methods are compared and tested. In [31] modified Euler's method, Richardson extrapolation and Runge-Kutta-Dormand-Price were studied for the application with the hypoplastic models proposed by Gudehus [17] and Bauer [16]. It was concluded that adaptive explicit methods are well suited to the highly nonlinear behaviour of the hypoplastic equation as it ensures sufficiently small step if needed. Furthermore, the implicit method failed when the large increment step was used. A similar study and conclusions regarding the implicit and explicit adaptive methods was presented in [32] where again the modified Euler method, the Richardson extrapolation, the Crank–Nicolson method and the Runge-Kutta-Felhberg method RKF23 and RKF45 with substeping were tested with the RKF45

method used as a benchmark. The model proposed by Wu and Kolymbas in [9] was used ass a referrenced model. Further implementaion of the hypoplastic models can be found in [30, 33, 34].

4. Online calibration software

Even though the development of the more advanced soil models goes continuously forward, the awareness of these models in the engineering community is rather limited and the basic elastoplastic models such as the Mohr-Coulomb or their enhancements are adopted. This state can be attributed the lack of knowledge or tools necessary to calibrate these advanced models. Nowadays, laboratories such as SG Geotechnika plc. provide the values of Mohr-Coulomb parameters in the laboratory protocol as the part of their service. Calibration of more advanced models, however, remains omitted.

To promote advanced soil models and to provide reliable and sufficient tools a calibration online application called ExCalibre (External Calibration) was developed in cooperation of The Czech Technical University in Prague, Charles University and SG Geotechnika plc.

This chapter is dedicated to the calibration software ExCalibre. The chapter is open by discussing the calibration softwares found in literature and the implemented approaches to the calibration of the soil model's parameters. Next, the parameters sensitivity analysis, program structrure, verifications and calibration performance will be thoroughly sescribed.

4.1 Calibration strategies

The need for reliable calibration tools, not only for a preliminary design but also for improvement of the design during construction work led to a development of numerous softwares identifying parameters of different soil models. The calibration procedures are regarded as the inverse analysis, since the parameters **m** of the constitutive model **M** are not known in advance but the reaction **R** of the system **S(M,m)** to the action **A** is [35] [36]

$$\mathbf{A} => \mathbf{S(M, m)} => \mathbf{R}. \tag{4.1.1}$$

The goal of calibration is to minimize the objective error function E which is defined as a function of a difference between the observation or experiment U_{exp} and simulation U_{num}. The most common is the least square method. More sophisticated formulas are also available in the litarature, see Eq. (4.1.2), where U^i_{exp} is the value of experimental data, U^i_{num} is the value of simulation and w_i is the weight of the point of interest i. N is the number of observed points [37].

$$E = \sqrt{\frac{1}{N}\sum_{i=1}^{N} w_i \left(\frac{U^i_{exp} - U^i_{num}}{U^i_{exp}}\right)^2} \times 100 \tag{4.1.2}$$

The calibration procedure itself can be in general regarded as ill-posed optimization problem, since the calibration offers non-unique solution to a given problem. In geotechnics, the problem is represented by a numerical simulation which ought to imitate the obseravation of the laboratory or field measurements obtained either a priori or during the construction works. The laboratory measurements usually consist of compression and shear experiments in order to obtain a proper image of a soil behaviour regarding copression characteristics and shear failure [36]. The typically conducted laboratory experiments are the oedometric test, isotropic compression test, drained and undrained triaxial test or direct shear test. The scheduled laboratory tests usually precede the construction works. Because the specimens intended for the laboratory test can be damaged during the sampling and handling, the advantage of the field experiments offering the possibility to execute the tests on the soil in its intact state can be carried out. The field tests include, e.g., penetration test and pressuremeter test and original design can be further improved with the monitoring of the excavation or boring works.

Consequently, the calibration procedures can be performed with the use of a single element method in the case of the laboratory experiments or Finite Element Methods in the case of problems concerning the studied geotechnical

structure. A combinations of both examples are often applied as the laboratory experiments are supported or further specified with the field measurements, such examples can be found in [35, 38, 39, 40]. The optimization methods solving the calibration are divided in to these fundamental groups.

Calibration Methods

- Deterministic methods
- Stochastic methods
- Combination

The deterministic methods can be referred to as optimization methods that do not involve any random search and the same solution is generated for a given input value. The most common examples are simplex method or gradient based methods. In order to obtain reliable results of the optimalization, the initial starting values have to be relatively close to the global minimum, otherwise the optimization process could find and remain in a local minimum. Another option is initiating the optimization process from multiple initial values [41]. This problem is even more relevant in the case of optimization with the multiple variables. The deterministic approaches can be found in[35, 37, 38, 39, 41, 42].

The stochastic methods can be referred to as optimization methods generating a random variables in pursue of the minimization of the objective function. Before the optimization itself, a sampling process in undertaken which can be classified as random or uniform. The advantage of stochastic approach is location of several minimums, thus better picture of the objective funstion properties is obtained and later can be decided which of the solutions is in the best agreement with the one's experiences. In the case of multi-objective optimization, the best solutions form so called Pareto frontier. [37, 40, 41, 43, 44, 45]

The calibration methods have been assessed and compared in many scientific articles. In [41] deterministic simplex method with stochastic genetic method on the calibration of elastoplastic Mohr-Coulomb model and strain hardening model were compared. It was pointed out that the genetic algorithms

was 12 times more expensive then the simplex method. Similar conclusions were found in [37]. It seems, however, necessary to perform stochastic optimization if the initial parameter's values cannot be closely specified or the problem contains more parameters to optimize. In addition, it has been shown in [37] that it is highly difficult to use deterministic method to optimize more parameters simultaneously due to their different sensitivity and coupling effect to certain experiments.

A performance and reliability of the calibration is significantly affected by the number of calibrated parameters and moreover types and number of experiments used for the calibration as each parameter can be sensitive to a certain type of loading. Furthermore, the experiments used fore the calibration should be fundamentally diverse as the coupling effect can be discovered between some parameters for a certain experiment [35].

Last but not least a correct execution of experiment is very important since the incorrect laboratory data inconveniently influence the quality of calibration results. Therefore, data used for the calibration should be sorted and in case of low quality omitted from the calibration [41].

Calibrations based on either deterministic or stochastic methods often used only a portion of model's parameters for the calibration and the rest is calibrated by the means of empirical relations. This assumption was usually based on the sensitivity analysis [35, 39, 37, 42, 41]. Interestingly, the objective error function E of the Cam-Clay model has smoother shape than simple Mohr-Coulomb model which imply better agreement of the advanced model with soil behaviour [41].

Very promising approach for the geotechnical engineering is improving the initial design parameters by the field monitoring. Such an approach, however, requires well executed initial calibration [38].

In conclusion, even though the stochastic methods are a powerful tool in the case of poorly defined problem and when there is not available enough conclusive data, it is more time demanding and requires higher knowledge of the stochastic methods to perform a correct sampling and to chose proper set of parameters from the results. Since advanced soil models have their parameters

well defined according to the thoroughly examined soil's asymptotic behaviour, i.e. well illustrated by the Normal Compression Line or Critical State Line, it is advantageous to use empirical calculations to obtain the initial values of models parameters for the deterministic methods such as Newton optimalization. Thus as long as the experiments are correctly performed and small number of parameters are optimized simultaneously, the rapid convergence towards global minimum is guaranteed.

4.2 Sensitivity analysis

A library of specimens from sixteen location in total was available for a development of the calibration software. The list of available locations including the number and types of available experiments can be found in Appendix A.

Properly defining the calibration procedure calls for a sensitivity analysis as it provides a sufficient evidence of the parameters effect on the model behaviour. The sensitivity can be evaluated by so called *scaled sensitivity*

$$SS_{ij} = \frac{\partial e_i}{\partial p_j} p_j \sqrt{w_i} \tag{4.2.1}$$

and *composite scaled sensitivity*

$$CSS_j = \sqrt{\frac{1}{N} \sum_{i=1}^{N} \left(\left(\frac{\partial e_i}{\partial p_j} p_j \sqrt{w_i} \right)^2 \right)} \tag{4.2.2}$$

proposed in [46], where p_j is the value of the j-th parameter, e_i represents, according to Eq. (4.2.1), the objective error function associated with the j-th value of the parameter p. The parameter w_i is the weight factor set to one. The sensitivity $\partial e_i / \partial p_j$ is calculated with the aid of the finite difference, where the step size is set to $p_j/100$. Summation goes through all observation, that is all specimens.

Five specimens were used to perform the sensitivity analysis. The value of CSS is calculated for each specimen separately in order to observe and compare

possible discrepancies in each individual specimen and parameter. Eventually, the overall CSS is calculated for all specimens. Parameters of each specimen for all three calibrated constitutive models Cam-Clay (CC), hypoplastic clay (HC) and hypoplastic sand (HS) are summarized in Tab. 4.2–Tab. 4.4. The sensitivity analysis was performed for all three models on one oedometric test and one undrained triaxial test in the case of fine grained soils and one oedometric test and one drained triaxial test in the case of coarse grained soils. It is worth noting that almost all specimens used for the sensitivity analysis were reconstituted except of a Metro2 oedometric test. The results of the sensitivity analysis nevertheless do not seem to be influenced by this condition.

In the case of triaxial tests, two analyses were conducted as well. The first objective function is evaluated on the vases of the deviatoric stress $E(q)$ and the second on the basis of axial deformation $E(\varepsilon_a)$. The particular spaces for the evaluation of the objective error function E in Tab. 4.1 were carefully chosen in accordance with the calibration procedures described in Chapter 2 *Parameteres and calibration procedures*. Similar sensitivity analyses can be found in [36, 39, 45]. Table 4.1 shows individual laboratory test with the corresponding stress/strain and stress/void ratio spaces and their objective error functions E.

Table 4.1: Sensitivity analysis charecteristics

	OED		CIUP		CID	
HC	$\ln \sigma_a \times \ln(e+1)$	$E(\ln(e+1))$	$\varepsilon_a \times q$	$E(q)$	-	-
			$\varepsilon_a \times q$	$E(\varepsilon_a)$		
CC	$\ln \sigma_a \times e$	$E(e)$	$\varepsilon_a \times q$	$E(q)$	-	-
			$\varepsilon_a \times q$	$E(\varepsilon_a)$		
HS	$\sigma_a \times e$	$E(e)$	-	-	$\varepsilon_a \times q$	$E(q)$
					$\varepsilon_a \times q$	$E(\varepsilon_a)$

Table 4.2: Hypoplastic clay parameters

	λ^*	κ^*	N	ν	φ
Metro1	0.065	0.015	0.799	0.01	33.5
Metro2	0.046	0.004	0.632	0.30	35.7
Hajek	0.041	0.006	0.637	0.27	36.0
Bilina1	0.048	0.008	0.728	0.25	28.1
Bilina2	0.063	0.007	0.999	0.32	26.9

Table 4.3: Elastoplastic Cam-Clay parameters

	λ	κ	e_0	ν	M_{cs}
Metro1	0.085	0.010	1.008	0.01	1.353
Metro2	0.059	0.010	0.790	0.01	1.449
Hajek	0.057	0.008	0.834	0.20	1.463
Bilina1	0.070	0.017	0.975	0.18	1.117
Bilina2	0.108	0.007	1.509	0.20	1.065

Table 4.4: Hypoplastic sand parameters

	h_s	n	e_{i0}	e_{c0}	e_{d0}	α	β	φ_{cv}
Dobrany	17676	0.479	1.234	1.028	0.519	0.04	3.7	41.1
Hrusovany	100	0.0500	2.326	1.938	0.969	0.03	3.9	42.6
Jablonec	100	0.050	2.788	2.323	1.162	0.01	1.8	42.6
Kralupy	17503	0.220	1.471	1.226	0.613	0.13	3.1	41.2
Stvanice	3010	0.218	1.775	1.479	0.739	0.14	4.0	35.8

4.2.1 Hypoplastic clay model

The sensitivity analysis performed on the hypoplactic clay model reveals that by far the most important parameter is N. Surprisingly, N has the highes impact on the results in cases of both oedometric and triaxial tests with λ^* being the second most important parameter, see Figs 4.1–4.3.

The impact of N is not only confirmed by each single CSS but also by the overall CSS by a large margin, see Figs. 4.3d, 4.3f, 4.3h. The precision of the model behaviour is thus mainly driven by the position of the isotropic normal compression line not only in the case of consolidation tests but, surprisingly, also in the case of triaxial test where in the comparison the critical state friction angle φ_c has a minor role. Consequently, a significant emphasis thus should be placed on the appropriate calibration of the parameters λ and N controlling the position of the isotropic normal compression line with especial emphasise on N. It is worth noting that the position of the CSL is correlated to the position of INCL by the value $\lambda^* \ln 2$.

The parameter κ^*, controlling the bulku modulus, appears as the third most influential parameter in the oedometric test, see Fig. 4.3d. Although with a comparatively smaller affect, this result is justified as the parameter κ^* controls the unloading and reloading part of the consolidation test. Since the specimens are reconstitued the over-consolidation ratio OCR is close to 1. Consequently, reloading and thus the influence of the parameter κ might be limited. Parameters ν and φ_c have a minor impact on the compression behaviour. Since the parameter ν controls the relation of K_i and G_i and only a small amount of the deviatoric stress q is produced during the oedometric test, the influence of ν should have been observed small, see Fig. 4.3d.

In the case of the triaxial test for $E(q)$, the critical state friction angle φ_c gains an importance, even though still comparatively smaller when comparing the $INCL$ controling parameters, see Fig. 4.3f. The effect of ν and κ is observed insignificant.

The overall effects of the parameters κ and ν on $E(\varepsilon_a)$ is also observed an insignificant. The parameter κ^* is observed to have two times larger impact on

the triaxial test than ν, see Fig. 4.3h. Since the observed effect of the parameter ν is insignificant, it can be calibrated as the last parameter to improve the model's nonlinear behaviour.

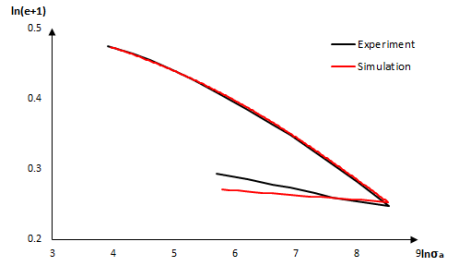

(a) Metro1 - Oedometric test

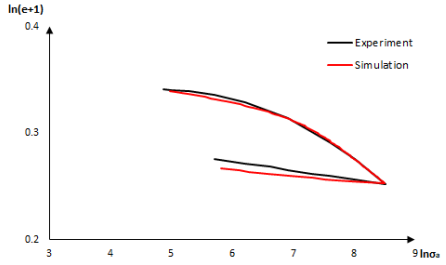

(b) Metro2 - Oedometric test

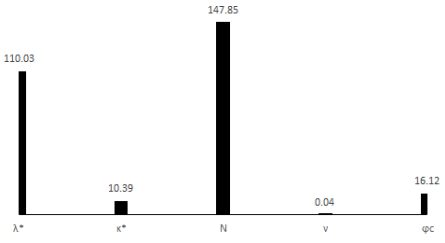

(c) Metro1 - CSS Oedometric test

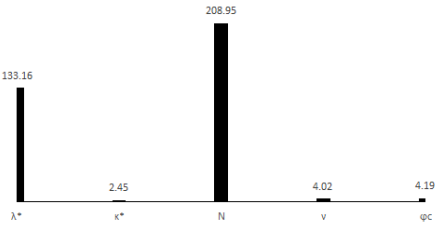

(d) Metro2 - CSS Oedometric test

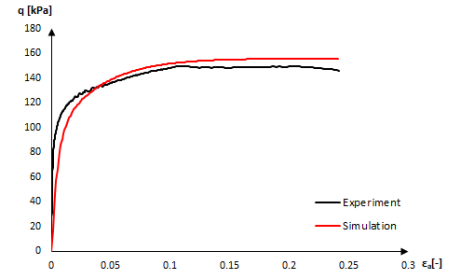

(e) Metro1 - CSS Undrained Triaxial test

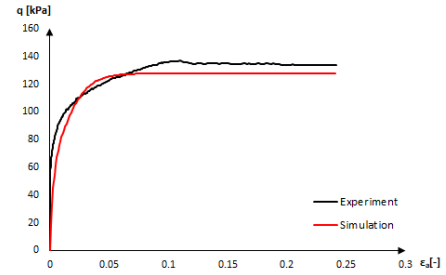

(f) Metro2 - CSS Undrained Triaxial test

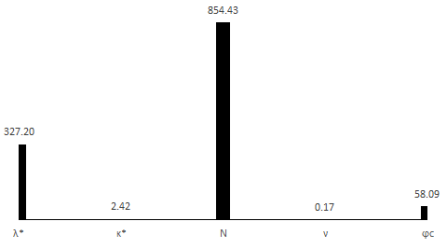

(g) Metro1 - CSSUndrained triaxial test $E(q)$

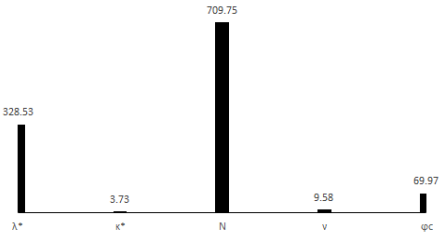

(h) Metro2 - CSS Undrained triaxial test $E(q)$

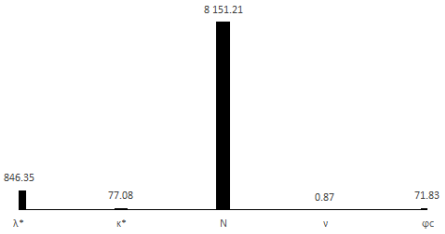

(i) Metro1 - CSS Undrained triaxial test $E(\varepsilon_a)$

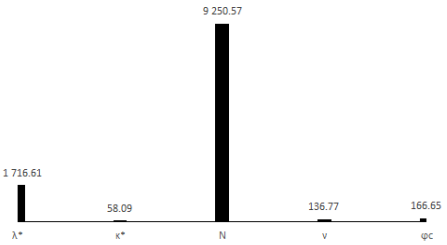

(j) Metro2 - CSS Undrained triaxial test $E(\varepsilon_a)$

Figure 4.1: Sensitivity analysis: Metro1, Metro2

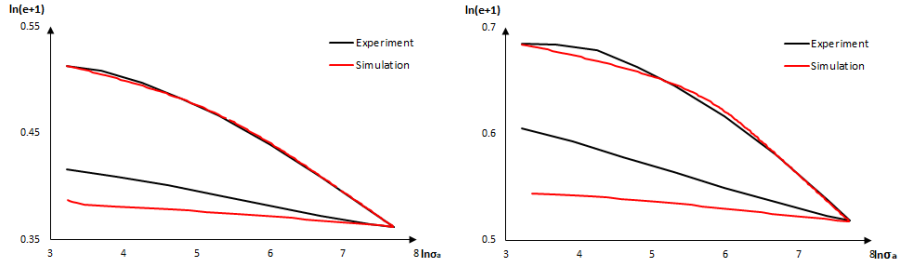

(a) Bilina1 - Oedometric test

(b) Bilina2 - Oedometric test

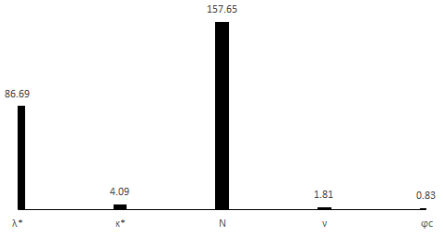

(c) Bilina1 - CSS Oedometric test

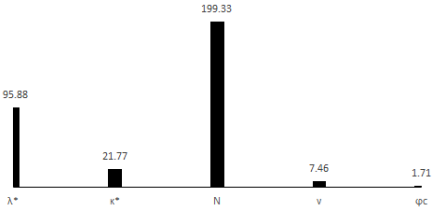

(d) Bilina2 - CSS Oedometric test

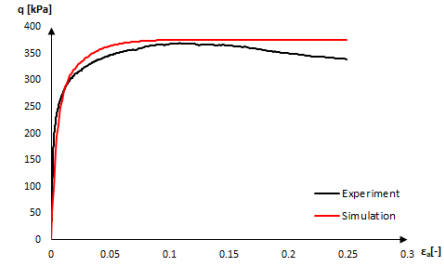

(e) Bilina1 - CSS Undrained Triaxial test

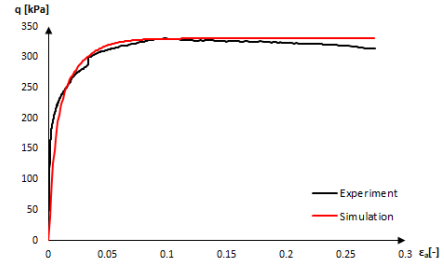

(f) Bilina2 - CSS Undrained Triaxial test

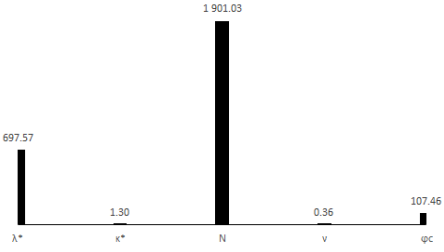

(g) Bilina1 - CSSUndrained triaxial test $E(q)$

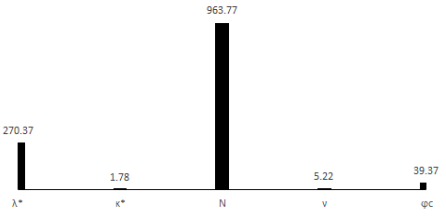

(h) Bilina2 - CSS Undrained triaxial test $E(q)$

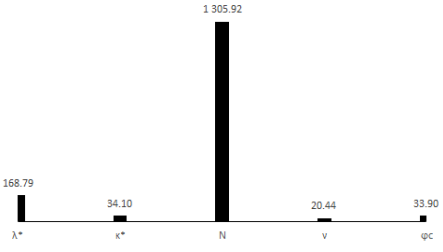

(i) Bilina1 - CSS Undrained triaxial test $E(\varepsilon_a)$

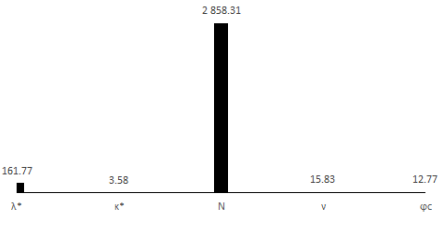

(j) Bilina2 - CSS Undrained triaxial test $E(\varepsilon_a)$

Figure 4.2: Sensitivity analysis: Bilina1, Bilina2

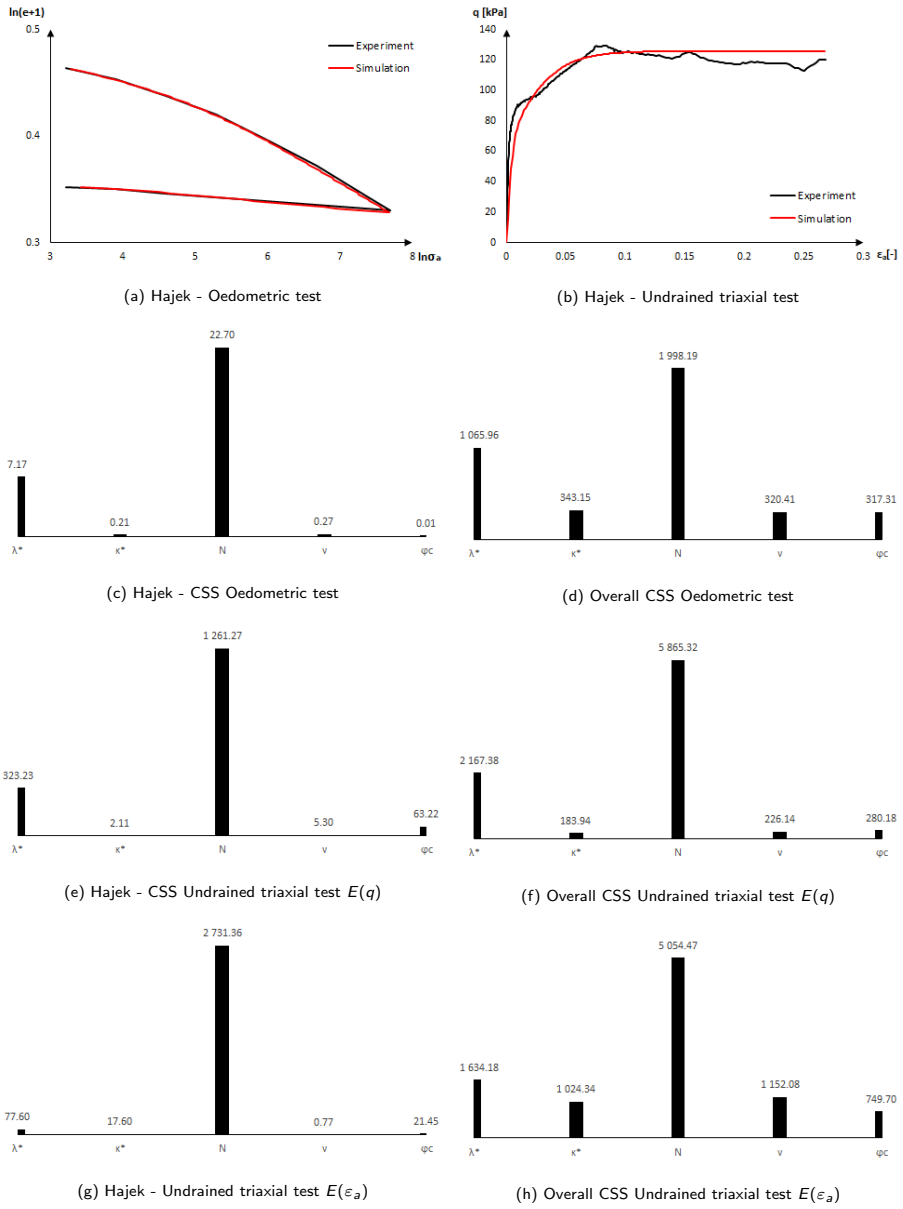

(a) Hajek - Oedometric test

(b) Hajek - Undrained triaxial test

(c) Hajek - CSS Oedometric test

(d) Overall CSS Oedometric test

(e) Hajek - CSS Undrained triaxial test $E(q)$

(f) Overall CSS Undrained triaxial test $E(q)$

(g) Hajek - Undrained triaxial test $E(\varepsilon_a)$

(h) Overall CSS Undrained triaxial test $E(\varepsilon_a)$

Figure 4.3: Sensitivity analysis: Hajek, Overall

4.2.2 Modified Cam-Clay model

The sensitivity analysis of the Modified Cam-Clay model revealed very similar effect of the parameters as in the case of hypoplastic clay model. This is particularly true in the case of oedometric tests and triaxial test with error function $E(q)$ where the error function are mostly sensitive to the parameters e_0 and λ. This is true with the exception of the specimen $Bilina2$ where is not established a clear leading parameter and the effect of the parameter λ is noticeably diminished. The overall sensitivity show the most influential parameters e_0 and λ, see Fig. 4.6d and Fig. 4.6f.

The sensitivity of triaxial test with the error function $E(\varepsilon_a)$ shows the highest sensitivity to Poisson's ratio ν, which controls the relation between bulk modulus K and shear modulus G. The second parameter is κ while the effect of parameters λ, e_0 and φ_c cannot be distinguished, see Fig. 4.6h. This is in contrast with the results of hypoplastic clay sensitivity study where the parameter ν has the least impact.

The Modified Cam-Clay model parameters have almost identical interpretation as the parameters of hypoplastic clay model. Furthermore, it was also observed in this sensitivity study that the Modified Cam-Clay model is sensitive to the parameters in idential way as the hypoplastic clay model. Therefore, it can be concluded that the calibration procedure can be defined in the same way for both hypoplastic clay a Modified Cam-Clay model.

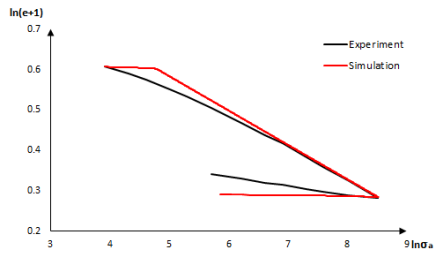

(a) Metro1 - Oedometric test

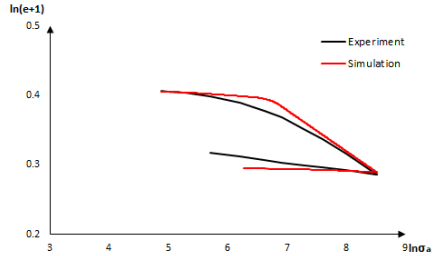

(b) Metro2 - Oedometric test

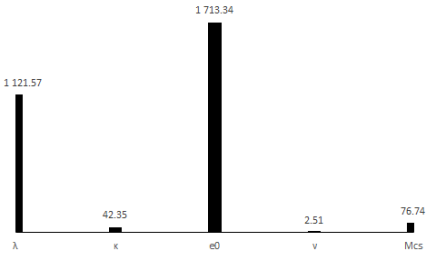

(c) Metro1 - CSS Oedometric test

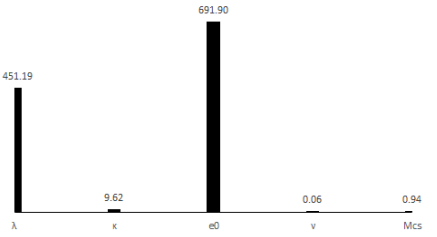

(d) Metro2 - CSS Oedometric test

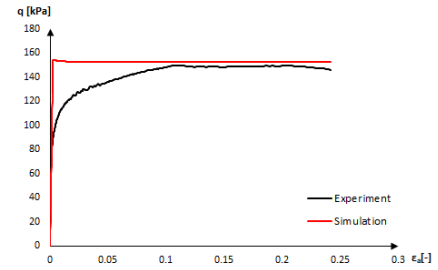

(e) Metro1 - CSS Undrained Triaxial test

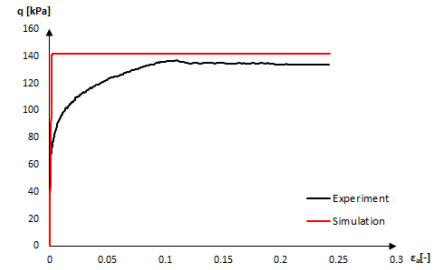

(f) Metro2 - CSS Undrained Triaxial test

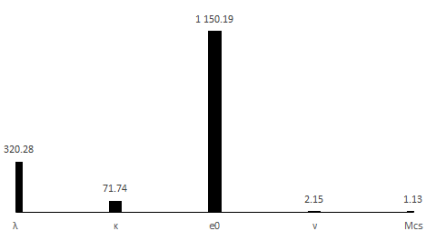

(g) Metro1 - CSSUndrained triaxial test $E(q)$

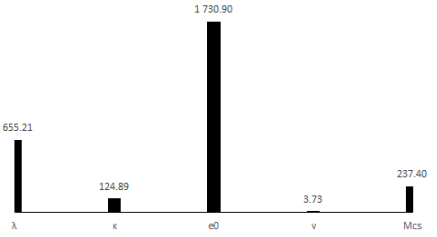

(h) Metro2 - CSS Undrained triaxial test $E(q)$

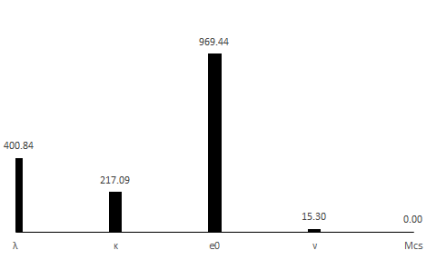

(i) Metro1 - CSS Undrained triaxial test $E(\varepsilon_a)$

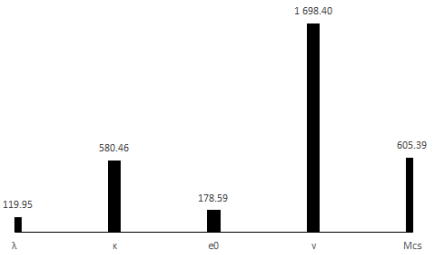

(j) Metro2 - CSS Undrained triaxial test $E(\varepsilon_a)$

Figure 4.4: Sensitivity analysis: Metro1, Metro2

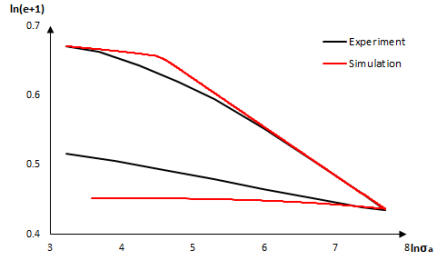

(a) Bilina1 - Oedometric test

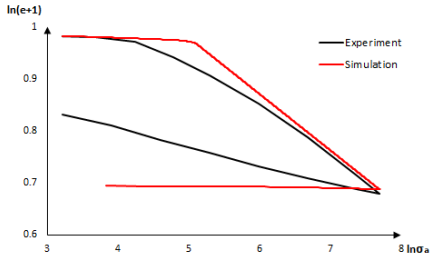

(b) Bilina2 - Oedometric test

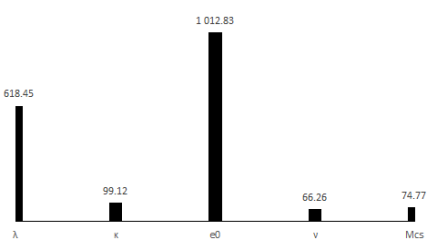

(c) Bilina1 - CSS Oedometric test

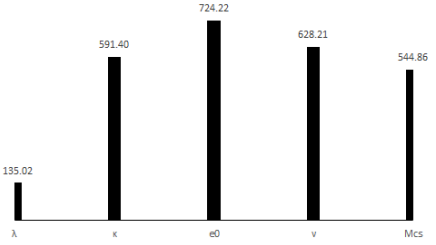

(d) Bilina2 - CSS Oedometric test

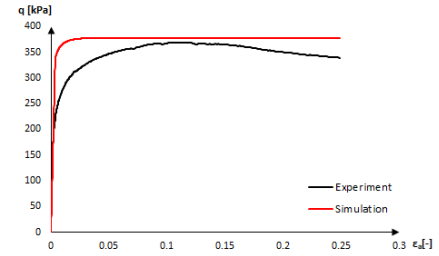

(e) Bilina1 - CSS Undrained Triaxial test

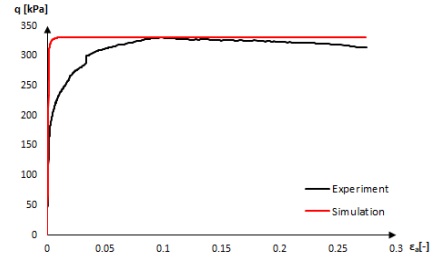

(f) Bilina2 - CSS Undrained Triaxial test

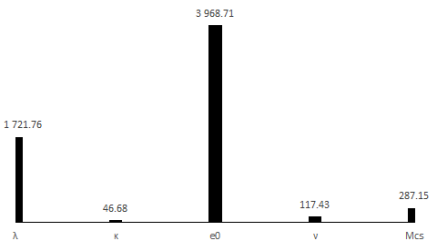

(g) Bilina1 - CSSUndrained triaxial test $E(q)$

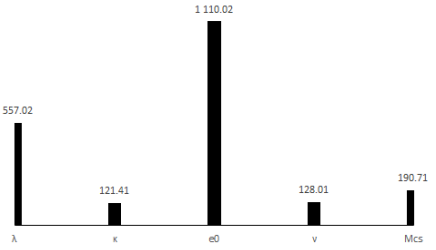

(h) Bilina2 - CSS Undrained triaxial test $E(q)$

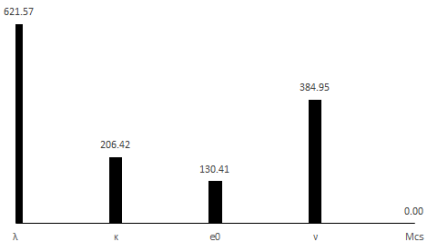

(i) Bilina1 - CSS Undrained triaxial test $E(\varepsilon_a)$

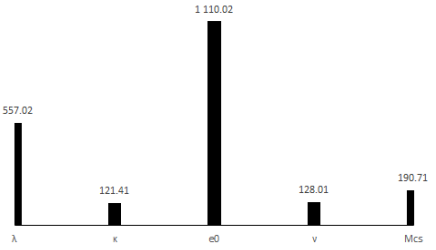

(j) Bilina2 - CSS Undrained triaxial test $E(\varepsilon_a)$

Figure 4.5: Sensitivity analysis: Bilina1, Bilina2

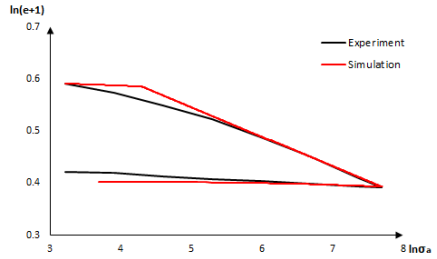

(a) Hajek - Oedometric test

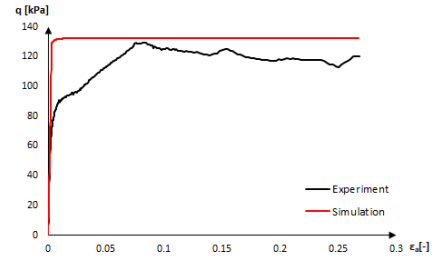

(b) Hajek - Undrained triaxial test

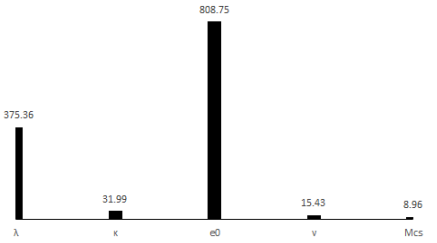

(c) Hajek - CSS Oedometric test

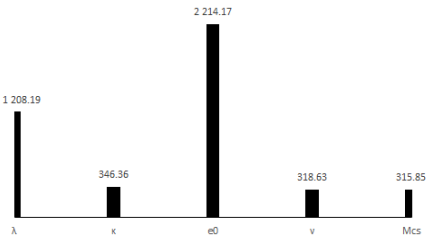

(d) Overall CSS Oedometric test

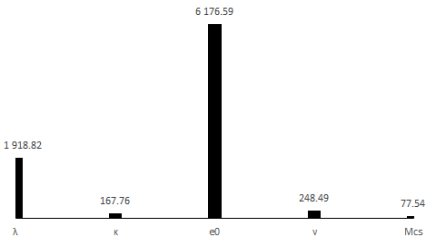

(e) Hajek - CSS Undrained triaxial test $E(q)$

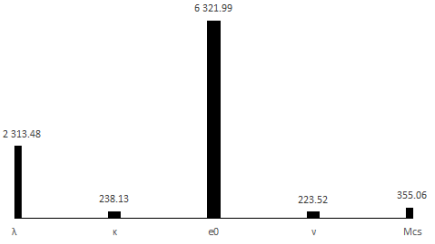

(f) Overall CSS Undrained triaxial test $E(q)$

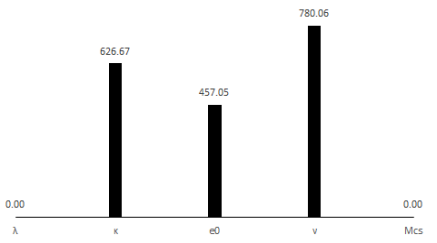

(g) Hajek - Undrained triaxial test $E(\varepsilon_a)$

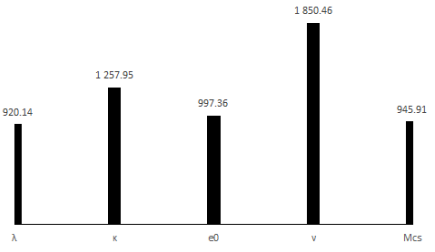

(h) Overall CSS Undrained triaxial test $E(\varepsilon_a)$

Figure 4.6: Sensitivity analysis: Hajek, Overall

4.2.3 Hypoplastic sand model

The sensitivity analysis of the oedometric test reveals the importance of the three comression related parameters h_s, n and e_{i0}, which is in accordance with the calibration procedures suggested in Chapter 2 *Parameteres and calibration procedures*. This trend is observed for all individual oedometric tests CSS_i and futher supproted by the overall CSS, see Fig. 4.9d

The parameter e_{c0} is recommended to be calibrated first either from the $CIUP$ test or oedometric test while considering the position of the initial state of the compression test being on the CSL. The parameters e_{i0} and e_{d0} then can be derived from the empirical relations. Considering the observed sensitivity it might be suggested to calibrate e_{i0} together with the parameters h_s and n by the means of multi-dimensional optimization. The parameters e_{c0} and e_{d0} are derived next using the same empirical relation or if possible to determine e_{c0} from the $CIUP$ test independently. Other parameters seem to have a little influence on the oedometric test and their evaluation from this test is not justifiable.

The highest impact on the triaxial test regarding $E(q)$ has the critical state fricion angle φ_c. This tendancy has been observed in each CSS. The second parameter is e_{c0}. Those two parameters control a location of the critical state. The lower the actual void ratio e is found bellow the corresponding critical state void ratio e_c the more significant is dilatancy and the higher the peak friction angle φ_p is. The critical frication angle φ_c influences a value of the critical state deviatoric stress q. The sensitivity analysis thus provides reasonable and justifiable results. Other parameters do not seem to have an overall unique position. However, it is worth pointing out the influence of the parameter α of the Jablonec specimen's $CSS - E(q)$, where due to the limiting value of the parameter α the results of the sensitivity analisys indicate the minor effect of this parameter.

In the case of CSS - E(ε_a) the results of the senstivity analysis are difficult to clearly evaluate since the overall CSS does not significantly stress out any parameter. The change of any parameter thus can have a similar effect on the simulation regarding $E(\varepsilon_a)$. However, following the calibration procedure from

Chapter 2 *Parameteres and calibration procedures* and assuming the parameters n, h_s, e_{c0}, e_{i0}, e_{d0} and φ_{cs} be alredy known, the parameter β is clearly observed as a leading parameter for the simulation of stiffness degradation of a drained triaxial test. The similar conclusion can be drawn when focusing on the $E(q)$ where the leading role is captured by the parameter α.

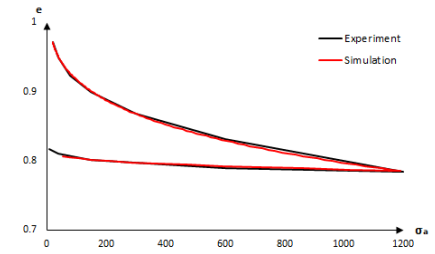

(a) Dobrany - Oedometric test

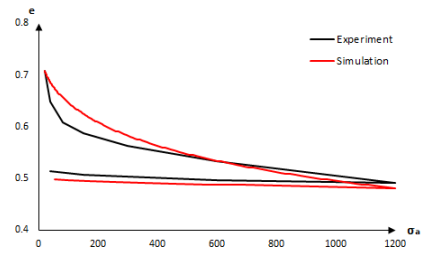

(b) Hrusovany - Oedometric test

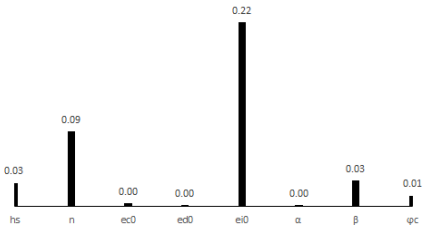

(c) Dobrany - CSS Oedometric test

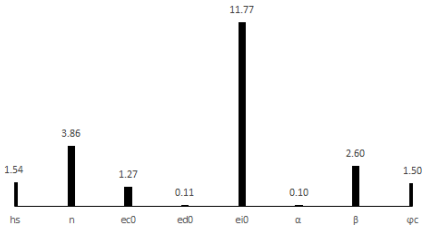

(d) Hrusovany - CSS Oedometric test

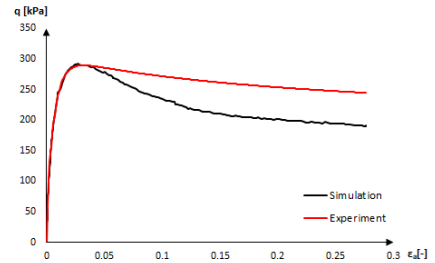

(e) Dobrany - Drained triaxial test

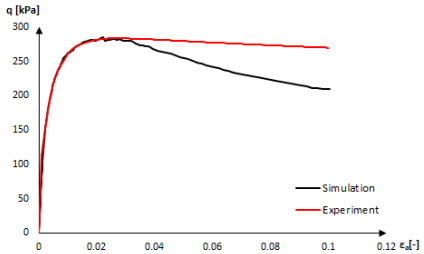

(f) Hrusovany - Drained triaxial test

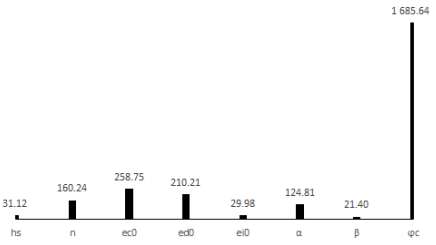

(g) Dobrany - CSS Drained triaxial test $E(q)$

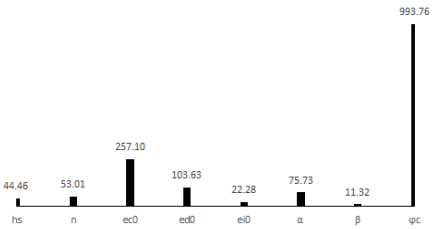

(h) Hrusovany - CSS Drained triaxial test $E(q)$

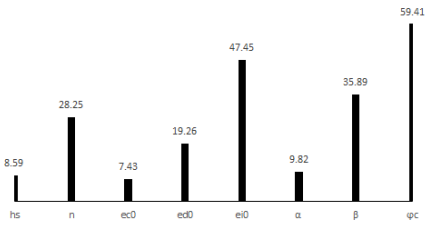

(i) Dobrany - CSS Drained triaxial test $E(\varepsilon_a)$

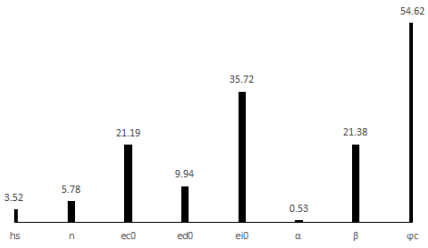

(j) Hrusovany - CSS Drained triaxial test $E(\varepsilon_a)$

Figure 4.7: Sensitivity analysis: Dobrany, Hrusovany

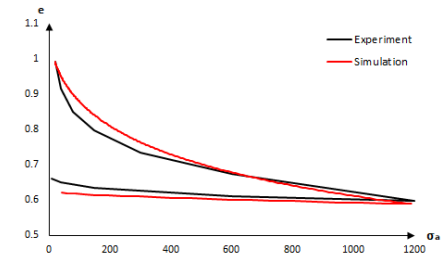

(a) Stvanice - Oedometric test

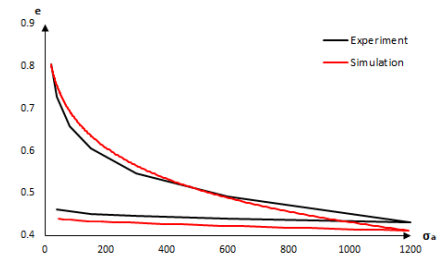

(b) Jablonec - Oedometric test

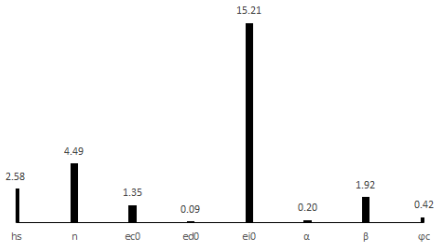

(c) Stvanice - CSS Oedometric test

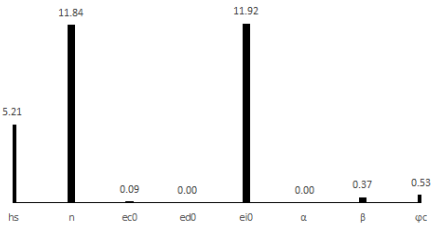

(d) Jablonec - CSS Oedometric test

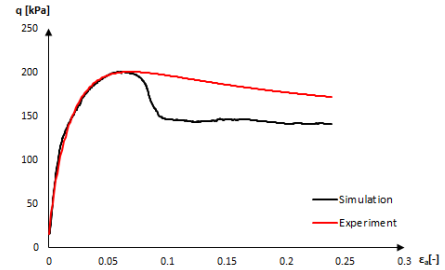

(e) Stvanice - Drained triaxial test

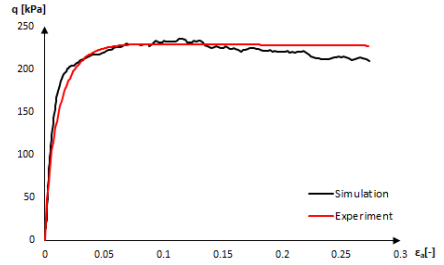

(f) Jablonec - Drained triaxial test

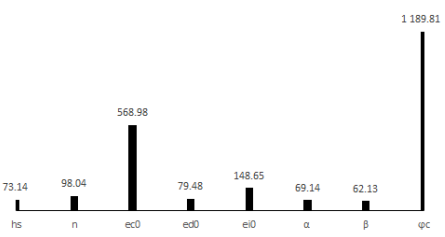

(g) Stvanice - CSS Drained triaxial test $E(\varepsilon_q)$

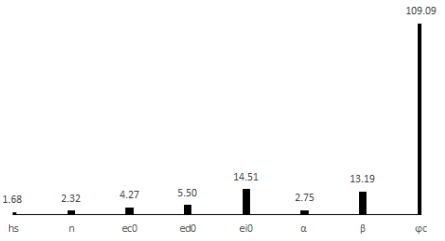

(h) Jablonec - CSS Drained triaxial test $E(\varepsilon_q)$

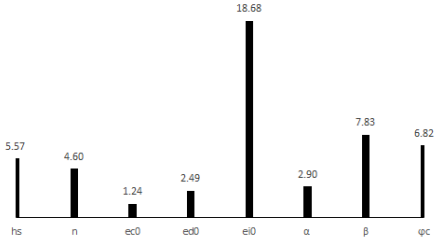

(i) Stvanice - CSS Drained triaxial test $E(\varepsilon_a)$

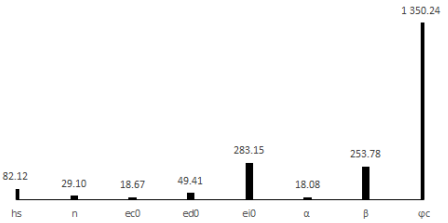

(j) Jablonec - CSS Drained triaxial test $E(\varepsilon_a)$

Figure 4.8: Sensitivity analysis: Stvanice, Jablonec

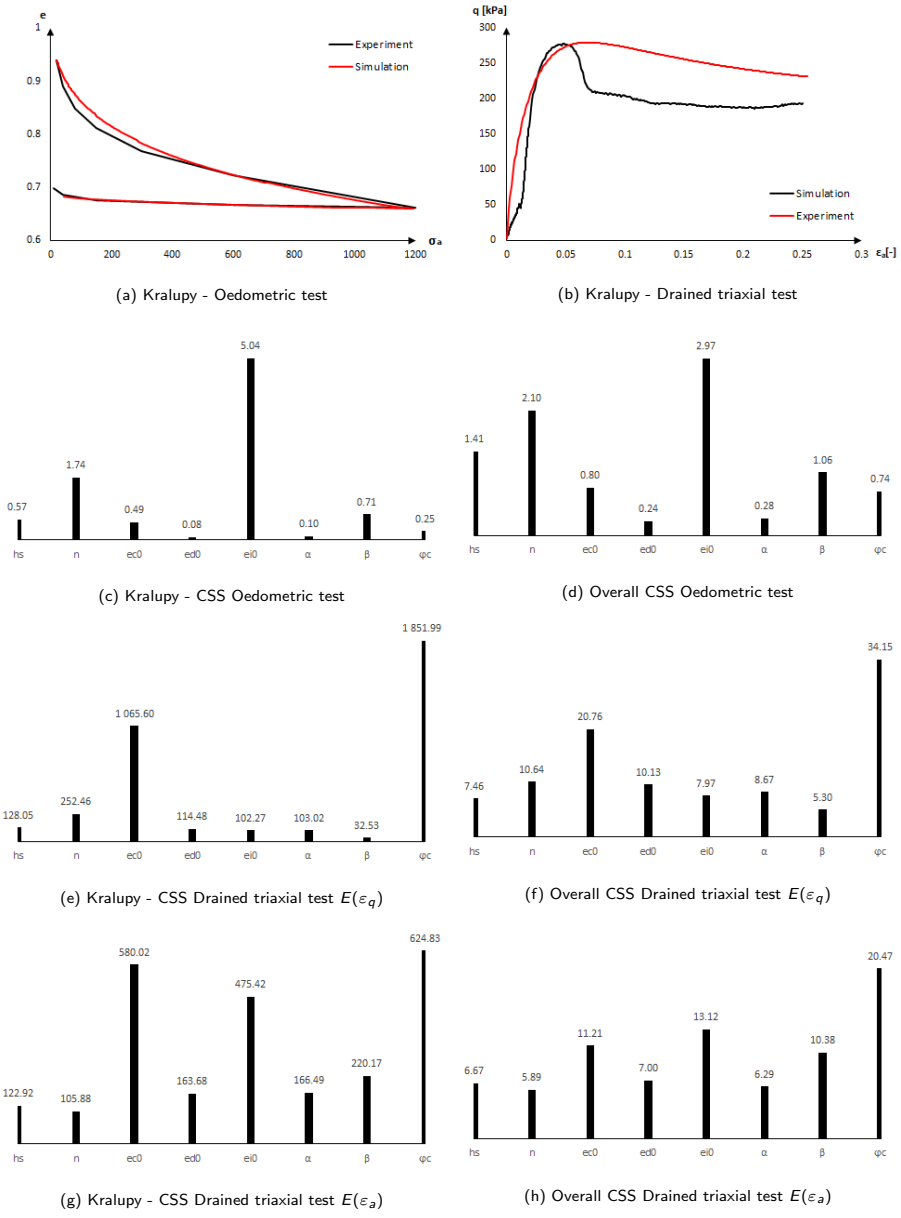

(a) Kralupy - Oedometric test

(b) Kralupy - Drained triaxial test

(c) Kralupy - CSS Oedometric test

(d) Overall CSS Oedometric test

(e) Kralupy - CSS Drained triaxial test $E(\varepsilon_q)$

(f) Overall CSS Drained triaxial test $E(\varepsilon_q)$

(g) Kralupy - CSS Drained triaxial test $E(\varepsilon_a)$

(h) Overall CSS Drained triaxial test $E(\varepsilon_a)$

Figure 4.9: Sensitivity analysis: Kralupy, Overall

Another method how to demonstrate the the effect of parameters is shown in Fig. 4.10a and Fig. 4.10c, which plot the normalised SS for the oedometric and triaxial tests $E(q)$. It can be observed from Fig. 4.10a that even though the parameters λ^* and N have a significant impact on the hypoplastic clay model's behaviour, they influence the model in an opposite way in both triaxial and oedometric test. The same is true in the case of Modified Cam-Clay model for the parameters e_0 and λ, see Fig. 4.10b.

In case of the parameters $\kappa*$ and ν the coupling effect can be seen for both oedometric and triaxial tests, which further ephasise the necessity to calibrate each model on the basis of different test.

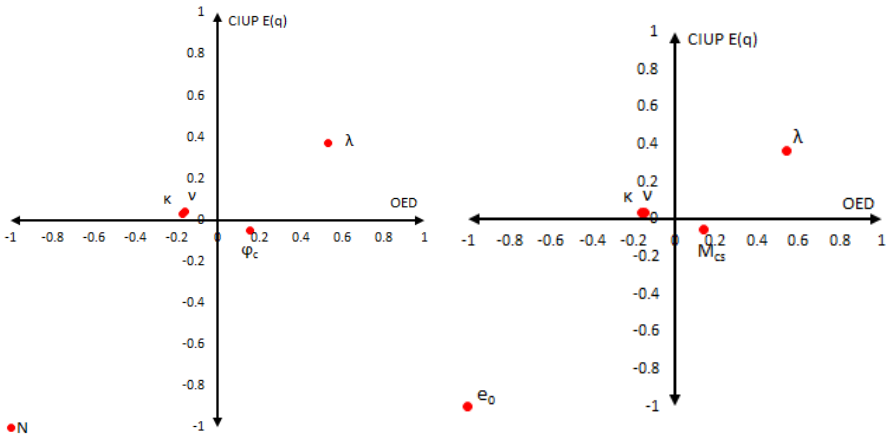

(a) Hypoplastic clay

(b) Modified Cam-Clay

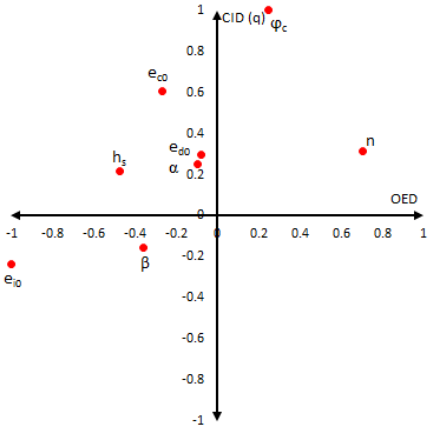

(c) Hypoplastic sand

Figure 4.10: Normalised SS

Normalised SS fot the hypoplastic sand reveals the highest sensitivity to the parameter φ_c in the case of triaxial test and to the parameter e_{i0} in the case of oedometric test. Furthermore, the opposite effect of parameters h_s and e_{i0} to the parameter n in confirmed. The coupling effect and a negligible sensititivity to the parameters e_{d0} and α in the case of oedometric test is shown once again when comparing with Fig. 4.9d.

The sensitivity analysis revealed the effects of the models parameters on the selected laboratory tests. Consequently, it indicates what parameteres should be under close scrutiny and what precision should be applied during the calibration. From the observations, it can be pointed out that the parameters controlling the asymptotic behaviour have a crutial impact on the models' behaviour. This can be observed for both clay models (N, λ^* and e_0, λ), and hypoplastic sand model (φ_c, e_{i0}, h_s,n).

It can be concluded that the parameters N and λ^* of the hypoplastic clay model, which control the position of the NCL and CSL in the $\ln p \times \ln(e+1)$, should be calibrated with the maximal precision and under the constant scrutiny as these parameters have the most significant impact on the model prediction. The calibration of these parameters from the results of the oedometric or isotropic consolidation test is straight forward. Even though the parameter φ_c does not have such an impact as the previous parameters, it is easily obtained from the triaxial shear test in $p \times q$ space given the fact that the critical state is reached during shearing. These free parameters influencing the model asymptotic behaviour. The parameters κ^* and ν influencing the stiffness and consequently the nonlinearity of the model behaviour and their impact is proven as less significant. However, small effect of κ^* can be caused due to chosen reconstituted condition of specimens. Evaluation of these parameters can be obtained by the parametric study of the consolidation test in $\ln p \times \ln(e+1)$ and triaxial shear test in $\varepsilon_a \times q$ space, respectively. It can be also concluded that due to the observed similar sensitivity of both clay models, they can be calibrated with a similar procedure.

The similar conclusion can be drawn for the hypoplastic sand model. The parameters e_{i0}, h_s and n controlling the isotropic NCL gain the highest signif-

icance for the consolidation test. The parameter e_{c0} reveals an importance in triaxial shear test with $E(q)$. The parameters controlling the position of the NCL and CSL should be thus calibrated with the maximal effort and precision. The parameter φ_c shows the highest impact on the triaxial shear test and its values can be obtained from the triaxial shear test as in the case of the hypoplastic clay model. The parameter β controls the shear stiffness and reveals that it has some impact on the oedometric test, consequently the recalibration of the oedomteric test parameters might be necessary after β is calibrated.

4.3 Matlab Beta version

In this section an assessment of the created calibration procedure for the Ex-Calibre software is described. The assessment was performed with help of Doc. Masin's group at Charles University. Bc. Igor Sula in particular was employed in the assessment works for the hypoplastic clay and hypoplastic sand model. Sula used his works and findings for his master degree thesis in [47]. The assessment itself was performed by combining a manual calibration performed by Charles University and automatic calibration procedures for a given laboratory test.

The initial calibration procedures were created and tested in Matlab 2014b since it uses a simple programming language and provides wide range of functional and graphical support for the academic programming and thus enables instant display of required data. In the Matlab version of the calibration software the sufficiency of Newton's optimization method regarding the convergence and shape of the objective functions was also tested. This is well represented in Fig. 4.11 and Fig. 4.12 which depict a converging iteration procedure for the parameter ν of the hypoplastic clay model and parameters h_s and n of the hypoplastic sand model, respectively. In Fig. 4.11 the objective error function is calculated for three experiments of an undrained triaxial test.

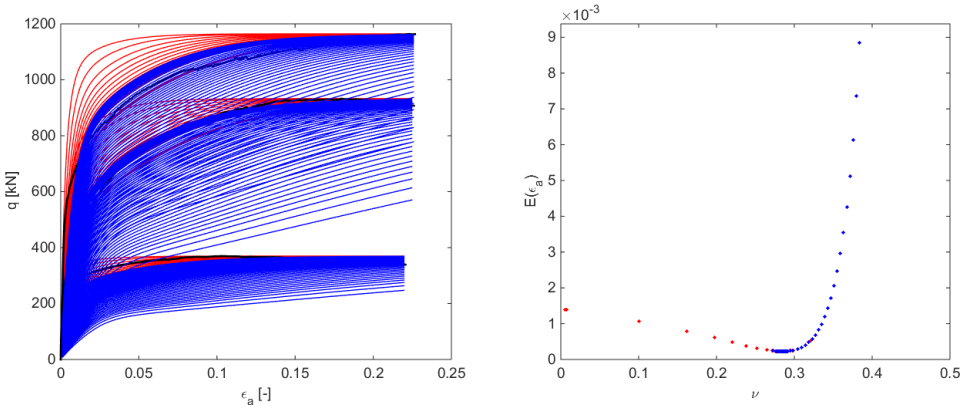

Figure 4.11: Iteration procedure - parameter ν

This figure undoubtedly indicates a smooth shape of the objective function and a distinguishable global minimum. Blue and red colours represents an itera-

tion procedure starting from two different initial values of the parameter ν. The iteration procedure for the parameters h_s and n in Fig. 4.12 does not exhibit the same smooth evolution of the objective function. However, an estimation of the global mininum is established more accurately as the step size of the iteration is decreased.

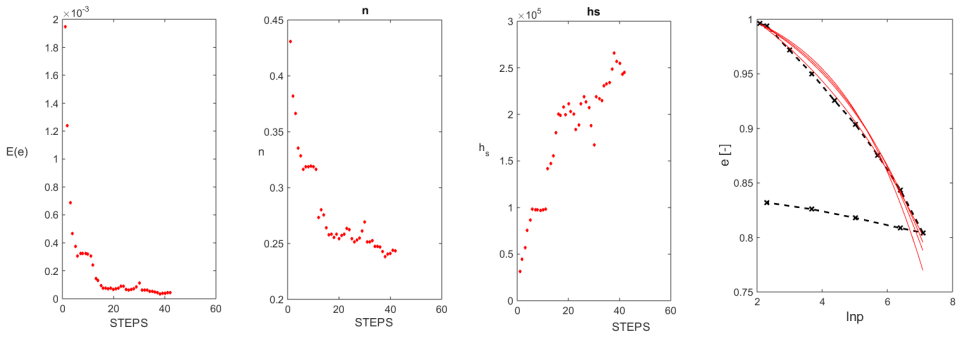

Figure 4.12: Iteration procedure - parameters h_s and n

During the testing phases it was pointed out that since the parameters do not always have a clearly established limiting values, it is reasonable to gradually decrease the itaration step size in order to obtain the most percise recults possible and at the same time to maintain a rapid convergence speed. In addition, the gradient iteration procedures were proven to be sufficient while sequential parameters calibration was applied in the clear hierachical order. This was possible due to a clear physical meaning of the model parameteres and their relevance for certain laboratory tests and importances revealed in the Section 4.2 *Sensitivity analysis*.

The calibration software for the hypoplastic clay and hypoplastic sand model created in Matlab software was compiled into a simple stand alone application that operates within a default folder. In order to simplify the comparative works, the calibration application requires the input data to be preset in the certain predefined *.xlsx format. The calibration results are eventually saved into the Output.xlsx and Output.txt files.

4.3.1 Hypoplastic clay model - Comparative study

In case of the hypoplastic clay, the assessment of the calibration procedures was performed on the laboratory sets from twelve locations. The comparative study was focused on comparing the following results:

- Oedometric test in $\ln p \times \ln(e+1)$ space
- CIUP triaxial test in $\varepsilon_a \times q$ space
- CIUP triaxial test in $p \times q$ space
- CID triaxial test in $\varepsilon_a \times \varepsilon_v$ space
- CID and CIUP triaxial test in $\varepsilon_a \times q$ space

In the thesis [47] in particular depicted and commented the calibration results of the specimens Bilina 1, Prackovice and Ujezd pod Troskami was discussed. For the sake of clarity, examples from the study and thesis [47] are displayied in the Fig. 4.13 for the specimens Bilina1 and Ujezd Pod Troskami. In both cases, the comparison of the oedometric test shows a significant discrepancy between a simulation and experiment at the end of the loading part. This was caused by inappropriate interpretation of the laboratory results. The laboratory results are delivered in engineering strains, which means that the strain are calculated with respect to the original shape of the specimen by

$$\varepsilon_a^{eng} = \frac{L_0 - L}{L_0}. \tag{4.3.1}$$

The engineering strains provides a reasonable estimate in the range of small deformations $\varepsilon < 0.2\%$. However, in the case of the soil laboratory experiments the resulting deformation can reach even more than $\varepsilon > 20\%$. Since the model is defined in the stress and strain rates, the deformation is calculated according to the state at the beginning of each loading increment. All the laboratory experiments, thus, should be transformed from engineering strains ε_a^{eng} to true strains ε_a^{nat} as is implied by

$$\varepsilon_a^{nat} = -\ln\left(\frac{L}{L_0}\right) = -\ln\left(1-\varepsilon_a^{eng}\right) \tag{4.3.2}$$

Unlike the engineering strains, the true strains are calculated with respect to the actual current length as

$$d\varepsilon_a^{nat} = \frac{dl}{L} \tag{4.3.3}$$

and

$$\int_0^{\varepsilon_a^{true}} d\varepsilon_a^{true} = \int_L^l \frac{dl}{L}. \tag{4.3.4}$$

It is worth noting that engineering and true strain are comparable up to the strains $\varepsilon \approx 0.2\%$.

Results of the Bilina1 undrained triaxial test are in a good match. Unlike the oedometric test, the initial void ratio of the triaxial test has to be adjusted according to the critical state so that the the simulation reaches the same deviatoric stress at the failure as the experiment. The initial void ratio of the undrained triaxial test is calibrated with respect to the deviatoric stress reached at the critical state. During the undrained shearing the void ratio remains the same. In the case of a drained test, however, it seems to be more appropriate to establish the initial void ratio with respect to the evolution of volumetric strain as Fig. 4.13d indicates. The study also revealed a significant impact of an extreme value of the parameter $\nu > 0.4$ on the unloading part of a consolidation test and indicates the importance of recalibration of the parameter κ from the consolidation test as it leads to the excessive swelling. This is depicted by Fig. 4.13b.

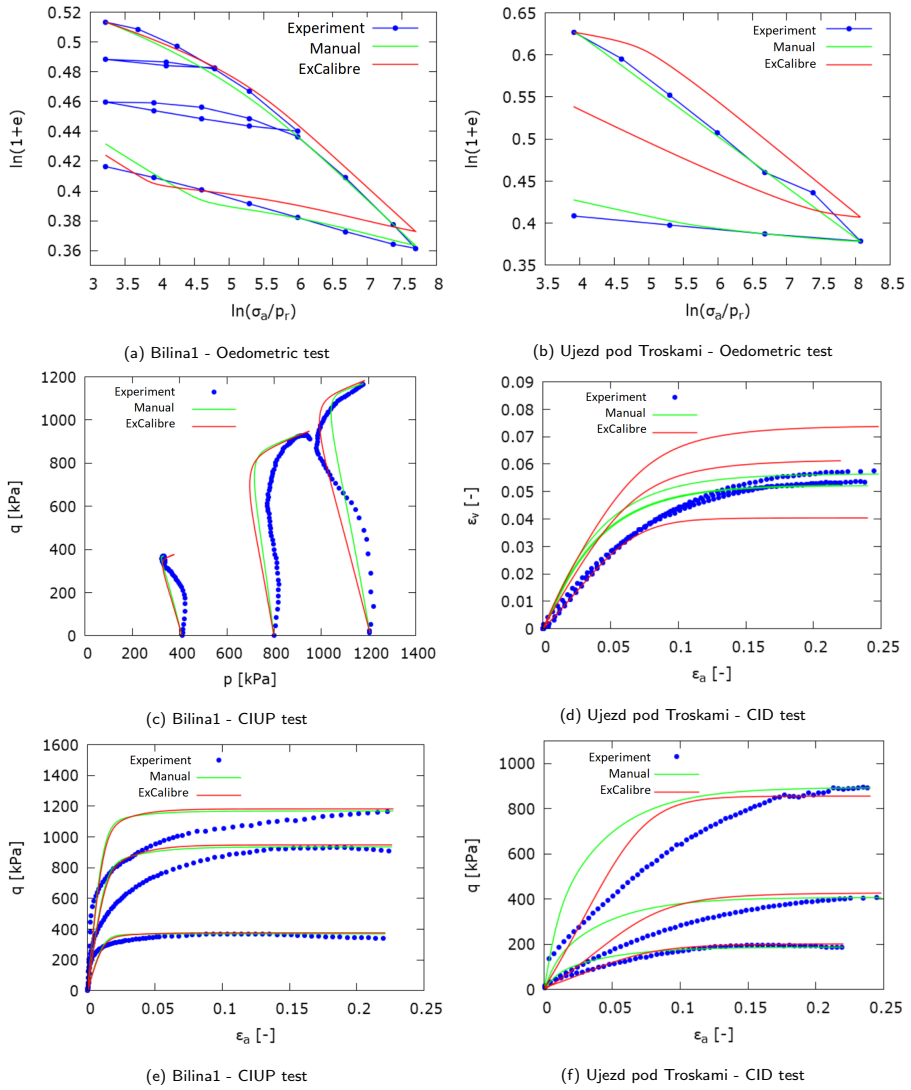

(a) Bilina1 - Oedometric test

(b) Ujezd pod Troskami - Oedometric test

(c) Bilina1 - CIUP test

(d) Ujezd pod Troskami - CID test

(e) Bilina1 - CIUP test

(f) Ujezd pod Troskami - CID test

Figure 4.13: Examples from the comparative study [47]

The assessment also encountered an error connected to the filtering out of an unloading and reloading paths from the experimend data. The calibration was also performed for each consolidation test separatelly and did not account for a differences between reconstituted and undisturbed specimens.

The comments from the comparative study can be summarized in several points:

- Transform engineering strains ε_a^{eng} to true strains ε_a^{true}
- Establish the initial void ratio of a drained triaxial test with respect to the evolution of the volumetric strain ε_v
- Adjust the parameter κ with respect to the new parameter ν
- Filtering out the reloading/unloading paths in the compression test
- Distinguish the reconstitued and undisturbed specimens in the calibration
- Enable a calibration of the model parameters from the multiple compression tests

4.3.2 Hypoplastic sand model - Comparative study

Similarly to the comparative study undertaken for the hypoplastic clay, the comparative study for hypoplastic sand model was performed on six sand soil specimens. Since the calibration procedures are more difficult owing to the higher number of the calibrated parameters the comparative study also found serious drawbacks regarding the calibration of the drained triaxial test. The examples of the comparative study are again taken from [47], more specifically the specimens from the locations Dobrany and Rohatec are presented. The results of the oedometric tests once again indicate the problem pointed out earlier, that is the difference between engineering ε^{eng} and true strains ε^{true}. However, the results of the triaxial test indicate more serious problem. Even though the calibration of the initial void ratio was calibrated from the evolution of the volumetric strain ε_v it has the same impact on the peak friction angle as the parameter α. This issue, together with the calibration performed with the aid of the engineering strains ε^{eng}, predicted an unrealistic behaviour which is documented in Fig. 4.14c and Fig. 4.14d by the excessive value of the peek friction angle φ_p.

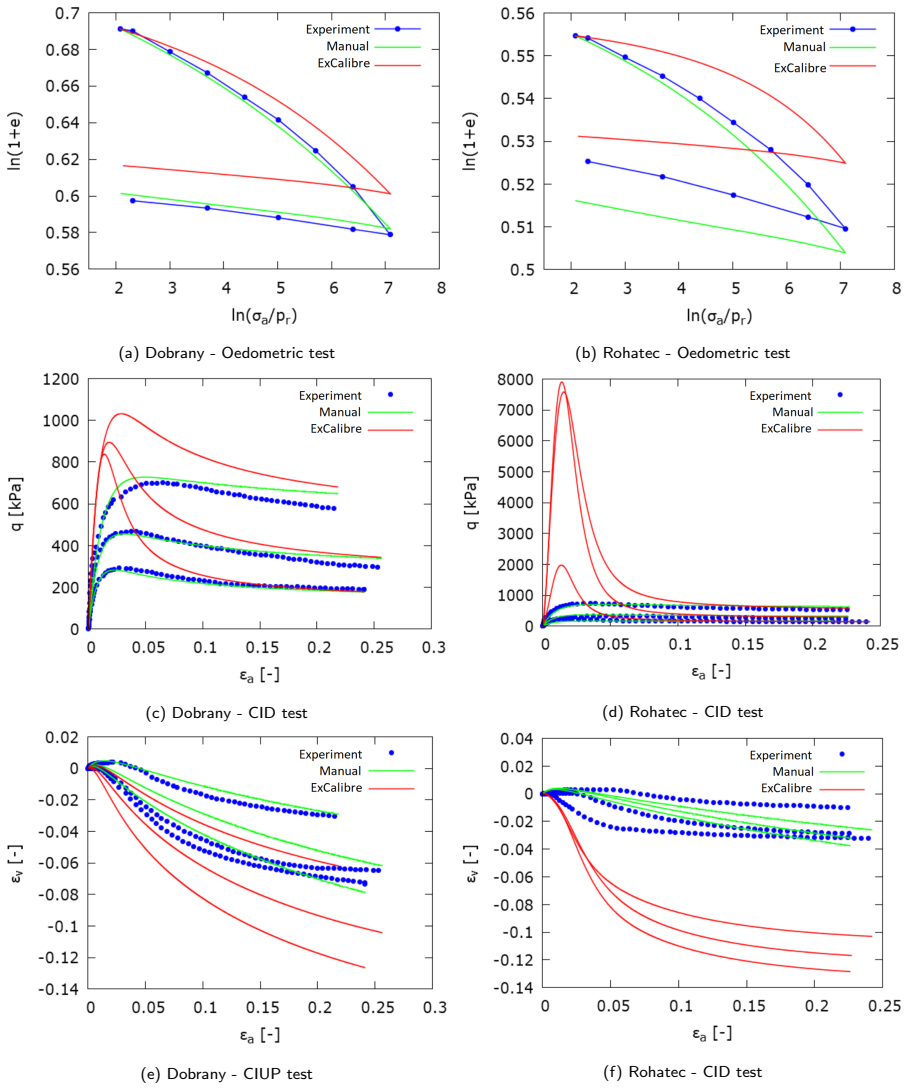

(a) Dobrany - Oedometric test

(b) Rohatec - Oedometric test

(c) Dobrany - CID test

(d) Rohatec - CID test

(e) Dobrany - CIUP test

(f) Rohatec - CID test

Figure 4.14: Examples from the comparative study [47]

All the specimens were of the reconstituted nature and distinguish between the undisturbed and reconstituted specimens was not necessary. However, to consider the specimens condition should be possible.

The comparative study on the hypoplastic sand model suggests to:

- Transfer engineering strains ε_a^{eng} to true strains ε_a^{true}
- Omit calibration of the initial void ratio from the triaxial drained test
- Filter out the reloading/unloading paths in the compression test
- Enable a calibration of the model parameters from the multiple compression tests

The feedback received from the comparative study was put under scrutiny and modifications of the calibration were made. However, the calibration of the initial void ratio of the drained send for the hypoplastic clay model remained calibrated on the basis of the peak friction angle φ_c and not volumetric strain ε_v, since the reached critical state void ratio during the appears only inside the shear band and thus does not represent the whole body of specimen. After the second review of the calibration software the calibration procedures were considered successful and the testing phase was completed. This enabled implementation into the C# language and creating the online calibration software ExCalibre.

4.4 C# version

The online software Excalibre was developed in Microsoft Visual Studio in co-operation with Ing. Tomas Janda, Ph.D and Ing. Stepan Benes. The Excalibre software is currently available at the website:

soilmodels.com/excalibre/

Each member of a team developed a separate libraries focused on a different issues, commonly known a projects. Tomas Janda developed a project called $DRIVER$ storing single element libraries for the hypoplastic clay, hypoplastic sand and Cam-Clay model. A single element software calculate the stress and strain evolution based on the initial and loading conditions. Stepan Benes work was focused on the development of the user interface called WEB. This section is dedicated to the description of the project $CALIBER$ storing methods used for the calibration of the advanced soil models parameters.

The software diagram is depicted in Fig. 4.15 which distinguishes two sections of the software. The blue box represents a simulation section which simulates a laboratory test according to the predefined state and loading conditions. This section directly interacts with $DRIVER$ and plots results in the user interface. The calibration section is represented by a green box. The input data are uploaded into the web application and once the model for a calibration is selected, the data are sent to $CALIBER$. Based on the calibration methods, the $CALIBER$ interacts with $DRIVER$. The progress of the calibration is simultaneously sent to WEB. Once the calibration is finished the results are displayed. These resuls include the values of the calibrated parameters and initial void ratios of the calibrated experiments. Chart plots for both experiment and simulated data are also available. The Excalibre software also provides an option of changing values of parameters or the initial void ratios accordingly and $RECALCULATE$ new results as Fig. fig:excalirbeDiagram indicates.

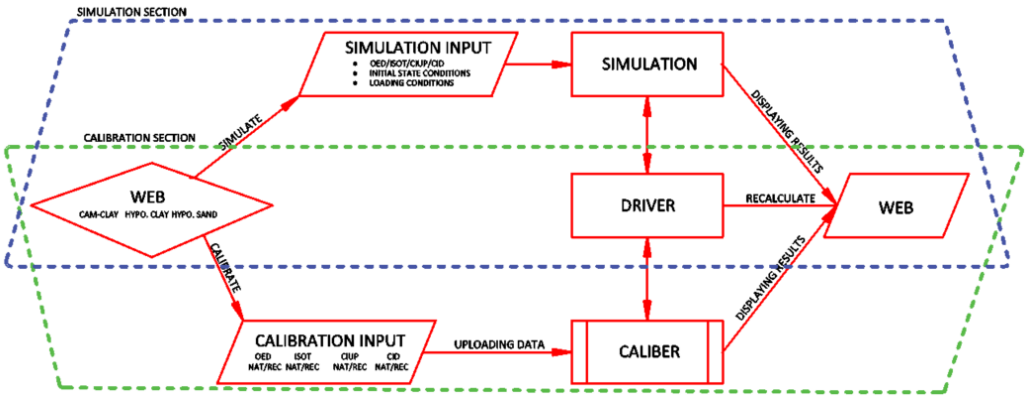

Figure 4.15: Diagram of the Excalibre software

Next sections thoroughly describe the *CALIBRATION INPUT* data, *CALIBER* methods.

4.4.1 Input data

The Excalibre input data are formed by laboratory experiment records ordered in *.xlsx file in the special form predefined for each laboratory experiment specially. The records of each experiment are saved in the separate sheet labeled with a code name characterizing the experiment and the nature of the specimen. The code itself consists of three parts. First part of the code name designates a type of the experiment as follows:

- OED - Oedometric test
- ISOT - Isotropic compression test
- CIUP - Undrained triaxial test with meassuring pore pressure
- CID - Drained Triaxial test

The nature of the specimen is further specified by a suffiex $-NAT$ or $-REC$ which are abbreviations of *natural* (undisturbed) or *reconstituted* (disturbed) specimen, respectively. Furthermore, each sheet is numbered with respect to the related experiment and its order in the sequence. The complete code

name of the sheet representing single oedometric experiment conducted on the natural undisturbed specimen and occurring as the first in the sequence of these tests reads as $OED - NAT - 1$. Similarly, the code name $CIUP - REC - 2$ thus represents an undrained triaxial test performed on the reconstituted specimen and it is second in the sequence of such experiment. An unlimited number or experiments and their combinations can be uploaded. The software will select each record for a separate calibration. However, it is worth noting that higher the number of uploaded experiments is, the higher the computational cost is. Each laboratory experiment data requires not only an initial void ratio to establish an initial state but also data records:

- OED
  - axial stress σ_a
  - axial strain ε_a
- CID
  - axial strain ε_a
  - volumetric strain ε_v
  - mean stress p
  - deviatoric stress q
- ISOT
  - mean stress p
  - volumetric strain ε_v
- CIUP
  - axial stress σ_a
  - mean stress p
  - deviatoric stress q

Appart from the experiment results, the data file also includes sheets with code names *IDX AND GRAD* and *NOTES*. The sheet *IDX AND GRAD* includes index characeristic:

- USCS classification
- Liquid limit W_L
- Plastic limit W_P
- Specific gravity G_s
- Angle of repose $\varphi_r ep$ (if provided)
- Records of the gradation test

Sheet *NOTES* consist of a general informations that can be helpful for the calibration or classification. Templates of the input data of gathered specimens are available to download from the website of the ExCalibre software and the corresponding calibrated parameters are also displayed.

4.4.2 Project Caliber

The methods of *CALIBER* PROJECT are divided into several separate source codes and classes with respect to their purpose. The source codes relevant to the calibration procedures are:

- SortData.cs
- Compression.cs
- Triaxial.cs
- Caliber.cs

Once the input data is uploaded, *WEB* creates an instance of the class *CaliberInput* which is filled with the list of uploaded laboratory tests, their records and conditions. Once the calibration is complete, *CALIBER* creates an instance of the class *CaliberOutput* and sent results to *WEB*. Hereinafter, a content of the mentioned source codes will be briefly discussed. More attention will be dedicated to the classes including calibration methods themselves.

4.4.3 Source code SortData.cs

This code includes several methods which deal with the experiment and simulated data and prepare the calibration return output, see Fig. 4.4.3.

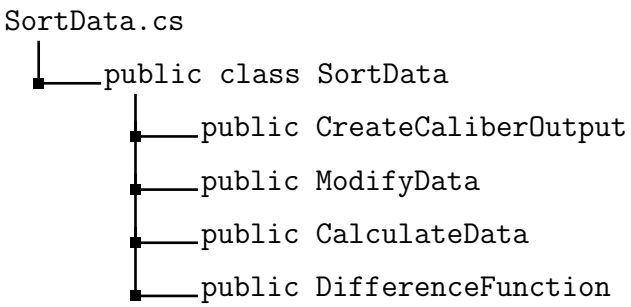

Fig.4.4.3: SortData.cs content

CreateCaliberOutput

Input: CaliberInput caliberInput

Output: CaliberOutput caliberOutput

This method receive a class *CaliberInput* data which stores the experiments recorded data ordered in IDictionary type values and creates an instance of the class *CaliberOutput*. Both these classes are defined out of the *Caliber* source files. The method *CreateCaliberOutput* employs variables of the IDictionary type. IDictionary is type that uses a *string* key word to store certain data and thus enables an easy search mechanism. The class *CaliberOutput* includes these data:

- IDictionary OedDriverInputs
- IDictionary CiupDriverInputs
- IDictionary CidDriverInputs
- IDictionary IsotDriverInputs
- IDictionary OedMeasuredData
- IDictionary CiupMeasuredData
- IDictionary CidMeasuredData
- IDictionary IsotMeasuredData
- IDictionary OedComputedData
- IDictionary CiupComputedData
- IDictionary CidCompuredData
- IDictionary IsotComputedData
- IDictionary CalibreMessages

IDictionaries with suffix *DriverInputs* includes data of the class *DrivedInputs*, which are crucial for a successful lunch of *DRIVER*, namely initial void ratio and stress state, loading conditions, type of experiment (OED, CIUP, CID, ISOT) and the parameters of selected constitutive model. As the name indicates, the suffix *MeassuredData* includes an experimentally measured data and *ComputedData* represents simulated data provided by *DRIVER*. The key word used in IDictionary matches with the name of the spreadsheet related to the given experiment, e.g. CIUP-NAT-2, OED-REC-1, etc.

ModifyData

Input: double PhiC
CaliberInput caliberInput

Output: IDictionary cidData
IDictionary ciupData
IDictionary compressionLoading
IDictionary compressionUnloading
CaliberOutput caliberOutput

The method *ModifyData* takes a care of a transforms the experimentally measured engineering strains ε^{eng} to true strains ε^{true}, excluding unloading/reloading parts of the compression test except for the last unloading step. This method loads the *MeasuredData* and *DriverInputs* in the *CalibreOutput*. It is common for all three constitutive models. Furthermore, the method creates data sets necessary for the calibration such as the $\ln p \times \ln(e+1)$ diagram for the hypoplastic clay model, $\ln p \times e$ diagram for the Cam-Clay model and $p \times e$ diagram for the hypoplastic sand model in case of the compression tests. These data are divided into the loading and unloading parts as some parameters are calibrated solely on the loading and some on the unloading parts. In addition, the pore pressure u calculated. The triaxial test data sets are created separately for drained and undrained conditions.

The method *CalculateData* is used at the end of the calibration to simulate a given experiment with respect to its initial conditions and saves the data

into ComputedData in the CaliberOutput.

DifferenceFunction

Input: double[,] experimentData
double[,] driverData

Output: double difference

The last method in Sortdata.cs is the $DifferenceFunction$. This method is used in the optmizing methods to calculate the objective error function by Eq. (4.1.2) with weight $w_i = 1$ on 100 points uniformly distributed along a given experiment data, see Section 4.1 for more details. The intermediate points are interpolated between two closest data points.

4.4.4 Source code Compression.cs

The source code is divided into two classes separated according to the constitutive model. The class *Clay* is composed of methods focusing on the hypoplastic clay and Cam-Clay model. There are six methods, three focused on a direct calculation of parameters λ^*, κ^*, N and subsequently their optimization, see Fig. 4.4.4. The calculation methods use Eqns. (2.0.20)–(2.0.24), see Section 2.0.2 for more details. The class Sand is similarly assembled and employes Eqns.(2.0.6)–(2.0.13) from Section 2.0.1. All optimization methods employ the Newton's optimization method.

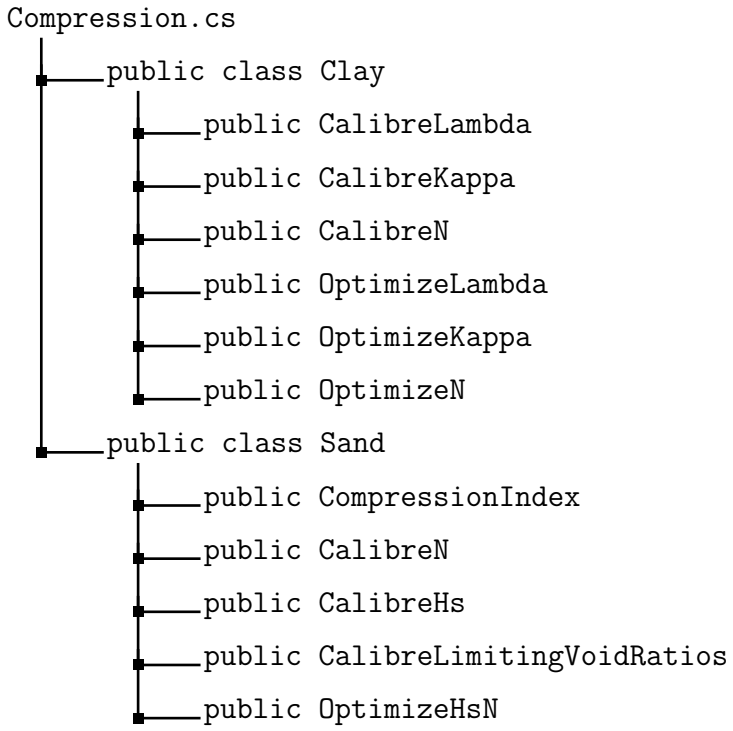

Fig.4.4.4 Compression.cs diagram

4.4.4.1 class Clay

CalibreLambda

Input: IDictionary compressionLoading

Output: double lambda

The parameter λ^* for the hypoplastic clay or λ for Cam-Clay model is calculated

from the tangent at the end of the loading step corresponding to a 1/100th of the applied mean stress p or axial loading stress σ_a. Parameter is calculated from Eq. (2.0.20).

CalibreKappa

Input: IDictionary compressionUnloading
double lambda

Output: double kappa

The parameter κ^* for the hypoplastic clay or κ for Cam-Clay model is calculated from the tangent at the beginning of the unloading step corresponding to a 1/100th of the applied mean stress p or the axial loading stress σ_a. The value of the parameter κ^* of κ is limited to the 1/5th of the parameter λ^* respective λ. It is provided by Eq. (2.0.21).

CalibreN

Input: IDictionary compressionLoading
double lambda

Output: double N

The parameter N is calculated with the aid of the parameter λ^* or λ as Eq. (2.0.24) or Eq. (2.0.22) implies.

OptimizeLambda

Input: IDictionary compressionLoading
CaliberOutput caliberOutput
ModelParams parameters

Output: double lambda

This method does not use the method *DifferenceFunction* from *SortData.cs* but rather calculates an objective function as a squared difference of tangents between the experimental and simulated data at the last loading step. The current tangent value is calculated from the last 1/100th of the applied loading stress, see Fig. 4.16.

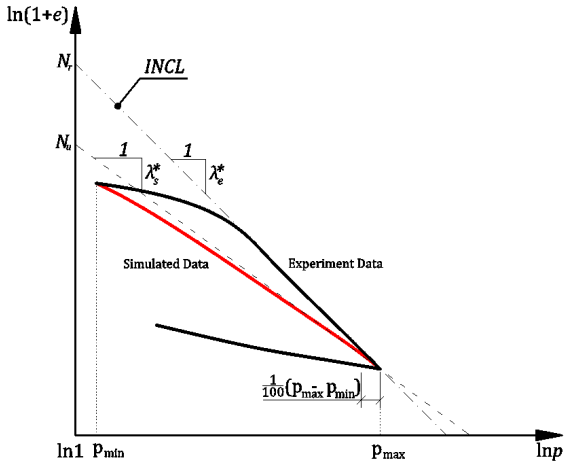

Figure 4.16: Optimization of the parameter λ^*

The tangents designated λ_s^* and λ_e^* stand for the simulated and experiment tangnents. The objective of the optimiation is to equilize the parameters, i.e. λ_s^* $= \lambda_e^*$.

OptimizeKappa

Input: IDictionary compression Loading
IDictionary compressionUnloading
CaliberOutput caliberOutput
ModelParams parameters

Output: double kappa

Since the parameter κ^* affects unloading as well as reloading part of the compression experiment, the objective function of the κ^* optimization uses $DifferenceFunction$ for both loading and unloading part of the compression test while a weight of the function w is distributed between the loading and unloading part as follows:

$$w_{load} = \frac{L_{load}}{L_{unload}}, \tag{4.4.1}$$

where

$$L = \sum_{i=1}^{n} \sqrt{(p_{i+1} - p_i)^2 + (e_{i+1} - e_i)^2}. \tag{4.4.2}$$

L represents the lenght of the compression diagram in $\ln p \times \ln(e+1)$ space for the loading (L_{load}) and unloading (L_{unload}) part of the diagram. Since the unloading part is often ommited, the objective function calculated from the loading part is multipied by the weight w_{load}, see Eq. (4.4.1). The weight of the unloading part is set $w_{unload} = 1$ in the case when unloading is available or $w_{unload} = 0$ in the case when unloading part is not available.

OptimizeN

Input: IDictionary compressionLoading
CaliberOutput caliberOutput
ModelParams parameters

Output: double N

This method uses the objetive function as the squared difference in $\ln(e + 1)$ for the hypoplastic model or difference in e for the Cam-Clay model between experimental and simulated data at maximal loading stress.

4.4.4.2 class Sand

The class *Sand* employs five method. Four are focused on a direct calculation of the hypoplastic sand parameters h_s and n and the compression index C_c accoring to the Eqns. (2.0.6)–(2.0.13). The method *OptimizeHsN* employs Newton's optimization method for the parameters h_s and n. When using Eq. (2.0.10) the initial limiting void ratios e_{i0}, e_{c0} and e_{d0} are backward calculated knowing the values h_s and n and at the same time considering that the initial void ratio of the compression test e_{init} is located on the CSL.

CompressionIndex

Input: IDictionary compressionLoading

Output: double[] Cc

The compression index is calculated according to Eqns. (2.0.6)–(2.0.9) for three points of the compression curve. The output of this method is a vector of three C_c values.

CalibreHs

Input: IDictionary compressionLoading
ModelParams parameters
double[] Cc

Output: double *hs*

The parameter h_s is calculated according to Eq. (2.0.11) with the aid of the compression index C_c corresponding to the center of the compression curve.

CalibreN

Input: IDictionary compressionLoading
ModelParams parameters
double[] Cc

Output: double *n*

The parameter n is calculated according to the Eqns. (2.0.12)–(2.0.13) from the parameter h_s and two values of C_c corresponding to the extemes of the compression curve.

CalibreLimitingVoidRatios

Input: IDictionary compressionLoading
ModelParams parameters
double[] eTemp

Output: ModelParams parameters
double[] eTemp

The limiting void ratios are calculated according to Eqns. (2.0.15)–(2.0.17). In the case that more compression experiments are presented, the vector eTemp

represents the initial state (void ration e_{init} and mean stress p) of the experiment which initial state occurs on CSL and relates to the maximal value of e_{c0} through Eq. (1.2.41). This comes from the assumption that in the case of the loose sand the parameter e_{c0} can be estimated as $e_{c0} = e_{max}$ and since the specimens of different densities can be presented, the specimen in the loosest state, e.g. has the highest initial void ratio e_{init}, is considered at the critical state and thus occuring on the CSL. Since the parameter e_{c0} is related to the mean stress $p =$ 0 kPa, e_{c0} is calculated with the aid of e_{temp} and Eq. (1.2.41).

For the void ratio of the maximal density $e_{d0} = 0.5 \times e_{c0}$ is given a condition that any initial void ratio cannot occur beneath limiting void ratio curve e_d with the safety 1.05 as

$$e_{d0} = \frac{e_d}{1.05 \exp\left[-\left(\frac{3p}{h_s}\right)^n\right]}. \tag{4.4.3}$$

The parameter e_{i0} is calculated according to Eq. (1.2.39).

OptimizeHsN

Input: IDictionary compressionLoading
ModelParams parameters
CaliberOutput caliberOutput
double[] eTemp

Output: ModelParams parameters
double[] eTemp

This method employs the Newton optimization method for two variables simultaneously since both marameters h_s and n define the shape of the same compression curve. For each combination of h_s and n the method CalibreLimitingVoidRatios is called. It recalibrates the parameters e_{i0}, e_{c0} and e_{d0} while the CSL goes through the state defined by e_{temp}. The output of the method are thus not only the updated parameters h_s and n but also the vector $eTemp$ and limiting void ratios.

4.4.5 Source code Triaxial.cs

Similarly to the code sourse *Compression.cs* the *Triaxial.cs* is also divided into two separate classes according to the constitutive model. The class *Clay* is dedicated to hypoplastic clay and Cam-Clay models and calibrates the parameter ν and the initital void ratios while the separate methods are created for the experiments *CID* and *CIUP*.

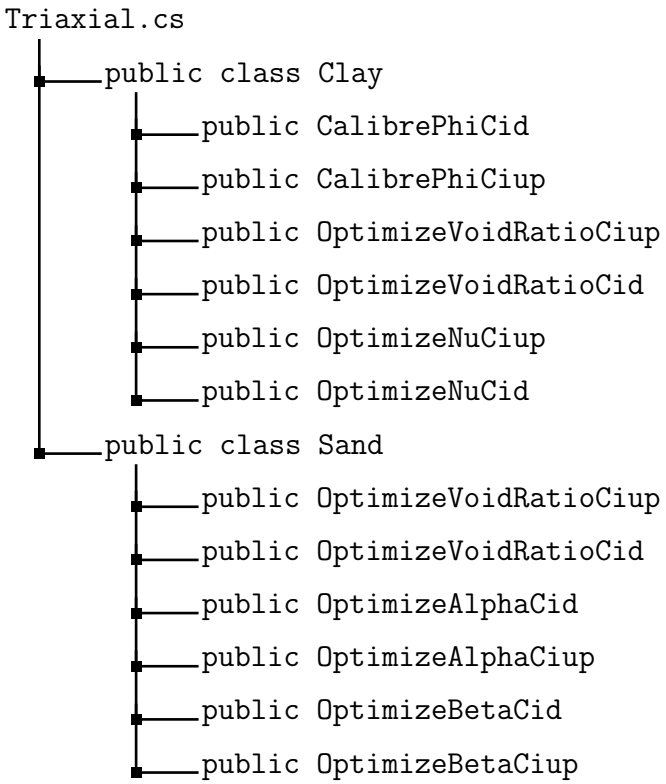

Fig. 4.4.5 Triaxial.cs diagram

4.4.5.1 class Clay

CalibrePhiCiup and **CalibrePhiCid**

Input: CaliberInput caliberInput
ModelParams parameters

Output: double Phi

These methods calculate the critical state friction angle φ_c according to Eqns. (2.0.1)–(2.0.5).

OptimizeVoidRatioCiup

Input: CaliberOutput caliberOutput
ModelParams parameters
IDictionary ciupData

Output: CaliberOutput caliberOutput

In the case of hypoplastic clay model, the method is optimizing the initial void ratio e_{init} according to the maximal reached deviatoric stress q with the aid of Newton's optimization method. If the Cam-Clay model is calibrated, the initial void ratio e_{init} is calculated by

$$e_{init} = e_0 + \kappa(\ln p_c - \ln p) - \lambda \ln p. \tag{4.4.4}$$

OptimizeVoidRatioCid

Input: CaliberOutput caliberOutput
ModelParams parameters
IDictionary cidData

Output: CaliberOutput caliberOutput

In the case of hypoplastic clay model, the method is optimizing the initial void ratio e_{init} according to the maximal deviatoric stress q if the peak friction angle φ_p is higher than the critical state friction angle φ_{cv}. if not, the objective error function is calculated by $DifferenceFunction$ on the entire experiment in the $\varepsilon_a \times q$ space. The critical state is considered to be reached at the end of the experiment. In the case of Cam-Clay model, the initial void ratio e_{init} is calculated from

$$p_c = \left(\frac{-q^2}{M^2} - p^2\right)\frac{1}{p} \tag{4.4.5}$$

and (4.4.6)

$$e_{init} = e_0 + \kappa(\ln p_c - \ln p) - \lambda \ln p. \tag{4.4.7}$$

The initial void ratio is thus optimized to reached the approximated value of the maximal deviatoric stress q and not the evolution of the volumetric strains.

OptimizeNnuCiup and **OptimizeNnuCid**

Input: CaliberOutput caliberOutput
ModelParams parameters
IDictionary ciupData

Output: double ν

Since ν is a stiffness controlling parameter, the objective error function is calculated on a difference of ε_a in the $\varepsilon_a \times q$ space. The difference function is calculated from the part of the diagram reaching $0.9 \times q_{max}$ (maximal deviatoric stress) in the case of hypoplastic clay model and $0.5 \times q_{max}$ in the case of Cam-Clay model.

4.4.5.2 class Sand

The class *Sand* is similarly dedicated to the parameters of the hypoplastic sand model α and β and initial void ratios, the methods are again divided according to the experiments CID and $CIUP$, see Fig. 4.4.5.

OptimizeVoidRatioCiup

Input: CaliberOutput caliberOutput
ModelParams parameters
IDictionary ciupData

Output: CaliberOutput caliberOutput

This method is optimizing the initial void ratio e_{init} according to the maximal deviatoric stress q at the end of the experiment. During the optimization, the method always checks whether e_{init} falls within the limiting void ratio curves e_i and e_d.

OptimizeVoidRatioCid

Input: CaliberOutput caliberOutput
ModelParams parameters
IDictionary ciupData

Output: CaliberOutput caliberOutput

This method is optimizing the initial void ratio e_{init} according to the maximal

deviatoric stress q if the peak friction angle φ_p is higher than the critical state friction angle φ_c. if not, the objective error function is calculated by DifferenceFunction on the entire experiment in the $\varepsilon_a \times q$ space. The critical state is said to be reached at the end of the experiment. Similarly to the OptimizeVoidRatioCiup the method again controls whether e_{init} falls within the limits of e_i and e_d.

OptimizeAlphaCid

Input: CaliberOutput caliberOutput
ModelParams parameters
IDictionary ciupData

Output: double α

Calibration of the parameter α is executed according to the value of the peak friction angle φ_p represented by the hardening/softening peak in the $\varepsilon_a \times q$ space. The objective error function is calculated as the difference between the peak of the simulation and the peak of the experiment data. If any peak is not observed the objective error function is calculated by *DifferenceFunction* while the whole diagram of $\varepsilon_a \times q$ is taken into the consideration.

OptimizeAlphaCiup

Input: CaliberOutput caliberOutput
ModelParams parameters
IDictionary ciupData

Output: double α

The parameter α controls the peak friction angle φ_p for the drained triaxial experiment. In the case of undrained triaxial experiments the degree of the overconsolidation can be characterized by the mobilized friction angle φ_{mob} and its counter part η in the meridian space $p \times q$. The parameter α is optimized by the minimizing of the objective error function of between the maximal simulated and measured η.

OptimizeBetaCid and **OptimizeBetaCiup**

Input: CaliberOutput caliberOutput
ModelParams parameters
IDictionary ciupData

Output: double β

As a stiffness governing parameter, β is calibrated from the $\varepsilon_a \times q$ space, while the objective error function is calculated from the part of the diagram reaching $0.9 \times q_{max}$.

4.4.6 Source code Caliber.cs

Caliber.cs is the main calibration code where all the calibration methods are linked together to calibrate each induvidual constitutive model. The file includes several public and several private classes and methods. The *public classes* and methods are accessible from other codes without restrictions, the *private classes*, however, include an auxiliary methods that are not ment to be accessed from the outside methods and serve only for the purposes of the calibration. The following structure depicts classes and methods included in Caliber.cs:

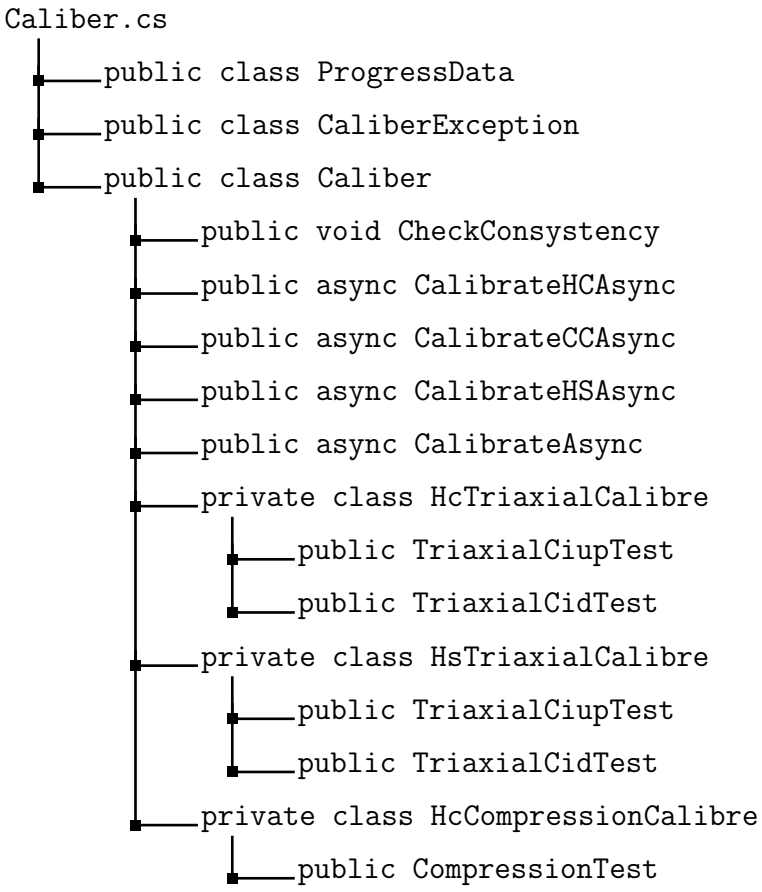

Fig.4.4.5 Caliber.cs diagram

public class ProgressData

This class contains method public ProgressData which returns progress of the calibration. This comes in favour in a particularly difficult and long lasting calibrations since *async* methods enables to return an intermediate calculation.

public class CaliberException

Contains public CaliberException method, which returns an information about stage and result of the calibration.

public class Caliber

This class includes three main calibration related methods, namely *CalibrateHCAsync*, *CalibrateCCAsync* and *CalibrateHSAsync*. They are asynchronic calibration procedures for the hypoplastic clay, Cam-Clay and hypoplastic sand model. These methods are consisting of various methods from *SortData.cs*, *Compression.cs* and *Triaxial.cs* placed in a specific sequance in order to provide the best possible calibration outcome.

The classes *HcTriaxialCalibre* and *HsTriaxialCalibre* are private classes relating to the hypoplastic clay and hypoplastic sand models, respectively. These classes include methods *TriaxialCiupTest* and *TriaxialCidTest*, which represent subprocedures of the superordinate method that are called from.

CalibrateHCAsync, *CalibrateCCAsync* and *CalibrateHSAsync* will be now discussed in detail as they represent the core of the calibration software.

4.4.7 CalibrateHCAsync/CalibrateCCAsync methods

This method consists of various methods placed in a specific order to create an effective and realiable calibration software for the hypoplastic clay model. The method is asynchronic and thus enables to continuously return the results of intermediate calculations. The process of the calibration is characterized by Fig. 4.4.6. So called flowcarts are a conveniet way of descripting such processes. The following symbols of the flowcharts are used:

The round boxes symbolizes the initial and final stage of the calibration procedure.

The simple box symbolizes a symple process consisting of a single method.

The complex box symbolizes a process consisnting of several mothods and possibly loops.

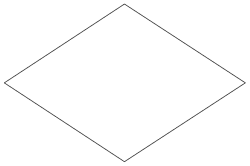

The rhombus symbolizes a point in the procedure where the decision YES/NO is made.

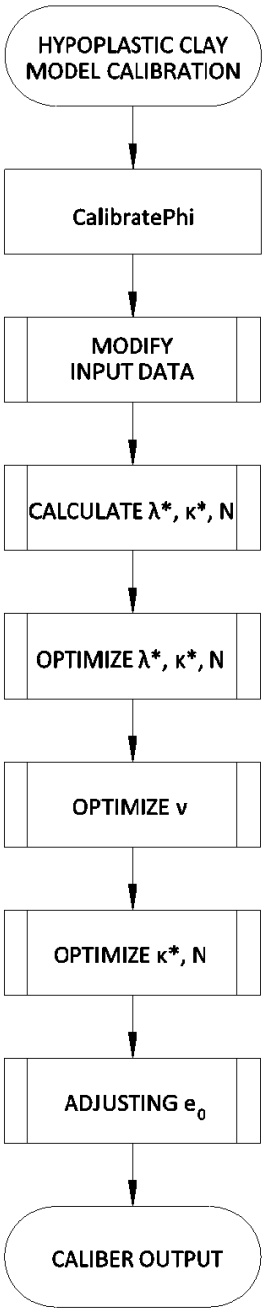

Fig.4.4.6 CalibrateHCAsync's diagram

Each individual step will be now discussed and more complex processes will be drawn out with the aid of the flowcharts symbols and methodology taken from literature.

Calibrate φ_c

At this point, the φ_c is calibrated by the method *CalibrePhiCiup* or *CalibrePhiCid* from the triaxial tests data with the aid of Eqns. (2.0.1)–(2.0.5). It is important to calibrate φ_c first as it is used lately in calculation of the radial stresses σ_r with the aid of the Jaky's formula.

Modify input data

This stage initiates a calibration output with the *CreateCalibrationOutput* method, which is at the end of calibration handed over to WEB. The modification of the data by the method *ModifyData* accounts for the transformation of engineering strain ε^{eng} to the true strain ε^{true}, filtering out unloading/reloading cycles, additional quantities such as void ratio e and pore pressure u, etc.

Calculate λ^*,κ^*, N

The initial values the parameters λ^*, κ^* and N of the hypoplastic clay or λ and κ and e_0 of the Cam-Clay model are calculated by the methods *CalibreLambda*, *CalibreKappa* and *CalibreN*. The graphical representation of this process is depicted in Fig. 4.17. This process distinguishes the *reconstituted* and *natural* specimens. The parameter λ^* is thus preferably calculated from the reconstituted specimens while κ^* and N are calculated from the natural undisturbed specimens. In the case that both *reconstituted* and *natural* specimens are available, it is esential to distinguish between the N_{rec} and N_{nat} as they might significantly differ due to difference in structure between these two specimens' states. The values of these parameters serve as initial estimates for the iterative procedures.

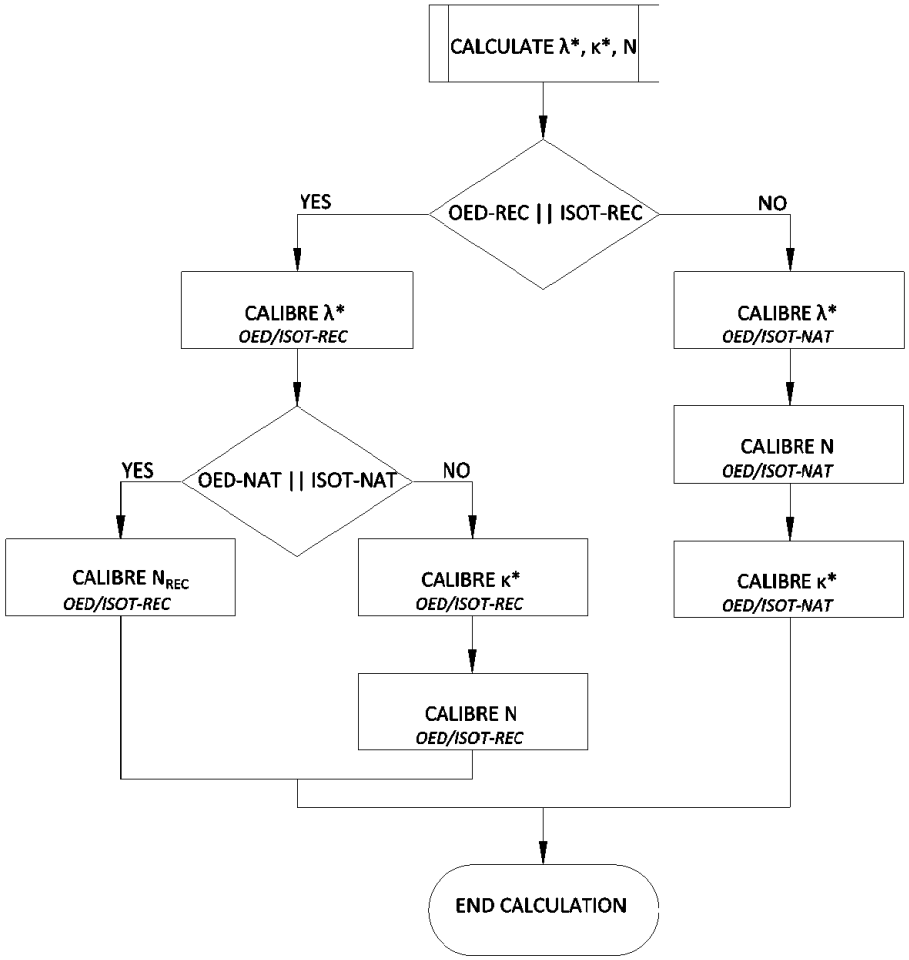

Figure 4.17: Flowchart of the initial λ^*, κ^* and N evaluation

Optimize λ^*,κ^*, N

Once the initial estimates are obtained, the optimization can be executed by methods *OptimizeLambda*, *OptimizeKappa*, *OptimizeN*. The process once again takes into account specimens condition, i.e. *reconstituted* or *natural*. If only the *reconstituted* specimens are available, the optimization of the parameters κ^* and N is executed, while λ^* is assumed to be well established by the calculation. This assumption has been confirmed by an observation of the calibration results. Similar process is employed for the *natural* specimens where one more condition is adopted. If there are *reconstituted* specimens the related N_{rec} has

to be calibrated, while λ^* is once again considered to be well established from the previous calculation process. If no *reconstitued* specimens are available the optimization of the parameter λ is executed since the direct calculation of λ^* performed on the *natural* specimens is usually not sufficient.

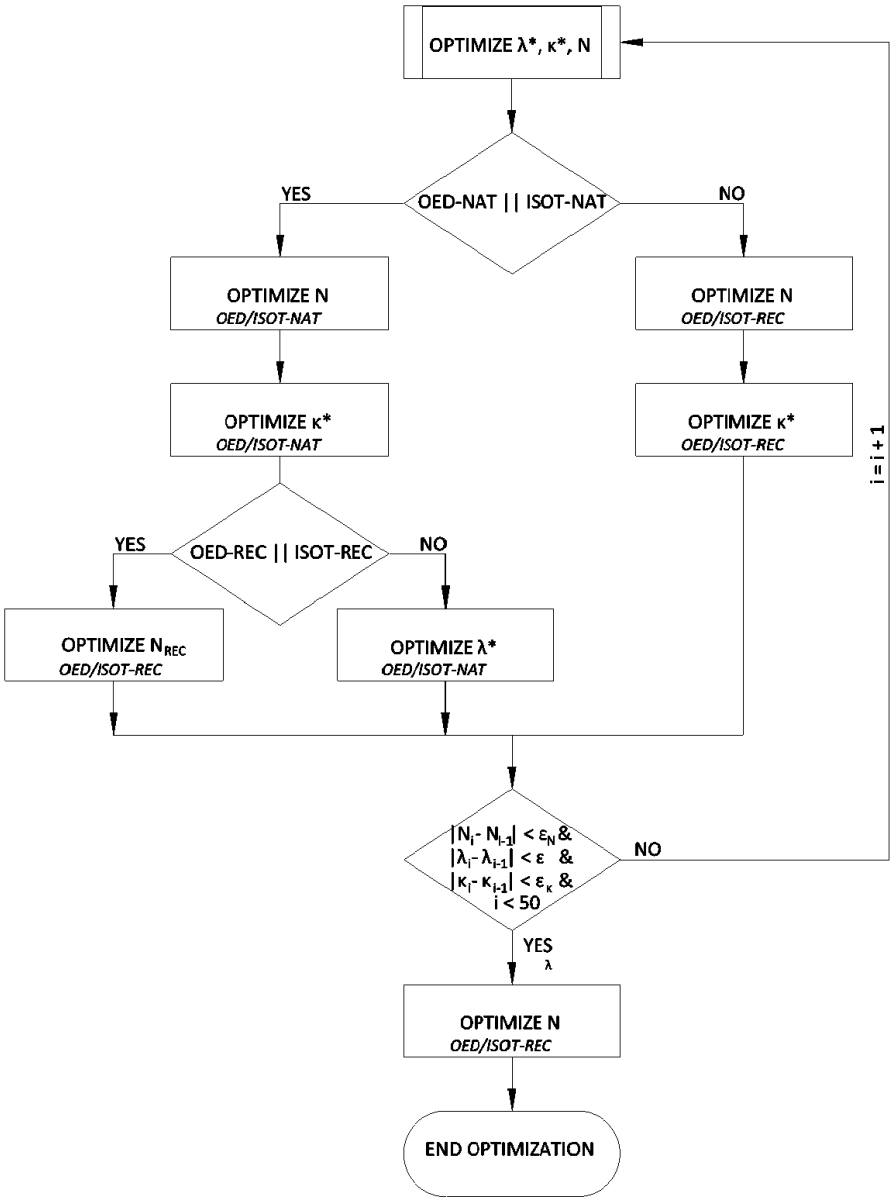

Figure 4.18: Flowchart of λ^*,κ^* and N optimization process

The optimization of each parameter is performed in the close succession while a small number of iterations in the individual methods for each parameter are chosen in order to obtain a smooth optimization process. This is promoted by the fact that each parameter has its own physical meaning. The whole iterative process undergoes in the loop, which is terminated by two conditions. Either the optimization has found the minimal extreme of the objective function E or the maximal number of iterations in the loop has been reach. Even though the maximal number of iterations is set to 50, the optimization was usually terminated due tu the minimal value of E with respect to the selected error ε_i within 10 iterations. Once the conditions are met, the iteration is terminated. The optimization of the parameter N is then carried out one more time since it has the highest impact on the model's prediction. This was well observed in the Section 4.2 *Sensitivity analysis*.

Optimize ν

Since parameter ν controls the relation of the bulk modulus K_i at the isotropic state and shear modulus G_i under undrained conditions, the optimization prefers undrained triaxial experiments to drained ones. Prior to the optimization of ν performed by the method *OptimizeNuCiup* or *OptimizeNuCid* it is necessary to find a proper initial void ratio e_{init}. The appropriate e_{init} that correlates with an deviatoric stress at the critical state in the case of undrained conditions is optimized by the method *OptimizeVoidRaioCiup*, while the *OptimizeVoidRaio-Cid* method is used to find e_{init} corresponding to the maximal deviatoric stress, see Fig. 4.19. Once the parameter e_{init} is adjusted, the optimization of ν is performed.

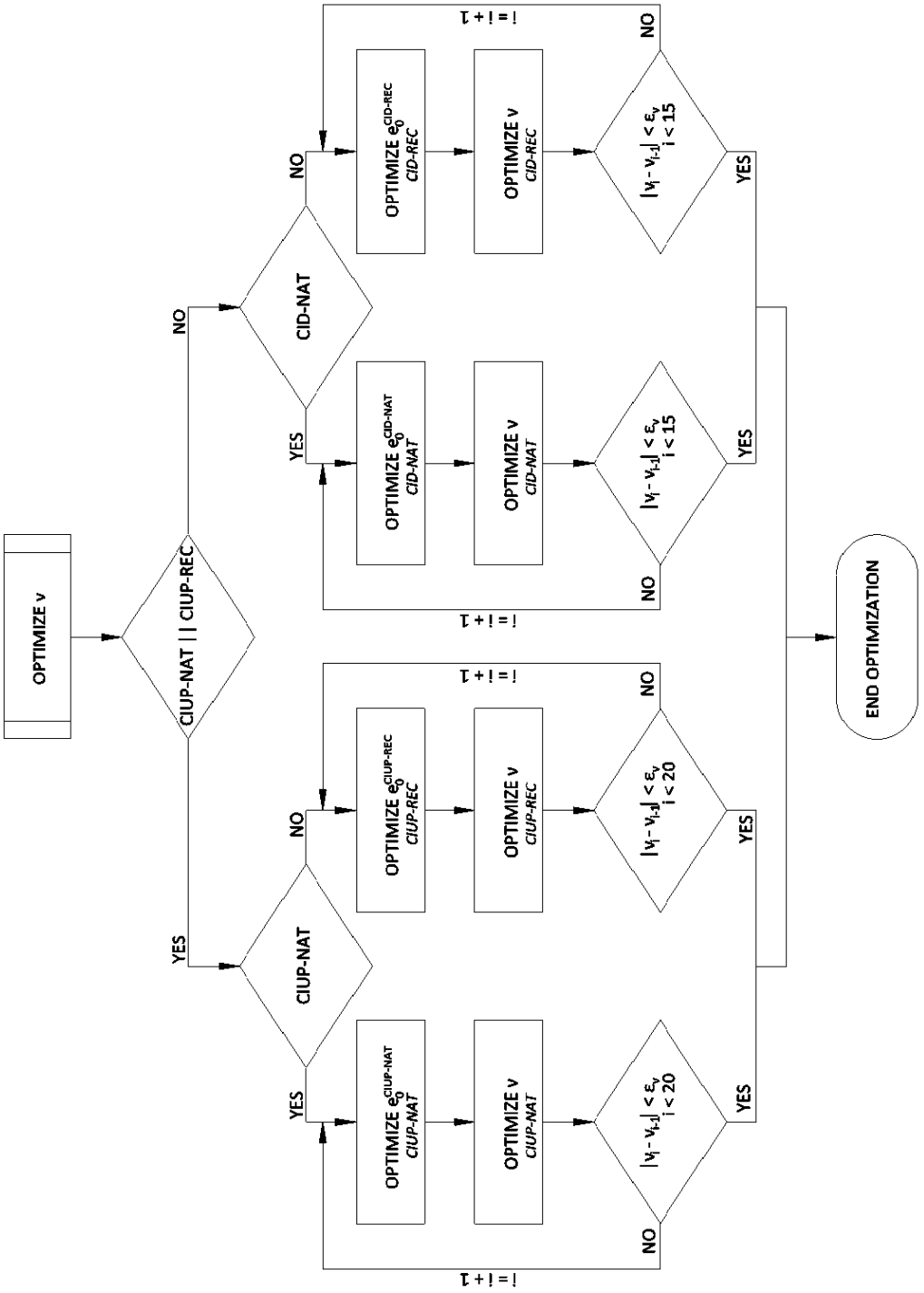

Figure 4.19: Flowchart of ν optimization

The process of two optimizations is placed in an outer loop, which are terminated by two conditions defined by the maximum iteration steps or by a minimum error. Since ν is a stiffness related parameter the calibration preferes to adopt *natural* undisturbed specimens as it better represents the structure of the soil. The same assumption is used for drained triaxial tests.

Optimize κ^*, N

As it was pointed out in the verification of the calibration methods in the Section 4.3.1, the parameter ν can at its higher values significantly influence the compression test, more espreciselly the swelling line. Thus an adaptation of the compression test is performed, see Fig. 4.20.

The process is structured in the same way as the *Optimize* λ^*, κ^*, N process. The parameter κ^* controlling the swelling line is optimized first using preferably the *natural* specimen. In the case when both natural and undisturbed specimens are available a modification of N_{rec} might be necessary and thus its optimization is performed.

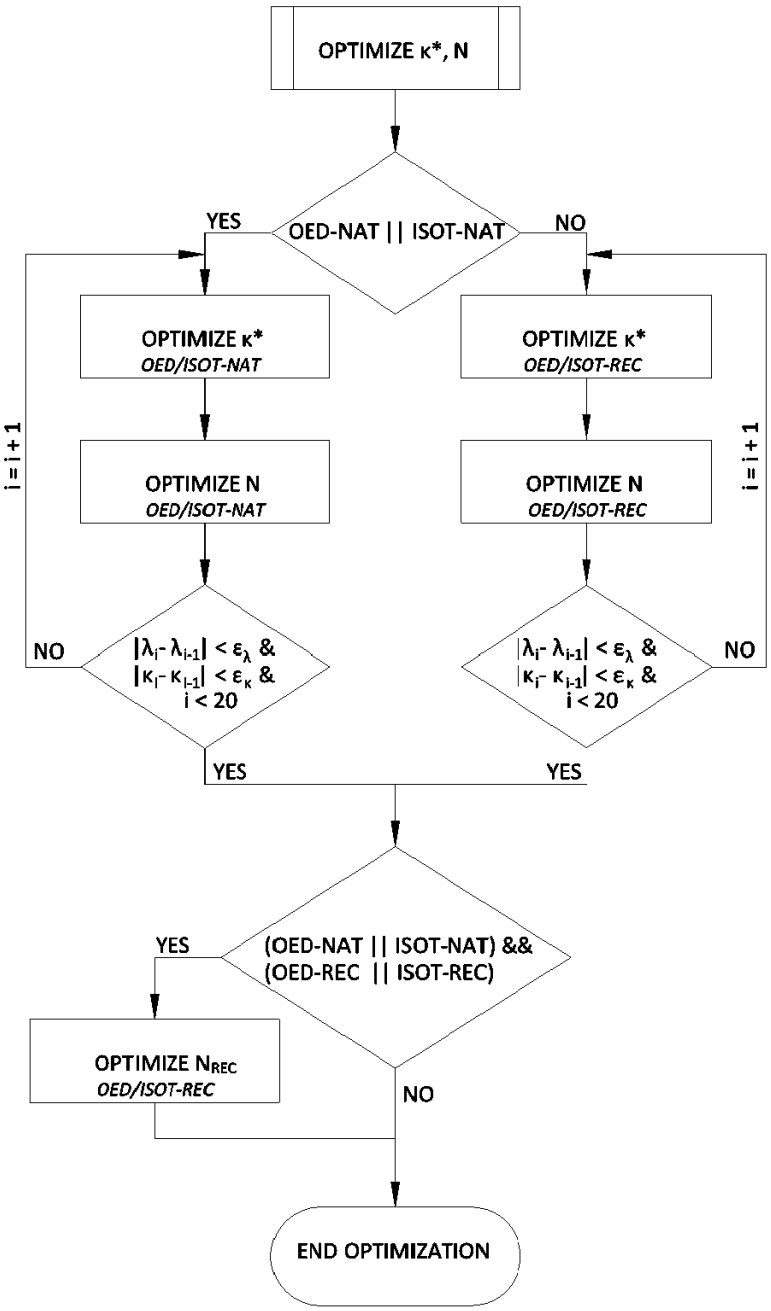

Figure 4.20: Diagram of the CalibrateHCAsync method

Adjusting e_{init}

The last optimization in the calibration procedure is concerned with the initial void ratios, see Fig. 4.4.6. This process goes though each available experiment and optimize its initial void ratio e_{init} and subsequently saves this void ratio into the output file. Providing that the parameter N_{rec} was calibrated, the initial void ratios of *reconstituted* compression samples are calculated so that the equality $N_{rec} = N$ is fulfilled. Subsequently, all the void ratios at each loading steps are adjusted.

Caliber output With the adjustment of e_{init}, the calibration is finished and thefofore, the last remaining step is to calculate a simulation of all the available tests according to their initial states and calibrated parameters and eventually save those data into the output file.

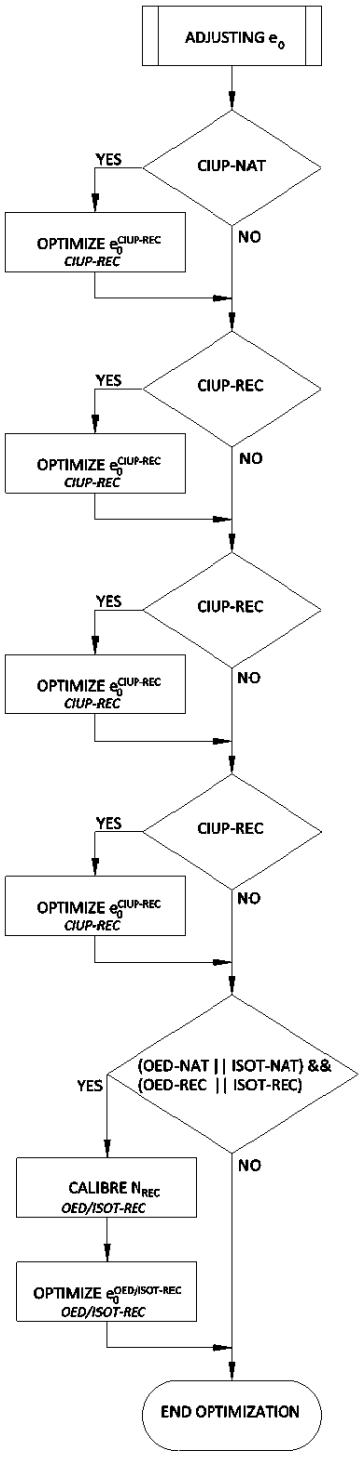

Fig.4.4.6 Diagram of the CalibrateHCAsync method

4.4.8 CalibrateHSAsync method

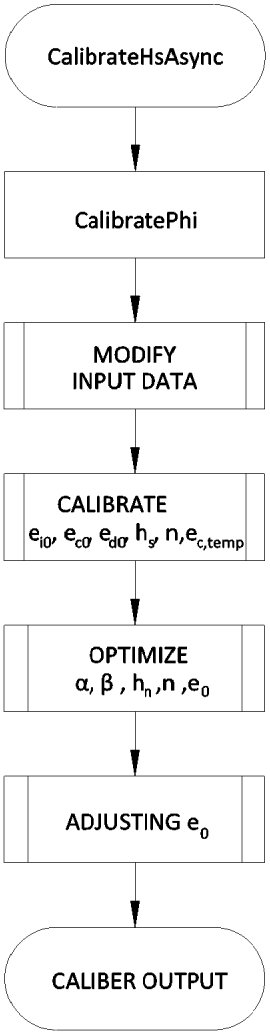

Fig.4.4.6 CalibrateHSAsync's diagram

Similarly to the *CalibrateHCAsync* this method is also asynchronic and starts with a calculation of the critical state friciton angle φ_c and modification of the uploaded data. Considering the performed sensitivitiy analysis, the hypoplastic sand model does not have that distinct impact of the parameters as hypoplastic clay model, therefore, the optimization of the compression driving parameters has to be performed even on the level of triaxial experiments. First, compression line controling parameters h_s, n, e_{i0}, e_{c0} and e_{d0} are optimized. The *OptimizeHsN* method uses more iteration steps on this level in order to get a good fit of the compression curve. In the next step parameters α and β are optimized with simultaneous optimization of the compression parameters with smaller number of steps and step sizes in order to provide smooth iteration process.

At the end of the optimization, adjustment of the initial void ratios is performed to fit the uploaded data. At last simulations to fill *caliberOutput SimulatedData* IDictionaries are carried out.

Calibrate e_{i0}, e_{c0} e_{d0}, h_s, n The calibration of the compression curve parameteres start with the evaluation of compression indexes C_c by *CompressionIndex* method which are need for further direct calculation of the parameters h_c and n by *calibreHs* and *calibreN* methods. Once these parameters are obtained the initial limiting void ratios e_{i0}, e_{c0} and e_{d0} are calcualted and the variable e_{temp} is related to compression experiment that provides the highest parameter e_{c0} by the *CalibreInitialVoidRatios* methods.
In the next step, the *OptimizeHsN* method using Newton's method for two variables h_s and n is used. A new set of the parameters e_{i0}, e_{c0} and e_{d0} is calculated for each combination of h_s and n. Unlike in the case of the hypoplastic clay model, this procedure makes no differences between the *reconstituted* and *natural* specimens as it is assumed that all the compression curves are driven in $p \times e$ by the same parameters h_s and n regardless of their initial void ratio.

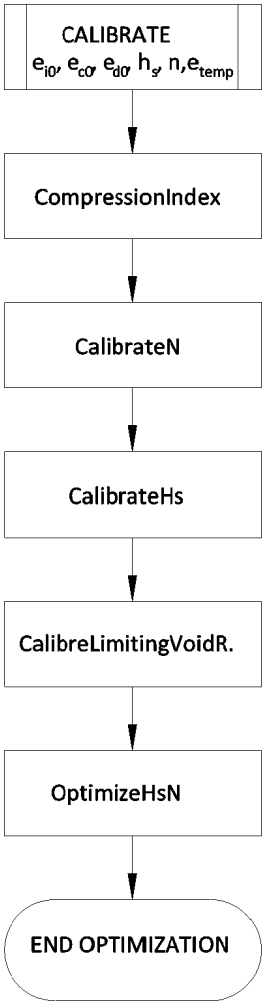

Fig.4.4.6 Flowchart of e_{i0}, e_{c0}, e_{d0}, h_s and n optimization

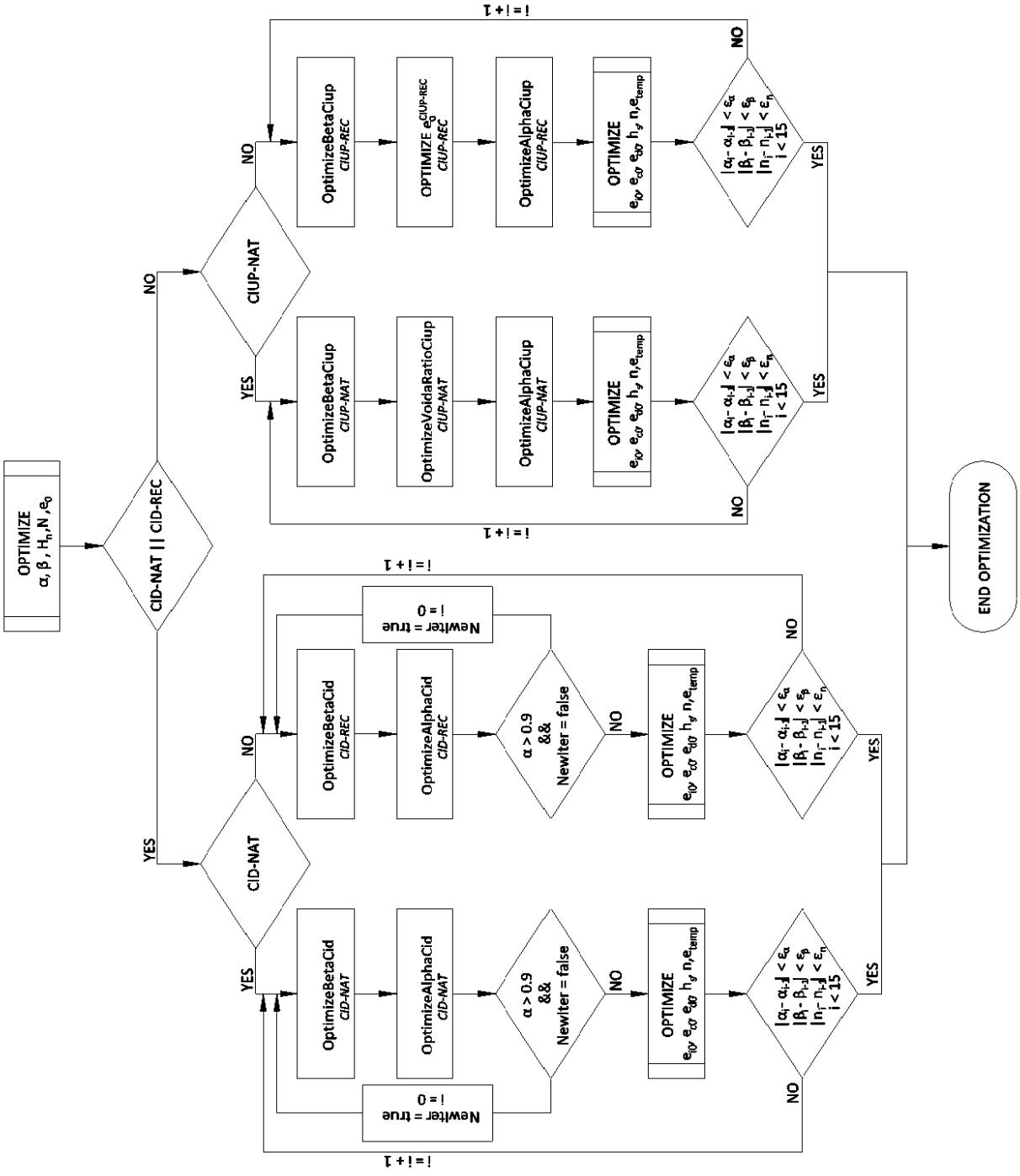

Fig.4.4.6 Flowchart of α and β optimization

Optimize α, β, e_{i0}, e_{c0} e_{d0}, h_s, n

This process resebles the process of *Optimize* ν of the *CalibrateHSAsync* method, however, the aditional parameter α controling the peak friction angle φ_c brings some more difficulties. Since the parameteres are originally defined for the drained condition, the drained triaxial experimets are preferred to undrained. If available, the *natural* specimens are preferred since they better represent conditions of the undisturbed soil mass.

The first parameter to calibrate is the stiffness governing parameter β. This aligns peeks states in $\varepsilon_a \times q$ of both simulation and experiment data. Then the parameter α can be calibrated. Since the parameter α has the similar impact on the model prediction as the initial void ratio of the specimen e_{init}, the calibration of the initial void ratio is here omitted. Keeping in mind that the parameters of the hypoplastic sand model do not have as distinguishable effect on the model prediction as the hypoplastic clay model the adjustment of the compression parameters e_{i0}, e_{c0} e_{d0}, h_s and n is executed. The outer loop is canceled once the terminating conditions are met.

There have been cases, when it was not possible to reach an overconsolidation states indicated by the experiment data even when $\alpha = 0.9$. This can be caused either by the inefficient maximal loading stress during a compression experiment or by the high density of the compression specimen which initial void ratio e_{init} was used to derive parameters e_{i0}, e_{c0} and e_{d0}. In such a case, the new iteration is started, while the void ratios at the end of the drained triaxial tests are taken into acount as they should be close to the CSL, although that it is not precise estimation since the void ratio at the critical state occurs only in the shear band itself but not in the rest of the specimen. The value of the variable e_{temp} from the compression test thus might be interchanged for the final value of the void ratio of the drained triaxial test.

In the case of the undrained triaxial test, the parameter β is optimized first similarly to the drained case. However, the optimization of the initial void ratio is performed and followed by the calibration of the parameter α. It is worth noting that the calibration based on the undrained experiments were performed only on

clays because the undrained triaxial tests for sand were not available. Finally, the optimization of the compression parameters e_{i0}, e_{c0} e_{d0}, h_s and n is performed.

Optimize e_{i0}, e_{c0} e_{d0}, h_s, n, e_{temp}

In the case that the parameter $\alpha < 0.9$ during iterations, the simple optimization method *OptimizeHsN* is lunched to adjust a compression curve according to the new parameters α and β. However, if this condition is not longer valid, the compression curve is calibrated only based on the direct calcualtions as shown in Fig. 4.4.6. The process *CHECK TRIAX* is not a method but rather a short code calculating the parameter e_{c0} based on the void ratio at the end of the triaxial test and parameters h_s and n accoring to Eq. (1.2.41).

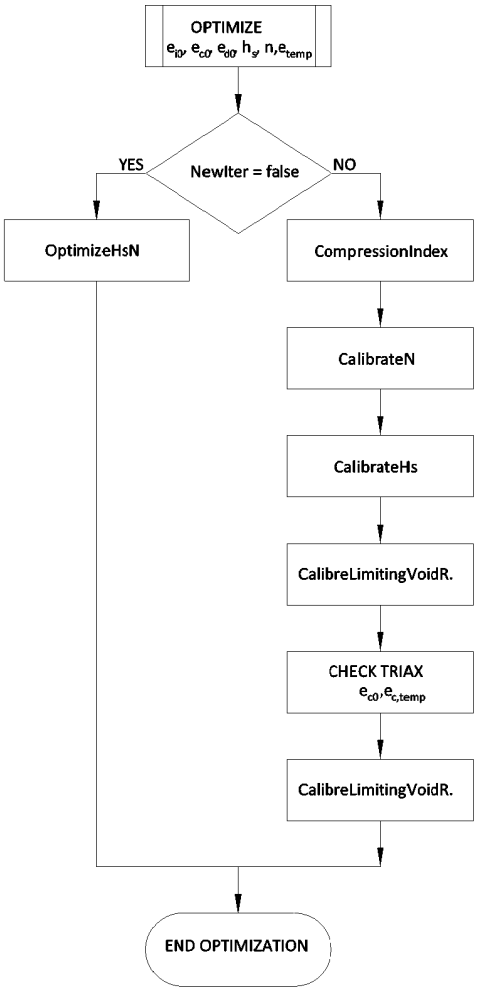

Fig.4.4.6 Flowchart of the compression subprocedure

This chapter presented calibration methods available in the literature which can be generally classified as stochastic or deterministic. Both methods have advantages and disadvantages characteristic to its nature. In this calibration software the determininistic Newton's optimization method was employed, bearing in mind the advantage of knowning the physical meaning of the models parameters.

In the next part the sensitivity analysis was introduced which aimed to refine and tune the calibration methods suggested in the literature. The hypoplastic clay model and Cam-Clay model showed a strong sensitivity to the asymptotic parameters λ^* and N or λ and e_0 while the hypoplastic sand model proved to be sensitive to more parameters. The next section shown calibration verification of the Matlab beta version which was verified in cooperation with Masin's team at Charles University in Prague.

For the sake of the clarity the calibration software ExCalibre regarding the used methods and procedures was thoroughly described. The calibration software was further used to calibrate the available specimens which models' parameters and soil characteristics are accesible on the ExCalibre website. Calibrated data were used in order to obtain a correlations between the models parameters and soil characteristics.

5. Correlations

This chapter is dedicated to the correlation analysis performed on the gathered specimens. The specimens were collected from seventeen localities of fine grained soils and ten localities of coarse grained soils. The data of the laboratory protocol contained not only records of the compression and triaxial experiments but also index characteristics, USCS classification and the particle size distribution.

The correlations were performed for both hypoplastic models by means of linear regression and correlation coefficient r. The correlations were sought both between the models parameters and soil characteristics and the models parameters itself. The linear regression for one variable is approximated by

$$\hat{y} = \beta_0 + \beta_1 x \tag{5.0.1}$$

with regression parameters β_0 and β_1 calculated according to Eqns. (5.0.2)–(5.0.7) as

$$\beta_0 = \bar{y} - \beta_1 \bar{x}, \tag{5.0.2}$$

$$\beta_1 = \frac{S_{xy}}{S_{xx}}, \tag{5.0.3}$$

where

$$S_{xx} = \sum_{i=1}^{n} x_i^2 - \sum_{i=1}^{n} x_i^2/n \tag{5.0.4}$$

$$S_{xy} = \sum_{i=1}^{n} x_i y_i - \sum_{i=1}^{n} x_i \sum_{i=1}^{n} y_i/n \tag{5.0.5}$$

$$\bar{x} = \frac{\sum_{i=1}^{n} x_i}{n} \tag{5.0.6}$$

$$\bar{y} = \frac{\sum_{i=1}^{n} y_i}{n}. \tag{5.0.7}$$

The correlation coefficient r is given by Eq. (5.0.8) [48]

$$r = \frac{S_{xy}}{\sqrt{S_{xx}}\sqrt{S_{yy}}}. \tag{5.0.8}$$

In case that nonlinear relation was observed between variables, either exponential functions given by

$$\hat{y} = \alpha e^{\beta x} \tag{5.0.9}$$

or power function

$$\hat{y} = \alpha x^{\beta} \tag{5.0.10}$$

were tested in order to characterize the behaviour. The parameters α and β are estimated as

$$\alpha = e^{\beta_0} \tag{5.0.11}$$

$$\beta = \beta_1 \tag{5.0.12}$$

The quality of the chosen model was then tested with the aid of the standardized residuals e_i^* defined as

$$e_i^* = \frac{y_i - \hat{y}_i}{s\sqrt{1 - \frac{1}{n} - \frac{x_i - \bar{x}}{S_{xx}}}}, \tag{5.0.13}$$

where s represents the standard deviation given by

$$s = \sqrt{\frac{\sum_{i=1}^{n}(x_i - \bar{x})}{n-1}}. \tag{5.0.14}$$

It is recommended that the standardized residuals should be limited within the boundaries $e_i^* < \pm 2$ [48]. The parameters of both models were calibrated for each specimen by the software ExCalibre and subsequently ordered into tables. Each specimen is presented in the tables and in the presented charts with a point coloured according to its USCS classification for a better overview. The specimens are coloured as follows:

- CH - red
- CL - pink
- SM - cian
- SC - blue
- SW - green

5.1 Hypoplastic clay model

Since the compression and shear behaviour of the fine grained soils can be influenced by its structure gained during a deposition and subsequent processes, the correlation analysis is firstly focused on the reconstituted soil specimens and secondly on the calibration differences between the reconstituted and natural undisturbed specimens.

5.1.1 Reconstituted specimens

The first correlations were performed on all reconstituted specimens of all classes according to USCS (Unified Soil Classification System). In cases when more specimens were available from one location, the separate input files were created for each of them. The specimens were calibrated by ExCalibre and sorted into Tab.B.1 together with soils specifications. This table and all correlations for the specimens are available in the Appendix B.

All the calibrations were checked and in some cases parameters κ and ν were slightly recalibrated to improve the calibration results so that the simulation better fits the experiment records. This, however, was not conducted to anyhow improve the correlations. No additional changes to the calibration were made. The following paragraphs are concerned with a discussion of the observed correlations for all specimens in order to provide a clear correlations and conclusions.

5.1.1.1 Discussion of the overall correlations

This section examines the correlations observed for all specimens. The relevant charts are also presented in the Appendix B.

The correlations between parameters reveal clear correlation $r = 0.934$ between the parameters N and λ^*, see Fig. 5.1. This correlation is in accordance with the observed behaviour of clay since a study published in [49] observed a similar correlation between the compression index C_c and void ratio e_1 at the mean stress $p = 1$ kPa for both reconstituted and natural specimens. The physical meaning of the compression index C_c and e_1 correspond to the parameters

N and λ^*. In addition, the correlation in Fig. 5.1 is also valid for USCS classes containing high percentage of sand content.

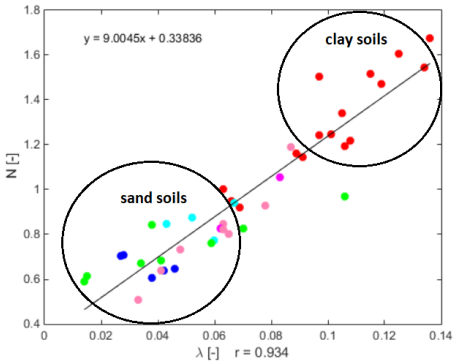

Figure 5.1: Correlation between the parameters λ^* and N^*

A week correlation is also observed for a content of sand and clay particles $r \approx 0.7 - r \approx 0.73$, see Fig. 5.2a. Correlations according to the Atterberg's limits also show an indisputable correlations with the parameters λ^* and N, see Fig. 5.2b. Such correlations between Atterberg's limits and the compression index were presented in [50, 51, 52]. Clearly, these correlations are valid only for the soils for which the Atterberg's limits can be determined.

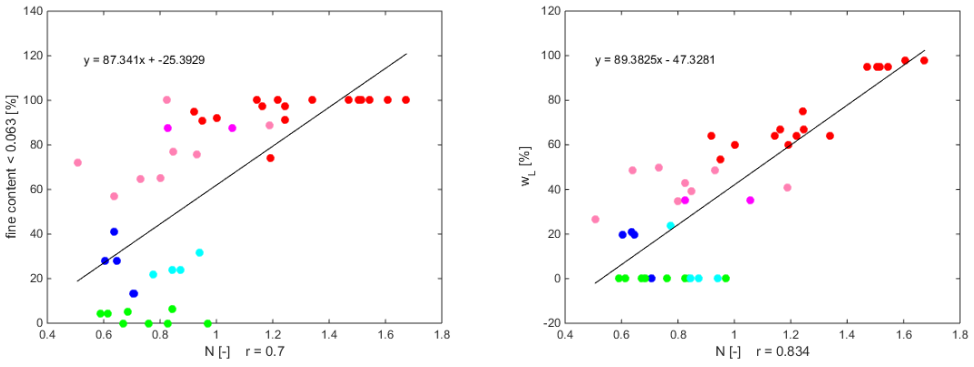

(a) Correlation between N and f[%]

(b) Correlation between N and W_L

Figure 5.2: Correlations for the parameter N

Even though the correlations of the parameter κ^* with the parameters λ^* and N are $r = 0.481$ and $r = 0.34$, respectively, there is indicated a clear

correlation from sand to clay USCS classes. However, a certain region of CH soil specimens does not follow this correlation path, see Fig. 5.3.

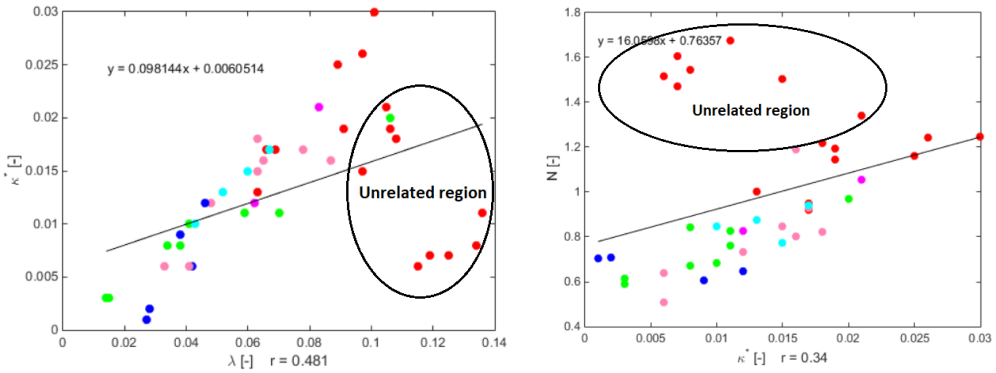

(a) Correlation between the parameters λ^* and κ^*

(b) Correlation between the parameters N and κ^*

Figure 5.3: Unrelated region of reconstituted specimens regarding the calibrated parameter κ^*

These are the specimens referred as Otaniemi and Vantilla and they are loaded only up to 50-130kPa during the compression test subjected additionally to the unloading/reloading loops. Although it seems that the transitional stress at the *NCL* is reached, e.g. the stress when the reloading path changes to the virgin loading path, see Fig. 5.4.

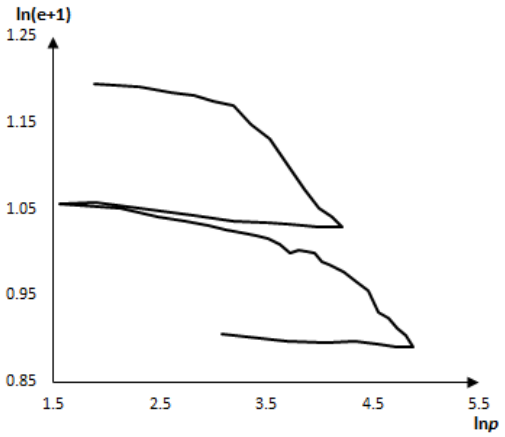

Figure 5.4: Otaniemi oedometric test $\ln p \times \ln(e+1)$

As a consequence of the low loading/unloading stress, a calibration of the parameter κ^* is highly influenced by the reloading part of experiment, which is not case

for the other reconstituted specimens. The parameter κ^* of these specimens also does not correlate with Atterberg's limits and create a separate group, therefore, it seems to be reasonable to omit these specimens in the case of correlations related to the parameter κ, see Fig. 5.3a. Furthermore, some specimens lack the unloading part of the compression test. Considering the fact that the parameter κ^* is optimized from both loading and unloading part of the compression test, the results of the calibration might be affected by the lack of the unloading part and thus should not be used for the correlation. This is related to the specimens *Komorany1-4*, *Boston*, *Koper1-2*.

The parameters κ^* and ν influence the triaxial test in an inverse proportion which can also be seen in the correlation of these parameters. It is rather troublesome to consider the coarse grained soils for the correlations related to the parameter ν since this parameter controls the ratio of the shear modulus G_i to the bulk modulus K_i at the isotropic state under the undrained conditions. The coarse grained soils, however, were subjected to the drained conditions and even simulation with the limiting values of the parameter $\nu = 0.01$ and $\nu = 0.4$ do not fit well the experimental data. The coarse grained specimens thus should not be considered for the correlations of ν since this stiffness driving parameter does not represent them well. Other correlations for the parameter ν were not observed.

The critical state friction angle φ_c is directly correlated with the content of sand particles and indirectly with the content of clay particles, see Fig.5.5a and Fig.B.5. This well represent the observed behaviour of the sandy soils reaching higher critical state friction angle than fine grained soils [53]. In case of the correlation φ_c to both clay and sand percentage content can be observed a distant point which belongs to the specimen *Koper*. The undrained triaxial experiments performed on these specimens shows significant fluctuations in the deviatoric stress q and thus its reliability is questionable, see Fig. 5.5b. It thus seems to be reasonable to again omit this specimen from the correlation calculations. Furthermore, the correlation related to the content of the clay particles also results in the correlation related to the Atterberg limits. Any correlation referred

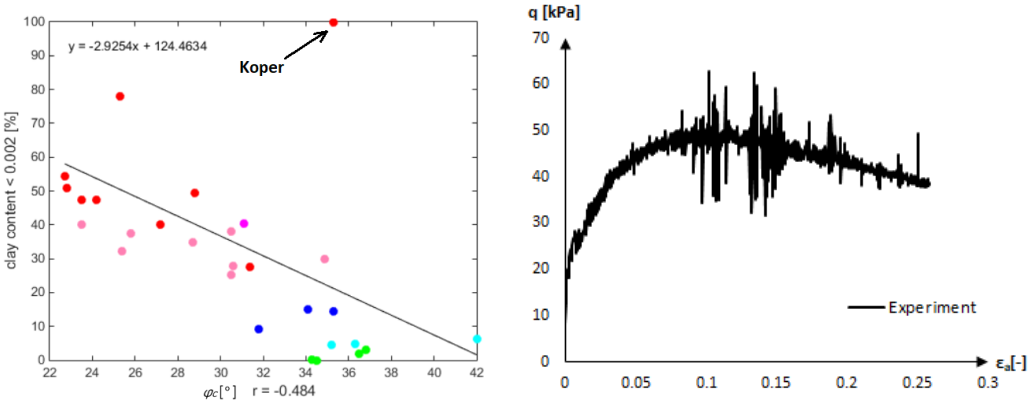

(a) Correlation between φ_c and sand content

(b) Koper Triaxil test $\varepsilon_a \times q$

Figure 5.5: Specimen Koper

to the particle distribution curve such as a diameter of the sieved particles used for the geotechnical calculations D_{10}, D_{30} and D_{60} or the coefficient of uniformity C_u and curvature C_z [54] were not observed. The following chapter is dedicated to the selected correlations for the hypoplastic clay model.

5.1.1.2 Final correlations

Considering the described defective or unreliable specimens, the specimens were sorted and the following correlations for the reconstituted specimens were observed.

Parameters λ^* and N

As it was already pointed out, the soil parameters λ^* and N are well correlated with Atterberg's limits and each other. The parameter N was correlated with the liquid limit w_L with correlation coefficient $r = 0.914$ and plastic index I_P with correlation coeficient $r = 0.893$, see Fig. 5.6.

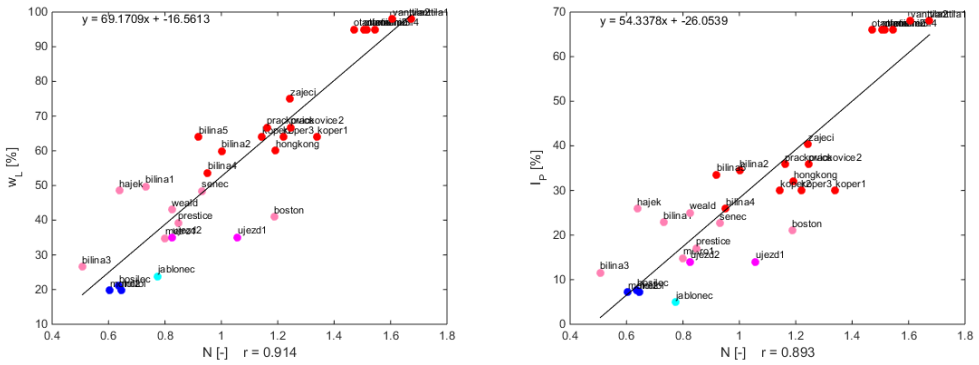

(a) Correlation between w_L and N

(b) Correlation between I_P and N

Figure 5.6: Correlation between Atterberg's limits and N

The estimation of the parameter N is more reasonable according to the liquid limit w_L because the specimens in Fig. 5.7a are placed in the more continuous manner and the correlation coefficient r reaches a higher value. The limits of the correlation thus would be $20\% < w_L < 100\%$, while an equation of the correlation reads

$$N = 0.2394 - 0.0144 \times w_L. \tag{5.1.1}$$

Similar correlations are observed for the parameter λ^* where the correlation coefficient is $r = 0.864$ with respect to the liquid limit w_L and $r = 0.83$ with respect to the plasticity index I_P, see Fig. 5.7.

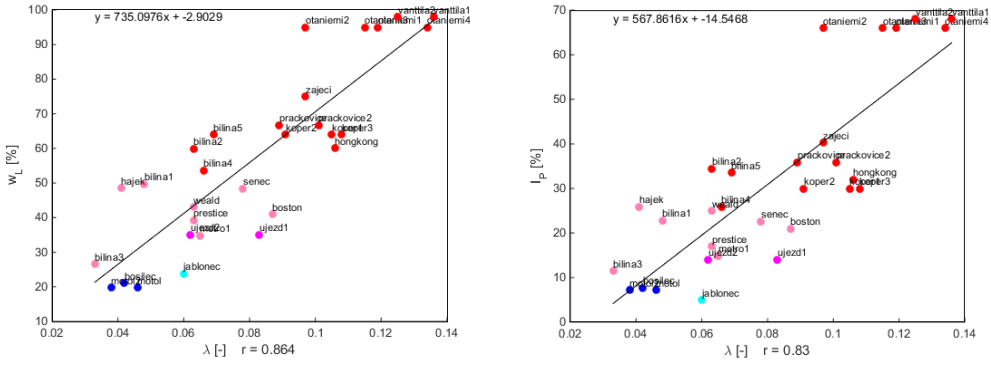

(a) Correlation between w_L and λ^*

(b) Correlation between I_P and λ^*

Figure 5.7: Correlation between Atterberg's limits and λ^*

Furthermore, the correlation between the parameters λ^* and N is well depicted in the Fig. 5.8 with correlation coefficient $r = 0.934$. The correlation is given by

$$N = 9.0045 \times \lambda^* + 0.33836. \tag{5.1.2}$$

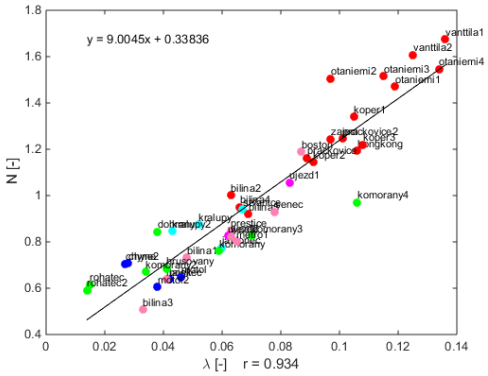

Figure 5.8: Correlation between the parameters N and λ^*

Parameter κ^*

The correlations for the parameter κ^* are shown in Fig. 5.9a. While a relatively small correlation was found between the parameter κ^* and plastic limit w_P $r = 0.716$, better correlation was observed between the parameters λ^* and κ^* where $r = 0.928$, see Fig. 5.9b. The correlation is defined by

$$\kappa^* = 0.2772 \times \lambda^* - 0.00248 \tag{5.1.3}$$

Interestingly, the lower values of the parameter κ^* belong to the coarse grained soil which usually exhibits small amount of swelling in comparison to the fine grained soil [53]. This correlation thus agrees with the laboratory observations.

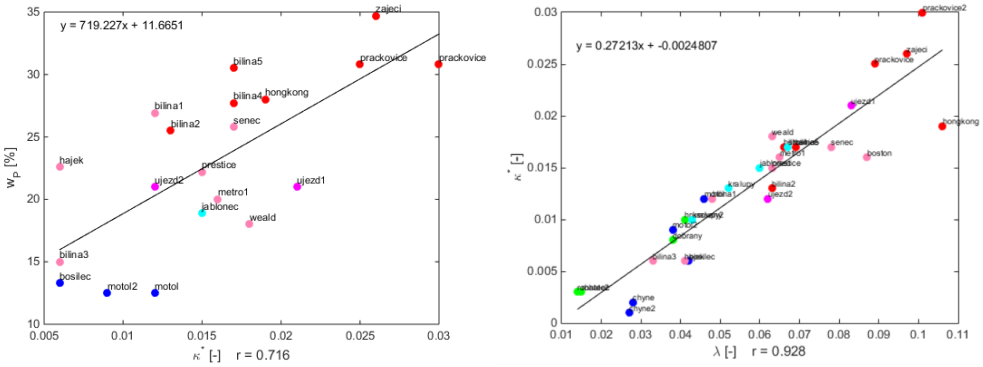

(a) Correlation between w_P and κ^*

(b) Correlation between κ^* and λ^*

Figure 5.9: Correlations for the parameter κ^*

Parameter φ_c

The parameter φ_c is well correlated with a content of fine and coarse size particles. The inverse proportion can be found for the content of clay particles $d < 0.002$mm with the correlation $r = -0.858$ and fine particles $0.002 < d < 0.063$ with the correlation $r = -0.822$. Similarly, the direct proportion is found for the content of the sand particles $0.063 < d < 2$mm with correlation coefficient as $r = 0.79$. The correlations depicted in Fig. 5.10 thus correspond to the observation when sand soils reach higher critical state friction angle φ_c than fine grained soils [53]. The strongest correlation is found for the content of clay particles. The equation of the linear regression is written as

$$\varphi_c = -0.3344 \times f + 39.4771, \tag{5.1.4}$$

where f stands for the content of clay particles in percent. It is worth mentioning that the correlation with the content of fine and sand particles also correlates with the Atterberg's limits, even though the correlations was found weak with $r = 0.558 - 0.739$.

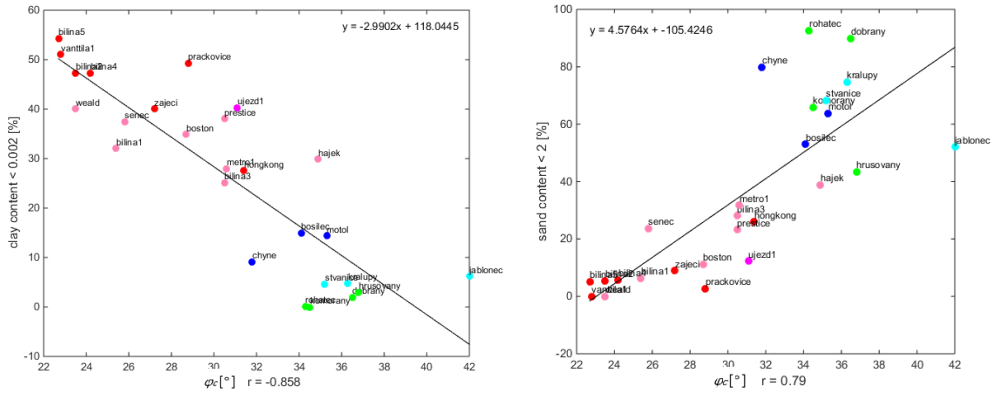

(a) Correlation between clay particles content and φ_c

(b) Correlation between sand particles content and φ_c

Figure 5.10: Correlations for the parameter φ_c

Parameter ν

Since the parameter ν often reaches the limiting value $\nu = 0.01$ for coarse grained soils and their simulations still do not match well the experimental data, these soils were left out.

The correlations for the stiffness controlling parameter ν was not clearly observed, neither for Atterberg's limits nor for the particle size content. Weak correlation, however, can be observed between the parameters λ^* with $r = -0.737$, κ^* with $r = -0.613$ and N with $r = -0.647$. Furthermore, it can be observed from Figs. 5.11a–5.11c that for the same parameter λ^*, κ^* or N one gets lower value of ν (higher shear stiffness) for the CL soils and higher value ν (lower shear stiffness) for CH soils.

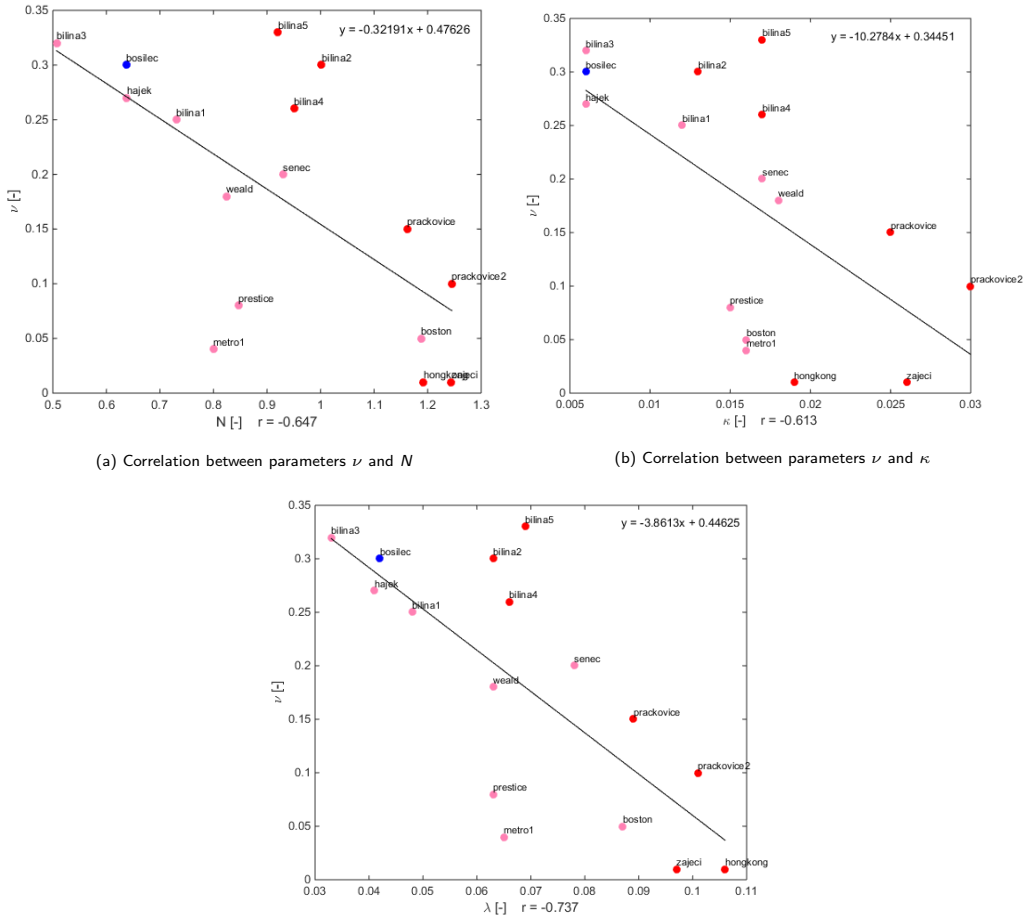

(a) Correlation between parameters ν and N

(b) Correlation between parameters ν and κ

(c) Correlation between parameters ν and λ

Figure 5.11: Correlations for the parameter ν

5.1.2 Natural undisturbed specimens

The next step is to test whether the obtained correlations can sufficiently capture the behaviour of natural undisturbed soils. This can be, however, tested only on the experiment protocols containing both natural and reconstituted specimens.

Given the fact that the parameters λ^*, N and φ_c can be regarded as an asymptotic states driving parameters independent of the soil structure, the parameter κ^* is often observed with a different inclinations for unloading/reloading at different stress levels (consolidation), see Fig. 5.12a. Thus, the determination of the parameter κ^* appears to be rather complicated using reconstituted sam-

ples. Given the fact that a structure is interacting a soil mass is modelled, the soil in its natural state is in concern. Therefore, it seems to be reasonable to determine the parameter κ^* based on the natural samples, this is also supported by Fig. 5.12b. The figure shows the results of the calibration executed by the application ExCalibre on the specimen designated as Bilina1 where the original calibration (green) resulted in the value of the parameter $\kappa^* = 0.006$. However, the calibration executed on the reconstituted specimen reached the value $\kappa^* = 0.012$. The clear contradiction can be seen in the lower value of the parameter κ^* for the natural specimen at a higher stress level shown in Fig. 5.12a, where κ^* reaches a higher value at a higher stress level. This is caused by the nature of the calibration, where the parameter κ^* is calibrated on both loading and unloading parts of the compression experiment while the minimum of the error function $E(\ln(e+1))$ is sought. Thus, the calibration executed on the natural compression specimen is more influenced by the reloading part of the experiment then in the case of a reconstituted specimen where the reloading part does not fully manifest its influence on the calibration.

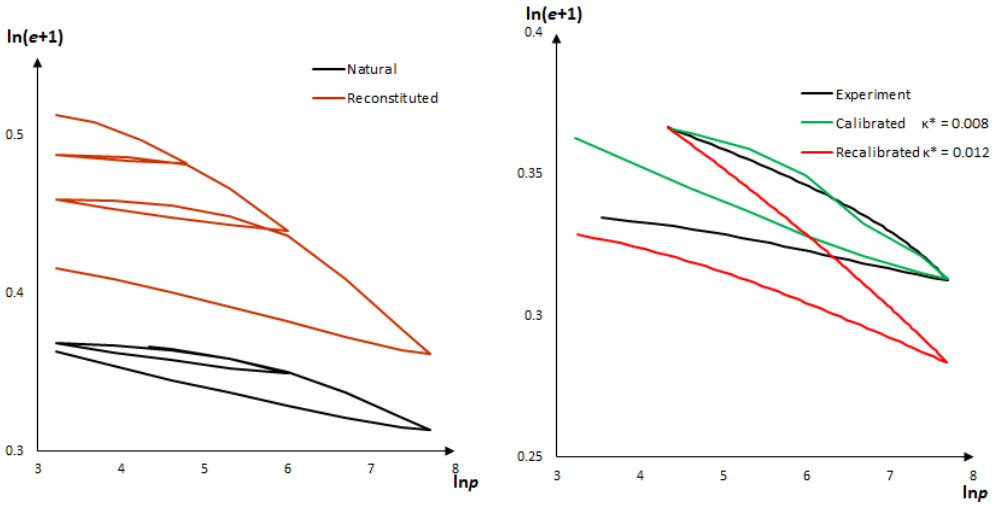

(a) Oedometric data records of Bilina1

(b) ExCalibre calibration results of Bilina1 OED-NAT-1

Figure 5.12: Bilina1 Oedometric experiments' records and calibration results

It is also worth noting that the recorded data might be also influenced by the consolidation behaviour of the soil, since the deformation of the loading step

during the experiment is recorded once the primary consolidation is considered to be finished or after a specific amount of time has passed since the last record.

Therefore, this section is dedicated to a study conducted on the parameters κ^* and ν only as their values differ for a different structures and states. These assumptions are illustrated in Fig. 5.13a and Fig. 5.13b. It can easily be deduced from Fig. 5.13a that the parameter κ^* reaches higher values for the reconstituted samples (red) and lower values for the natural specimens (black), i.e., lower bulk modulus K for the reconstituted specimens and higher for the natural specimens. This is in accordance with aforesaid conclusions regarding the specimen Bilina1. The parameter ν in Fig. 5.13b is changing randomly for both reconstituted and natural specimens.

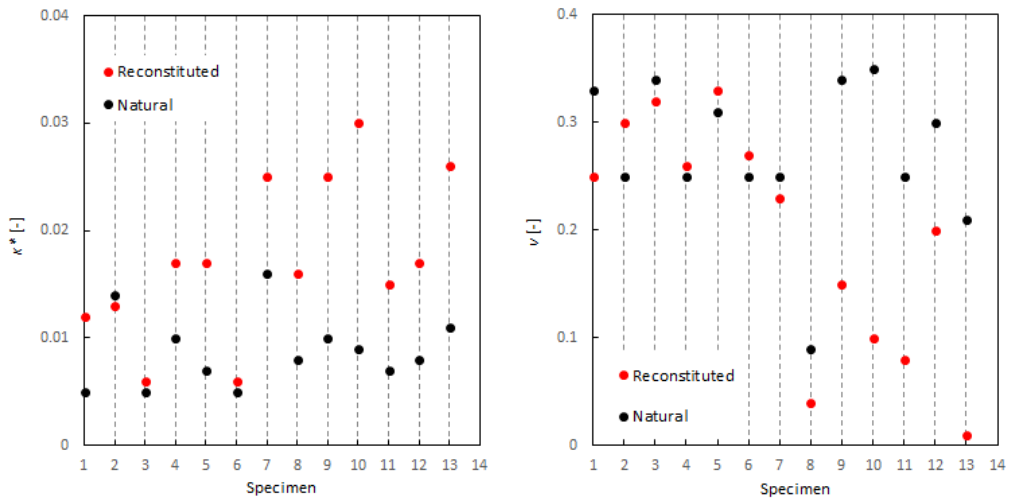

(a) Variations in κ^*

(b) Variations in ν

Figure 5.13: Variation in κ^* and ν for reconstituted (red) and natural (black) specimens

Parameter κ^*

Since it was observed that the change in the value of the parameter κ^* is linked to the reloading part of the compression experiment, the correlations were also created for the experiments initial void ratio e_{init} and the parameter κ^*. The values of e_{init} for both reconstituted and natural oedometric specimens together with calibrated parameters are presented in Tab. B.2 in Appendix B.

The correlation between the parameter κ^* and the initial state is illustrated in Fig. 5.14a, where $\Delta\kappa^*$ is calculated as a difference between the natural and reconstituted values of κ^* and ΔN is calculated according to

$$\Delta N = \ln(e_{init}^{nat} + 1) - N_{rec}. \tag{5.1.5}$$

The parameter N_{rec} represents the parameter N calibrated on the reconstituted specimen and e_{init}^{nat} represents the initial void ratio of a natural compression experiment. This correlation was performed only on the natural specimens to find a dependency on the position of the initial void e_{init} according to NCL. In this case the correlation coefficient reaches a remarkable value $r = 0.826$.

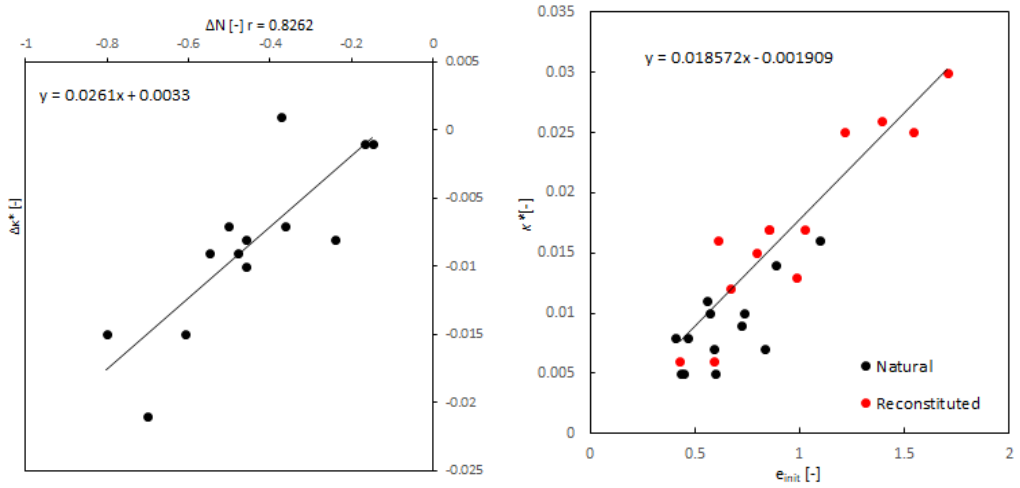

(a) Change of κ^* with change of dN

(b) Evolution of κ^* with initial void ratio

Figure 5.14: Effects of the initial state on the parameter κ^*

Even better correlation r =0.911 was found directly for the parameter κ^* and initial void ratio e_{init}. This correlation is well illustrated in Fig. 5.14b and it

was executed for both natural and reconstituted specimens. The linear regression equation is given by

$$\kappa^* = 0.018571 \times e_{init} - 0.0019089. \tag{5.1.6}$$

The correlations, however, were not found for the overconsolidation ratio OCR which can once again lead to the conclusion that the calibration of κ^* is strongly influenced by the amount of reloading during the compression experiment.

Parameter ν

In order to find the correlations between the parameter ν and initial states of triaxial tests, a new calibration was executed with the aid of ExCalibre. The calibration data were prepared so that each data set was consisting of just one triaxial test and thus each triaxial test refers to a specific value of ν. These values can be found in Tab.B.3 and Tab.B.4 in Appendix B. However, there were only few locations with natural triaxial specimens. The comparison of the natural and reconstituted specimens for different initial states are displayed in Fig. 5.15.

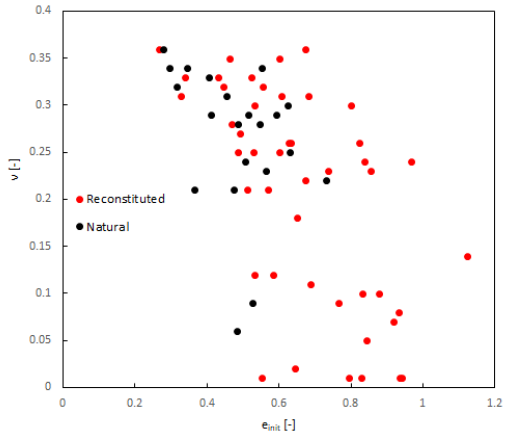

Figure 5.15: Parameter ν of reconstituted and natural triaxial specimens

This comparison, however, did not revealed any correlations.

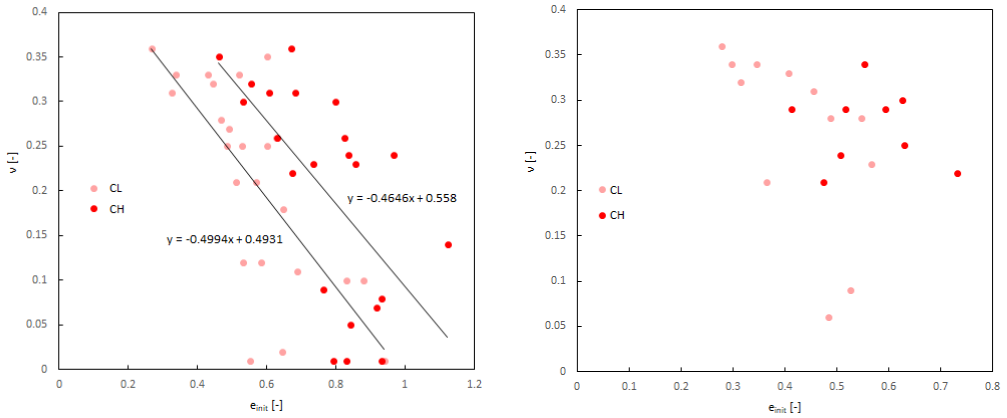

(a) Reconstituted specimens

(b) Natural specimens

Figure 5.16: Correlation between the parameter ν and initial void ratio e_{init}

The relations depicted in Fig. 5.16a distinguishes correlations between classes CL and CH. The stiffness controlling parameter ν was not possible to properly correlate with any characteristics. However, it was observed for both reconstituted Fig. 5.16a and natural Fig. 5.16b specimens that the fine grained soil class CL reached lower values of ν for the same initial void ratio and the class CH reached the higher value. The value of parameter ν can be roughly estimated from the correlations Fig. 5.16a $\nu \approx 0.2 - 0.3$. The table of calibrated parameters for both reconstituted and natural triaxial specimens is again provided in the Appendix B.

5.2 Hypoplastic sand model

The correlations for the hypoplastic sand parameters were sought in the similar manner as in case of the hypoplastic clay model. All the specimens of all USCS classes were used in pursuit of correlations, however, only the reconstituted specimens were used in the case of fine grained soil because it is not in general possible to extract sand specimens in its undisturbed form and subsequently subject to further testing.

In case of sand specimens difficulties in a calibration of the oedometric test were encountered when an initial sharp drop in void ratio e in the $\ln p \times e$ space is observed and the S shape of the loading part is produced, see Fig. 5.17. Since the initial state for the calibration should be loose but not collapsible [16], the initial loading part of the compression tests representing a convex shape were excluded. It was observed that sufficient value to be omitted from the oedometric test is σ_a = 40kPa. This value is designated by the red colour in Fig. 5.17. Furthermore, it was also pointed in [16] that Eq. (1.2.37) does not well suit stress state $\sigma_a \approx 0$.

The oedometric tests were once again divided into the separate files and calibrated. The calibrated parameters for all available specimens are presented in the Appendix C in Tab. B.1 together with correlation charts.

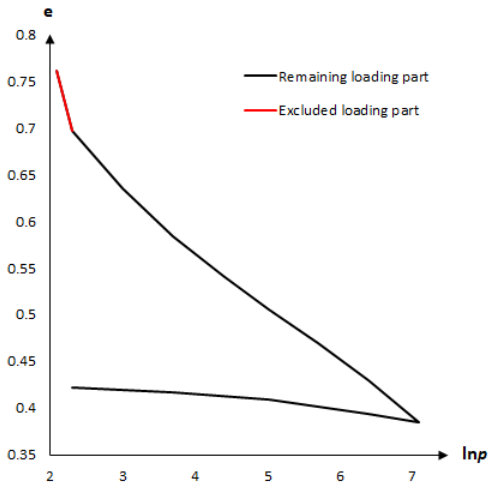

Figure 5.17: Excluded loading part of oedometric tests - Motol

5.2.1 Discussion of the overall correlations

5.2.1.1 Parameter h_s

Unlike the hypoplastic clay model, where the INCL is defined by two parameters λ^* and N, the hypoplastic sand model defines INCL by Eq. (1.2.37) with three parameters h_s, n and e_{i0}. It is possible to observe an increasing changes in a magnitude of the parameter h_s with decreasing content of fine particles, see Tab. C.1. While the value of h_s of the specimens with a high content of fine particles is relatively small, $h_s < 1000$ in case of CH and $h_s < 2500$ in case of CL, the values of the parameter h_s for the soils with high sand reach up to $h_s = 58,583$. The values of the parameter h_s in case of the location Rohatec is considerably higher, in particular $h_s = 2.68 \times 10^6$ in case of *Rohatec1* and $h_s = 0.44 \times 10^6$ in case of *Rohatec2*. These specimens exhibit relatively small deformations during the oedometric test in comparison with *Dobrany*, *Komorany* and *Hrusovany*. Therefore, it seem to be reasonable to exclude these specimens from the correlations relating to the parameters h_s, n and e_{i0}. The effect of the clay and sand particles is then illustrated in Fig. 5.18. This figure shows a tendency of soils with higher content of clay particles towards lower value of the parameter h_s. The opposit is true in case of increasing content of sand particles.

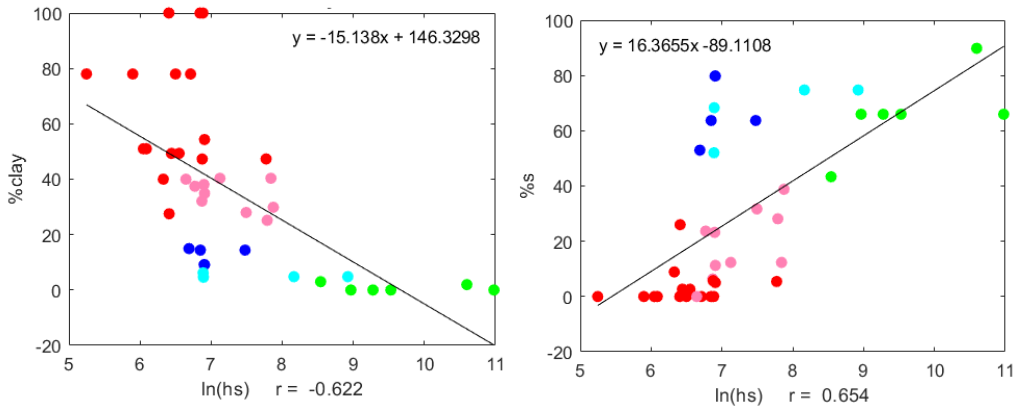

(a) Correlation between the clay partiles content and h_s

(b) Correlation between the sand particles content and h_s

Figure 5.18: Correlations for the parameter h_s

The correlations between the natural logarithm of the parameter h_s and

other parameters then show a good correlation with the parameter e_{i0} which controls the position of the INCL in the $\ln p \times e$ space, see Fig. 5.19a. This figure might also suggest a more nonlinear relation in case when all soil classes are employed. A similar correlation was found between the parameters N and λ^* of the hypoplastic clay model. A correlation between h_s and n in Fig. 5.19b shows a similar correlation even though there are three oedometric samples from the location *Komorany* belonging to the SW class, namely *Komorany1*, *Komorany3* and *Komorany4* that are calibrated with high value of the parameter n.

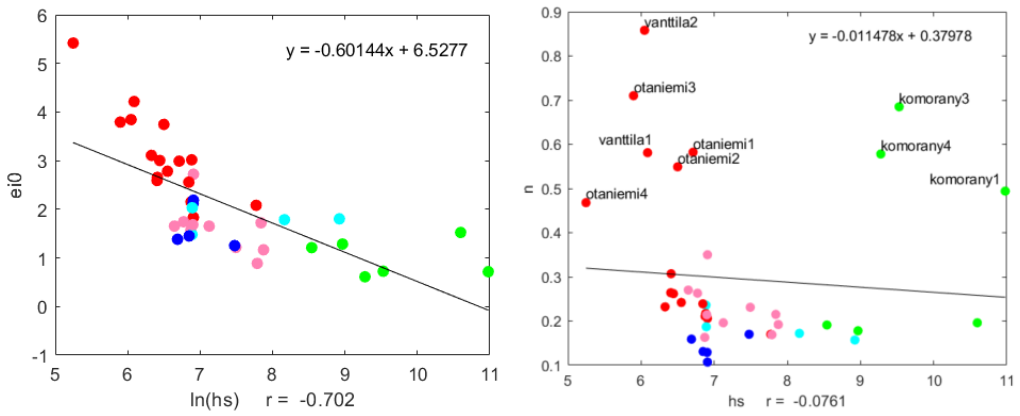

(a) Correlation between the parameters h_s and e_{i0}

(b) Correlation between the parameters h_s and n

Figure 5.19: Correlations of the parameter h_s with parameters n and e_{i0}

This is probably due to the nature of the calibration. When the overconsolidation is not reached even for a value of the parameter $\alpha = 0.9$ while simulating the triaxial tests, see Fig. 4.4.6, the optimization of the parameters h_s and n is no longer conducted and they are directly evaluated by Eqns. (2.0.6)–(2.0.13). This scenario happaned specificaly in the case of aforementioned specimens *Komorany*. The reason is illustrated in Fig. 5.20 where it is shown that the only oedometric specimen occuring above the critical state reached in the triaxial test is *Komorany2*. The second group with a relatively high value of n belongs to location *Otaniemi* and *Vantila*. These specimens are loaded during the oedometric test only upto a low stress level $\sigma_a = 100$kPa and the curvature of the loading part in the $\ln p \times e$ space is therefore high. This results in a high value of the parameter n. The maximal value of the parameter n then lies beneath the value

0.4.

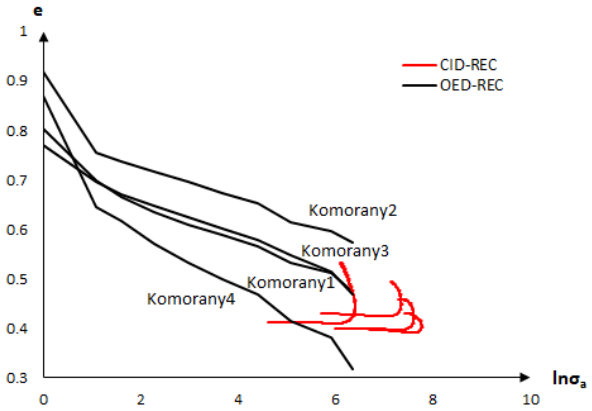

Figure 5.20: Performed experiments of the Komorany specimens in $\ln \sigma_a \times e$

Similarly correlated is the parameter h_s with the critical state friction angle φ_c in Fig.5.21, which thus reflects a correlation of both parameters with content of sand particles, see Fig. 5.18b and Fig. 5.10b.

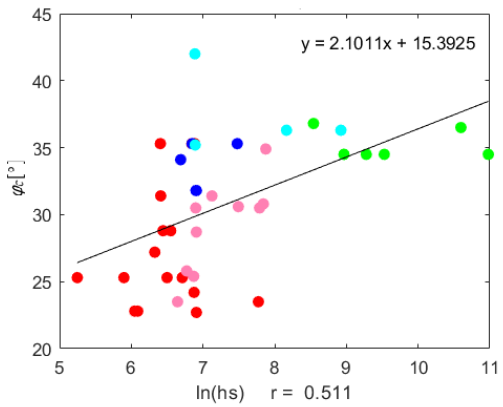

Figure 5.21: Correlations between the parameters h_s and φ_c

5.2.1.2 Parameter n

The parameter n was found to be correlated solely for the coarse grained soils. This is illustrated in Fig. 5.22a showing correlation with the parameter β. This figure show a direct proportional correlation for coarse grained soils except for

the specimen *Bosilec*. The fine grained soil on the other hand keep the a value $\beta \approx 9$, which is set as a limiting value for calibration. The only fine grained specimens with a lower value belong to location Ujezd. It worths noting that the parameter β of all coarse grained soils is calibrated based on the *drained triaxial test* except of the specimen *Bosilec* and moreover, β of all the specimens of fine grained soils, exept of the specimen *Ujezd*, is calibrated on the *undrained triaxial test*. The correlation thus shows a distinct difference in calibration of the parameter β on the basis of drained or undrained triaxial test which might be further affected by the particle properties such as shape, angularity etc.

Correlation between the parameters n and β is shown in Fig. 5.22b. The correlation is once again indicated only for a coarse grained soils while fine grained soil creates a separate cloud.

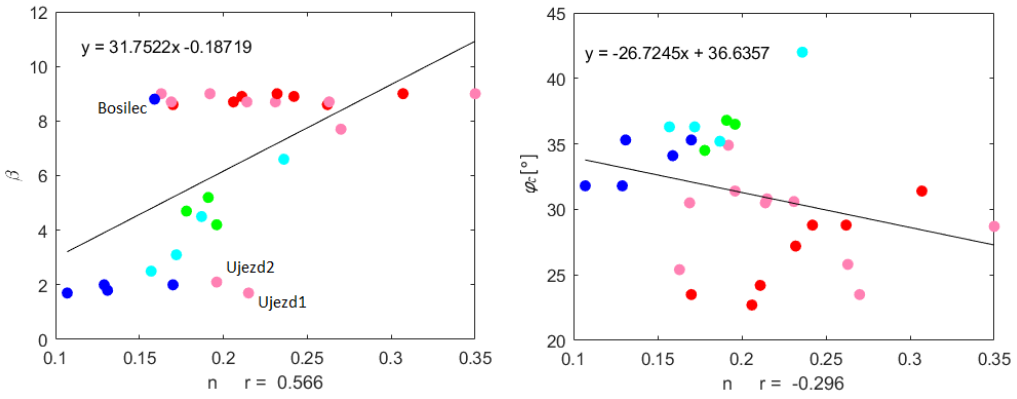

(a) Correlation between the parameter n and β

(b) Correlation between the parameter n and φ_c

Figure 5.22: Correlations of the parameter n with parameters β and φ_c

The study published in [1] described correlation of the parameter n with gradation characteristics, namely d_{50} and Cc. This trend described in [1] was confirmed in this study and can be once again seen in both Fig. 5.23a and Fig. 5.23b only for coarse grained soils.

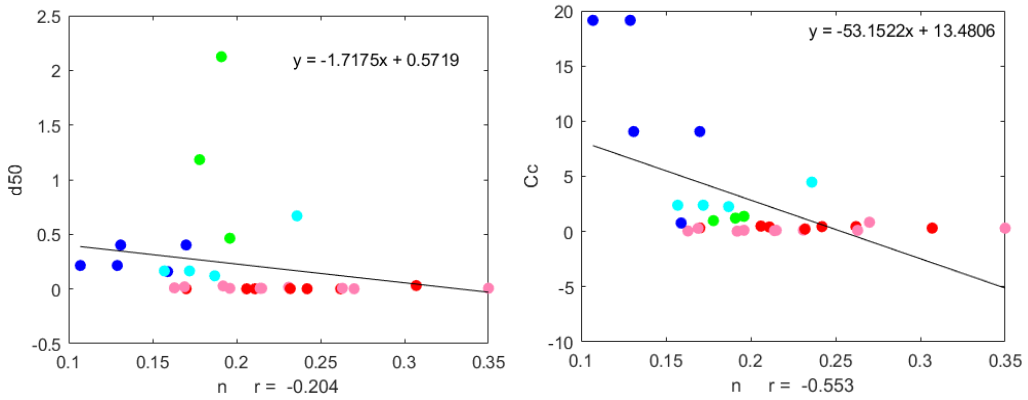

(a) Correlation between the parameter n and d_{50}

(b) Correlation between the parameter n and Cc

Figure 5.23: Correlations of the parameter n with gradation characteristics

An interesting relation is shown for a content of fine particles in Fig. 5.24a and sand particles in Fig.5.24b. Even though the correlation parameter r is low, it can be clearly observed that lower values of the parameter n is related to higher content of sand particles and the opposite is true for the content of clay particles.

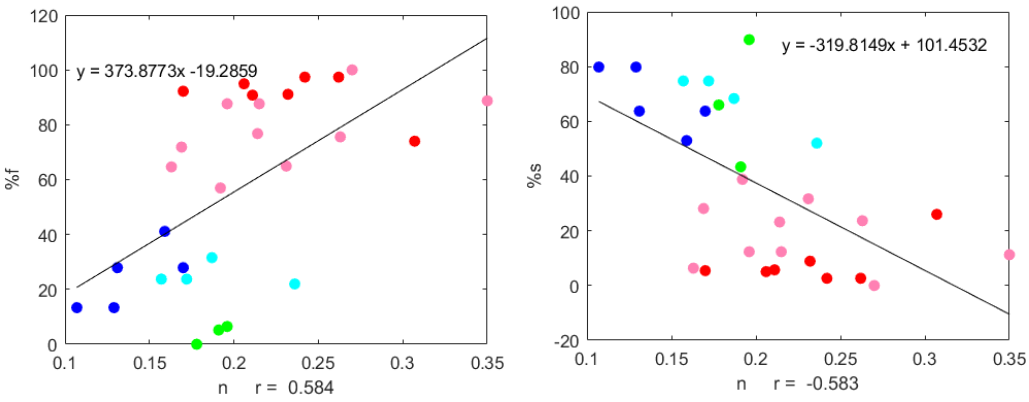

(a) Correlation between the fine particles content and n

(b) Correlation between the sand particles content and n

Figure 5.24: Correlations of the parameter n with particles content

5.2.1.3 Parameters e_{i0}, e_{c0}, e_{d0}

This correlation is focused solely on the parameter e_{c0} since the parameters e_{d0} and e_{i0} are directly derived from the parameter e_{c0}. The parameter e_{c0} is correlated with the parameter φ_c in Fig. 5.25, where an inverse proportion for the coarse grained soils is observed. This correlation is further strengthen by

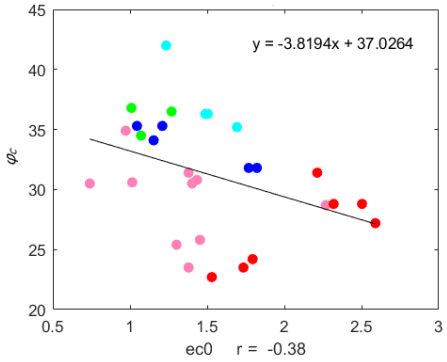

Figure 5.25: Correlation between the parameters e_{c0} and φ_c

correlation with a content of sand particles in Fig. 5.26a, since a direct proportion was observed in Fig. 5.10b between the content of sand particles and the critical state friction angle φ_c. The correlation with Atterberg's limits shows a direct proportion. However, some specimens lacks a description of this quantities, see Fig. 5.26.

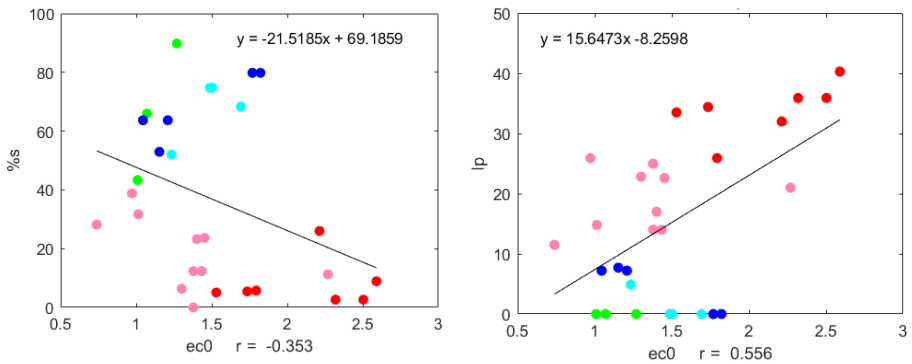

(a) Correlation between the sand content and e_{c0}

(b) Correlation between the plastic index I_p and e_{c0}

Figure 5.26: Correlations of the parameter e_{c0} with I_p and content of sand particles

5.2.1.4 Parameter α

It was pointed out in [1] that the peak fricion angle φ_p decreases with increasing C_u. This was confirmed in Fig. 5.27 where the parameter α is correlated with C_u which directly controls φ_p.

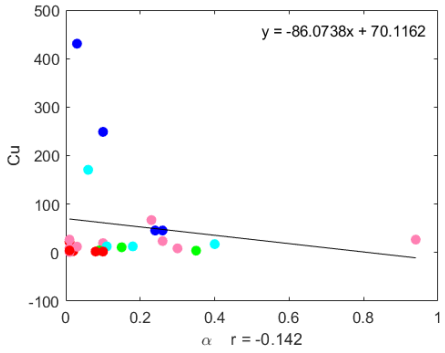

Figure 5.27: Correlation of the parameter α with Cu

Furthermore, an indirect correlation with the critical state friction angle φ_c for coarse grained soils was observed, see Fig.5.28.

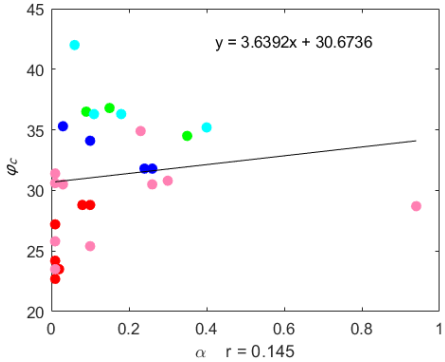

Figure 5.28: Correlation between the parameters α and φ_c

5.2.1.5 Parameter β

A stiffness driving parameter β was well correlated with the parameter n in Fig. 5.22a. Any further correlations were not possible to observe.

5.2.2 Final correlations

Unlike in case of the hypoplastic clay model, where it was possible to observe the correlations for various USCS classes, the hypoplastic sand model was less feasible to properly correlate with respect to all USCS classes. Therefore, the main focus is on the coarse grained soils.

Parameter h_s

It was shown in Fig. 5.19a, where a natural logarithm of h_s with e_{i0} was correlated, that a nonlinear behaviour between these parameters might exist for various soil classes. Figure 5.29 suggesteds a nonlinear regresion estimated by Eq. (5.0.10) and simlified to

$$\hat{y} = 277 \times (\ln h_s)^{-2.5} \tag{5.2.1}$$

with correlation coefficiend $r = 0.789$.

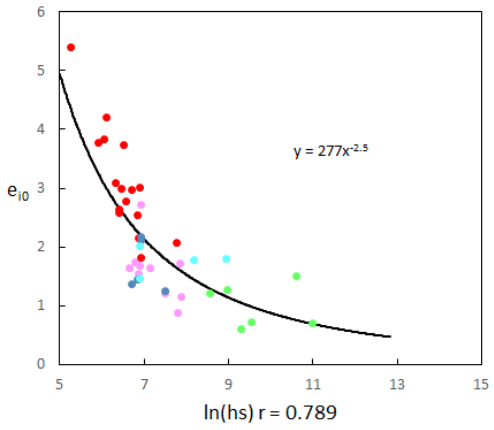

Figure 5.29: Correlation between the parameters h_s and e_{i0}

The standardized residuals of the nonlinear model are shown Fig. 5.30. Given the fact that the values of e_i^* are small, the model should be well determined.

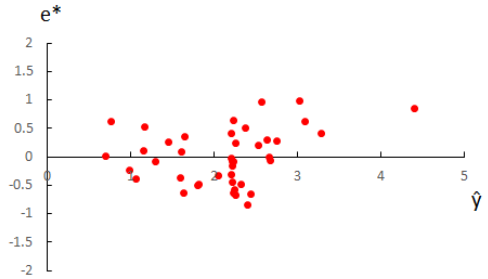

Figure 5.30: Residuals e^*

In case of solely coarse grained soils, the correlation between these two parameters is even more significant with correlation coefficient $r = 0.879$. Thus the trend is preserved, see Fig. 5.31.

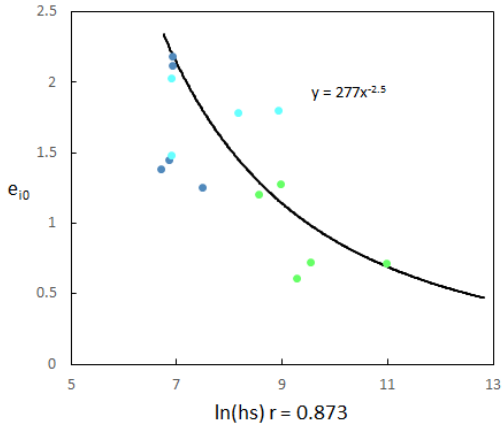

Figure 5.31: Correlation between the parameters h_s and e_{i0}

The correlation between the content of clay particles and parameter h_s in Fig. 5.31 was observed similarly to the parameter N in hypoplastic clay model with correlation coefficient $r = 0.737$ and equation of the regression line given by

$$clay\% = -2.5032 \ln h_s + 27.2671. \tag{5.2.2}$$

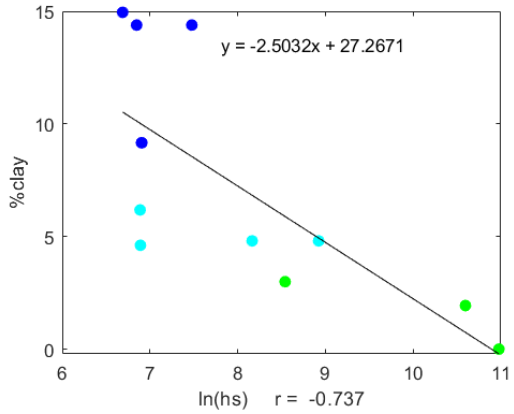

Figure 5.32: Correlation of the sand particles content with h_s

Parameter n

As it was suggested initially good correlations were found between the parameters n and β with correlation coefficient $r = 0.900$, see Fig. 5.33 and between the parameters n and φ_c with correlation coefficient $r = 0.862$, see Fig. 5.34.

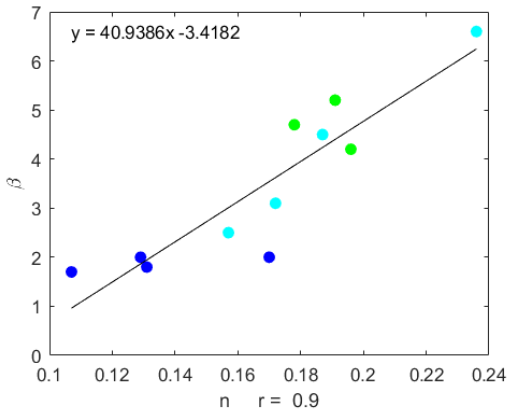

Figure 5.33: Correlation between the parameters n and β

$$\beta = 40.9366n - 3.4182. \tag{5.2.3}$$

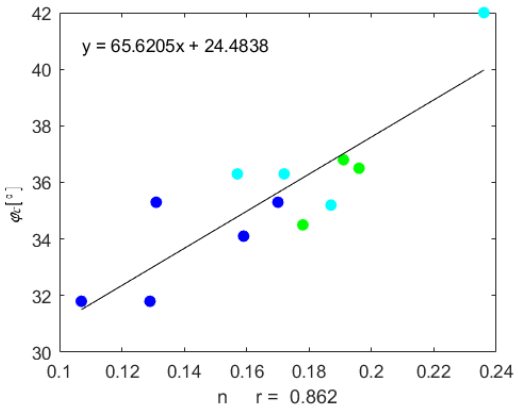

Figure 5.34: Correlation between the parameters n and φ_c

$$\varphi_c = 65.6205n + 24.4838 \tag{5.2.4}$$

In [1] a correlation between the parameter n and gradation characteristics d_{50} and C_u was provided in the form

$$n = 0.366 - 0.0341x, \tag{5.2.5}$$

where

$$x = \frac{C_u}{d_{50}}. \tag{5.2.6}$$

The data from [1] were extracted and complemented with the calibrated data, see Fig. 5.35. Data were calibrated individually for each oedometric test. The inversely proportional pattern of the calibrated and extracted data can be observed in Fig. 5.35 suggesting a bilinear relation. Furthermore, it was also pointed out in [1] that the data values of n were obtained by a simple calculation according to Eqns. (2.0.6)–(2.0.11) and there was not provided a clear evidence of how well the calculated parameters represents the observed behaviour. Therefore, the lack of data does not allow to make a clear conclusion on this particular correlation.

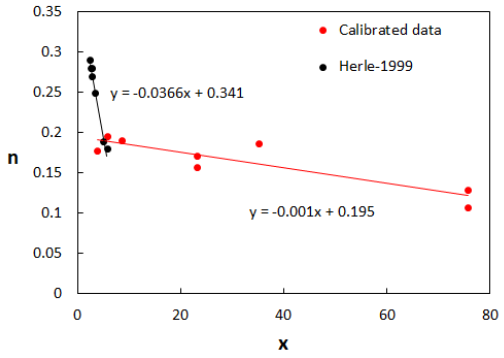

Figure 5.35: Data from [1] complemented with calibrated data

Parameters e_{i0}, e_{c0}, e_{d0}

The correlation of the initial limiting void ratios is limited to the parameter e_{c0} since the parameters e_{d0} and e_{i0} are derived from it, see Section 2. The best correlation for e_{c0} was found for Atterberg's limits, which is illustrated for the liquid limit W_L in Fig. 5.36. Calculation of the initial void ratios on the basis of Atterbeg's limits was also proposed in [17]. Unfortunately, not enough coarse grained soils had these properties determined and the correlation is mainly drawn owing to the data of the fine grained soils, see Fig. 5.36.

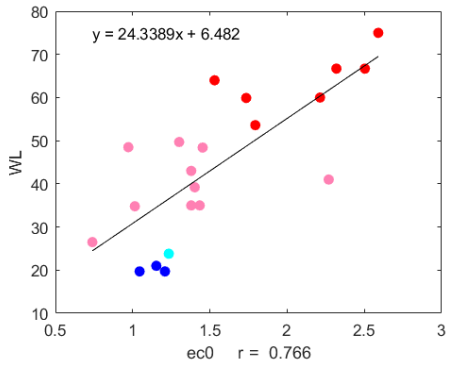

Figure 5.36: Correlation between the parameter e_{c0} and liquid limit W_L

Parameter α

The most suitable correlation was found between the parameter α and content of clay partcles, see Fig. 5.37. The inverse proportion implies that with increasing

content of sand the peak friction angle φ_p increases similarly to the critical state friction angle φ_c.

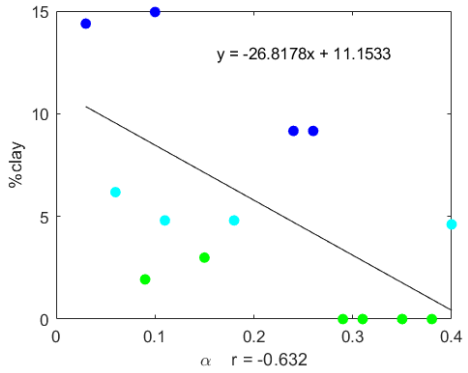

Figure 5.37: Correlation between the clay particles content and α

Parameter β

The best correlation was found between the parameter β and n as already mentioned above.

Parameter φ_c

Correlations for the parameter φ_c were already established in the section dedicated to the hypoplastic clay model.

5.3 Summary of the observerd correlations

The correlations for both hypoplastic models were performed in this chapter with simple linear and nonlinear regression adopted. The hypoplastic clay parameters were possible to correlate on the whole range of soil classes for the reconstituted soil as illustrated in Appendix B. In the case of parameters λ^*, κ^* and N it was possible to find a clear mutual linear correlation. These parameters were further correlated with Atterberg's limits. These parameters were clearly selected in Section 4.2 *Sensitivity analysis* as the crucial parameters for the model relevant simulation. Given the fact that the parameters λ^* and N are independent of the soil state, i.e., reconstituted or natural, the correlation of the parameters λ and N can be considered as a key finding. The critical state friction angle φ_c was found to be well correlated with the content of clay and sand particles, which corresponds to the observations. The correlations for the parameters κ^* and ν was also performed on the natural specimens. Even though the parameter κ^* was found to be directly correlated with the initial void ratio, the parameter ν was not possible to properly correlate. However, in Section 4.2 *Sensitivity analysis*, it was revealed that the hypoplastic model is the least sensitive to the parameter ν. Furthermore, the values of parameter ν of calibrated specimens were observed to fall within the limits $\nu \in < 0.2, 0.3 >$. Therefore, it is reasonable to estimate parameter ν within those boundaries.

The hypoplastic sand model, however, was not possible to conclusively correlate as rather trends were observed then the sound correlations. Experiments executed on the reconstituted soils were used for the correlation study. However, the fine grained soils were predominantly left out as they did not well correlate and created a separate groups in the correlation plots. The parameter h_s was observed to correlate with the initial void ratio e_{i0} even with the fine grained soils. The nonlinear relation was suggested and this relation can be seen as a counterpart to the correlation between the parameters N and λ^*. The parameter n controlling the nonlinear shape of NCL was observed to well correlate with the stiffness driving parameter β and with the critical state friction angle φ_c. It was observed in case of the parameter β that the fine grained soil distinctly reached

the limiting value of the parameter β and created a non-correlating group. This might be caused by the nature of calibration as well as characteristics of the soil grains. Correlations from the study [1] were complemented with new data and compared. The proposed trend of the parameter n with the variable x from [1] was verified although the complemented chart created a bilinear line. It is worth noting that the parameters calibrated in [1] were determined using Eqns. (2.0.6)–(2.0.11). The comparison of all calibrated data were not presented. The initial void ratio was found to be well correlated with Atterberg's limits. However, these characteristics were not determined for all coarse grained soils and thus the clear conclusion cannot be in this case proposed. The parameter α was found to be inversely correlated with the content of clay particles.

The correlation was performed only on the available specimens and it might be necessary to extract data from available publications or libraries such as laboratory data available by Prof. Torsten Wichtmann to make better conclusions. This is particularly true in the case of hypoplastic sand model.

6. Hypoplastic sand model implementation to GEO5 FEM

The final chapter is dedicated to the implementation of Wolffersdorff's hypoplastic sand model described in the Section 1.2.2. The model was implemented into the GEO5 FEM (Finite Element Method) software and thus complemented the library of constitutive models.

The reliability of the implementation was tested against software Triax developed by Masin [55].

6.1 Element model in GEO5

Two-element model was created to test the implementation of the hypoplastic sand model in GEO5 FEM. To properly simulate a stress distribution in FEM, the axisymmetric analysis was selected instead of plain strain. The difference in both analyses is well characterized by Fig. 6.1.

The plain strain analysis, see Fig. 6.1a, considers a infinite length of the FEM model along its longitudinal axis which results in zero strains in this direction, i.e. $\varepsilon_z = 0$, however, the stress σ_z is calculated from the Hook's law. Therefore, all the quantities of stresses, strains and loadings are conveniently determined for the longitudinal length of 1m as Fig. 6.1a indicates. This analysis is, therefore, suitable for a design of structures where the longitudinal dimension considerably exceeds the transverse dimensions such as foundation pits, tunnels and other structures related to traffic. The following quantities are associated with the plain strain analysis

$$\boldsymbol{\sigma}^T = (\sigma_x, \sigma_y, \sigma_{xy}, \sigma_z), \tag{6.1.1}$$

$$\boldsymbol{\varepsilon}^T = (\varepsilon_x, \varepsilon_y, 2\varepsilon_{xy}, \varepsilon_z). \tag{6.1.2}$$

The axisymmetric analysis represents the body symmetric along its vertical

axis showing Fig. 6.1b, where Θ represents a circumferential direction and r a diameter. Furthermore, the resulting circumferential strain is defined as $\varepsilon_\Theta = u/r$ and thus is not zero. The axisymmetric model is suitable for structures symmetric along the vertical axis such as circular foundations or foundation piles. These stress and strain quantities are related to the axisymmetric analysis

$$\boldsymbol{\sigma}^T = (\sigma_x, \sigma_y, \sigma_{xy}, \sigma_\Theta), \tag{6.1.3}$$

$$\boldsymbol{\varepsilon}^T = (\varepsilon_x, \varepsilon_y, 2\varepsilon_{xy}, \varepsilon_\Theta). \tag{6.1.4}$$

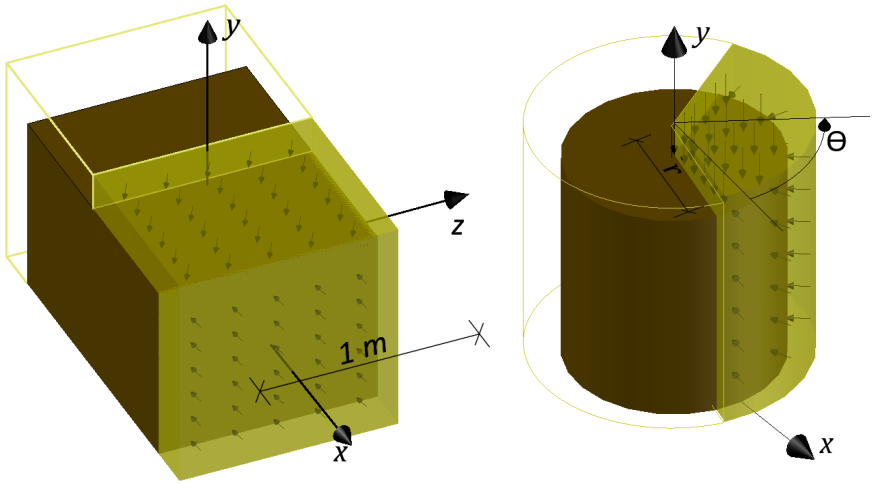

(a) Plain strain analysis

(b) Axisymmetric analysis

Figure 6.1: Analyses employed in GEO5 FEM

6.1.1 Two-elements model

The axisymmetric model was created in the GEO5 FEM consisting of two elements as depicted in Fig. 6.2. This setting of the model is complemented for individual tests with particular boundary conditions in the form of supports elements and imposed stresses and strains.

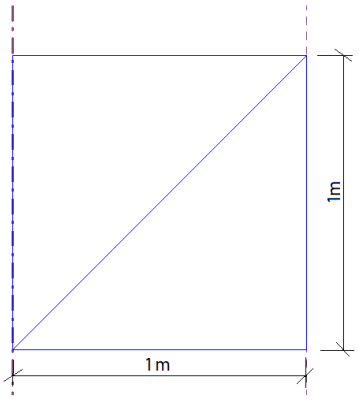

Figure 6.2: Two elements model

Verification of the implementation was tested on the sand specimen Dobrany with parameters of the hypoplastic sand model calibrated by ExCalibre; the values are presented in Tab. 6.1. The weight of soil γ was set to 0 kN/m^3.

Table 6.1: Doprany - Values of hypoplastic sand parameters

h_s	n	e_{i0}	e_{c0}	e_{d0}	α	β	φ_c
52635	0.178	1.507	1.250	0.629	0.178	4.2	36.5

6.1.2 Oedometric test

To simulated the oedometric test, the boundary conditions were set such that the horizontal movement was restricted while the vertical movement was enabled. A simulation of the oedometric test was driven by stress, see Fig. 6.6.

The simulation of the specimen Dobrany was divided into three phases: consolidation, loading, unloading. Since the loading phase of the oedometric test starts from the vertical stress state σ_a = 8kPa and the initial void ratio e_{init} = 0.996, the consolidation phase, see Fig. 6.3a, was underwent with an elastic material. In this way, the vertical consolidation would rise upto σ_a = 8kPa and the initial void ratio e_{init} would be at the required value once the loading is initiated.

The specimen is loaded upto σ_a = 1200kPa and subsequently unloaded

down to 10kPa.

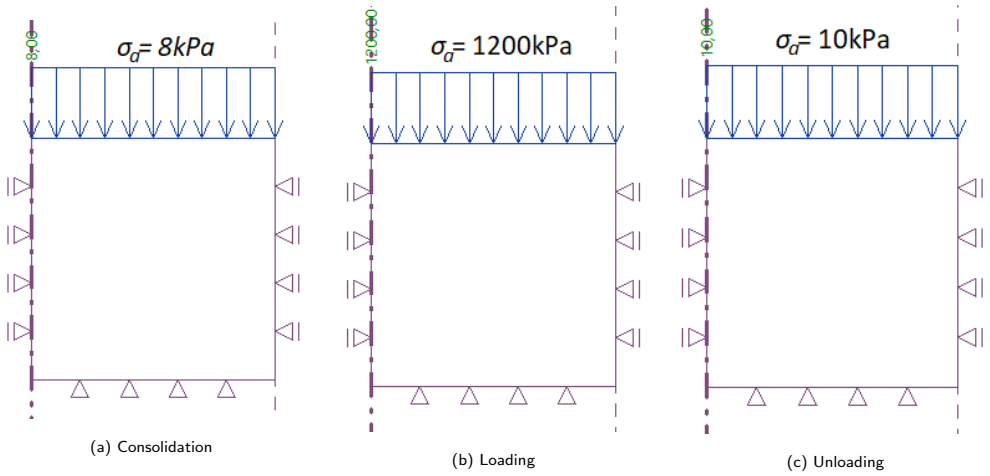

(a) Consolidation (b) Loading (c) Unloading

Figure 6.3: Dobrany - simulation of oedometric test

6.1.3 Triaxial test

The drained triaxial test CID-REC-1 is simulated in a similar manner with two-elements model. The boundary conditions of this model allow both vertical and horizontal movement while the axis is fixed. The test procedure is split once again to preset consolidation (initial stress level) and vertical loading.

The consolidation is driven by strain as Fig. 6.4a shows. Because the loading of the experiment starts from a combination of stresses $p = 50.92$kPa and $q = 2.76$kPa, the strain driven consolidation is non-uniformly distributed along the surface of model with axial and radial strain set to $\varepsilon_a = 1.1 \times 10^{-3}$ and $\varepsilon_r = 1.0 \times 10^{-3}$, respectively. In order to initiate the loading phase with $e_{init} = 0.508$, the elastic material was used for consolidation phase.

The loading phase was induced by a vertical strain $\varepsilon_a = 0.276$, see Fig. 6.4b.

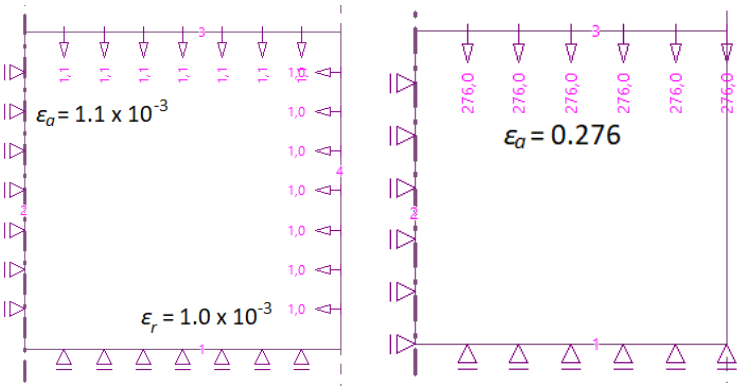

(a) Consolidation (b) Loading

Figure 6.4: Dobrany - simulation of oedometric test

6.2 Implementation

In GEO5 FEM, it is possible to obtain the calculated state variables for a given point with aid of the tool called Monitors. In general, only the final values of calculated variables are available for a given phase and a complete history of the evaluated quantities is not available. However, to implement the hypoplastic sand model, the source code of GEO5 FEM software was available and therefore, it was possible to debug GEO5 and let all the state variables write into a text file and later graphically displayed.

6.2.1 Two-elements model Verification

Prior to the implementation, the two-elements model was tested on the hypoplastic clay model [19] which is implemented in the GEO5 FEM and software Triax. The Bilina1 specimen and its oedometric experiment was selected for the simulation, the parameters are gathered in Tab. 6.2. The simulation was performed with the void ratio $e_{init} = 0.443$. The specimen was loaded upto $\sigma_a = 2415$kPa and unloaded down to $\sigma_a = 7.56$kPa.

Table 6.2: Bilina1 - Values of hypoplastic clay parameters

λ^*	κ^*	N	r	φ_c
0.049	0.005	0.692	0.330	25.4

The comparison of both softwares GEO5 FEM and Triax simulation of the oedometric experiment is displayed in Fig. 6.5. Only small deviations were observed between the two simulations. Each software uses a different method for integration of a differential constitutive equation. The software GEO5 FEM uses Runge-Kutta-Felberg 45, see Section 3.0.3, while Triax uses Euler method, see Section 3.0.2; a step size and preset limiting error also play a role. The two element model is thus sufficient to perform a comparative study between numerical simulations and experiments.

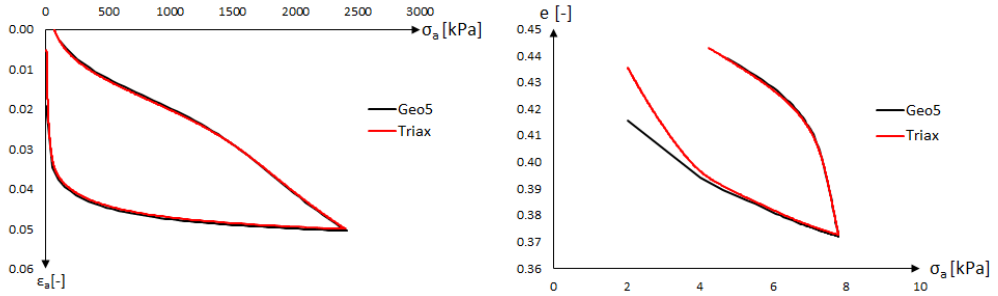

(a) $\sigma_a \times \varepsilon_a$ (b) $\ln \sigma_a \times e$

Figure 6.5: Comparisson of Bilina1 simulations

6.2.2 Hypoplastic sand model verification

The simulation of the oedometric and drained triaxial experiment for the specimen Dobrany is shown in Fig. 6.6. The comparisons are complemented with simulation results of a single element used in ExCalibre. The comparisons indicates the hypoplastic sand model is well implemented.

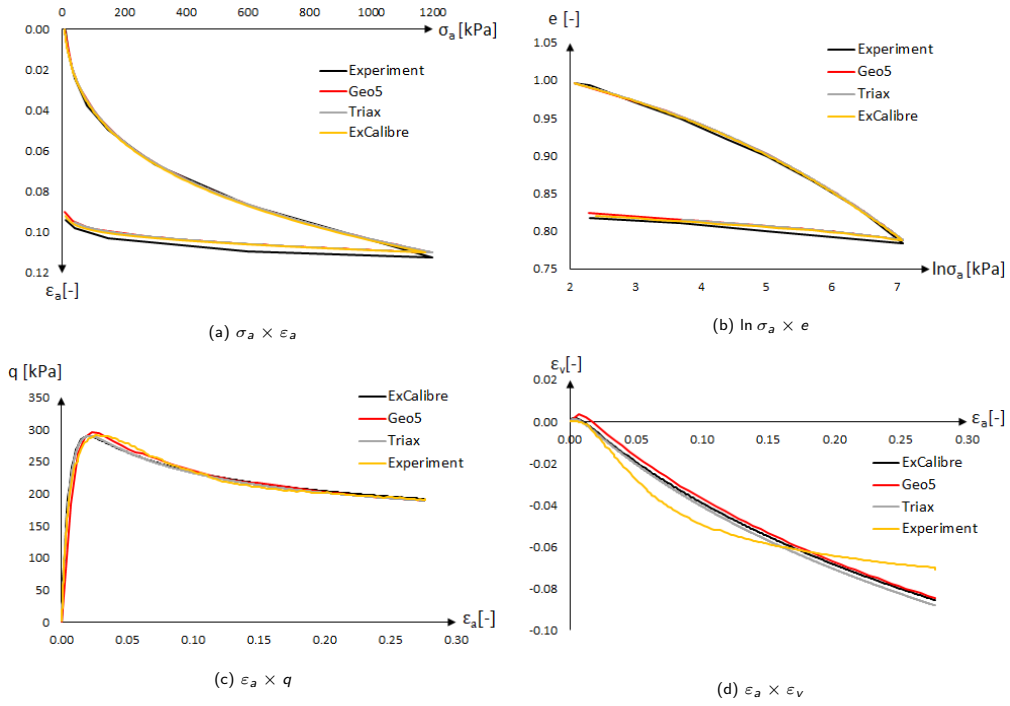

(a) $\sigma_a \times \varepsilon_a$ (b) $\ln \sigma_a \times e$

(c) $\varepsilon_a \times q$ (d) $\varepsilon_a \times \varepsilon_v$

Figure 6.6: Comparisson of Dobrany simulations

The drawback of the implementation was revealed once the void ratio e comes close or beneath the void ratio at the max density e_d, which evolution is defined by Eq. (1.2.37)–(1.2.40). This was revealed during the simulation of unloading of oedometric test. The relation between the void ratio e and the limiting void ratio e_d influences the pyknotropy factor f_d in Eq. (1.2.34) through Eq.(1.2.35). Since the value of void ratio e should not be bellow the limiting void ratio e_d the limiting value of the pyknotropy factor should be $f_d = 0$. The hypoplastic equation defined by Eq. (1.2.17) then transforms into the hypoelastic form given by

$$\mathring{\boldsymbol{\sigma}} = f_b(e, \boldsymbol{\sigma}) f_e(e) \mathbf{L}(\hat{\boldsymbol{\sigma}}) : \mathbf{D}. \tag{6.2.1}$$

Therefore, a switch function was implemented. Once the void ratio e reaches its limiting value e_{d0}, the pyknotropy factor holds $f_d = 0$, which secures that f_d does not decrease to a negative value.

6.3 Simulations in GEO5

Apart from the two-elements model, a large scale model was tested as well in order to fully test the reliability of the implementation. A simple model of the foundation with loading and unloading phase was tested with the parameters of the hypoplastic sand model selected according to Tab. 6.1 for the specimen Dobrany. The plain strain analysis was used in this case.

6.3.1 Foundation

The FEM model was created in dimensions 30 $\times$ 15m with the structure of foundation in the middle of the model. The length of the element edge was chosen $L = 1$m with the area of radius $r = 5$m around the foundation refined to the length of $L = 0.1$m, see Fig. 6.7.

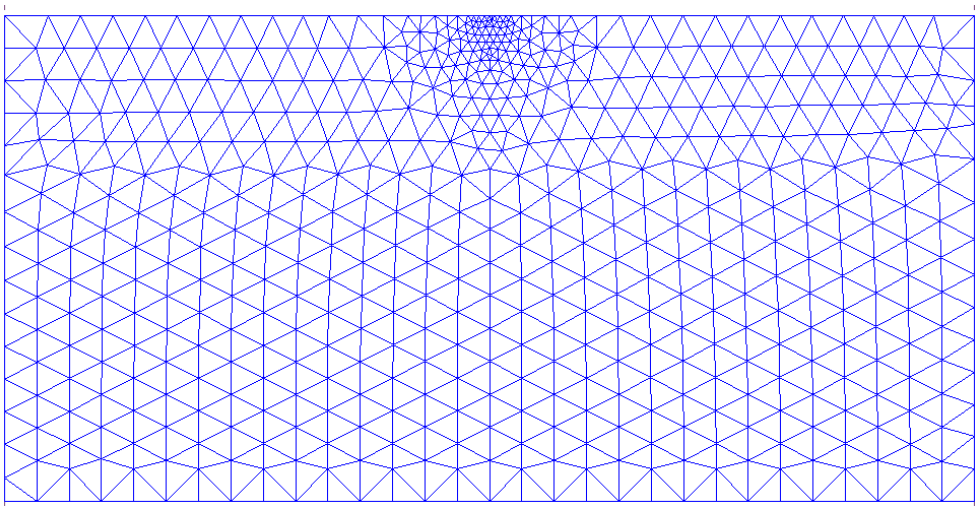

Figure 6.7: FEM mesh in GEO5

The construction of foundation was divided into three phases:

- Initiating stress state
- Loading
- Unloading

The geostatic stress was initiated similarly to simulation of the laboratory experiments by the elastic analysis in the first stage. The weight of the soil was set $\gamma = 20$ kN/m^3 and a uniform vertical loading of the surface of the value f_z = 10kPa was applied. To obtain an accurate values of beneath the foundation, the tool Monitor was used.

The structure o foundation was selected of an infinite stiffness and width of 2m. The loading of the foundation was driven by settlement in the magnitude w_z = 120mm, which is a maximal average settlement of the foundation supporting a structure of building according to ČSN EN 1997. The results of the second phase are displayed in Fig.6.8. The maximal vertical stress σ_z reached in the middle of the foundation during the loading is $\sigma_z = 76.47$kPa, which is clearly within the limits of the performed oedometric test, which was loaded approximately upto σ_a = 1200kPa. A distribution of the settlement in Fig. 6.8b and distribution of the void ratio in Fig. 6.8c well illustrates a restriction of the plastic zone beneath the foundation and transformation of and distribution of loading to the soil mass.

The unloading in the phase three was executed so that the vertical stress beneath the foundation decrease to the initial value of $\sigma_z = 10$kPa, see Fig. 6.9a. The resulting settlement is $w_z = 100$mm, which is shown in Fig. 6.9b, while redistribution of the void ratio e in the soil mass can be seen in Fig. 6.9c.

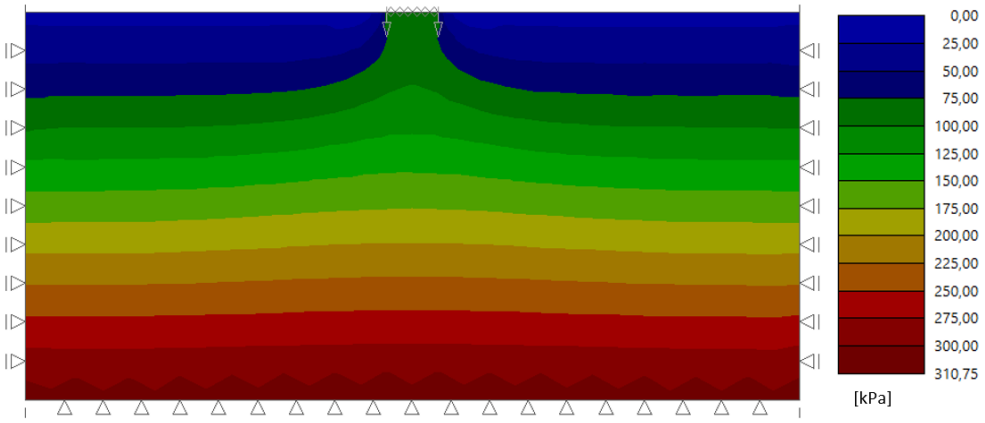

(a) Distribution of vertical stress σ_z

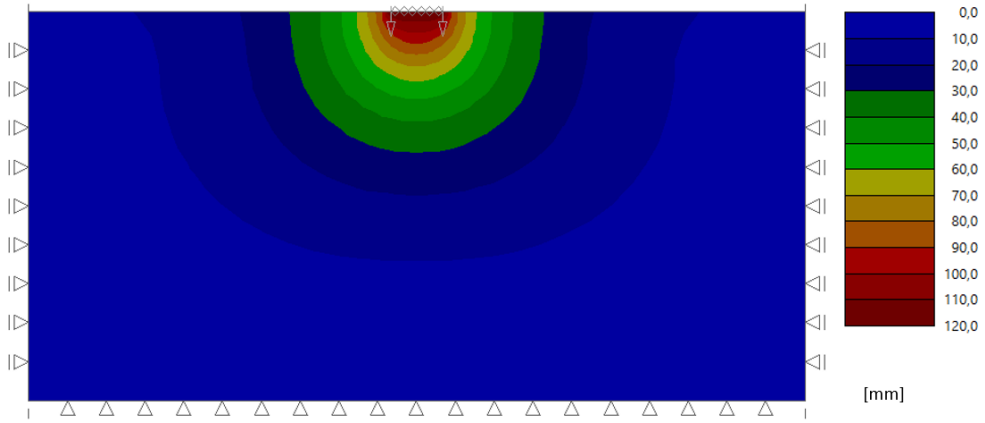

(b) Distribution of vertical settlement w_z

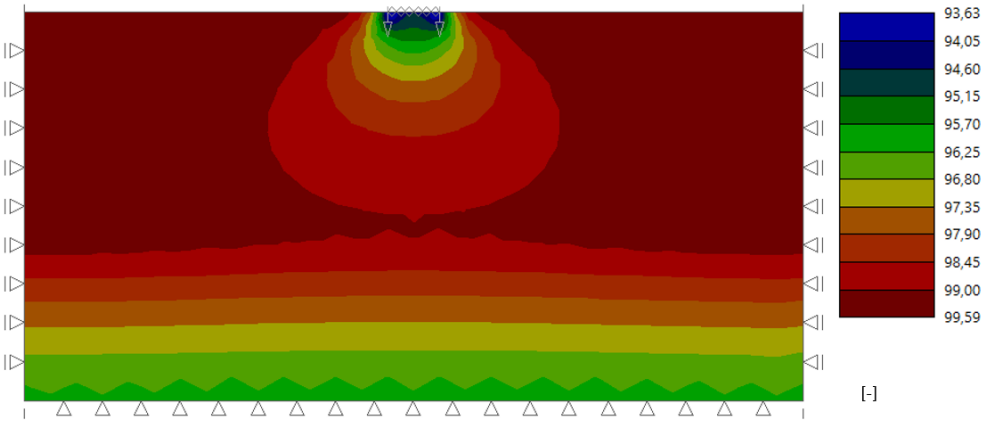

(c) Distribution of void ratio e

Figure 6.8: Foundation settlement - Phase 2

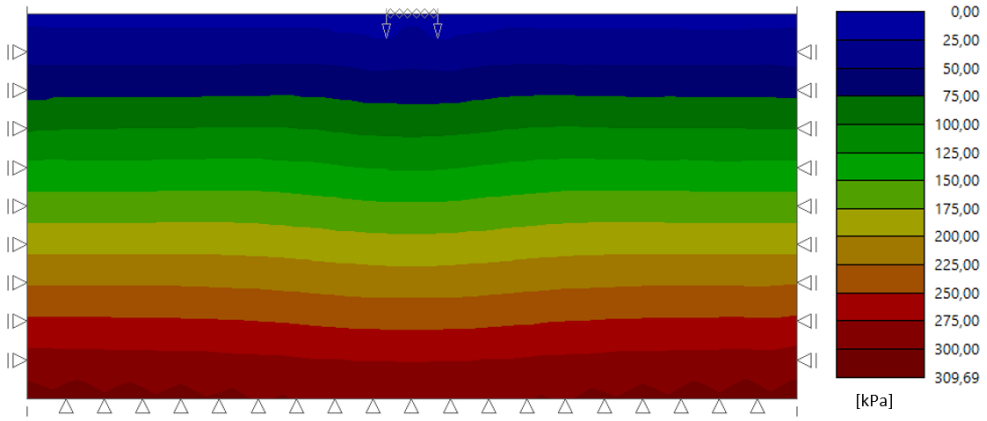

(a) Distribution of vertical stress σ_z

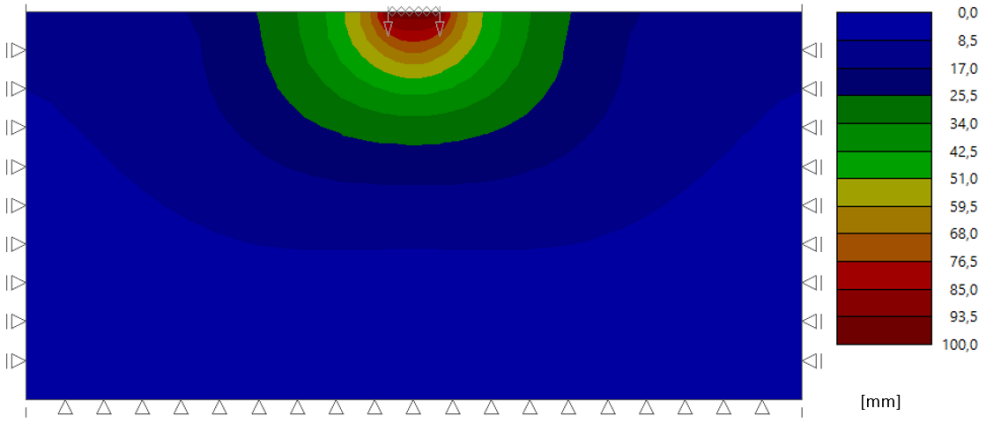

(b) Distribution of vertical settlement w_z

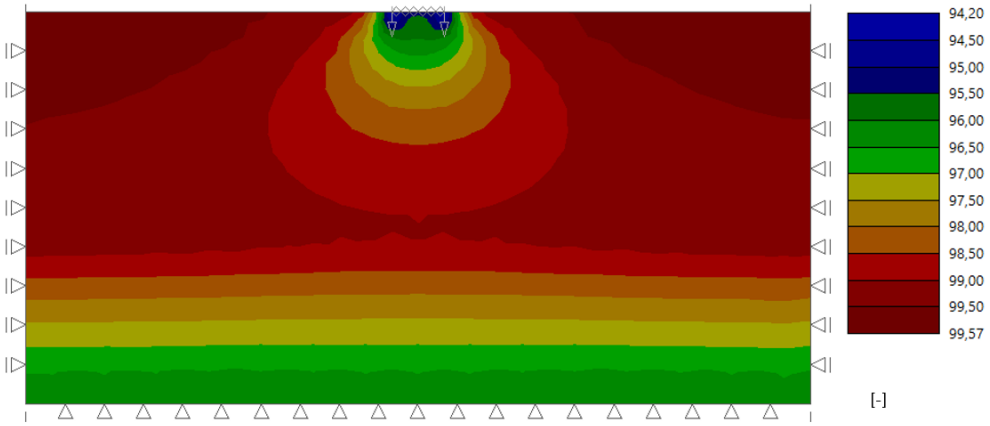

(c) Distribution of void ratio e

Figure 6.9: Foundation settlement - Phase 3

Conclusions

This thesis was concerned with the advanced constitutive models and development of the calibration procedures aiming at facilitating their use in various engineering tasks. Three constitutive models were selected to well represent the group of the critical state models, namely, the elastoplastic Modified Cam-Clay [2], Wolffersdorff's hypoplastic sand [4] and Masin's hypoplastic clay model [3].

The first chapter was dedicated to the theoretical description of elastoplastic and hypoplastic models. Each theory was described with leading constitutive equations and relevant examples. A distinct feature of the elastoplastic models is a switch function $h(F)$ changing a model response from elastic to plastic or elastoplastic once the yield surface F is reached. This results in a separation of the elastic $\mathrm{d}\boldsymbol{\varepsilon}_{el}$ and plastic $\mathrm{d}\boldsymbol{\varepsilon}_{pl}$ component of the total strains $\mathrm{d}\boldsymbol{\varepsilon}_{tot}$ increments. Furthermore, the elastoplastic models require an assumption of direction of the plastic increment occurring perpendicular to the plastic potential G. The switch function is source of undesired obstacles in implementation as the intersection of loading path in the stress space with the yield surface has to be precisely determined to change a model response.

The hypoplastic models do not possess the switch function $h(F)$ and an evolution of state variables is given by one tensorial function. The initial works on hypoplasticity showed that the models inherently possess a limit and boundary surface as a consequence of particularly selected tensorial function [9]. Niemunis later in [15] derived relations to independently determine the direction of the strain increment $\mathbf{m}$ and the shape of the limit surface f.

The recommended calibration procedures for both hypoplastic models were

reviewed and other methods were suggested where needed in the third chapter. The fourth chapter was dedicated to the solution method of differential functions and Newton's optimization methods used in the thesis.

The calibration software ExCalibre was described in the fifth chapter which calibrates parameters of the three selected constitutive models on the bases of laboratory experiments. The development of the calibration software itself was preceded with an assessment of published calibration softwares and approaches to the evaluation of the models parameters. Even though the deterministic method suffer from a localization of the local minimum, when provided with a reliable initial guess the convergence is stable and prompt. In case of the critical state models the asymptotic driving parameters can be well estimated directly from the laboratory experiments while a stiffness driving parameters can be optimized independently. Therefore, a deterministic approach was selected for the optimization processes.

In order to properly determine the optimization procedures for each constitutive model a sensitivity study was conducted. This study aimed at finding an importance and effect of each parameter on models predictions. Therefore, experiments of five fine grained soil were chosen for the sensitivity study in case of the Cam-Clay and hypoplastic clay model and five coarse grained soils were selected in case of the hypoplastic sand model. The sensitivity study revealed a crucial importance of the asymptoty driving parameters in all three cases. Conveniently, both the Cam-Clay and hypoplastic clay model showed identical sensitivities which implied that the parameters of both models can be calibrated with the same calibration methods. The study performed on the fine grained soils revealed the most important parameters N and λ^* in case of the hypoplastic clay model and e_0 and λ in case of the Can-Clay model, which control the position of INCL in the $\ln p \times e$ space. This was found with respect to the error functions $E(\varepsilon_a)$ in case of oedometric tests and $E(q)$ in case of undrained triaxial tests. The critical state friction angle φ_c was found as the third most important parameter, however, with a less significant effect. The models were observed to be less sensitive towards the stiffness driving parameters κ^*, κ and ν, but an increased

importance was found for the error function $E(\varepsilon_a)$ in case of undrained triaxial tests. This was particularly true for the Cam-Clay model. It is worth noting that the specimens selected for the sensitivity study were in reconstituted state and this might have caused a less significant sensitivity for the parameter κ^* in case of oedometric tests. The sensitivity study performed on the hypoplastic sand model have shown a similar effect of the *INCL* controlling parameters, namely parameters h_s, n and e_{i0} in case of the oedometric test. However, for triaxial drained test the highest senstitivity was observed for the critical state friction angle φ_c for both error functions $E(\varepsilon_a)$ and $E(q)$. The parameters α and β did not show distinct impacts in the model model prediction. The observed sensitivities were considered when developing the calibration software.

The last section of the fifth chapter was dedicated to the thorough description of the calibration software ExCalibre. Developed calibration procedures were tested and subsequently approved after cooperation with Masin's team at the Charles University in Prague. The software was written in the $C\#$ code and is currently available on *www.soilmodels.com*. The software was tested on the experiments gathered from twenty six locations of various classes and classify according to USCS. Parameters of each of these soils are available in the library on the website of the software.

The correlations in the sixth chapter were sought for both hypoplastic models. Even though some experiments were removed from the correlations due to the concerns regarding the quality, they were still important during the verification of the calibration software. The correlation of the hypoplastic clay model was divided into two parts. First, it was focused solely on the correlations for reconstituted soils since the specimens are often tested in its natural undisturbed form. A strong correlation was observed between the parameters N a λ^* with $r = 0.934$. These parameters were further correlated with Atterbergs's limits where the correlation coefficient appear approximately $r \approx 0.9$. The parameter κ^* was found to be well correlated with the parameter λ^* where $r = 0.923$. The critical state friction angle was directly correlated with content of sand ($r = 0.79$) and indirectly with the content of clay particles ($r = -0.856$). The parameter ν

was not possible to properly calibrate, however, a trend of correlation with the parameter λ^* was observed. Interestingly, the hypoplastic model was possible to well correlate across the USCS classes. Given the fact that the parameters λ^*, N and φ_c control the asymptotic behaviour of the model, the parameters κ^* and ν was observed of a distinct differences between reconstituted and natural specimens. The parameter κ^* was then observe to well correlate with the initial void ratio where $r = 0.826$. The parameter ν was not possible to further correlate with any available attributes by the means of the linear and nonlinear regression.

The hypoplastic sand model was possible to correlate predominantly with coarse grained soils. Nonlinear regression was used for the correlation between the parameters h_s and e_{i0} for various USCS classes. This correlation was also confirmed for the coarse grained soils only. The parameter n was found to be well correlated with the parameters β and φ_c. In case of the parameter n, the complementary study was also performed with the data extracted from [1]. The premise that n indirectly correlates with d_{50} and directly with C_u was confirmed. However, the complemented data created a bilinear chart. The initial limiting void ratios represented by e_{c0} was found to be correlated with Atterberg's limits. Unfortunately, these data were not available for all coarse grained soils. The parameter α, which affects the peak fricion angle φ_p, was indirectly correlated with a content of clay particles. This implies a similarity with the critical state friction angle φ_c.

The last chapter was briefly dedicated to the implementation of the hypoplastic sand model into the GEO5 FEM software. The implementation was tested against the software Triax, developed by Masin. Triax is a single element software simulation basic laboratory experiments for various constitutive models. The primary testing of the implementation was executed on a two-elements model. Suitability of the two-elements model was initially tested on the hypoplastic clay model. The basic laboratory experiments were simulated and compared with Triax and ExCalibre. Once verified, the implementation was tested on a large scale model simulating simple loading and unloading of a foundation. It was then revealed the complication during an unloading once the void ratio e

reaches its limiting value e_d. It was determined that once the void ratio reaches the value $e = e_d$ thy pyknotropy function holds $f_d = 0$ and void ratio keeps $e = 0$.

The purpose of this thesis was to facilitate the use of the advanced soil models and thus extend their use into practice since these models are predominantly used in academic studies. Free to use software ExCalibre does not require any additional skill and knowledge regarding the advanced constitutive models and provides prompt and reliable calibration. The software ExCalibre now gathers an uploaded data in an exchange for the use. Therefore, the collection of soil used for the correlations will be extended in the future and the correlations will be improved even though the correlation performed in this study showed significant trends.

Appendices

A. Available specimens

Table A.1: Available locations and performed experiments

Location	USCS	OED		ISOT		CID		CIUP	
		NAT	REC	NAT	REC	NAT	REC	NAT	REC
Dobrany	SW	-	1	-	-	-	3	-	-
Hrusovany	SW	-	1	-	-	-	3	-	-
Chyne	SC	-	2	-	-	-	3	-	-
Jablonec	SM	-	1	-	-	-	3	-	-
Komorany	SW	-	4	-	-	-	4	-	-
Kralupy	SM	-	2	-	-	-	3	-	-
Motol	SC	-	2	-	-	-	3	-	-
Rohatec	SP	-	2	-	-	-	3	-	-
Stvanice	SM	-	1	-	-	-	3	-	-
Bangkok	CH	1	-	-	-	5	-	5	-
Bilina 1	CL	1	1	-	-	-	-	3	3
Bilina 2	CH	1	1	-	-	-	-	3	3
Bilina 3	CL	1	1	-	-	-	-	3	3
Bilina 4	CH	1	1	-	-	-	-	3	3
Bilina 5	CH	1	1	-	-	-	-	3	3
Bosilec	SC	1	1	-	-	-	-	-	3
Boston	CL	-	1	-	-	-	-	-	3
Brno	CH	1	-	-	-	-	-	4	-
Otaniemi	CH	-	-	-	4	-	-	3	-
Vantilla	CH	-	-	-	2	-	-	5	-
Hajek	CL	1	1	-	-	-	-	3	3
Hong Kong	CH	-	-	-	1	-	2	-	4
Koper		3	3	-	-	-	-	3	-
Metro 1	CL	1	1	-	-	-	-	3	3
Metro 2	CL	1	-	-	-	-	-	3	3
Prackovice	CH	2	2	-	-	-	-	-	3
Prestice	CL	1	1	-	-	-	-	-	3
Senec	CL	1	1	-	-	-	-	-	3
Ujezd	CL	-	2	-	-	-	6	-	-
Weald	CL	-	1	-	-	-	3	-	3

B. Hypoplastic clay correlations

Table B.1: Table of reconstituted specimens characteristics

Location	λ	W	N	ν	φ	USCS	wL	wP	Ip	%f	%s	d10	d30	d60	Cu	Cc	clay%
bilina1	0.048	0.012	0.731	0.25	25.4	CL	49.7	26.9	22.8	64.64221	6.34406	0.001596	0.001596	0.031157	19.51589	0.05124	32.08014
bilina2	0.063	0.013	1.002	0.3	23.5	CH	59.9	25.5	34.4	92.21576	5.434984	0.001378	0.001378	0.004261	3.091862	0.32343	47.32068
bilina3	0.033	0.006	0.507	0.32	30.5	CL	26.5	15	11.5	71.85315	28.14685	0.001388	0.003691	0.032989	23.76712	0.297462	25.15796
bilina4	0.066	0.017	0.951	0.26	24.2	CH	53.6	27.7	25.9	90.79121	5.731267	0.001407	0.001407	0.003424	2.43293	0.411027	47.28817
bilina5	0.069	0.017	0.92	0.33	22.7	CH	64	30.5	33.5	94.92523	5.074771	0.001343	0.001343	0.002728	2.031892	0.492152	54.32436
bosilec	0.042	0.006	0.637	0.3	34.1	SC	21	13.3	7.7	41.1363	52.95757	0.0014	0.019417	0.348284	248.8543	0.773507	14.95385
boston	0.087	0.016	1.188	0.05	28.7	CL	41	20	21	88.73656	11.26344	0.000473	0.001354	0.012635	26.6967	0.306775	34.88483
chyne	0.028	0.002	0.707	0.4	31.8	SC	0	0	0	13.33064	79.82594	0.005347	0.157889	0.243616	45.55769	19.13627	9.162461
chyne2	0.027	0.001	0.706	0.4	31.8	SC	0	0	0	13.33064	79.82594	0.005347	0.157889	0.243616	45.55769	19.13627	9.162461
dobrany	0.038	0.008	0.843	0.01	36.5	SW	0	0	0	6.464707	89.82964	0.129842	0.32139	0.576085	4.43682	1.380901	1.933044
hajek	0.041	0.006	0.638	0.27	34.9	CL	48.5	22.6	25.9	56.95184	38.80278	0.001309	0.00207	0.087857	67.10376	0.037264	29.86095
hongkong	0.106	0.019	1.192	0.01	31.4	CH	60	28	32	74	26	0.002	0.00528	0.044634	22.3172	0.312246	27.5
hrusovany	0.041	0.01	0.685	0.01	36.8	SW	0	0	0	5.199965	43.35325	0.273377	0.99654	2.988679	10.93246	1.215483	2.993781
jablonec	0.06	0.015	0.775	0.01	42	SM	23.8	18.9	4.9	21.96239	52.03571	0.006277	0.173535	1.071327	170.6879	4.478516	6.180411
komorany	0.059	0.011	0.76	0.01	W	SW	0	0	0	0	65.9722	0.412414	0.820123	1.646576	3.992534	0.990474	0
komorany2	0.034	0.008	0.67	0.01	34.5	SW	0	0	0	0	65.9722	0.412414	0.820123	1.646576	3.992534	0.990474	0
komorany3	0.07	0.011	0.826	0.01	34.5	SW	0	0	0	0	65.9722	0.412414	0.820123	1.646576	3.992534	0.990474	0
komorany4	0.106	0.02	0.97	0.01	34.5	SW	0	0	0	0	65.9722	0.412414	0.820123	1.646576	3.992534	0.990474	0
koper1	0.105	0.021	1.34	0.24	35.3	CH	64	34	30	100	0	0.0013	0.0013	0.0013	1	1	100
koper2	0.091	0.019	1.144	0.26	35.3	CH	64	34	30	100	0	0.0013	0.0013	0.0013	1	1	100
koper3	0.108	0.018	1.219	0.23	35.3	CH	64	34	30	100	0	0.0013	0.0013	0.0013	1	1	100
kralupy	0.052	0.013	0.874	0.01	36.3	SM	0	0	0	23.74944	74.74826	0.015874	0.087795	0.203564	12.82392	2.385372	4.803895
kralupy2	0.043	0.01	0.845	0.12	36.3	SM	0	0	0	23.74944	74.74826	0.015874	0.087795	0.203564	12.82392	2.385372	4.803895
metro1	0.065	0.016	0.8	0.04	30.6	CL	34.8	20	14.8	64.94788	31.69649	0.001303	0.002419	0.034721	26.65665	0.129439	27.9628
motol	0.046	0.012	0.647	0.01	35.3	SC	19.7	12.5	7.2	27.90686	63.70999	0.00137	0.085576	0.590066	430.8374	9.061926	14.38916
motol2	0.038	0.009	0.605	0.01	35.3	SC	19.7	12.5	7.2	27.90686	63.70999	0.00137	0.085576	0.590066	430.8374	9.061926	14.38916
otaniemi1	0.119	0.007	1.47	0.16	25.3	WW	95	29	66	100	0	0.002	0.002	0.002	1	1	78
otaniemi2	0.097	0.015	1.506	0.01	25.3	CH	95	29	66	100	0	0.002	0.002	0.002	1	1	78
otaniemi3	0.115	0.006	1.515	0.15	25.3	CH	95	29	66	100	0	0.002	0.002	0.002	1	1	78
otaniemi4	0.134	0.008	1.545	0.13	25.3	CH	95	29	66	100	0	0.002	0.002	0.002	1	1	78
prackovice	0.089	0.025	1.162	0.15	28.8	CH	66.7	30.8	35.9	97.35778	2.642224	0.00131	0.00131	0.002926	2.232792	0.44787	49.33054
prackovice2	0.101	0.03	1.245	0.1	28.8	CH	66.7	30.8	35.9	97.35778	2.642224	0.00131	0.00131	0.002926	2.232792	0.44787	49.33054
prestice	0.063	0.015	0.847	0.08	30.5	CL	39.2	22.2	17	76.78132	23.21868	0.001359	0.001359	0.016691	12.28544	0.081397	38.07983
rohatec	0.015	0.003	0.615	0.13	34.3	SP	0	0	0	4.147722	92.67834	0.188071	0.355948	0.61119	3.249779	1.102238	0.148298
rohatec2	0.014	0.003	0.59	0.15	34.3	SP	0	0	0	4.147722	92.67834	0.188071	0.355948	0.61119	3.249779	1.102238	0.148298
senec	0.078	0.017	0.93	0.2	25.8	CL	48.4	25.8	22.6	75.57708	23.67326	0.00135	0.00135	0.012056	8.928096	0.112006	37.44518
stvanice	0.067	0.017	0.94	0.01	35.2	SM	0	0	0	31.55076	68.33324	0.009252	0.058164	0.161896	17.49883	2.258589	4.610634
ujezd1	0.083	0.021	1.057	0.28	31.1	CI	35	21	14	87.64989	12.35011	0.0013	0.0013	0.011283	8.679487	0.115214	40.33333
ujezd2	0.062	0.012	0.826	0.25	31.1	CI	35	21	14	87.64989	12.35011	0.0013	0.0013	0.011283	8.679487	0.115214	40.33333
vanttila1	0.136	0.011	1.674	0.09	22.8	CH	98	30	68	100	0	0.002	0.002	0.002771	1.385714	0.721649	51
vanttila2	0.125	0.007	1.607	0.2	22.8	CH	98	30	68	100	0	0.002	0.002	0.002771	1.385714	0.721649	51
weald	0.063	0.018	0.824	0.18	23.5	CL	43	18	25	100	0	0.002	0.002	0.002367	1.183333	0.84507	40
zajeci	0.097	0.026	1.244	0.01	27.2	CH	75	34.7	40.3	91.10379	8.896209	0.001355	0.001355	0.005889	4.347418	0.230022	40.00867

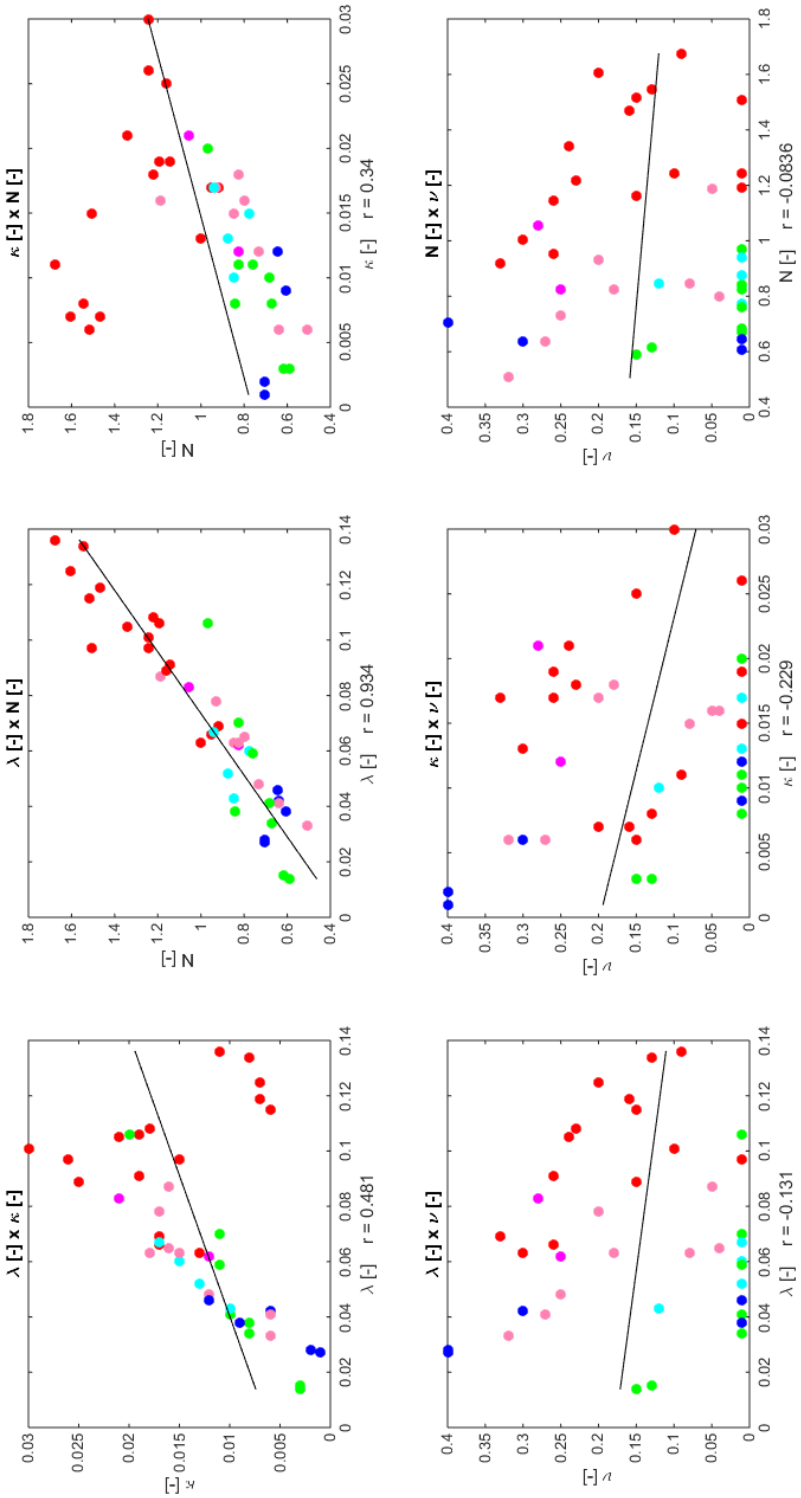

Figure B.1: Parameters correlations

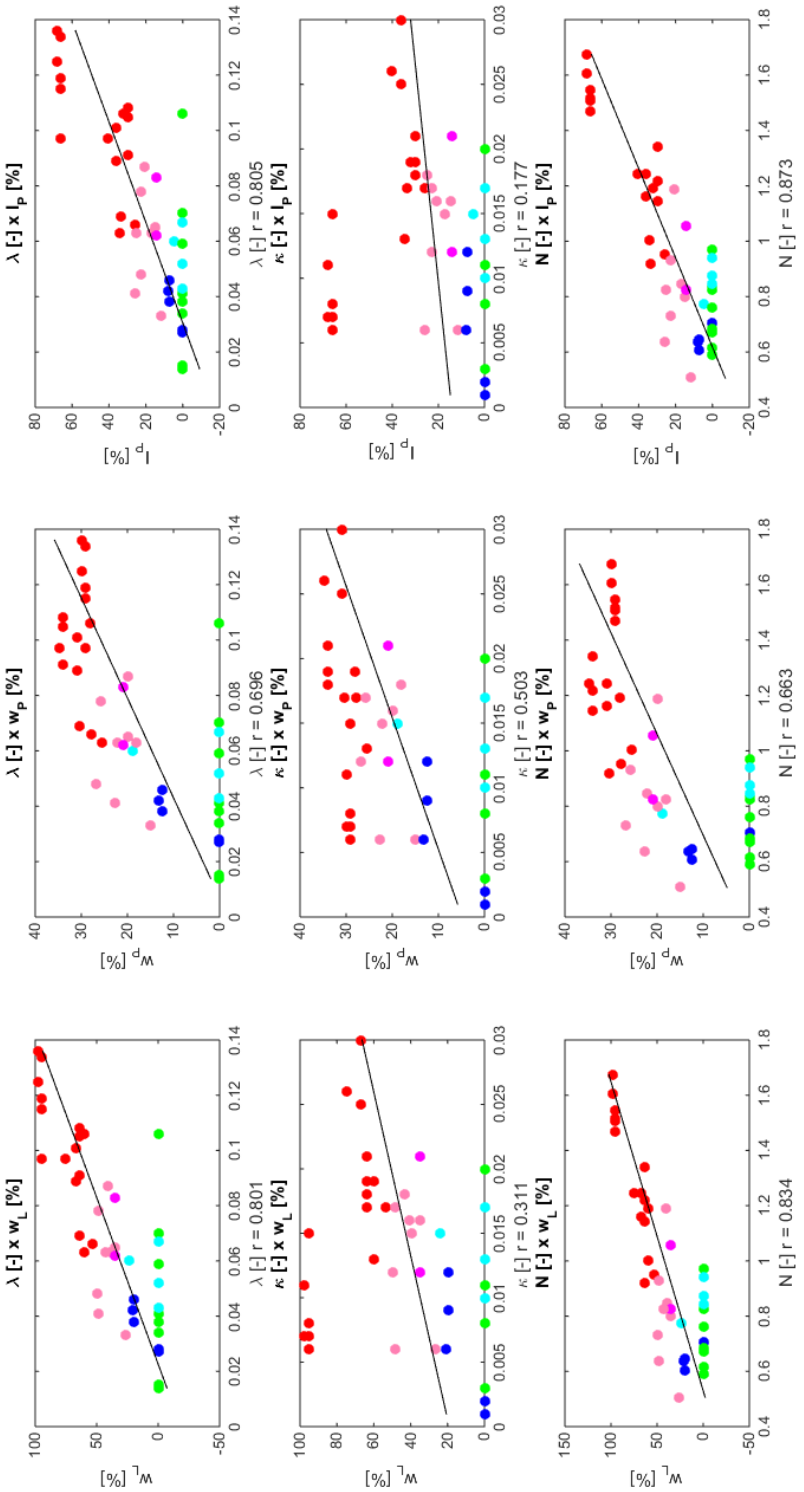

Figure B.2: Atterberg limits and parameters correlations 1

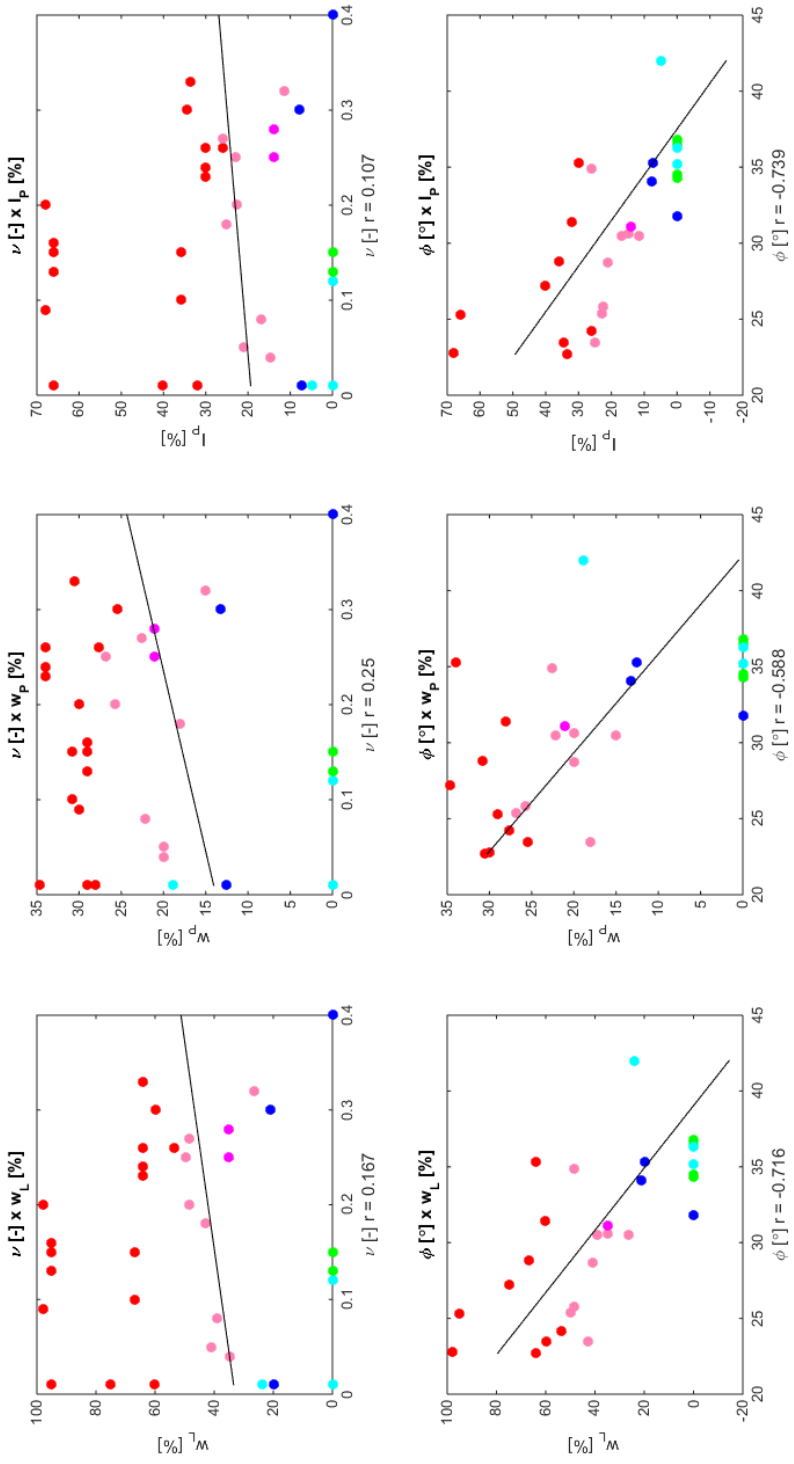

Figure B.3: Atterberg limits and parameters correlations 2

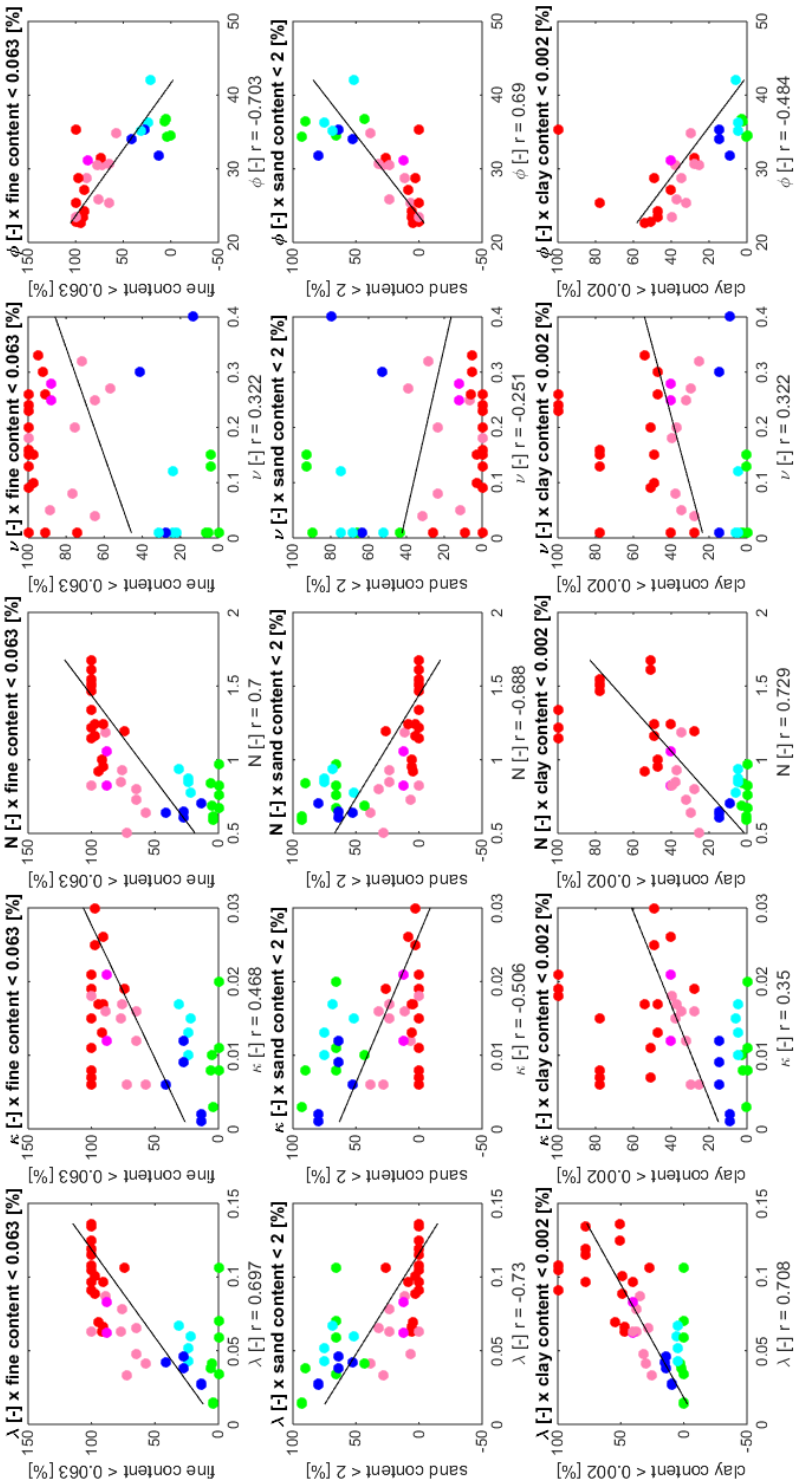

Figure B.4: Index and parameters correlations

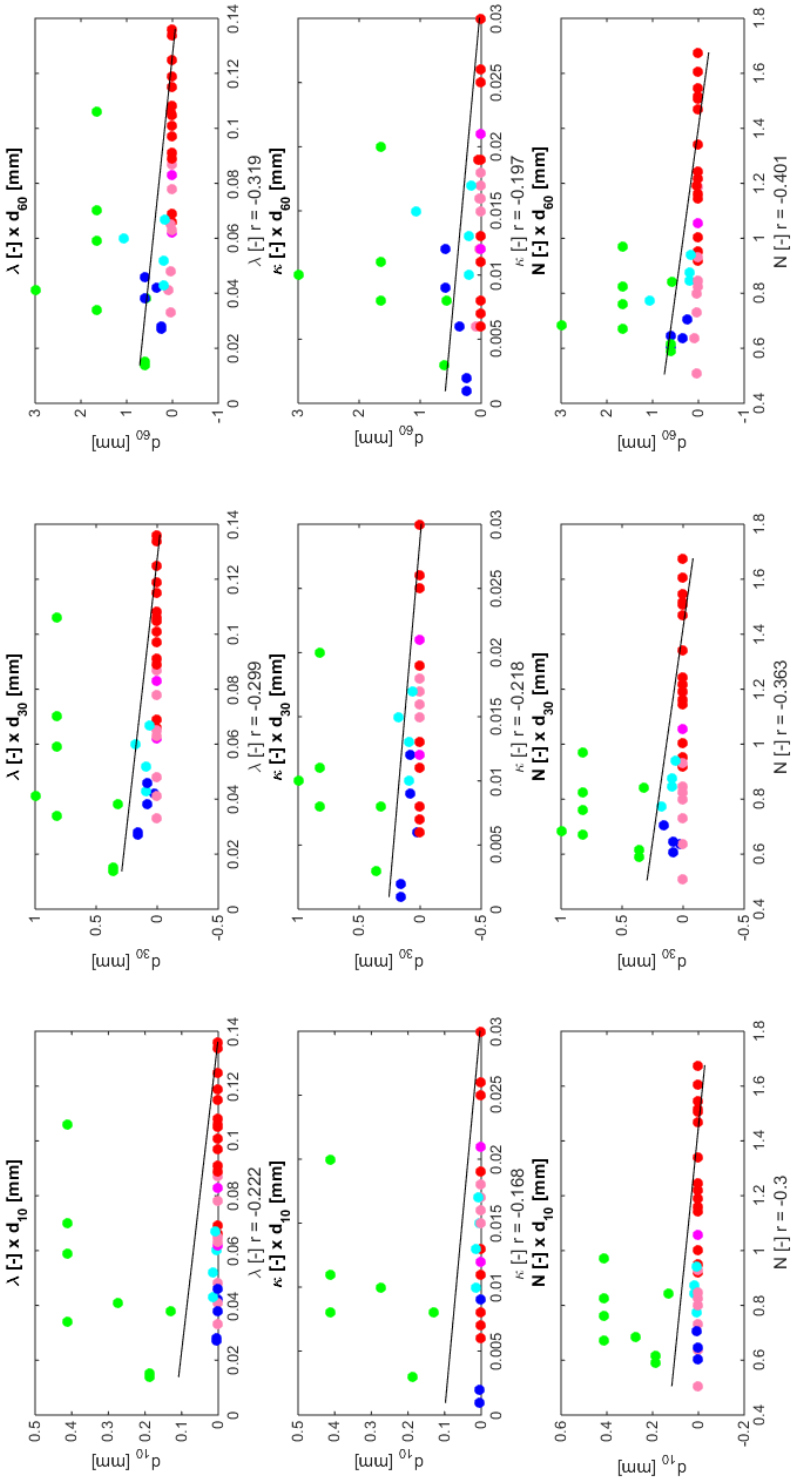

Figure B.5: Gradation and parameters correlations 1

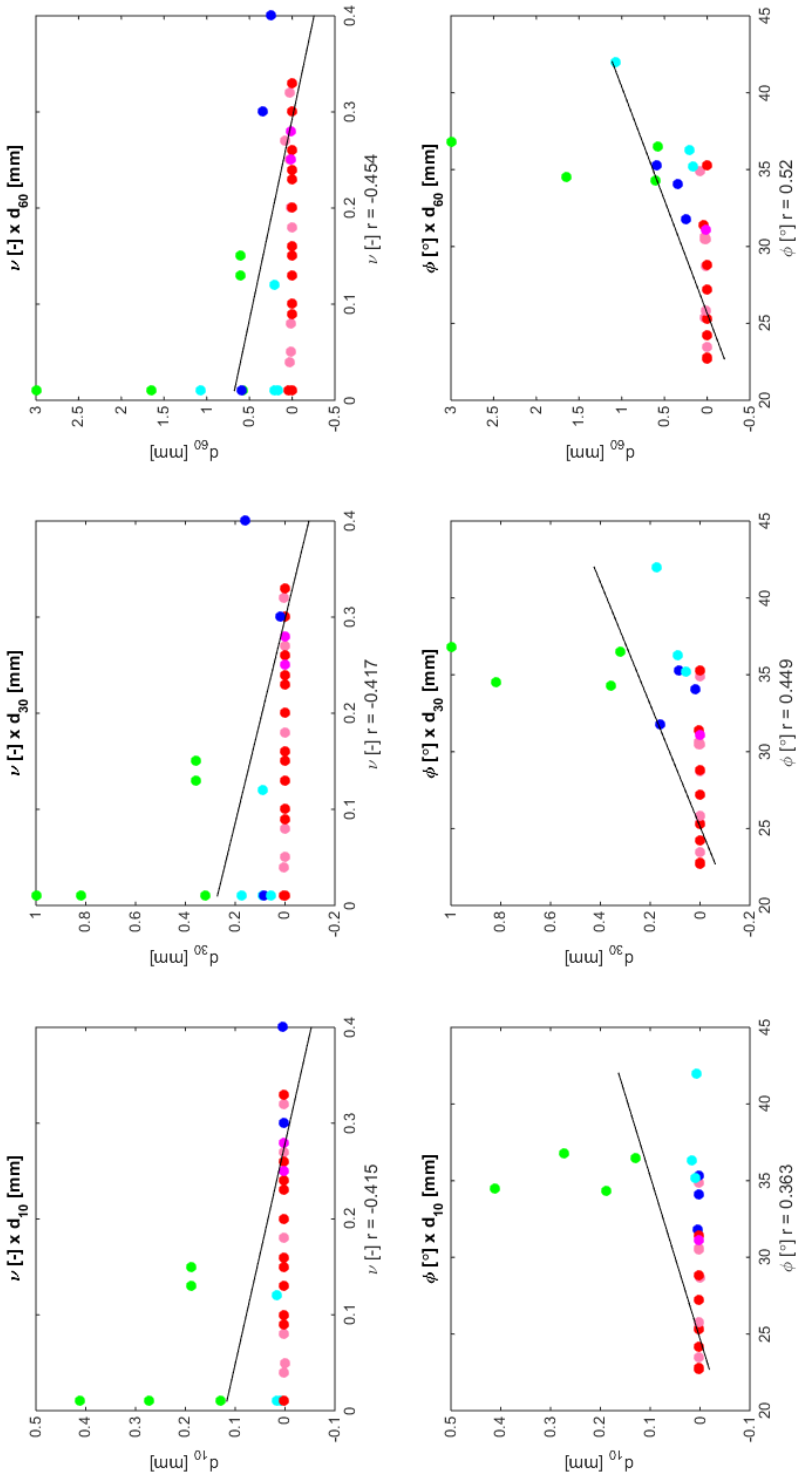

Figure B.6: Gradation and parameters correlations 2

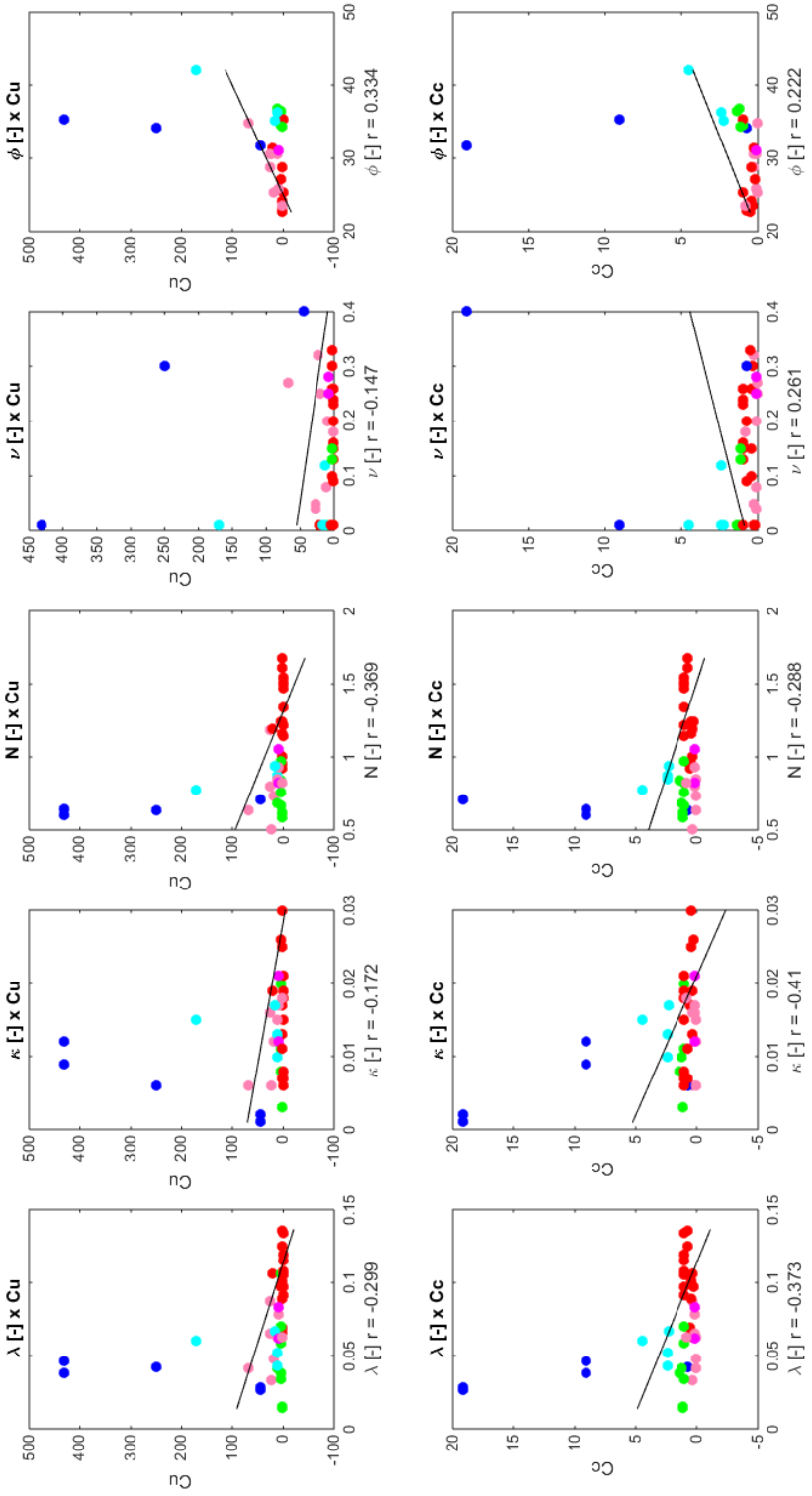

Figure B.7: Gradation and parameters correlations 3

	Location	e_{init}	λ*	κ*	N	v	ϕ	USCS	wL	wP	Ip	%f	%s	d_{10}	d_{30}	d_{60}	Cu	Cc	clay%
Reconstituted	bilinska1	0.6708	0.048	0.012	0.731	0.25	25.4	CL	49.7	26.9	22.8	64.6422	6.34406	0.0016	0.0016	0.03116	19.5159	0.05124	32.0801
	bilinska2	0.9824	0.063	0.013	1.005	0.3	23.5	CH	59.9	25.5	34.4	92.2158	5.43498	0.00138	0.00138	0.00426	3.09186	0.32343	47.3207
	bilinska3	0.4273	0.033	0.006	0.507	0.32	30.5	CL	26.5	15	11.5	71.8532	28.1468	0.00139	0.00369	0.03299	23.7671	0.29746	25.158
	bilinska4	1.021	0.066	0.017	0.951	0.26	24.2	CH	53.6	27.7	25.9	90.7912	5.73127	0.00141	0.00141	0.00342	2.43293	0.41103	47.2882
	bilinska5	0.8521	0.069	0.017	0.92	0.33	22.7	CH	64	30.5	33.5	94.9252	5.07477	0.00134	0.00134	0.00273	2.03189	0.49215	54.3244
	hajek	0.5909	0.041	0.006	0.638	0.27	34.9	CL	48.5	22.6	25.9	56.9518	38.8028	0.00131	0.00207	0.08786	67.1038	0.03726	29.861
	koper3	1.2136	0.108	0.025	1.219	0.23	35.6	C	64	34	30	100	0	0.0013	0.0013	0.0013	1	1	100
	metro1	0.6073	0.065	0.016	0.8	0.04	30.6	CL	34.8	20	14.8	64.9479	31.6965	0.0013	0.00242	0.03472	26.6566	0.12944	27.9628
	prackovic	1.5451	0.089	0.025	1.162	0.15	28.8	CH	66.7	30.8	35.9	97.3578	2.64222	0.00131	0.00131	0.00293	2.23279	0.44787	49.3305
	prackovic	1.7055	0.101	0.03	1.245	0.1	28.8	CH	66.7	30.8	35.9	97.3578	2.64222	0.00131	0.00131	0.00293	2.23279	0.44787	49.3305
	prestice	0.7942	0.063	0.015	0.847	0.08	30.5	CL	39.2	22.2	17	76.7813	23.2187	0.00136	0.00136	0.01669	12.2854	0.0814	38.0798
	senec	0.8538	0.078	0.017	0.93	0.2	25.8	CL	48.4	25.8	22.6	75.5771	23.6733	0.00135	0.00135	0.01206	8.9281	0.11201	37.4452
	zajeci	1.3895	0.097	0.026	1.244	0.01	27.2	CH	75	34.7	40.3	91.1038	8.89621	0.00135	0.00135	0.00589	4.34742	0.23002	40.0087
Natural	bilinska1	0.4426	0.048	0.005	0.684	0.33	25.4	CL	49.7	26.9	22.8	64.6422	6.34406	0.0016	0.0016	0.03116	19.5159	0.05124	32.0801
	bilinska2	0.8835	0.063	0.014	0.975	0.25	23.5	CH	59.9	25.5	34.4	92.2158	5.43498	0.00138	0.00138	0.00426	3.09186	0.32343	47.3207
	bilinska3	0.4313	0.033	0.005	0.507	0.34	30.5	CL	26.5	15	11.5	71.8532	28.1468	0.00139	0.00369	0.03299	23.7671	0.29746	25.158
	bilinska4	0.5679	0.066	0.01	0.873	0.25	24.2	CH	53.6	27.7	25.9	90.7912	5.73127	0.00141	0.00141	0.00342	2.43293	0.41103	47.2882
	bilinska5	0.5878	0.069	0.007	0.947	0.31	22.7	CH	64	30.5	33.5	94.9252	5.07477	0.00134	0.00134	0.00273	2.03189	0.49215	54.3244
	hajek	0.5999	0.041	0.005	0.683	0.25	34.9	CL	48.5	22.6	25.9	56.9518	38.8028	0.00131	0.00207	0.08786	67.1038	0.03726	29.861
	koper3	1.0942	0.108	0.016	1.241	0.25	35.6		64	34	30	100	0	0.0013	0.0013	0.0013	1	1	100
	metro1	0.4063	0.065	0.008	0.801	0.09	30.6	CL	34.8	20	14.8	64.9479	31.6965	0.0013	0.00242	0.03472	26.6566	0.12944	27.9628
	prackovic	0.7367	0.089	0.01	1.124	0.34	28.8	CH	66.7	30.8	35.9	97.3578	2.64222	0.00131	0.00131	0.00293	2.23279	0.44787	49.3305
	prackovic	0.7216	0.101	0.009	1.233	0.35	28.8	CH	66.7	30.8	35.9	97.3578	2.64222	0.00131	0.00131	0.00293	2.23279	0.44787	49.3305
	prestice	0.8331	0.063	0.007	0.976	0.25	30.5	CL	39.2	22.2	17	76.7813	23.2187	0.00136	0.00136	0.01669	12.2854	0.0814	38.0798
	senec	0.465	0.078	0.008	0.92	0.3	25.8	CL	48.4	25.8	22.6	75.5771	23.6733	0.00135	0.00135	0.01206	8.9281	0.11201	37.4452
	zajeci	0.5571	0.097	0.011	1.098	0.21	27.2	CH	75	34.7	40.3	91.1038	8.89621	0.00135	0.00135	0.00589	4.34742	0.23002	40.0087

Table B.2: Table of natural and reconstituted oedometric specimens characteristics

Location		e_{min}	λ^*	κ^*	N	ν	ϕ	USCS	w_L	w_P	I_P	%f	%s	d_{10}	d_{30}	d_{60}	Cu	Cc	clay%
bilinska2	CIUP3	0.672	0.063	0.012	1.003	0.36	23.2	CH	59.9	25.5	34.4	92.2158	5.43498	0.00138	0.00138	0.00426	3.09186	0.32343	47.3207
bilinska2	CIUP2	0.683	0.063	0.013	1.003	0.31	23.5	CH	59.9	25.5	34.4	92.2158	5.43498	0.00138	0.00138	0.00426	3.09186	0.32343	47.3207
bilinska2	CIUP1	0.8	0.063	0.011	1	0.3	26.9	CH	59.9	25.5	34.4	92.2158	5.43498	0.00138	0.00138	0.00426	3.09186	0.32343	47.3207
bilinska4	CIUP3	0.533	0.066	0.017	0.951	0.3	23.9	CH	53.6	27.7	25.9	90.7912	5.73127	0.00141	0.00141	0.00342	2.43293	0.41103	47.2882
bilinska4	CIUP2	0.632	0.066	0.017	0.95	0.26	25.3	CH	53.6	27.7	25.9	90.7912	5.73127	0.00141	0.00141	0.00342	2.43293	0.41103	47.2882
bilinska4	CIUP1	0.673	0.066	0.017	0.949	0.22	26.8	CH	53.6	27.7	25.9	90.7912	5.73127	0.00141	0.00141	0.00342	2.43293	0.41103	47.2882
bilinska5	CIUP3	0.462	0.069	0.017	0.92	0.35	22.5	CH	64	30.5	33.5	94.9252	5.07477	0.00134	0.00134	0.00273	2.03189	0.49215	54.3244
bilinska5	CIUP2	0.556	0.069	0.017	0.919	0.32	24	CH	64	30.5	33.5	94.9252	5.07477	0.00134	0.00134	0.00273	2.03189	0.49215	54.3244
bilinska5	CIUP1	0.607	0.069	0.016	0.917	0.31	24.9	CH	64	30.5	33.5	94.9252	5.07477	0.00134	0.00134	0.00273	2.03189	0.49215	54.3244
hongkong	CIUP4	0.765	0.106	0.015	1.192	0.09	32.3	CH	60	28	32	74	26	0.002	0.00528	0.04463	22.3172	0.31225	27.5
hongkong	CIUP3	0.736	0.106	0.015	1.192	0.23	30.9	CH	60	28	32	74	26	0.002	0.00528	0.04463	22.3172	0.31225	27.5
hongkong	CIUP2	0.794	0.106	0.015	1.192	0.01	30.6	CH	60	28	32	74	26	0.002	0.00528	0.04463	22.3172	0.31225	27.5
hongkong	CIUP1	0.83	0.106	0.014	1.192	0.01	32.2	CH	60	28	32	74	26	0.002	0.00528	0.04463	22.3172	0.31225	27.5
prackovice1	CIUP3	0.836	0.089	0.022	1.163	0.24	28.5	CH	66.7	30.8	35.9	97.3578	2.64222	0.00131	0.00131	0.00293	2.23279	0.44787	49.3305
prackovice1	CIUP2	0.824	0.089	0.022	1.163	0.26	28.4	CH	66.7	30.8	35.9	97.3578	2.64222	0.00131	0.00131	0.00293	2.23279	0.44787	49.3305
prackovice1	CIUP1	0.932	0.089	0.022	1.16	0.08	31.6	CH	66.7	30.8	35.9	97.3578	2.64222	0.00131	0.00131	0.00293	2.23279	0.44787	49.3305
prackovice2	CIUP3	0.856	0.101	0.025	1.245	0.23	28.5	CH	66.7	30.8	35.9	97.3578	2.64222	0.00131	0.00131	0.00293	2.23279	0.44787	49.3305
prackovice2	CIUP2	0.842	0.101	0.025	1.241	0.05	31.6	CH	66.7	30.8	35.9	97.3578	2.64222	0.00131	0.00131	0.00293	2.23279	0.44787	49.3305
prackovice2	CIUP1	0.967	0.101	0.025	1.245	0.24	28.4	CH	66.7	30.8	35.9	97.3578	2.64222	0.00131	0.00131	0.00293	2.23279	0.44787	49.3305
zajeci	CIUP3	0.917	0.097	0.024	1.244	0.07	26.4	CH	75	34.7	40.3	91.1038	8.89621	0.00135	0.00135	0.00589	4.34742	0.23002	40.0087
zajeci	CIUP2	0.934	0.097	0.024	1.243	0.01	28	CH	75	34.7	40.3	91.1038	8.89621	0.00135	0.00135	0.00589	4.34742	0.23002	40.0087
zajeci	CIUP1	1.123	0.097	0.024	1.242	0.14	29.6	CH	75	34.7	40.3	91.1038	8.89621	0.00135	0.00135	0.00589	4.34742	0.23002	40.0087
bilinska1	CIUP3	0.43	0.048	0.011	0.73	0.33	25.1	CL	49.7	26.9	22.8	64.6422	6.34406	0.0016	0.0016	0.03116	19.5159	0.05124	32.0801
bilinska1	CIUP2	0.445	0.048	0.01	0.73	0.32	25.4	CL	49.7	26.9	22.8	64.6422	6.34406	0.0016	0.0016	0.03116	19.5159	0.05124	32.0801
bilinska1	CIUP1	0.511	0.048	0.011	0.728	0.21	28.1	CL	49.7	26.9	22.8	64.6422	6.34406	0.0016	0.0016	0.03116	19.5159	0.05124	32.0801
bilinska3	CIUP3	0.268	0.033	0.003	0.506	0.36	30.5	CL	26.5	15	11.5	71.8532	28.1468	0.00139	0.00369	0.03299	23.7671	0.29746	25.158
bilinska3	CIUP2	0.327	0.033	0.006	0.507	0.31	30.1	CL	26.5	15	11.5	71.8532	28.1468	0.00139	0.00369	0.03299	23.7671	0.29746	25.158
bilinska3	CIUP1	0.338	0.033	0.005	0.506	0.33	31.2	CL	26.5	15	11.5	71.8532	28.1468	0.00139	0.00369	0.03299	23.7671	0.29746	25.158
boston	CIUP3	0.832	0.087	0.016	1.188	0.1	28.9	CL	41	20	21	88.7366	11.2634	0.00047	0.00135	0.01264	26.6967	0.30677	34.8848
boston	CIUP2	0.879	0.087	0.015	1.188	0.1	29	CL	41	20	21	88.7366	11.2634	0.00047	0.00135	0.01264	26.6967	0.30677	34.8848
boston	CIUP1	0.941	0.087	0.018	1.188	0.01	27.8	CL	41	20	21	88.7366	11.2634	0.00047	0.00135	0.01264	26.6967	0.30677	34.8848
hajek	CIUP3	0.468	0.041	0.006	0.638	0.28	34.4	CL	48.5	22.6	25.9	56.9518	38.8028	0.00131	0.00207	0.08786	67.1038	0.03726	29.861
hajek	CIUP2	0.492	0.041	0.006	0.637	0.27	35.8	CL	48.5	22.6	25.9	56.9518	38.8028	0.00131	0.00207	0.08786	67.1038	0.03726	29.861
hajek	CIUP1	0.53	0.041	0.006	0.637	0.25	36	CL	48.5	22.6	25.9	56.9518	38.8028	0.00131	0.00207	0.08786	67.1038	0.03726	29.861
metro_01	CIUP3	0.486	0.065	0.014	0.801	0.25	28.8	CL	34.8	20	14.8	64.9479	31.6965	0.0013	0.00242	0.03472	26.6566	0.12944	27.9628
metro_01	CIUP2	0.533	0.065	0.013	0.796	0.12	35.8	CL	34.8	20	14.8	64.9479	31.6965	0.0013	0.00242	0.03472	26.6566	0.12944	27.9628
metro_01	CIUP1	0.553	0.065	0.014	0.798	0.01	33.5	CL	34.8	20	14.8	64.9479	31.6965	0.0013	0.00242	0.03472	26.6566	0.12944	27.9628
prestice	CIUP3	0.57	0.063	0.015	0.847	0.21	30.8	CL	39.2	22.2	17	76.7813	23.2187	0.00136	0.00136	0.01669	12.2854	0.0814	38.0798
prestice	CIUP2	0.645	0.063	0.016	0.848	0.02	28.7	CL	39.2	22.2	17	76.7813	23.2187	0.00136	0.00136	0.01669	12.2854	0.0814	38.0798
prestice	CIUP1	0.688	0.063	0.014	0.845	0.11	32.6	CL	39.2	22.2	17	76.7813	23.2187	0.00136	0.00136	0.01669	12.2854	0.0814	38.0798
senec	CIUP3	0.522	0.069	0.016	0.861	0.33	25.3	CL	48.4	25.8	22.6	75.5771	23.6733	0.00135	0.00135	0.01206	8.9281	0.11201	37.4452
senec	CIUP2	0.602	0.069	0.017	0.86	0.25	27.1	CL	48.4	25.8	22.6	75.5771	23.6733	0.00135	0.00135	0.01206	8.9281	0.11201	37.4452
senec	CIUP1	0.649	0.069	0.017	0.858	0.18	30.3	CL	48.4	25.8	22.6	75.5771	23.6733	0.00135	0.00135	0.01206	8.9281	0.11201	37.4452
weald_clay	CIUP3	0.602	0.063	0.016	0.826	0.35	23.3	CL	43	18	25	100	0	0.002	0.002	0.00237	1.18333	0.84507	40
weald_clay	CIUP2	0.584	0.063	0.016	0.824	0.12	24.1	CL	43	18	25	100	0	0.002	0.002	0.00237	1.18333	0.84507	40
weald_clay	CIUP1	0.627	0.063	0.016	0.825	0.26	22.4	CL	43	18	25	100	0	0.002	0.002	0.00237	1.18333	0.84507	40

Table B.3: Table of reconstitited triaxial specimens characteristics

Location		e_{init}	λ^*	κ^*	N	ν	ϕ	USCS	W_L	W_P	I_P	%f	%s	d_{10}	d_{30}	d_{60}	Cu	Cc	clay%
bilinska1	CIUP3	0.345	0.048	0.005	0.685	0.34	25.4	CL	49.7	26.9	22.8	64.6422	6.34406	0.0016	0.0016	0.03116	19.5159	0.05124	32.0801
bilinska1	CIUP2	0.364	0.048	0.006	0.682	0.21	26.2	CL	49.7	26.9	22.8	64.6422	6.34406	0.0016	0.0016	0.03116	19.5159	0.05124	32.0801
bilinska1	CIUP1	0.406	0.048	0.005	0.683	0.33	28.4	CL	49.7	26.9	22.8	64.6422	6.34406	0.0016	0.0016	0.03116	19.5159	0.05124	32.0801
bilinska3	CIUP3	0.277	0.033	0.004	0.508	0.36	29.3	CL	26.5	15	11.5	71.8532	28.1468	0.00139	0.00369	0.03299	23.7671	0.29746	25.158
bilinska3	CIUP2	0.297	0.033	0.005	0.508	0.34	28.6	CL	26.5	15	11.5	71.8532	28.1468	0.00139	0.00369	0.03299	23.7671	0.29746	25.158
bilinska3	CIUP1	0.315	0.033	0.005	0.508	0.32	29.3	CL	26.5	15	11.5	71.8532	28.1468	0.00139	0.00369	0.03299	23.7671	0.29746	25.158
hajek	CIUP3	0.487	0.041	0.005	0.684	0.28	33.5	CL	48.5	22.6	25.9	56.9518	38.8028	0.00131	0.00207	0.08786	67.1038	0.03726	29.861
hajek	CIUP2	0.546	0.041	0.005	0.685	0.28	28.9	CL	48.5	22.6	25.9	56.9518	38.8028	0.00131	0.00207	0.08786	67.1038	0.03726	29.861
hajek	CIUP1	0.565	0.041	0.002	0.684	0.23	31.4	CL	48.5	22.6	25.9	56.9518	38.8028	0.00131	0.00207	0.08786	67.1038	0.03726	29.861
metro_01	CIUP3	0.455	0.065	0.007	0.805	0.31	26.1	CL	34.8	20	14.8	64.9479	31.6965	0.0013	0.00242	0.03472	26.6566	0.12944	27.9628
metro_01	CIUP2	0.483	0.065	0.009	0.803	0.06	28.4	CL	34.8	20	14.8	64.9479	31.6965	0.0013	0.00242	0.03472	26.6566	0.12944	27.9628
metro_01	CIUP1	0.525	0.065	0.007	0.8	0.09	31.3	CL	34.8	20	14.8	64.9479	31.6965	0.0013	0.00242	0.03472	26.6566	0.12944	27.9628
bilinska2	CIUP3	0.625	0.063	0.013	0.975	0.3	24.1	CH	59.9	25.5	34.4	92.2158	5.43498	0.00138	0.00138	0.00426	3.09186	0.32343	47.3207
bilinska2	CIUP2	0.63	0.063	0.013	0.975	0.25	24.3	CH	59.9	25.5	34.4	92.2158	5.43498	0.00138	0.00138	0.00426	3.09186	0.32343	47.3207
bilinska2	CIUP1	0.732	0.063	0.013	0.973	0.22	25.3	CH	59.9	25.5	34.4	92.2158	5.43498	0.00138	0.00138	0.00426	3.09186	0.32343	47.3207
bilinska4	CIUP3	0.412	0.066	0.01	0.873	0.29	24	CH	53.6	27.7	25.9	90.7912	5.73127	0.00141	0.00141	0.00342	2.43293	0.41103	47.2882
bilinska4	CIUP2	0.473	0.066	0.01	0.871	0.21	25.5	CH	53.6	27.7	25.9	90.7912	5.73127	0.00141	0.00141	0.00342	2.43293	0.41103	47.2882
bilinska4	CIUP1	0.506	0.066	0.01	0.872	0.24	26	CH	53.6	27.7	25.9	90.7912	5.73127	0.00141	0.00141	0.00342	2.43293	0.41103	47.2882
bilinska5	CIUP3	0.516	0.069	0.007	0.948	0.29	21	CH	64	30.5	33.5	94.9252	5.07477	0.00134	0.00134	0.00273	2.03189	0.49215	54.3244
bilinska5	CIUP2	0.553	0.069	0.006	0.946	0.34	23.3	CH	64	30.5	33.5	94.9252	5.07477	0.00134	0.00134	0.00273	2.03189	0.49215	54.3244
bilinska5	CIUP1	0.592	0.069	0.007	0.946	0.29	24	CH	64	30.5	33.5	94.9252	5.07477	0.00134	0.00134	0.00273	2.03189	0.49215	54.3244

Table B.4: Table of natural triaxial specimens characteristics

C. Hypoplastic sand correlations

Location	h_s	n	e_{s0}	e_{c0}	α	β	Φ	e_{g0}	USCS	W_L	W_P	I_P	%clay	%f	%s	d_{10}	d_{30}	d_{50}	d_{60}	C_u	C_c
bilinska1	963	0.163	1.561	1.301	0.1	9	25.4	0.651	CL	49.7	26.9	22.8	32.08014	64.64221	6.34406	0.00160	0.00160	0.01019	0.03116	19.51589	0.05124
bilinska2	2376	0.17	2.082	1.735	0.02	8.6	23.5	0.868	CH	59.9	25.5	34.4	47.32068	92.21576	5.43498	0.00138	0.00138	0.00240	0.00426	3.09186	0.32343
bilinska3	2414	0.169	0.887	0.739	0.26	8.7	30.5	0.369	CL	26.5	15	11.5	25.15796	71.85315	28.14685	0.00139	0.00369	0.01993	0.03299	23.76712	0.29746
bilinska4	968	0.211	2.153	1.794	0.01	8.9	24.2	0.897	CH	53.6	27.7	25.9	47.28817	90.79121	5.73127	0.00141	0.00141	0.00229	0.00342	2.43293	0.41103
bilinska5	1000	0.206	1.836	1.53	0.01	8.7	22.7	0.765	CH	64	30.5	33.5	54.32436	94.92523	5.07477	0.00134	0.00134	0.00145	0.00273	2.03189	0.49215
bosilec	803	0.159	1.384	1.153	0.1	8.8	34.1	0.577	SC	21	13.3	7.7	14.95385	41.13630	52.95757	0.00140	0.01942	0.15942	0.34828	248.85432	0.77351
boston	1000	0.35	2.722	2.269	0.94	9	28.7	1.134	CL	41	20	21	34.88483	88.73656	11.26344	0.00047	0.00135	0.00684	0.01264	26.68670	0.30677
chyne	995	0.129	2.123	1.769	0.26	2	31.8	0.885	SC	0	0	0	9.16246	13.33064	79.82594	0.00535	0.15789	0.21504	0.24362	45.55769	19.13627
chyne2	1000	0.107	2.187	1.822	0.24	1.7	31.8	0.911	SC	0	0	0	9.16246	13.33064	79.82594	0.00535	0.15789	0.21504	0.24362	45.55769	19.13627
dobrany	39986	0.196	1.523	1.269	0.09	4.2	36.5	0.635	SW	0	0	0	1.93304	6.46471	89.82964	0.12984	0.32139	0.46409	0.57609	4.43682	1.38090
hajek	2632	0.192	1.167	0.972	0.23	9	34.9	0.486	CL	48.5	22.6	25.9	29.86095	56.95184	38.80278	0.00131	0.00207	0.02792	0.08786	67.10376	0.03726
hongkong	608	0.307	2.656	2.213	0.01	9	31.4	1.107	CH	60	28	32	27.50000	74.00000	26.00000	0.00200	0.00528	0.03152	0.04463	22.31720	0.31225
hrusovany	5119	0.191	1.211	1.009	0.15	5.2	36.8	0.504	SW	0	0	0	2.99378	5.19986	43.35325	0.27338	0.99554	2.12495	2.98868	10.93246	1.21548
jablonec	980	0.236	1.481	1.234	0.06	6.6	42	0.617	SM	23.8	18.9	4.9	6.18041	21.96239	52.03571	0.00628	0.17354	0.66896	1.07133	170.68795	4.47852
komorany	58583	0.494	0.717	0.597	0.31	3.3	34.5	0.299	SW	0	0	0	0.00000	0.00000	65.97220	0.41241	0.82012	1.18310	1.64658	3.99253	0.99047
komorany2	7828	0.178	1.285	1.071	0.35	4.7	34.5	0.535	SW	0	0	0	0.00000	0.00000	65.97220	0.41241	0.82012	1.18310	1.64658	3.99253	0.99047
komorany3	13739	0.685	0.726	0.637	0.38	4.9	34.5	0.302	SW	0	0	0	0.00000	0.00000	65.97220	0.41241	0.82012	1.18310	1.64658	3.99253	0.99047
komorany4	10685	0.578	0.612	0.648	0.29	6.8	34.5	0.255	SW	0	0	0	0.00000	0.00000	65.97220	0.41241	0.82012	1.18310	1.64658	3.99253	0.99047
koper1	976	0.217	3.018	2.515	0.15	8.7	35.3	1.258	CH	64	34	30	100.00000	100.00000	0.00000	0.00130	0.00130	0.00130	0.00130	1.00000	1.00000
koper2	938	0.239	2.558	2.131	0.14	8.8	35.3	1.066	CH	64	34	30	100.00000	100.00000	0.00000	0.00130	0.00130	0.00130	0.00130	1.00000	1.00000
koper3	605	0.264	2.592	2.16	0.12	8.8	35.3	1.08	CH	64	34	30	100.00000	100.00000	0.00000	0.00130	0.00130	0.00130	0.00130	1.00000	1.00000
kralupy	3514	0.172	1.786	1.488	0.18	3.1	36.3	0.744	SM	0	0	0	4.80389	23.74944	74.74826	0.01587	0.08779	0.16546	0.20356	12.82392	2.38537
kralupy2	7500	0.157	1.804	1.503	0.11	2.5	36.3	0.751	SM	0	0	0	4.80389	23.74944	74.74826	0.01587	0.08779	0.16546	0.20356	12.82392	2.38537
metro1	1796	0.231	1.217	1.014	0.01	8.7	30.6	0.507	CL	34.8	20	14.8	27.96280	64.94788	31.69649	0.00130	0.00242	0.01612	0.03472	26.65665	0.12944
motol	1767	0.17	1.253	1.045	0.03	2	35.3	0.522	SC	19.7	12.5	7.2	14.38916	27.90686	63.70999	0.00137	0.08558	0.40277	0.59007	430.83737	9.06193
motol2	942	0.131	1.451	1.209	0.03	1.8	35.3	0.605	SC	19.7	12.5	7.2	14.38916	27.90686	63.70999	0.00137	0.08558	0.40277	0.59007	430.83737	9.06193
otaniemi1	821	0.582	2.991	2.492	0.95	9	25.3	1.246	CH	95	29	66	78.00000	100.00000	0.00000	0.00200	0.00200	0.00200	0.00200	1.00000	1.00000
otaniemi2	665	0.549	3.746	3.122	0.95	9	25.3	1.561	CH	95	29	66	78.00000	100.00000	0.00000	0.00200	0.00200	0.00200	0.00200	1.00000	1.00000
otaniemi3	364	0.71	3.793	3.161	0.95	8.9	25.3	1.58	CH	95	29	66	78.00000	100.00000	0.00000	0.00200	0.00200	0.00200	0.00200	1.00000	1.00000
otaniemi4	190	0.468	5.419	4.516	0.95	8.9	25.3	2.258	CH	95	29	66	78.00000	100.00000	0.00000	0.00200	0.00200	0.00200	0.00200	1.00000	1.00000
prackovice	699	0.242	2.783	2.319	0.1	8.9	28.8	1.159	CH	66.7	30.8	35.9	49.33054	97.35778	2.64222	0.00131	0.00131	0.00206	0.00293	2.23279	0.44787
prackovice2	628	0.262	3.003	2.503	0.08	8.6	28.8	1.251	CH	66.7	30.8	35.9	49.33054	97.35778	2.64222	0.00131	0.00131	0.00205	0.00293	2.23279	0.44787
prestice	991	0.214	1.683	1.402	0.03	8.7	30.5	0.701	CL	39.2	22.2	17	38.07983	76.78132	23.21868	0.00136	0.00136	0.00628	0.01669	12.28544	0.08140
rohatec	2685999	0.14	1.096	0.914	0.11	3.3	34.3	0.457	SP	0	0	0	0.14830	4.14772	92.67834	0.18807	0.35595	0.48301	0.61119	3.24978	1.10224
rohatec2	437512	0.091	1.317	1.098	0.13	3.9	34.3	0.549	SP	0	0	0	0.14830	4.14772	92.67834	0.18807	0.35595	0.48301	0.61119	3.24978	1.10224
senec	873	0.263	1.744	1.453	0.01	8.7	25.8	0.727	CL	48.4	25.8	22.6	37.44518	75.57708	23.67326	0.00135	0.00135	0.00669	0.01206	8.92810	0.11201
stvanice	984	0.187	2.032	1.693	0.4	4.5	35.2	0.847	SM	0	0	0	4.61063	31.55076	68.33324	0.00925	0.05816	0.12054	0.16190	17.49883	2.25859
ujezd1	2544	0.215	1.721	1.434	0.3	1.7	30.8	0.717	CI	35	21	14	40.33333	87.64989	12.35011	0.00130	0.00130	0.00620	0.01128	8.67949	0.11521
ujezd2	1242	0.196	1.654	1.379	0.01	2.1	31.4	0.689	CI	35	21	14	40.33333	87.64989	12.35011	0.00130	0.00130	0.00620	0.01128	8.67949	0.11521
vamtila1	441	0.581	4.216	3.514	0.95	9	22.8	1.757	CH	98	30	68	51.00000	100.00000	0.00000	0.00200	0.00200	0.00200	0.00277	1.38571	0.72165
vamtila2	423	0.858	3.844	3.203	0.95	8.7	22.8	1.602	CH	98	30	68	51.00000	100.00000	0.00000	0.00200	0.00200	0.00200	0.00277	1.38571	0.72165
weald	769	0.27	1.654	1.379	0.01	7.7	23.5	0.689	CL	43	18	25	40.00000	100.00000	0.00000	0.00200	0.00200	0.00200	0.00218	1.18333	0.84507
zajeci	560	0.232	3.108	2.59	0.01	9	27.2	1.295	CH	75	34.7	40.3	40.00867	91.10379	8.89621	0.00135	0.00135	0.00337	0.00589	4.34742	0.23002

Table C.1: Table of reconstituted specimens characteristics

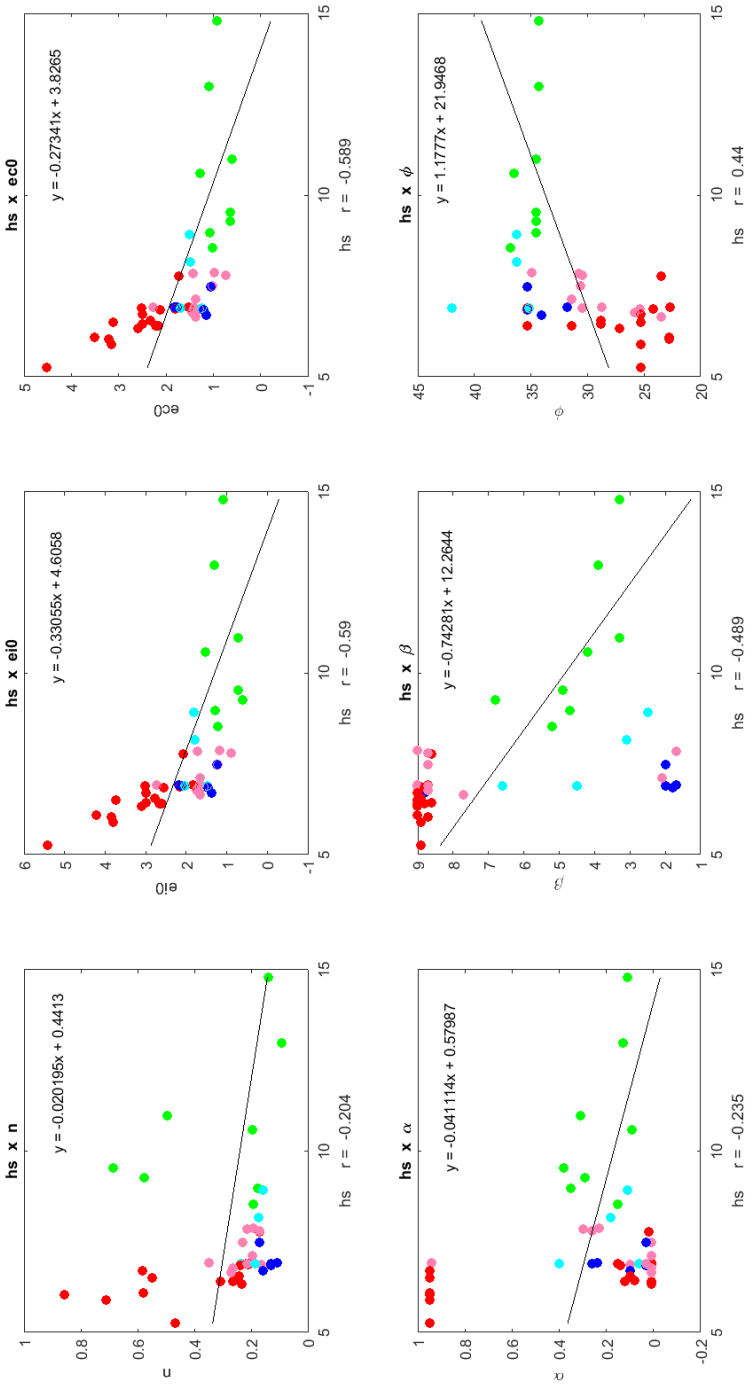

Figure C.1: Correlation between parameters: h_s

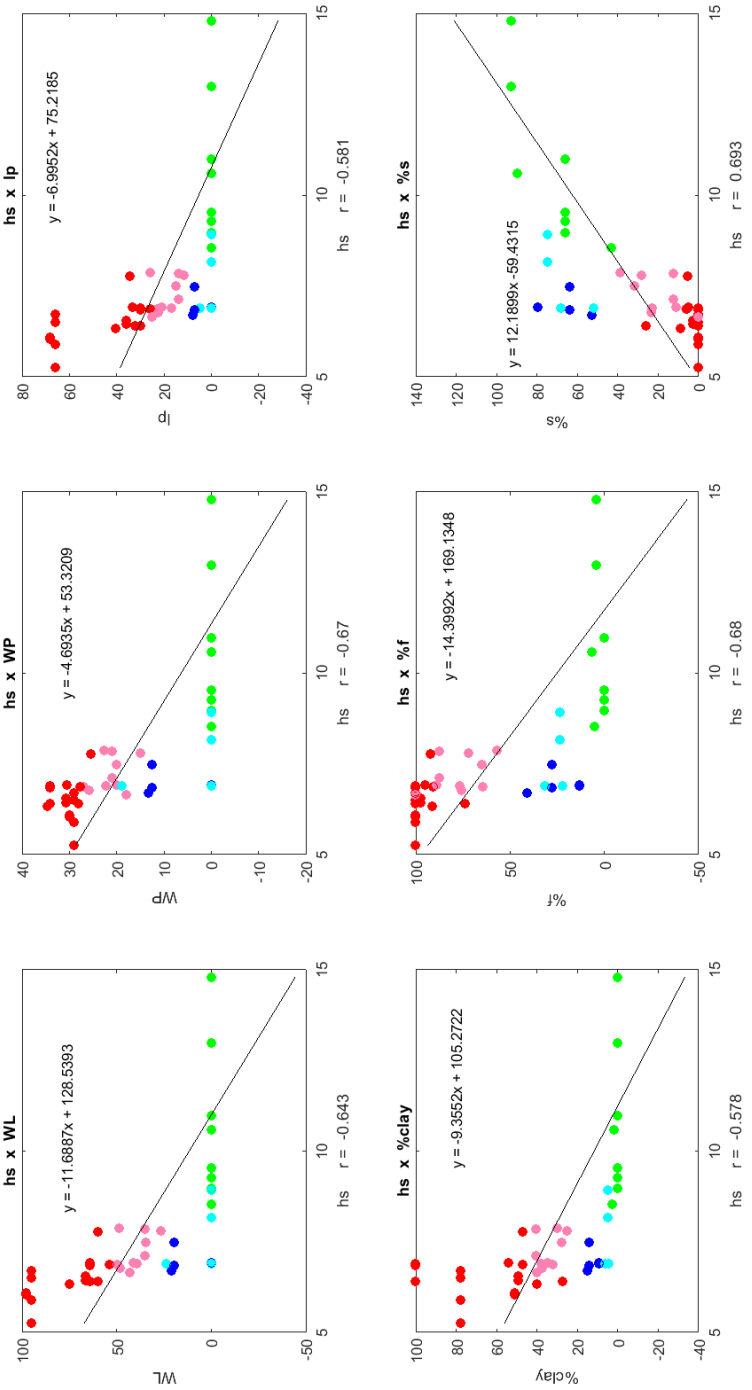

Figure C.2: Correlation for Atterberg's limits and particle contens: h_s

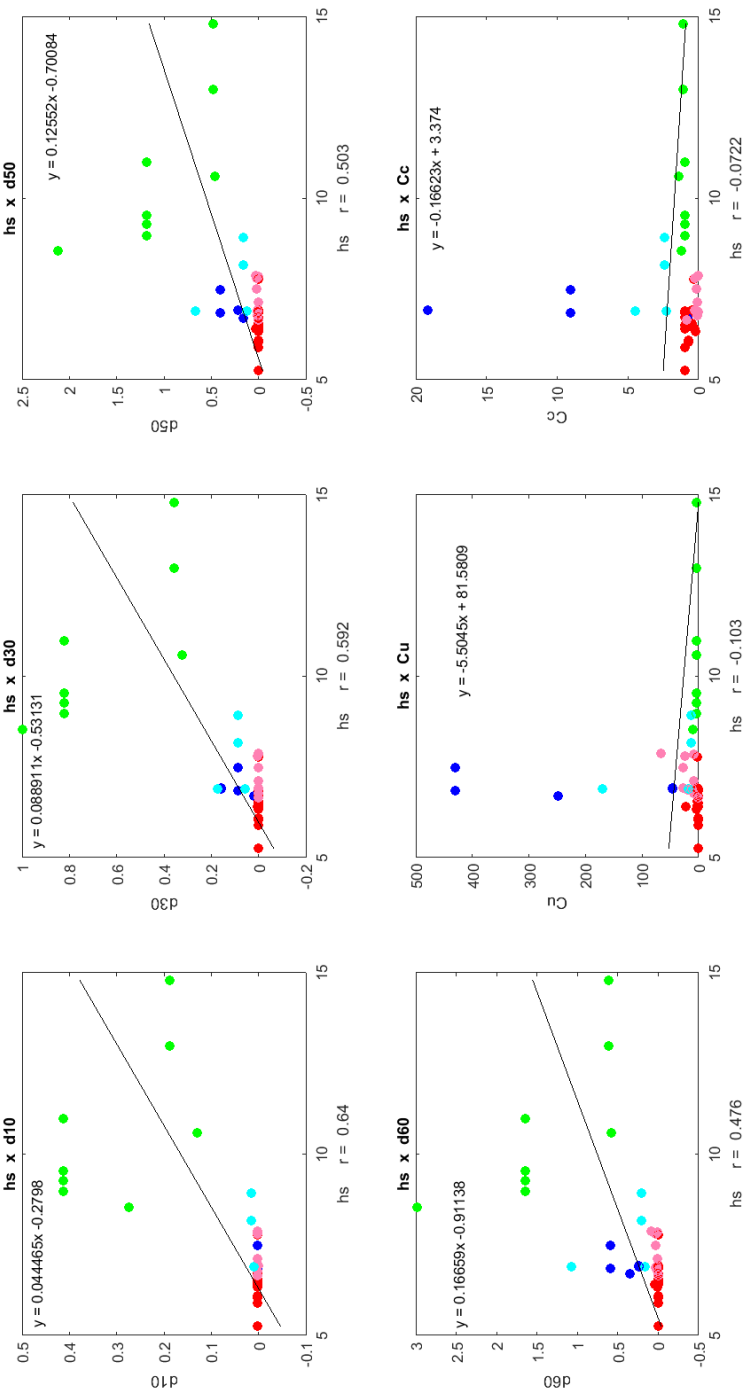

Figure C.3: Gradation characteristics: h_s

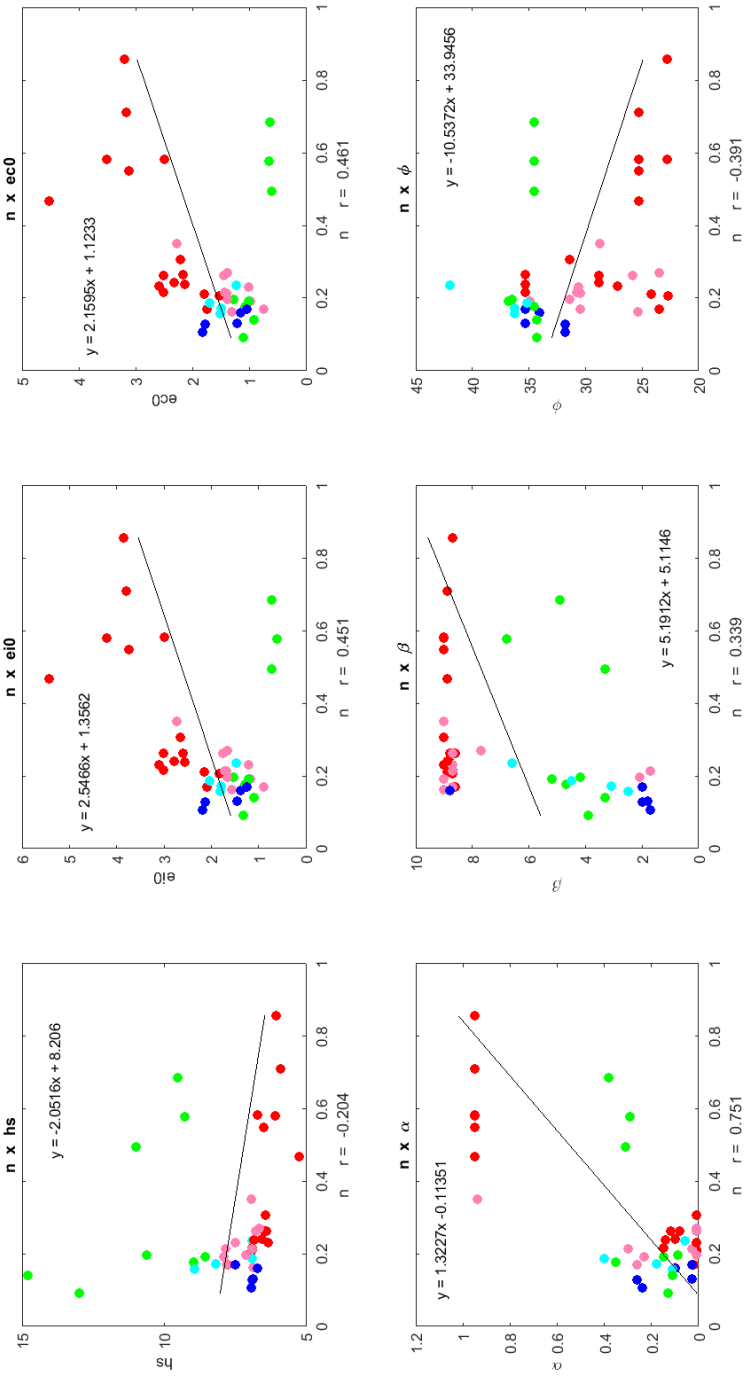

Figure C.4: Correlation between parameters: n

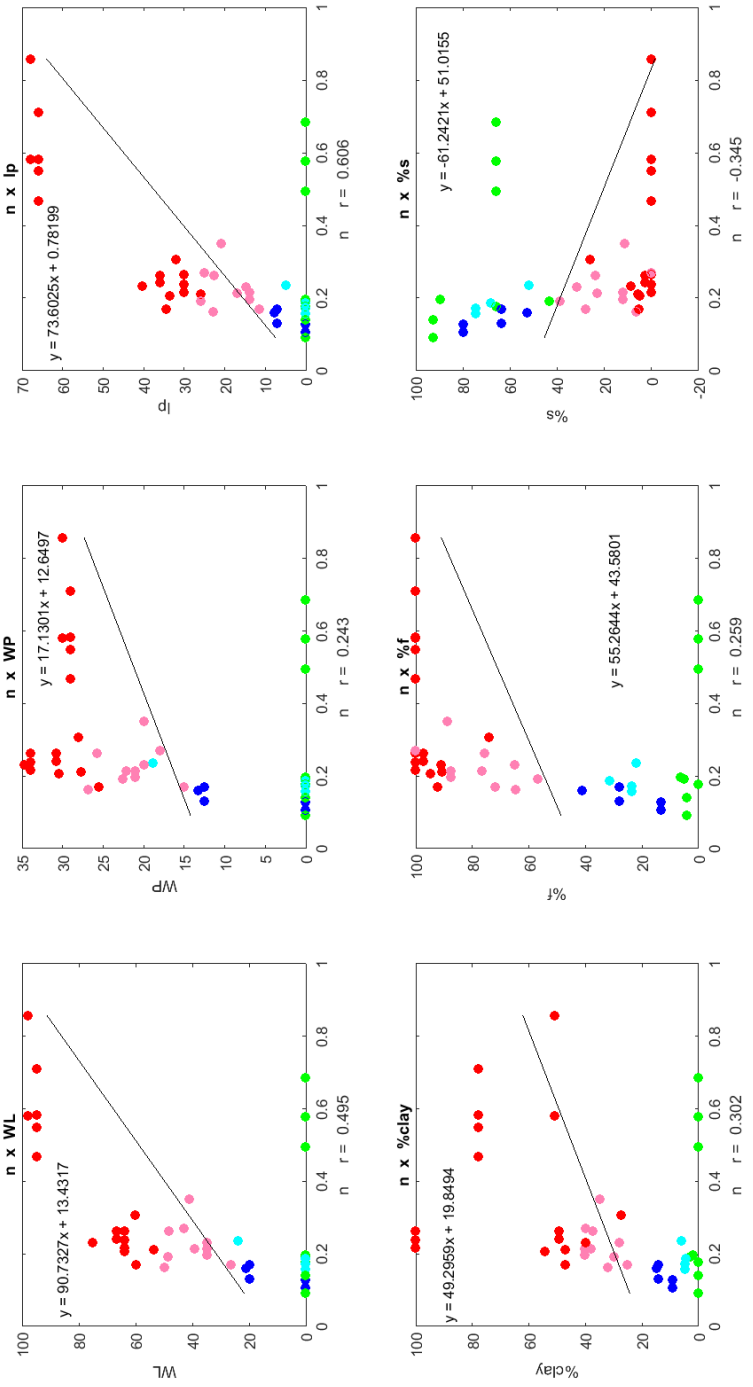

Figure C.5: Correlation for Atterberg's limits and particle contens: *n*

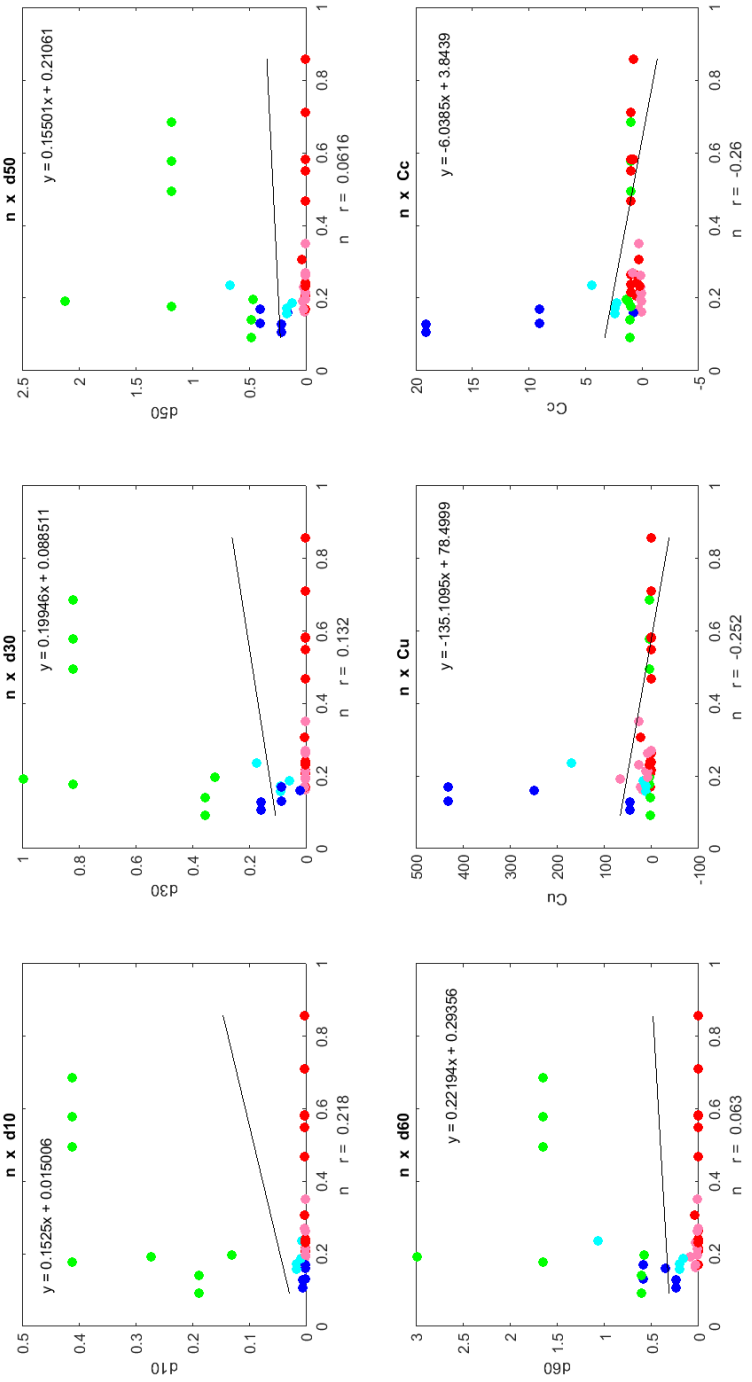

Figure C.6: Gradation characteristics: *n*

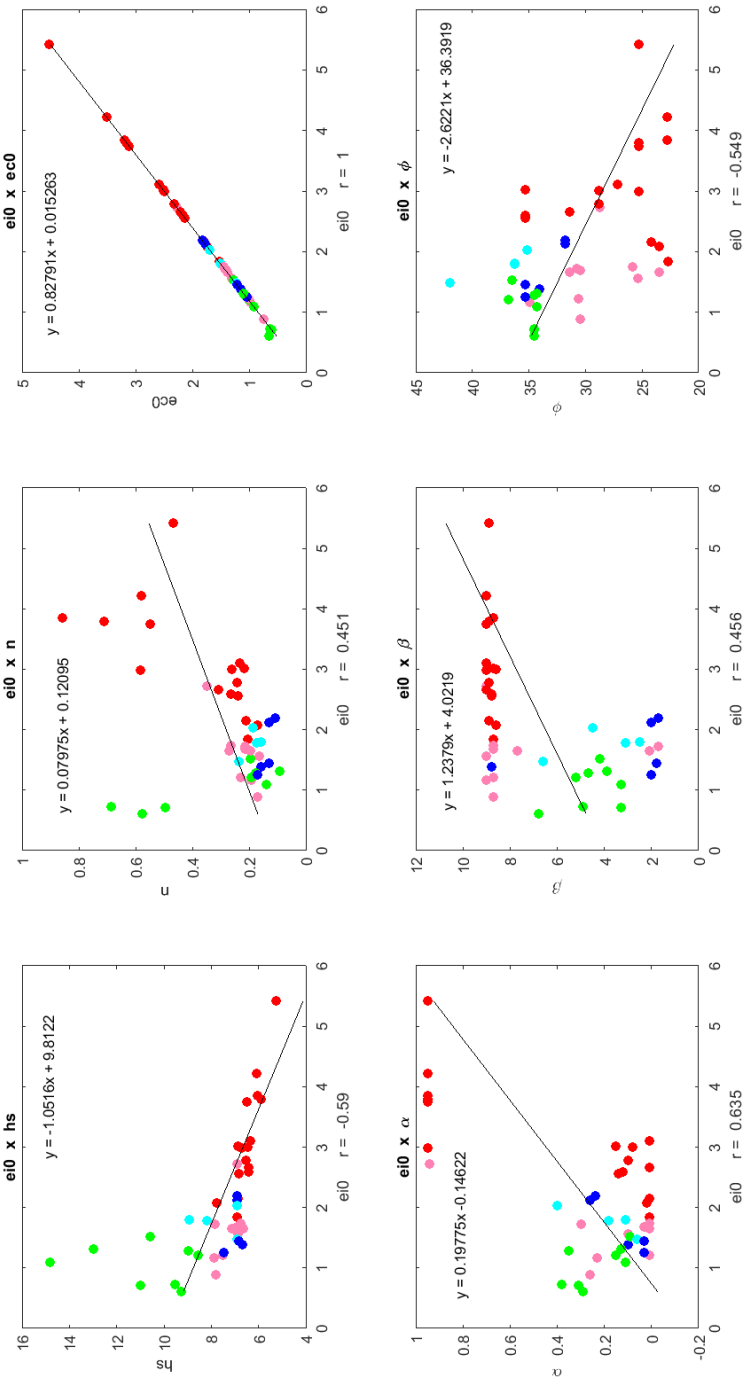

Figure C.7: Correlation between parameters: e_{i0}

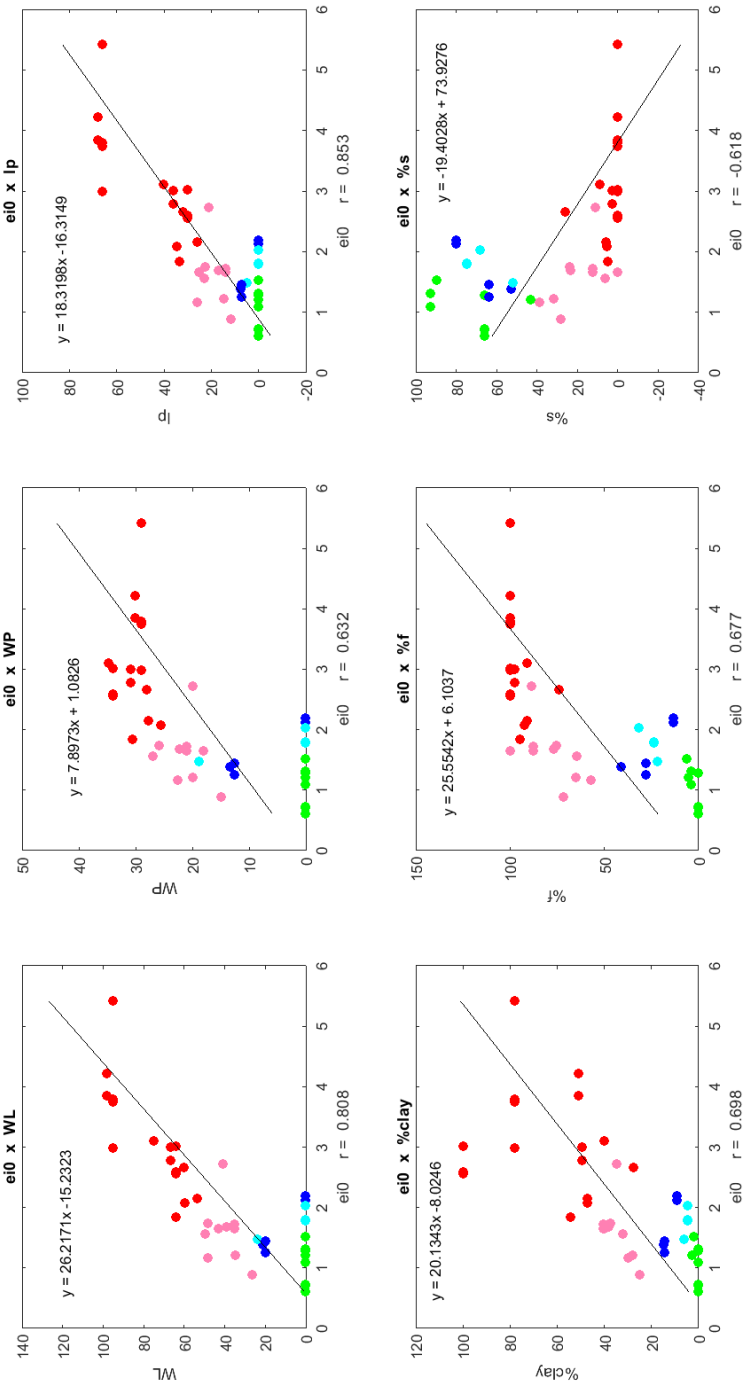

Figure C.8: Correlation for Atterberg's limits and particle contens: e_{i0}

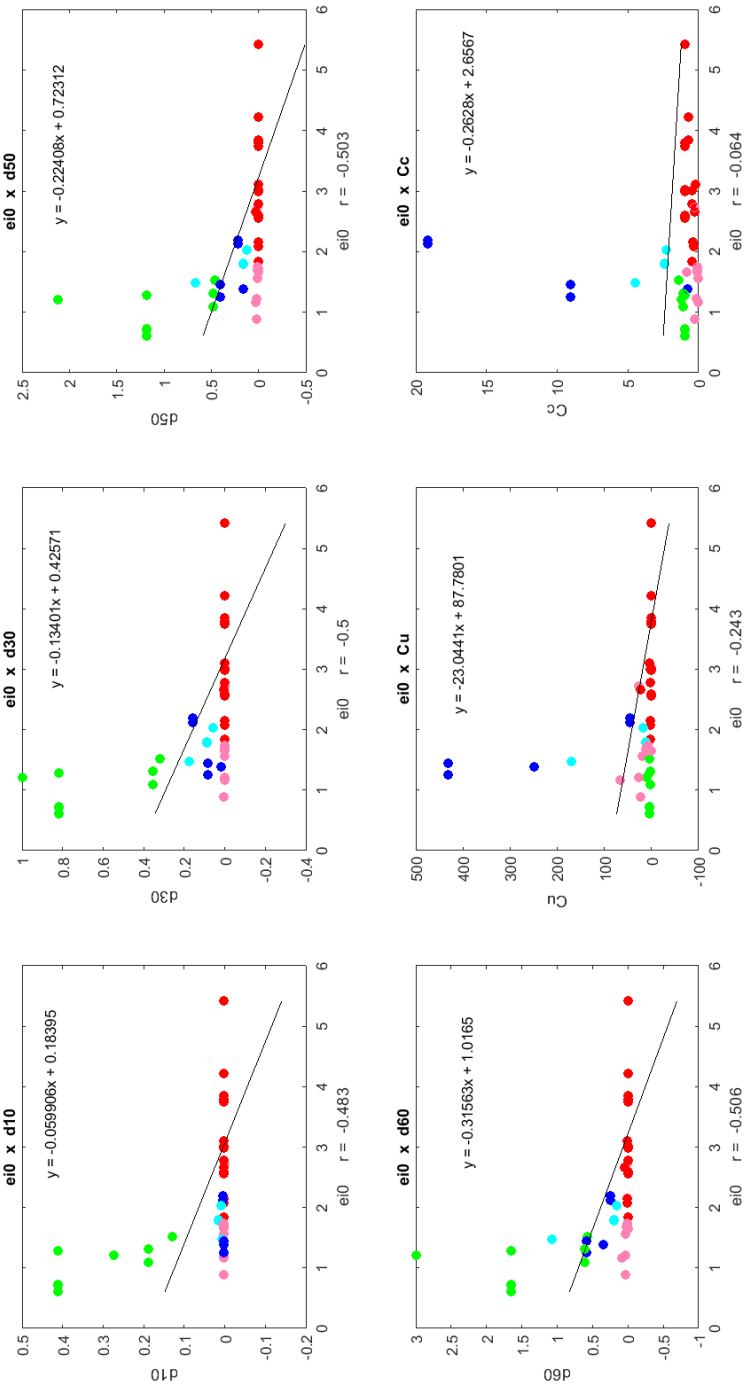

Figure C.9: Gradation characteristics: e_{i0}

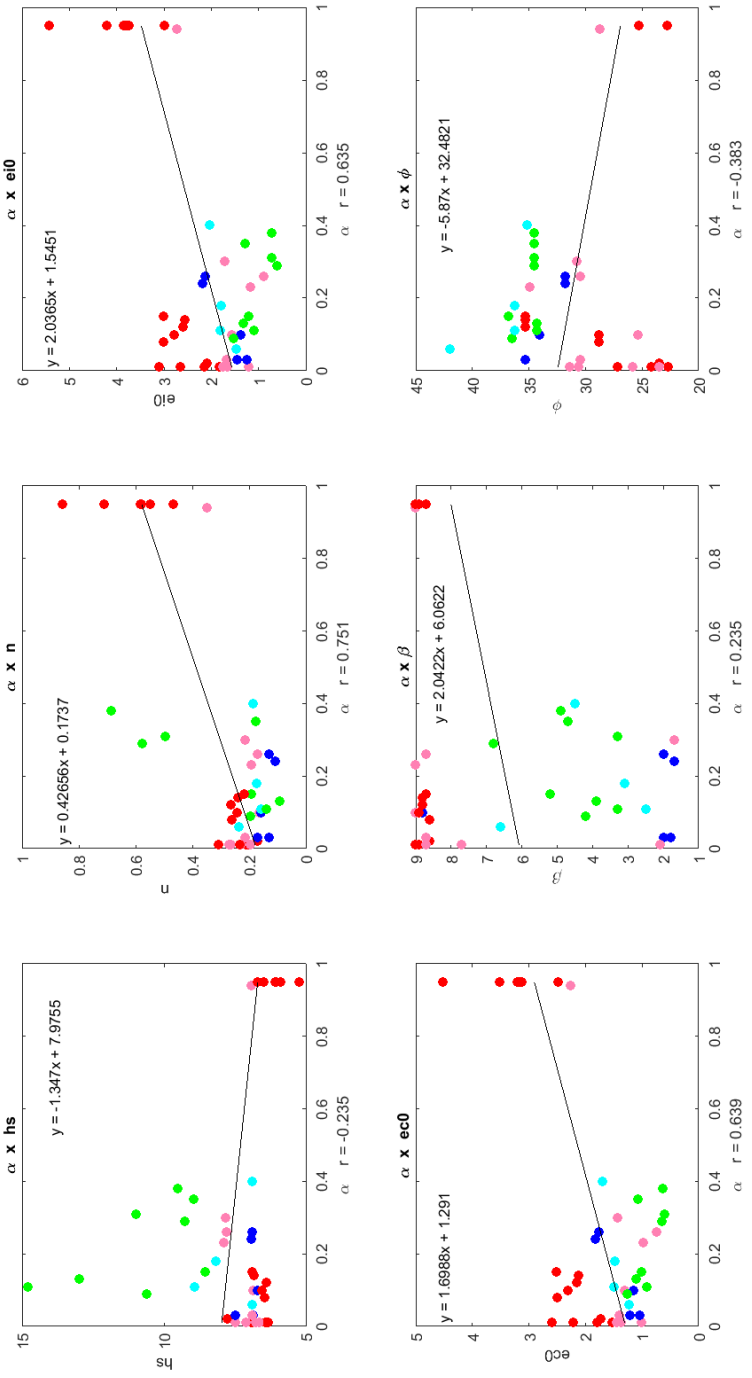

Figure C.10: Correlation between parameters: α

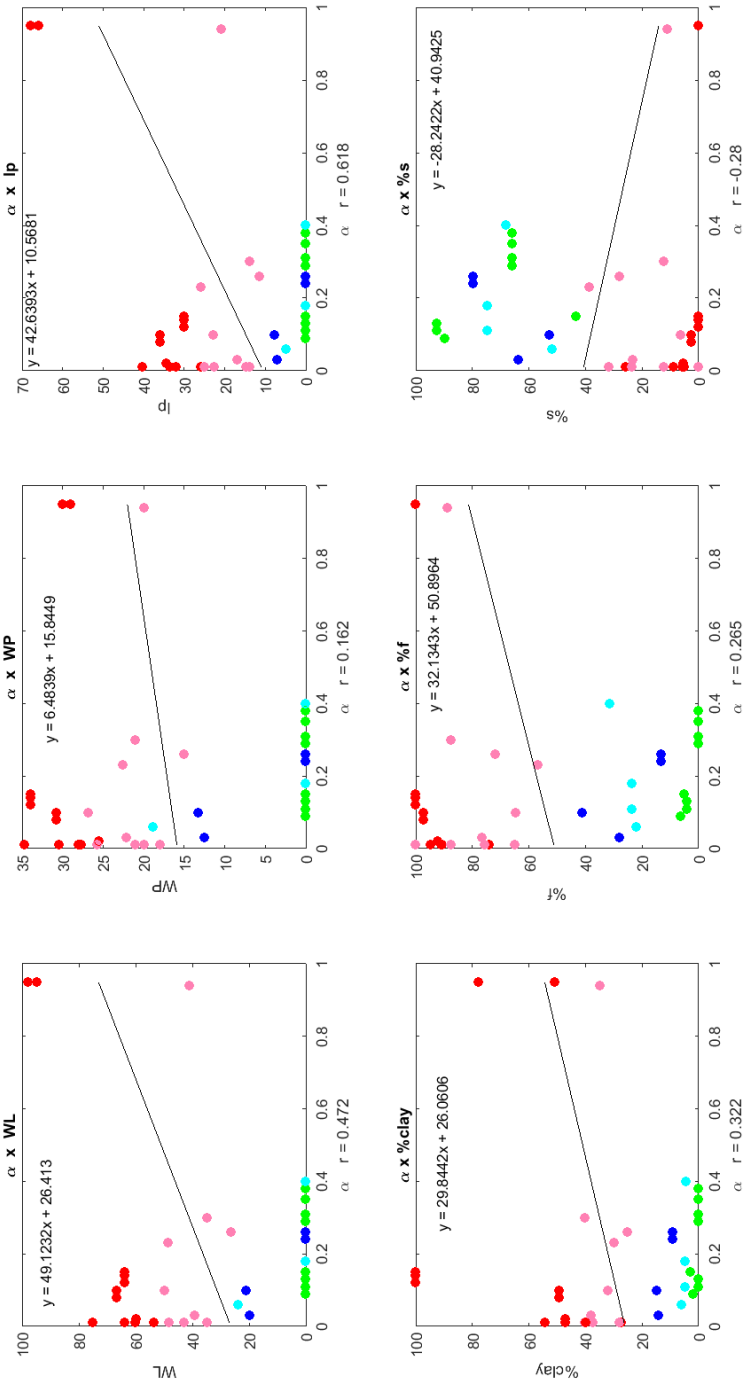

Figure C.11: Correlation for Atterberg's limits and particle contens: α

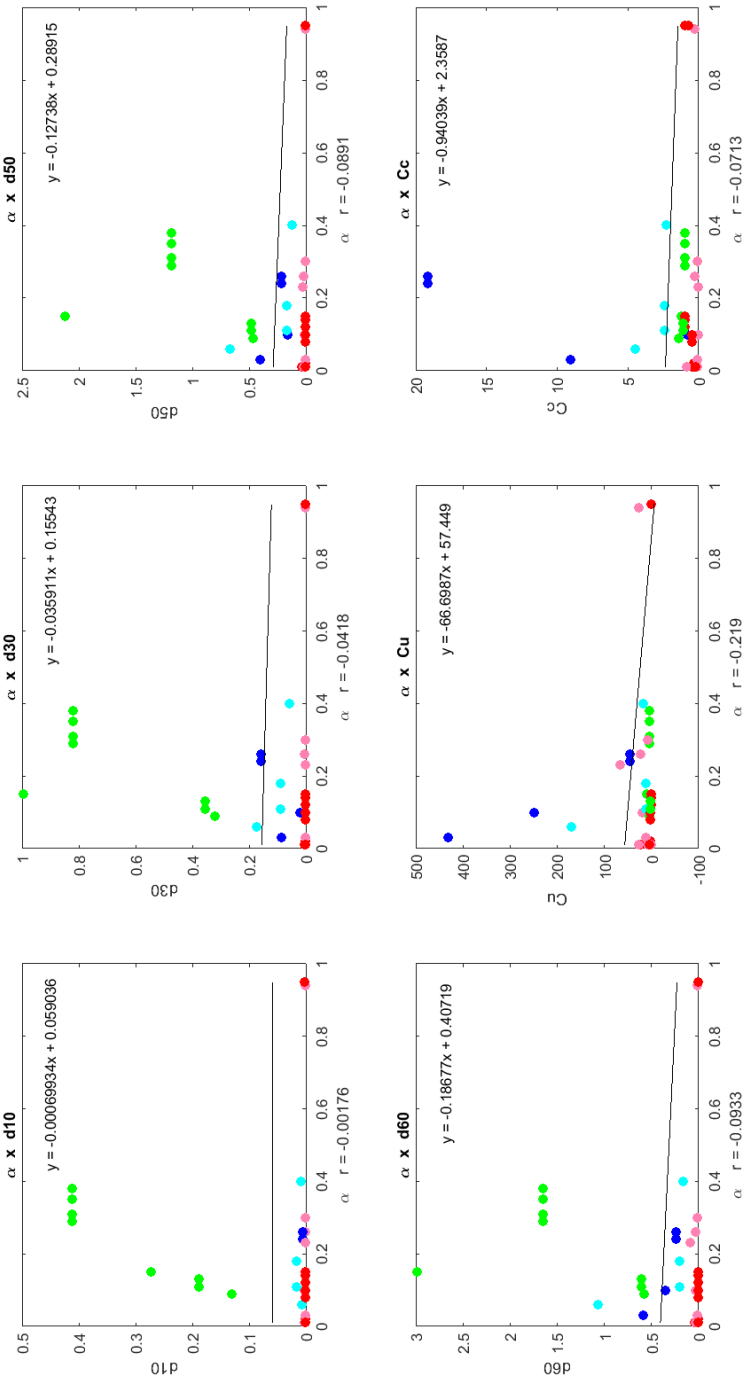

Figure C.12: Gradation characteristics: α

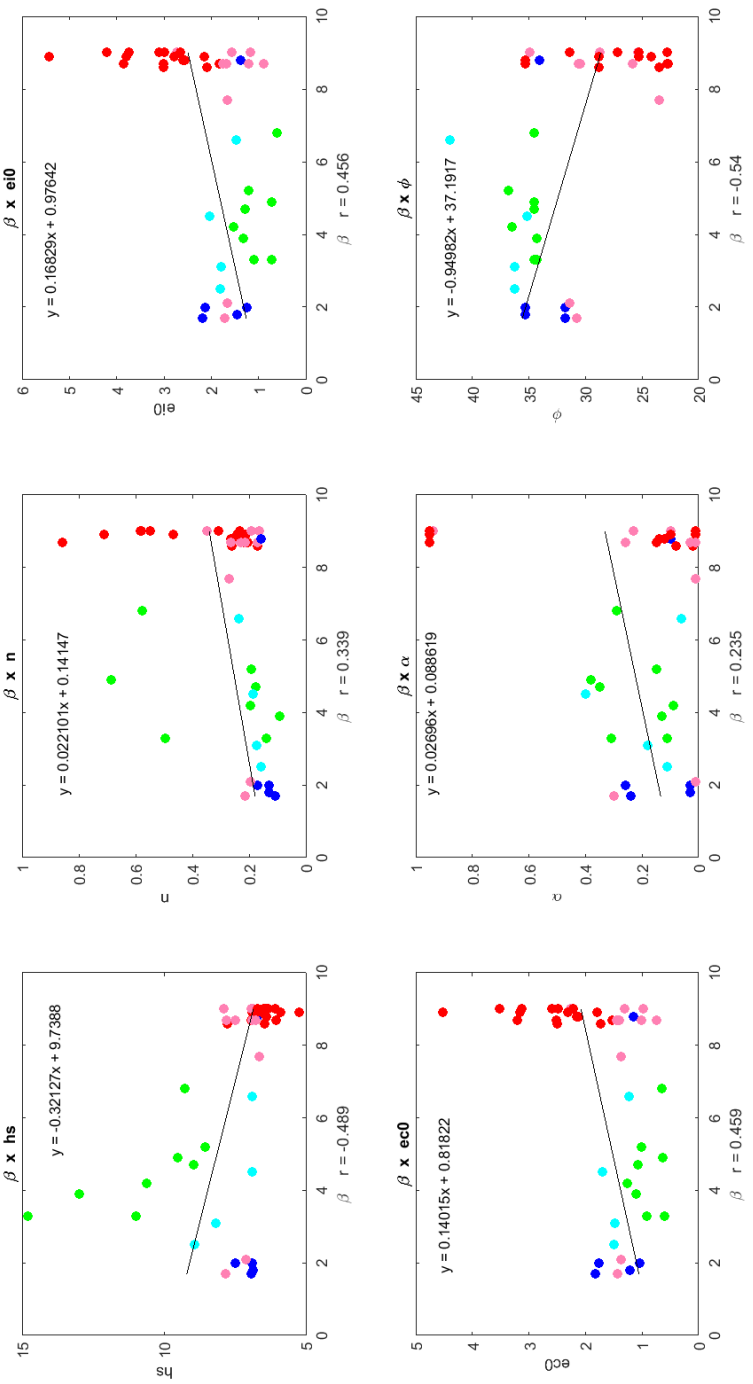

Figure C.13: Correlation between parameters: β

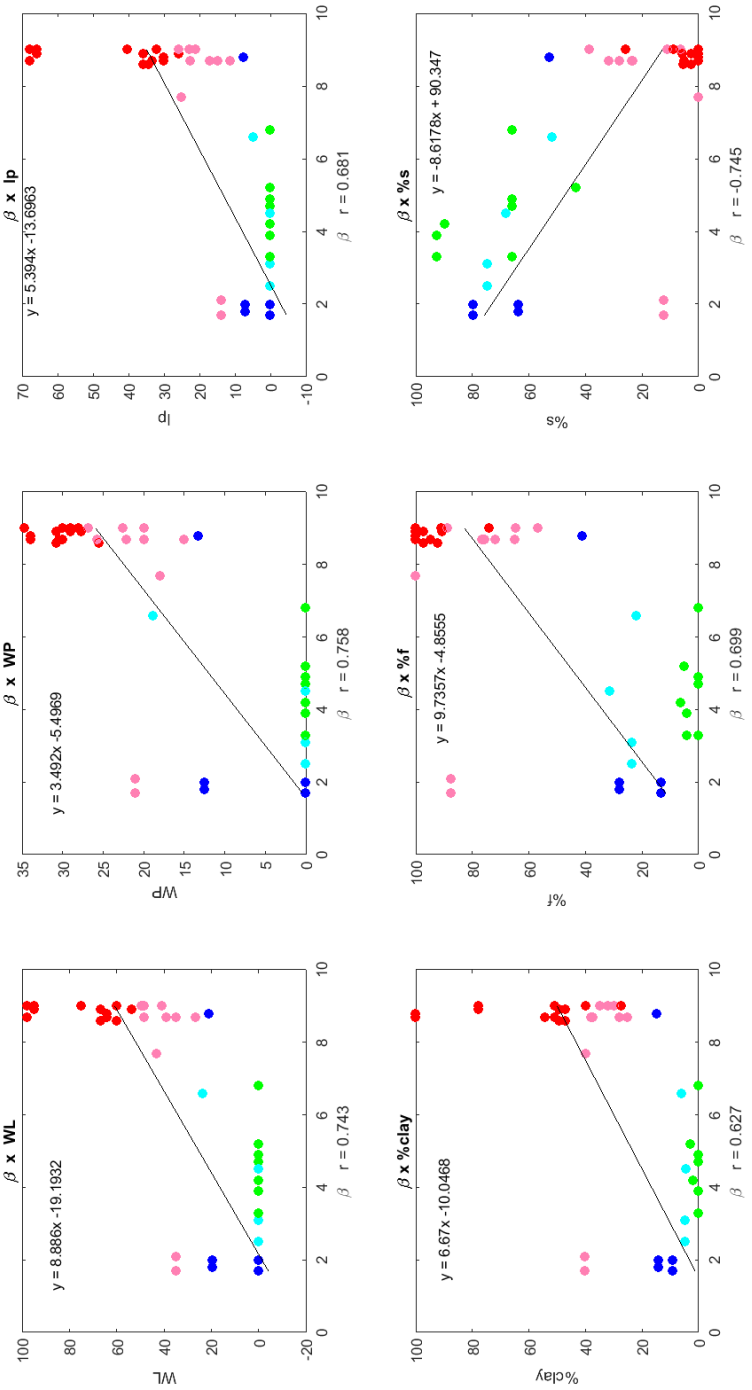

Figure C.14: Correlation for Atterberg's limits and particle contens: β

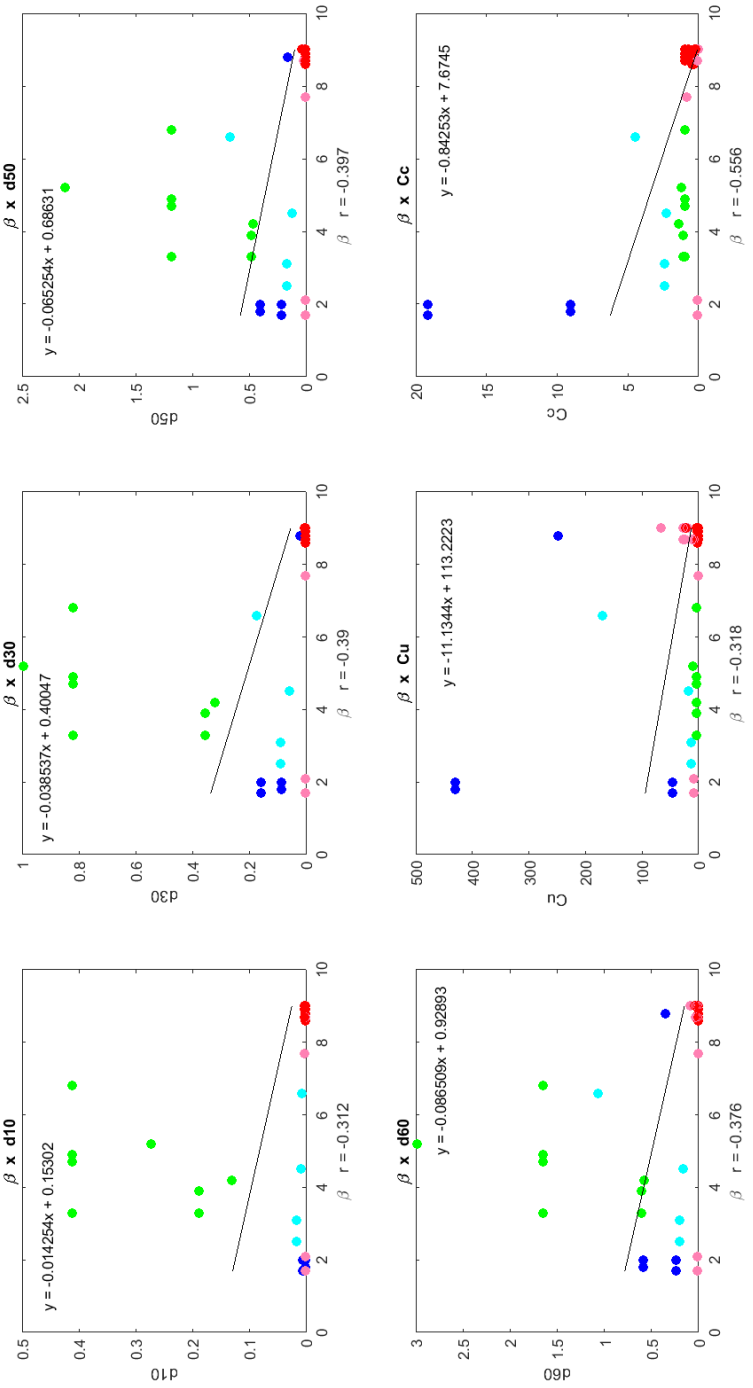

Figure C.15: Gradation characteristics: β

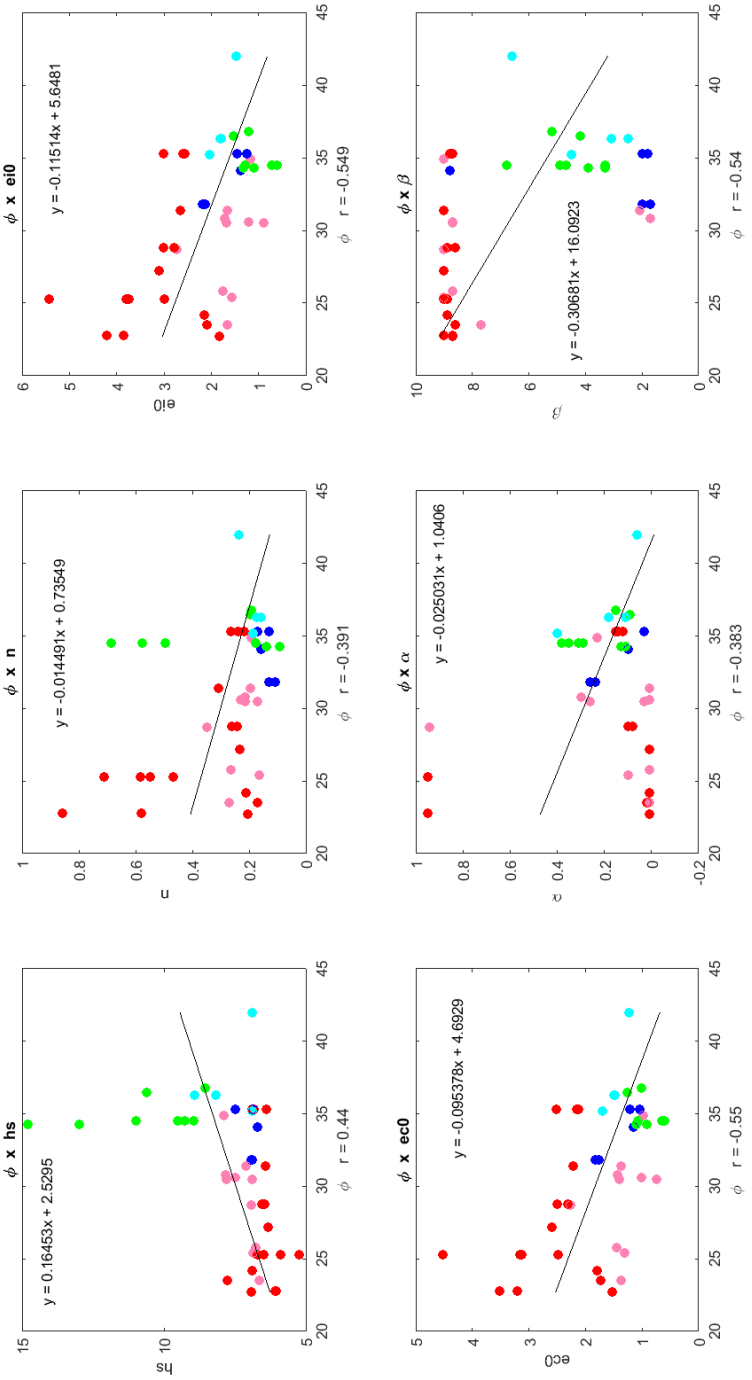

Figure C.16: Correlation between parameters: φ_c

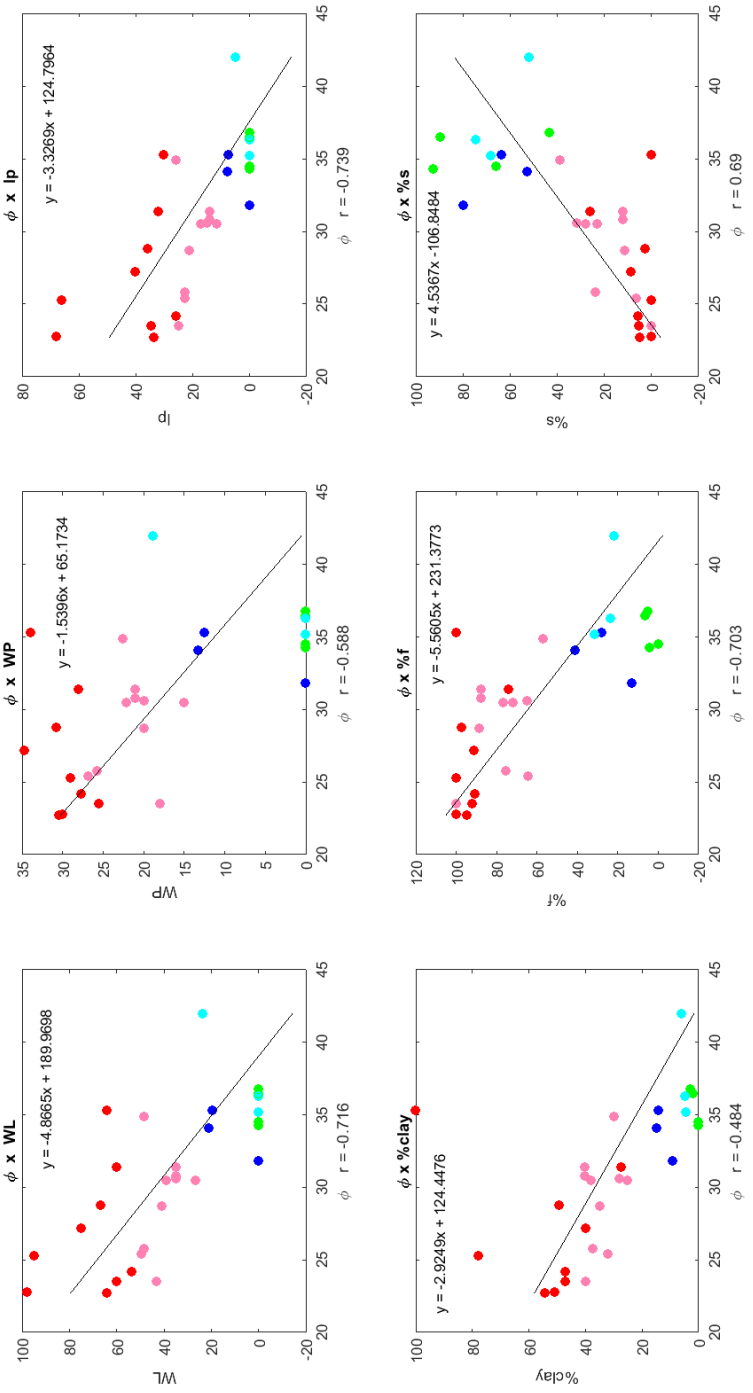

Figure C.17: Correlation for Atterberg's limits and particle contens: φ_c

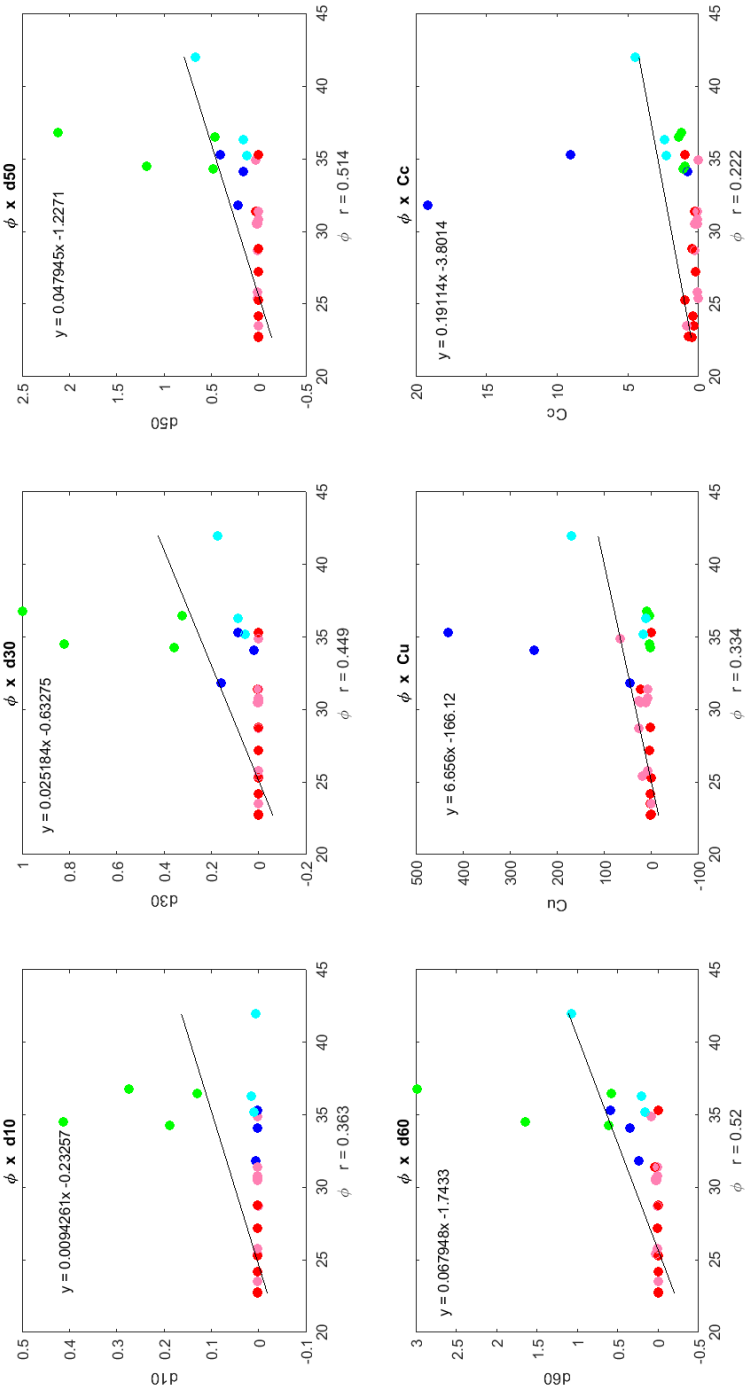

Figure C.18: Gradation characteristics: φ_c

Bibliography

[1] I. Herle and G. Gudehus, "Determination of parameters of a hypoplastic constitutive model from properties of grain assemblies," *Mechanics of Cohesive-frictional Materials: An International Journal on Experiments, Modelling and Computation of Materials and Structures*, vol. 4, no. 5, pp. 461–486, 1999.

[2] K. Roscoe and J. Burland, *On the generalised stress–strain behaviour of "wet" clay*, 1968, vol. 14, no. 3.

[3] D. Masin, "Clay hypoplasticity with explicitly defined asymptotic states," *Acta Geotechnica*, pp. 481–496, 2013.

[4] P. A. Wolffersdorff, "A hypoplasatic relation for granular materials with a predefined limit state surfaces," *Mechanics of cohesive-frictional materials*, vol. 1, pp. 251–271, 1996.

[5] W. F. Hosford, *Fundamentals of engineering plasticity*, 2013, ISBN:978-1-107-03755-7.

[6] M. Šejnoha, *Finite element analysis in geotechnical design*, 2012.

[7] P. W. Anrew Schofield, *Critical State Soil Mechanics*, 1968, ISBN:0598492771.

[8] J. W. Hai-Sui Yu, Cuong Khong, "A unified plasticity model for cyclic behaviour of clay and sand," *Mechanics Research Communications*, vol. 34, pp. 97–114, 2007.

[9] D. Kolymbas and W. Wu, "Numerical testing of the stability criterion for hypoplastic constitutive equations," *Mechanics of Materials*, vol. 9, no. 3, pp. 245–253, 1990.

[10] C. C. Wang, "A new representation theorem for isotropic functions: An answer to professor g. f. smith's criticism," 1970.

[11] D. Masin, "Hypoplasticity for practical applications, course handouts," 2015, [Online] Available: https://web.natur.cuni.cz/uhigug/masin/hypocourse.

[12] E. B. W. Wu and D. Kolymbas, "Hypoplastic constitutive model with critical state for granular materials," *Mechanics of Materials*, vol. 23, pp. 46–69, 1996.

[13] W. Wu, E. Bauer, and D. Kolymbas, "Hypoplastic constitutive model with critical state for granular materials," *Mechanics of materials*, vol. 23, no. 1, pp. 45–69, 1996.

[14] P.-A. Von Wolffersdorff, "A hypoplastic relation for granular materials with a predefined limit state surface," *Mechanics of Cohesive-frictional Materials: An International Journal on Experiments, Modelling and Computation of Materials and Structures*, vol. 1, no. 3, pp. 251–271, 1996.

[15] A. Niemunis, *Extended hypoplastic models for soils*. Inst. für Grundbau und Bodenmechanik, 2003, vol. 34.

[16] E. Bauer, "Calibration of a comprehensive hypoplastic model for granular materials," *Soils and foundations*, vol. 36, no. 1, pp. 13–26, 1996.

[17] G. Gudehus, "A comprehensive constitutive equation for granular materials," *Soils and foundations*, vol. 36, no. 1, pp. 1–12, 1996.

[18] A. Niemunis and I. Herle, "Hypoplastic model for cohesionless soils with elastic strain range," *Mechanics of Cohesive-frictional Materials: An Inter-*

national Journal on Experiments, Modelling and Computation of Materials and Structures, vol. 2, no. 4, pp. 279–299, 1997.

[19] D. Masin, "A hypoplastic constitutive model for clays," *International Journal for Numerical and Analytical Methods in Geomechanics*, vol. 29, no. 4, pp. 311–336, 2005.

[20] I. Herle and D. Kolymbas, "Hypoplasticity for soils with low friction angles," *Computers and Geotechnics*, vol. 31, no. 5, pp. 365–373, 2004.

[21] D. Masin and I. Herle, "State boundary surface of a hypoplastic model for clays," *Computers and Geotechnics*, vol. 32, no. 6, pp. 400–410, 2005.

[22] ——, "Improvement of a hypoplastic model to predict clay behaviour under undrained conditions," *Acta Geotechnica*, vol. 2, no. 4, p. 261, 2007.

[23] D. Masin, "Hypoplastic cam-clay model," *Géotechnique*, vol. 62, no. 6, pp. 549–553, 2012.

[24] ——, "Asymptotic behaviour of granular materials," *Granular Matter*, vol. 14, no. 6, pp. 759–774, 2012.

[25] ——, "A hypoplastic constitutive model for clays with meta-stable structure," *Canadian Geotechnical Journal*, vol. 44, no. 3, pp. 363–375, 2007.

[26] L. F. Shampine, *Numerical solution of ordinary differential equations*. CRC Press, 1994, vol. 4.

[27] P. Moin, *Fundamentals of engineering numerical analysis*. Cambridge University Press, 2010.

[28] A. Anandarajah, *Computational methods in elasticity and plasticity: solids and porous media*. Springer Science & Business Media, 2011.

[29] S. W. Sloan, "Substepping schemes for the numerical integration of elastoplastic stress–strain relations," *International journal for numerical methods in engineering*, vol. 24, no. 5, pp. 893–911, 1987.

[30] W. Fellin, M. Mittendorfer, and A. Ostermann, "Adaptive integration of constitutive rate equations," *Computers and Geotechnics*, vol. 36, no. 5, pp. 698–708, 2009.

[31] Y. Ding, W. Huang, D. Sheng, and S. W. Sloan, "Numerical study on finite element implementation of hypoplastic models," *Computers and Geotechnics*, vol. 68, pp. 78–90, 2015.

[32] S. Wang, W. Wu, C. Peng, X. He, and D. Cui, "Numerical integration and fe implementation of a hypoplastic constitutive model," *Acta Geotechnica*, pp. 1–17, 2018.

[33] C. Tamagnini, D. Salciarini, and R. Ragni, "Implementation of 6–dof hypoplastic macroelement in a finite element code," in *COM. Geo 2012: proceedings of the 3rd international conference on computing for geospatial research and applications*. Association for Computing Machinery Washington, DC, USA, 2013, pp. 60–71.

[34] C. Tamagnini, G. Viggiani, R. Chambon, and J. Desrues, "Evaluation of different strategies for the integration of hypoplastic constitutive equations: Application to the cloe model," *Mechanics of Cohesive-frictional Materials: An International Journal on Experiments, Modelling and Computation of Materials and Structures*, vol. 5, no. 4, pp. 263–289, 2000.

[35] R. Zentar, P. Y. Hicher, and G. Moulin, "Identification of soil parameters by inverse analysis," *Computers and Geotechnics*, vol. 28, no. 2, pp. 129–144, 2001.

[36] Z.-Y. Yin, Y.-F. Jin, J. S. Shen, and P.-Y. Hicher, "Optimization techniques for identifying soil parameters in geotechnical engineering: Comparative study and enhancement," *International Journal for Numerical and Analytical Methods in Geomechanics*, vol. 42, no. 1, pp. 70–94, 2018.

[37] S. Levasseur, Y. Malécot, M. Boulon, and E. Flavigny, "Soil parameter identification using a genetic algorithm," *International Journal for Numerical and Analytical Methods in Geomechanics*, vol. 32, no. 2, pp. 189–213, 2008.

[38] B. Lecampion, A. Constantinescu, and D. Nguyen Minh, "Parameter identification for lined tunnels in a viscoplastic medium," *International Journal for Numerical and Analytical Methods in Geomechanics*, vol. 26, no. 12, pp. 1191–1211, 2002.

[39] M. Calvello and R. J. Finno, "Selecting parameters to optimize in model calibration by inverse analysis," *Computers and Geotechnics*, vol. 31, no. 5, pp. 410–424, 2004.

[40] L. T. Nguyen and T. Nestorović, "Nonlinear kalman filters for model calibration of soil parameters for geomechanical modeling in mechanized tunneling," *Journal of Computing in Civil Engineering*, vol. 30, no. 2, p. 04015025, 2015.

[41] A. Papon, Y. Riou, C. Dano, and P.-Y. Hicher, "Single-and multi-objective genetic algorithm optimization for identifying soil parameters," *International Journal for Numerical and Analytical Methods in Geomechanics*, vol. 36, no. 5, pp. 597–618, 2012.

[42] Z.-Y. Yin and P.-Y. Hicher, "Identifying parameters controlling soil delayed behaviour from laboratory and in situ pressuremeter testing," *International Journal for Numerical and Analytical Methods in Geomechanics*, vol. 32, no. 12, pp. 1515–1535, 2008.

[43] Z.-Y. Yin, Y.-F. Jin, S.-L. Shen, and H.-W. Huang, "An efficient optimization method for identifying parameters of soft structured clay by an enhanced genetic algorithm and elastic–viscoplastic model," *Acta Geotechnica*, vol. 12, no. 4, pp. 849–867, 2017.

[44] Y.-F. Jin, Z.-Y. Yin, S.-L. Shen, and D.-M. Zhang, "A new hybrid real-coded genetic algorithm and its application to parameters identification of soils,"

Inverse Problems in Science and Engineering, vol. 25, no. 9, pp. 1343–1366, 2017.

[45] Y.-F. Jin, Z.-Y. Yin, S.-L. Shen, and P.-Y. Hicher, "Investigation into moga for identifying parameters of a critical-state-based sand model and parameters correlation by factor analysis," *Acta Geotechnica*, vol. 11, no. 5, pp. 1131–1145, 2016.

[46] M. C. Hill, "Methods and guidelines for effective model calibration," in *Building Partnerships*, 2000, pp. 1–10.

[47] I. Sula, *Development of calibration methods for hypoplastic models*, 2018, in Czech.

[48] R. E. Walpole and R. H. Myers, *Probability and statistics for engineers and scientists*. Pearson Education, 1993.

[49] Z. Hong, L.-L. Zeng, Y.-J. Cui, Y.-Q. Cai, and C. Lin, "Compression behaviour of natural and reconstituted clays," *Géotechnique*, vol. 62, no. 4, pp. 291–301, 2012.

[50] Z. Hong, J. Yin, and Y.-J. Cui, "Compression behaviour of reconstituted soils at high initial water contents," *Géotechnique*, vol. 60, no. 9, pp. 691–700, 2010.

[51] B. Tiwari and B. Ajmera, "New correlation equations for compression index of remolded clays," *Journal of Geotechnical and Geoenvironmental Engineering*, vol. 138, no. 6, pp. 757–762, 2011.

[52] M. W. Zaman, M. R. Hossain, H. M. Shahin, and M. A. Al Alam, "A study on correlation between consolidation properties of soil with liquid limit, in situ water content, void ratio and plasticity index."

[53] J. Atkinson, *Fundamentals of Ground Engineering*. CRC Press, 2014.

[54] J. Knappett and R. F. Craig, *Craig's soil mechanics*. CRC press, 2012.

[55] D. Masin, "Triax element driver," https://soilmodels.com/triax/, 2018.